INVESTIGATION OF SURFACE MODIFICATION OF PEROVSKITE WITH DIFFERENT CATALYSTS

Donglai Mao

A Thesis Submitted for the Degree of PhD
at the
University of St Andrews

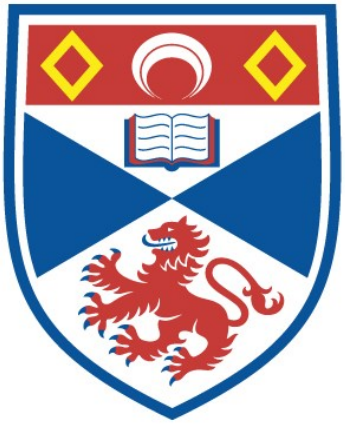

2016

Investigation of surface modification of perovskite with different catalysts

Donglai Mao

Supervised by Professor John T. S. Irvine

University of
St Andrews

This thesis is submitted in partial fulfilment for the degree of PhD
at the
University of St Andrews

August 2016

DECLARATION

1. Candidate's declarations:

I, Donglai Mao hereby certify that this thesis, which is approximately 46000 words in length, has been written by me, and that it is the record of work carried out by me, or principally by myself in collaboration with others as acknowledged, and that it has not been submitted in any previous application for a higher degree.

I was admitted as a research student in January, 2011 and as a candidate for the degree of PhD in September, 2012; the higher study for which this is a record was carried out in the University of St Andrews between 2012 and 2016.

I, Donglai Mao received assistance in the writing of this thesis in respect of language, grammar, spelling and syntax which was provided by Dr Scott Patrick and Dr Cristian Savaniu

Date …… signature of candidate ……

2. Supervisor's declaration:

I hereby certify that the candidate has fulfilled the conditions of the Resolution and Regulations appropriate for the degree of PhD in the University of St Andrews and that the candidate is qualified to submit this thesis in application for that degree.

Date …… signature of supervisor ……

3. Permission for publication:

In submitting this thesis to the University of St Andrews I understand that I am giving permission for it to be made available for use in accordance with the regulations of the University Library for the time being in force, subject to any copyright vested in the work not being affected thereby. I also understand that the title and the abstract will be published, and that a copy of the work may be made and supplied to any bona fide library or research worker, that my thesis will be electronically accessible for personal or research use unless exempt by award of an embargo as requested below, and that the library has the right to migrate my thesis into new electronic forms as required to ensure continued access to the thesis. I have obtained any third-party copyright permissions that may be required in order to allow such access and migration, or have requested the appropriate embargo below.

The following is an agreed request by candidate and supervisor regarding the publication of this thesis:

PRINTED COPY

Embargo on all or part of print copy for a period of 1 year on the following ground:

- Publication would preclude future publication

Supporting statement for printed embargo request:

Require 12 months embargo for future paper publication.

ELECTRONIC COPY

Embargo on all or part of electronic copy for a period of 1 year on the following ground:

- Publication would preclude future publication

Supporting statement for electronic embargo request:

Require 12 months to write papers for future publications.

Date …… signature of candidate …… signature of supervisor ……

ACKNOWLEDGMENTS

First of all, I would like to express my most sincere gratitude to my supervisor Prof. John T. S. Irvine for giving me the opportunity to study towards a PhD in his research group, giving me guidance when I felt lost in my PhD research, motivating me when I felt unconfident, and helping and supporting me when I had problems. It's been a great pleasure to study in his research group since everyone is so friendly and supportive. I could not have asked for a better supervisor and mentor for my PhD.

I would also like to sincerely thank many other members in the JTSI research group who have assisted me throughout my PhD. I'm very grateful to Dr Cristian Savaniu, for teaching me so many things, helping me so much with my research, and being such a good teacher and friend to me. Especially, I really appreciate his help in correcting my thesis. I should also thank Dr Dragos Neagu, for his constructive advice on my research project designs, experimental setups, data analysis and many other things. I would also like to thank Dr Maarten Verbraeken, for his assistance with VT-XRD experiment setups and data analysis; Dr David Miller, for teaching me how to use the TEM instrument and study my samples; Dr Samir Boulfrad for helpful discussions and showing me how to perform particle size analysis; and Dr George Carins and Dr Mark Tham for helping me with XRD data analysis using Rietveld Refinement. Many thanks to Dr Paul Connor, Dr Mark Cassidy, Dr Xiangling Yue, Dr Georgios Triantafyllou, Dr Chengsheng Ni, Dr Lanying Lu and Dr Jaeha Myung for sharing their time for discussions and advising me on my experiment designs and data analysis. I also would like to thank Mrs Julie Nairn for her help with experimental matters.

I would also like to thank many other people in the Chemistry department for their help and instructions with my experiments, including Mr Ross Blackley (SEM, TEM), Mrs Silvia Williamson (TGA), Dr Yuri Andreev (VT-XRD), Mr George Anthony and Mr Brian Walker for making different parts of equipment for my experiment.

I am very thankful to Dr Scott Patrick for helping me with my thesis correction and being so supportive during my PhD. Many thanks to my friends especially Dr Bing Liu, Miss Iona Ross, and Dr Thuy Muhl for making my PhD life so happy and enjoyable, I

really enjoyed the time with you.

I would also like to thank the China Scholarship Council and St Leonard Scholarship for the financial support.

Finally, I would like to express my sincere gratitude to my parents and my sister, without whom I could hardly have progressed this far. They have always been very supportive to me in their own ways.

ABSTRACT

The increasing energy requirements of mankind have stimulated the need to search for renewable clean energy in order to protect the environment. Proton Exchange Membrane Fuel Cells (PEMFC) are one of the most promising types of fuel cell among the entire range of power generation devices. However, the high quantity of noble metal catalysts used in PEMFCs hinders their commercialization due to the associated high cost. Decreasing the amount of noble metal catalysts without sacrificing the performance of the fuel cell is therefore desirable.

This thesis explores the possibility of modifying the perovskites with small quantities of the most commonly used catalysts (Ni, Ru and Pd) on its surface, with the intention to create a potentially cost-effective electrode material for PEMFC. The perovskites employed in this thesis include two of the most commonly studied perovskite materials, A-site deficient titanate based perovskites and $LaCrO_3$ based perovskites. The concept of the modification method is to combine two of the most promising state of the art methods, impregnation and exsolution, to improve the properties of the perovskite. Instead of incorporating the catalyst in the whole lattice of the perovskite, the impregnation method was used to dope the catalyst into the surface of the perovskite only. The exsolution of the doped catalysts from the perovskite was then attempted. This would theoretically produce nanoparticles with certain parts of its body anchored inside the perovskite, thus avoiding the catalyst agglomeration problem which has been reported for the normal impregnation method.

The A-site deficient titanate perovskite used to investigate surface doping modifications is $La_{0.4}Sr_{0.4}Ga_xTi_{1-x}O_{3-x/2}$ (LSGT). At first, a Ni catalyst was used to explore the possibility and optimal experimental conditions for catalyst doping of the perovskite from the surface and subsequent exsolution. The microstructure of the LSGT scaffold was optimized for later experiments. The results from the Ni doping study were then applied to the surface doping of Pd and Ru catalysts. This work demonstrates the possibility of incorporating Ni, Ru and Pd catalysts into the surface of A-site deficient titanate LSGT perovskite, using a pre-reduction treatment. The doped Ni and Pd catalysts managed to exsolve to the surface of the perovskite as nanoparticles after

reduction treatment. However, the Ru catalyst did not exsolve under the same experimental conditions. It has been found that different catalysts require different conditions to be able to dissolve into the perovskite for example, the heating atmosphere. In addition, the mechanism of incorporating Pd into the A-site deficient titanate has been studied, showing that the Pd is doped into the A-site deficient titanate in the form of Pd^{2+} with square planar 4-fold coordination on the B-site.

The $LaCrO_3$ based perovskite employed for studying the incorporation of a catalyst into the surface of the perovskite was $La_{0.75}Sr_{0.25}Cr_{0.5}Mn_{0.5}O_3$ (LSCM). The possibility of doping ruthenium into the surface of LSCM perovskite with the aid of a ball milling process has been explored by VT-XRD. It has been demonstrated that the Ru catalysts are able to dissolve into the lattice of LSCM perovskite on oxidation and exsolve as nanoparticles upon reduction. In addition, the addition of a Ru catalyst into the LSCM has been shown to improve the reducibility of the perovskite. Then the possibility of incorporating a Pd catalyst into the surface of LSCM perovskite was investigated. It was found that the Pd was unable to be doped into the LSCM perovskite due to the fact that the structure of LSCM was not rigid enough to accommodate the deficiencies introduced by Pd.

Catalytic tests of RWGS reactions were carried out with a few selected samples to preliminarily investigate the influence of the catalyst coating on the performance of the perovskite. It has been demonstrated that the catalyst coating technique was helpful in improving the catalytic activity of the perovskites.

The possibility of incorporating the catalyst into the perovskite from the surface and exsolving it afterwards depends on the properties of the host lattice and the catalyst itself, such as the sizes of the host lattice and the catalyst cations, the stability of the host lattice, etc. Through careful matching of the catalyst and the host lattice of the perovskite, the incorporation of the catalyst into the perovskite surface can be a promising method for decreasing the amount of catalyst required and therefore developing cost-efficient electrode materials for PEMFC.

Table of Contents

Chapter 1

Introduction

1.1 Worldwide Energy Requirements

With the rapidly growing human population and continued development of the economy, it is expected that global demand for energy services will grow by as much as an order of magnitude by 2050, while primary energy demands are expected to increase by 1.5–3 times as shown in Figure 1-1 [1]. Accompanying the increasing energy demand, global warming has become one of the most worrying environmental issues to date. This is caused by emissions such as CO_2, which are derived from the burning of fossil fuels as an energy source. Currently, the main sources of energy generation are oil, natural gas, coal, nuclear, hydro and renewable energy such as biomass, wind and solar. In order to meet future energy demands, potential ideas have been suggested, including improving energy efficiency, reducing the consumption of fossil fuels, and increasing the environmentally friendly energy supply, i.e. renewable sources and fuel cells. Fuel cell is a great solution to issues caused by the burning of fossil fuels if they are fuelled by hydrogen derived from non-fossil fuel sources. Fuel cells have the advantage of better constancy of the energy supply compared to unpredictable renewable sources such as solar, wind and wave power. However, the cost of fuel cells is one the main obstacles for their commercialization [2-4].

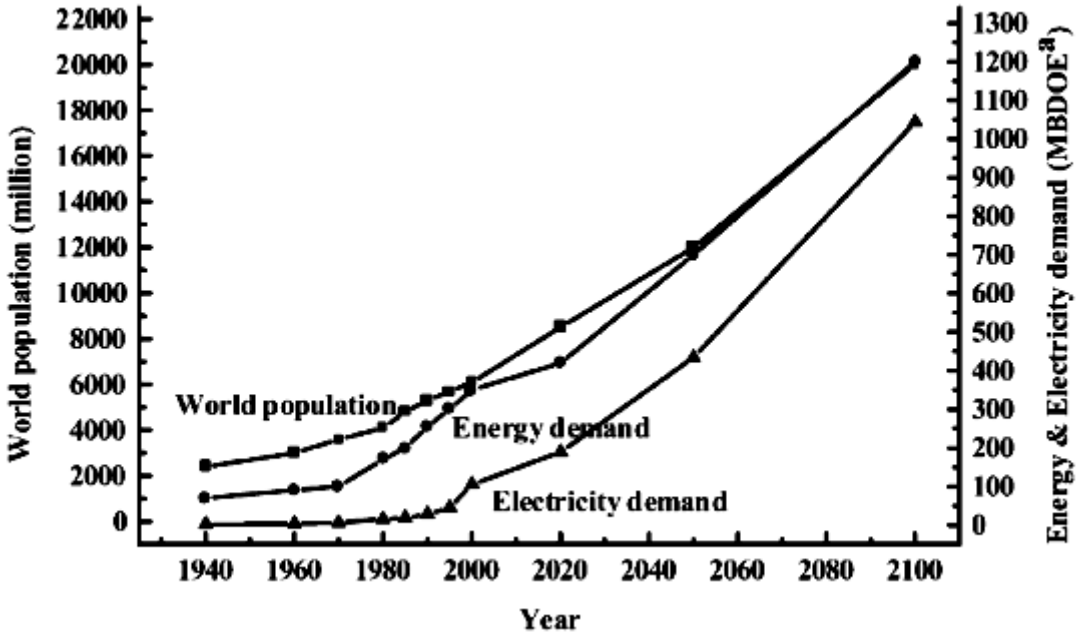

Figure 1-1 Actual and estimated world population, energy and electricity demands (Millions of barrels per day of oil equivalent) [1]

1.2 Fuel Cells

1.2.1 Introduction to Fuel Cells

In the early nineteenth century, the concept of a fuel cell had effectively been demonstrated by Humphry Davy. After this, Christian Friedrich Schönbein discovered the principle of fuel cells in 1838. One year later, William Grove, an English lawyer turned scientist, gained prestige by inventing the first fuel cell which generated electricity from an electrochemical reaction between hydrogen and oxygen over a platinum catalyst [5]. In the following years, a lot of effort was put into developing this area of research and continuous progress has been made [6, 7]. A particularly notable example is that, in 1960, fuel cells were successfully applied to the on-board electrical systems on the Apollo journey to the moon. In the mid-1980s, in the US, Canada and Japan, government agencies significantly increased their funding for fuel cell R&D. In 2007, the fuel cell industry began its road to commercialization. Today, fuel cells are widely used in the area of military applications (skid-mounted generators), portable products (torches, battery chargers), small personal electronics (mp3 players, cameras), stationary power plants (large stationary combined heat and power (CHP)), uninterruptible power supplies (UPS)), and transportation (fuel cell electric vehicles, trucks and buses) [8].

A fuel cell is an energy conversion unit that converts a gaseous fuel (hydrogen, natural gas, gasified coal) to electrical energy and heat by the electrochemical combination of a fuel with an oxidant. A fuel cell operates like a battery, but does not run down or require any recharging. Power can be continuously produced from it as long as fuel and oxidant are supplied. The distinct mechanism of a fuel cell is its ability to convert chemical energy directly to electrical energy. It is not limited by the Carnot cycle of a heat engine and is much more efficient in energy conversion than any conventional thermo–mechanical system thus extracting more electricity from the same amount of fuel. Additionally, with no vibration and combustion during its operation, it is virtually noise and pollution free. Moreover, this technology also presents flexibility and modularity as it does not suffer appreciably from problems of lubrication, wear, leakage and heat loss, which affect the reliability of traditional heat engines [9]. It is very competitive in

replacing a suite of power supplies in many portable, stationary and transport applications, from battery chargers to home heating and powering cars. In brief, a fuel cell is an efficient, quiet, clean and reliable power generation device which is the most universal energy solution ever created.

A fuel cell unit normally contains several single cells which consist of anode and cathode sandwiched around an electrolyte as shown in Figure 1-2. The hydrogen fuel is fed to the anode, which splits into protons (hydrogen ions) and electrons. The protons pass through the electrolyte, while the electrons create a separate current to power an external circuit before reaching the cathode. In the meantime, the oxygen from the air travels through the cathode and forms electrically charged oxygen ions that combine with the hydrogen ions passed across the electrolyte, forming water molecules and releasing heat. The electrolyte prevents any direct contact between the anode and the cathode, and passes the charged ions from one electrode to the other. Depending on which side of the fuel cell generates water, it can either be an oxygen ion conductor (in which water is formed on the fuel side, see Figure 1-2a), or a hydrogen ion (proton) conductor (in which water is formed on the oxidant side, see Figure 1-2b) [10].

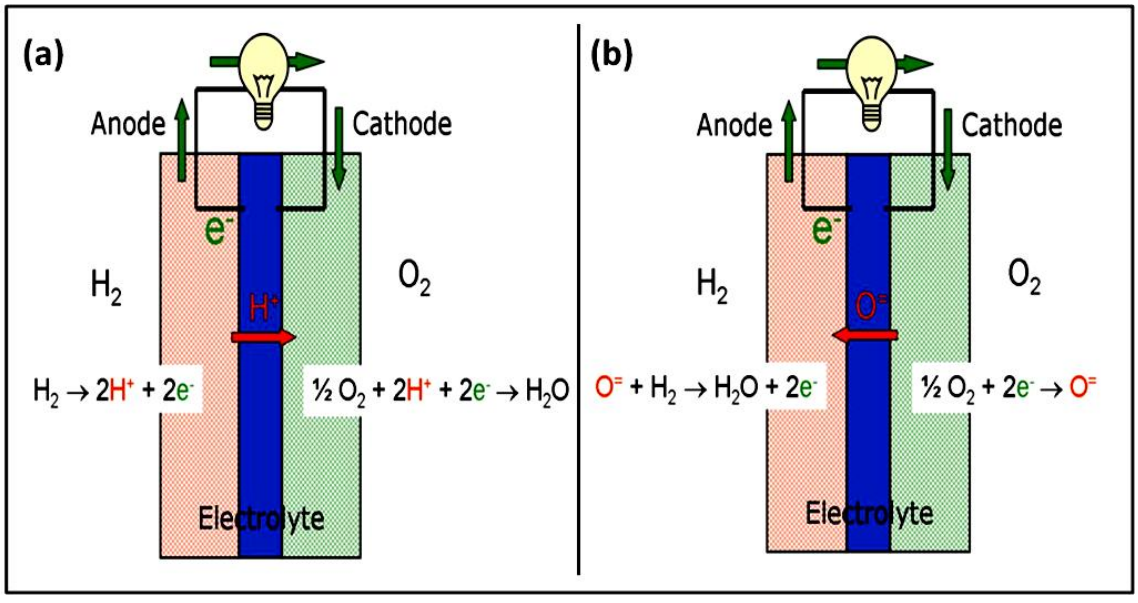

Figure 1-2 Schematic illustration of elements and operating principles of fuel cells: a. fuel cell with proton conducting electrolyte, b. fuel cell with oxide ion conducting electrolyte [11]

Despite the fact that all types of fuel cell have a similar operating principle, the materials and fuels used for different types of fuel cell may vary considerably from one another. In addition, the state of the electrolyte (i.e. whether it is liquid or solid)

determines the operating temperature of the fuel cell. Fuel cells are, therefore, generally sorted by their operating temperature and by the chemical characteristics of the electrolyte, as summarised in Table 1-1 [8, 12].

	Proton exchange membrane fuel cells (PEMFC)	Alkaline fuel cells (AFC)	Phosphoric acid fuel cells (PAFC)	Molten carbonate fuel cells (MCFC)	Solid oxide fuel cells (SOFC)
Electrolyte	Ion Exchange Membranes	Mobilized or Immobilized Potassium Hydroxide	Immobilized Liquid Phosphoric Acid	Immobilized Liquid Molten Carbonate	Ceramic
Operating Temperature	80°C	120°C - 150°C	200°C	650°C	800-1000°C
Charge Carrier	H+	OH-	H+	CO3-2	O-2
External Reformer for CH4	Yes	Yes	Yes	No	No
Catalyst	Platinum	Platinum	Platinum	Nickel	Perovskites
Prime Cell Components	Carbon-based	Carbon-based	Graphite-based	Stainless-based	Ceramic
Product Water Management	Evaporative	Evaporative	Evaporative	Gaseous Product	Gaseous Product
Usable rejected Heat recovery	Negligible	Negligible	Yes	Yes	Yes
Gaseous/ Liquid Water formation	Cathode	Anode	Cathode	Anode	Anode
Fuel	Pure H2 (tolerates CO2)	Pure H2	Pure H2 (tolerates CO2, 1.5% CO)	H2, CO, CH4, other hydrocarbons	H2, CO, CH4, other hydrocarbons
Electrical Efficiency	35%	40-60%	40-50%	50-60%	50-65%
Applications	Vehicles, small stationary	Submarines, spacecraft	Stationary	Stationary	Stationary

Table 1-1 Technical characteristics of different fuel cells [8, 12]

1.2.2 Proton exchange membrane fuel cells (PEMFCs)

Among all of the different types of fuel cells as can be seen from Table 1-1, Proton Exchange Membrane Fuel Cells (PEMFCs) are favoured for applications in cars and mass transportation as they have higher power densities than traditional internal combustion engines. In addition, PEMFCs have the advantages of relatively quick start-up time, rapid response to varying loads, and low operating temperatures compared to some other fuel cells. However, one remaining challenge is the resilience of different components of the fuel cell, e.g. the membrane electrode assembly (MEA), which may decide the life of the fuel cell. In order to improve the efficiency of the PEM fuel cell and reduce the CO poisoning effect on the Pt catalyst on the anode side, high temperature PEMFCs (HTPEMFC) have been developed which increase the working temperature range from 80°C to 100-200°C. The increase in the working temperature of the PEMFC makes it more difficult to find suitable electrode materials to work in the fuel cell [13-16]. In addition, it is well known that PEMFCs use platinum as the catalyst, especially the original PEMFCs which required a large amount of platinum. Although the price of the platinum has become lower over the last five years, platinum is still more expensive than other noble metals (see Figure 1-3). Currently, the main obstacles for the commercialization of the PEMFCs are the high cost and issues with longevity.

As a result of the challenges mentioned above, a lot of research has focused on minimizing the platinum loading by increasing the surface area of Pt nanoparticles, alloying Pt with other metal catalysts (Pt-M: M = Ru, Sn, Fe, Mo, Co, Ni, W, etc.), replacing the platinum with other cheaper metal catalysts or developing platinum free electrocatalysts, while enhancing the durability and performance of the MEA [17-25]. It has been reported that Pt nanoparticles which have high surface areas would agglomerate during the operation of the PEMFC, causing degradation of the cell performance [26, 27]. The advantages and limitations of other different types of catalysts commonly used for PEMFCs are shown in Table 1-2 [28]. Pd, Ru and Au catalysts have been reported to give very good performance in PEM fuel cells in place of a Pt catalyst [29-35]. However, the price of the above catalysts is still quite expensive if used on a large scale (see Figure 1-3). A lot of attention has also been paid to developing Pt-free catalysts which include transition metal oxides, macrocycles [36],

carbides [37], nitrides [38], oxynitrides [39], carbonitrides [40] and chalcogenides [41]. Although promising results have been reported for some of the materials, Pt-based catalysts still exhibit the best performance so far. More research is still needed to develop more cost-effective and efficient catalysts.

Catalyst type	Advantages	Limitations
Pt-based catalysts	Excellent characteristics of high activities for fuel cell reactions	High cost and relatively low stabilities
Modified Pt-based catalyst	Low cost and high durability under optimized conditions	Uncertainty for long-term applications
Pt-free non-noble catalysts	Low-cost and extensive resources	Relatively low activities

Table 1-2 Advantages and limitations of different types of catalysts for PEMFC [28]

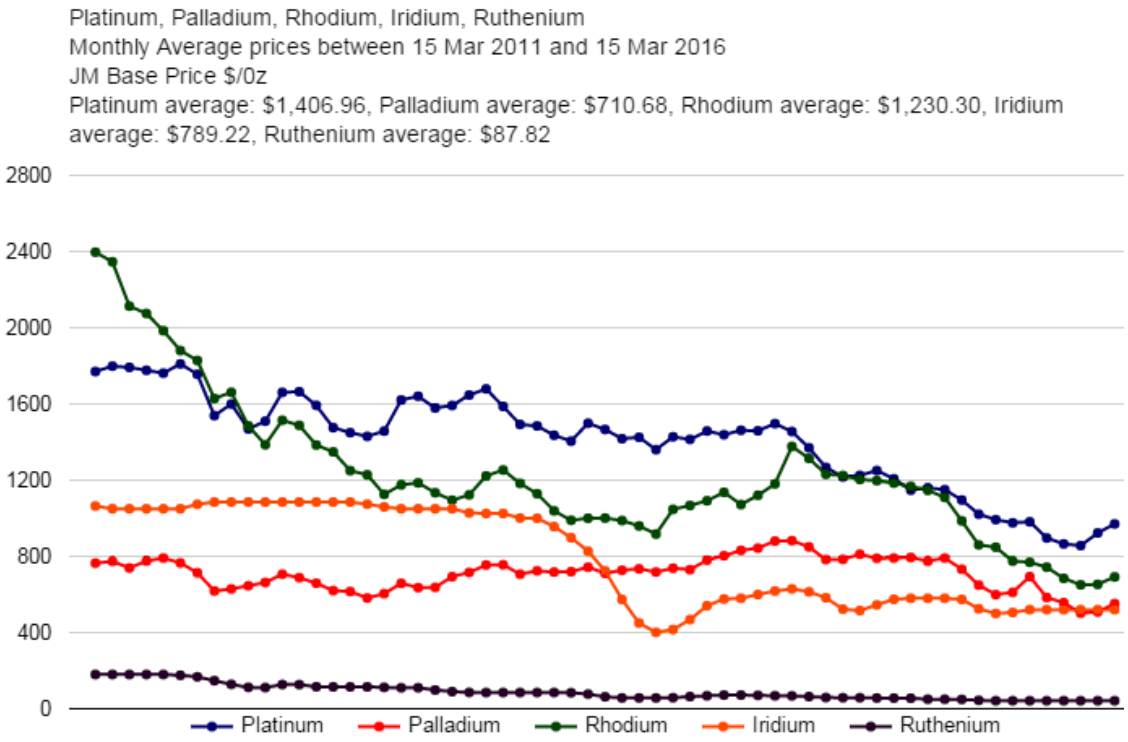

Figure 1-3 Monthly average prices of different noble metals within the last five years [42]

Due to their high electrical conductivity and outstanding catalytic activity, perovskite materials (ABO_3) have received considerable attention for study as non-noble catalysts for metal air batteries (MAB) and low temperature fuel cells (LTFC) in recent years.

Perovskite materials in MAB and LTFC applications have been demonstrated to show high activity and stability towards the electrochemical reactions (hydrogen oxidation reaction and oxygen reduction reaction, ORR) [43-49]. In addition, when being used as electrocatalyst in metal air batteries, the roundtrip efficiency (see Eq. 1-1) of perovskite materials have been reported to be higher than for the noble-metal catalysts [46, 49]. However, most of the research has focused on fuel cells using basic media. There were relatively few reports detailing the use of perovskite as an electrocatalyst in acidic environments, which are normally used in PEMFC.

$$\text{roundtrip efficiency (\%)} = \left(\frac{\text{energy}_{\text{discharge}}}{\text{energy}_{\text{charge}}}\right) \times 100\% = \left(\frac{\text{V}_{\text{discharge}}}{\text{V}_{\text{charge}}}\right) \times 100\% \qquad 1\text{-}1$$

L. Villaseca *et al.* synthesized $La_{0.94}MnO_{3+\delta}$ and $La_{0.7}Sr_{0.3}MnO_{3+\delta}$ perovskites and showed promising results for both samples towards the ORR in a PEMFC environment [50]. Approximately 90% of the elements in the Periodic Table are able to form perovskite oxides [51]. In addition, perovskite is known for being able to accommodate more than one type of cation in the A and B sites. Therefore, a greater variety of desired properties can be mixed together compared to the use of single materials. The physical and chemical properties of perovskite oxides can be adjusted by altering their composition, offering a fantastic chance for application in numerous areas [52]. There is definitely great potential to explore the applications of perovskite materials to replace Pt catalysts in PEMFC. The perovskite materials which have been studied as potential electrode materials in this thesis are derived from two of the most commonly studied perovskites: $SrTiO_3$ (strontium titanate) and $LaCrO_3$ (lanthanum chromite) since both of them exhibit reasonable electronic conductivities and excellent stability in a wide variety of fuel cells working environments [53-55]. More details of the structure and properties of perovskites will be introduced in the next section.

1.3 Background on perovskite oxide

1.3.1 The crystal structure of the perovskite

Perovskite-type oxides have the general chemical formula of ABO_3 with A being the larger cation and B being the smaller one. An ideal ABO_3 perovskite structure is cubic

as shown in Figure 1-4. A simple way to look at the perovskite structure is by considering the lattice as a cube in which B-site cations are located at the corners in 6-fold coordination with the oxygen anions, while A-site cations are located in the centre of the cube in 12-fold coordination with oxygen anions. The oxygen anions are placed in the middle of the cube boundaries. Another way of visualizing the perovskite structure is that the whole perovskite structure consists of a network of corner-sharing BO_6 octahedra in which the larger A-site cations are located in the central position [52, 56].

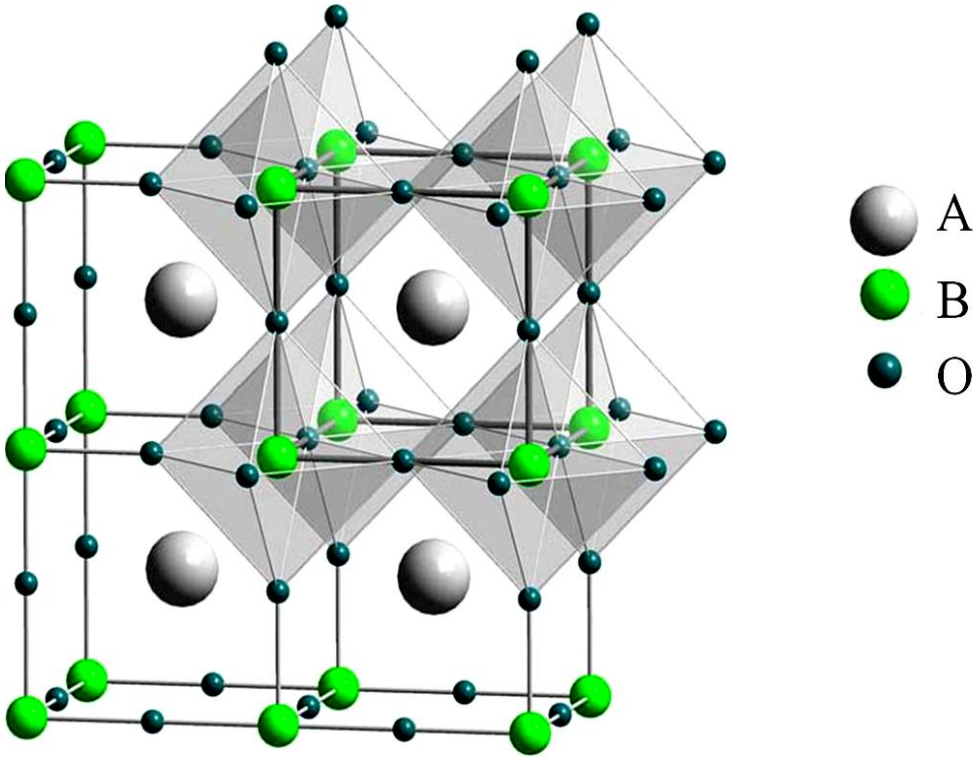

Figure 1-4 Schematic plot of ideal ABO_3 perovskite structure, adapted with permission from Ref. [57]

1.3.2 Cation substitution in the perovskite

Quite often, in order to endow the perovskite oxide with improved or more versatile properties for different applications, the A and/or B site of the perovskite is substituted with other cations. As a result of the replacement, the amount of defects can be increased if the dopants have different valences from the parent cations. Depending on which site the dopant is going to replace in the perovskite, and also the valence of the dopant, different types of vacancies will be introduced in the perovskite. When the B-site of the perovskite is substituted with cations with lower valence, oxygen ion

vacancies will be formed in the perovskite. Alternatively, when cations with higher valence substitute the B-site of the perovskite, oxygen interstitials will be generated in the perovskite. By replacing the A-site of the perovskite with cations of higher valence, A-site vacancies will be introduced into the perovskite. Meanwhile, when the valence of the dopant is lower than that of the parent cations in the A-site, oxygen vacancies will be introduced into the perovskite. The increase in the number of defects in the perovskite will potentially change the structure of the material and thus alter the diffusion pathways of oxygen ions which would eventually improve the catalytic activity, electronic conductivity or ion conductivity of the perovskite [52].

There are many factors influencing the probability of successfully incorporating other cations into the perovskite. Among all of these different facets, the size and the formal oxidation state (charge) of the dopants relative to the original perovskite cations have the biggest influence on deciding whether it is possible for the substitution to happen. In general, larger cations will fit in the A-site of the perovskite with higher oxygen coordination numbers (8-12), whereas smaller cations will occupy the B-site of the perovskite with lower oxygen coordination numbers (4-6). Therefore, the size of the cations dominates which site they will take in the perovskite. This can be understood better by looking at the plot in Figure 1-5, which shows the ionic radii as a function of coordination number for a few classic cations in perovskites. Apparently, the ionic radii and coordination zone for the A-site cations is very different from that of the B-site cations [58]. Following the above result, once the perovskite system is known, it is possible to estimate which site the dopant will occupy in the lattice according to the size of the cations.

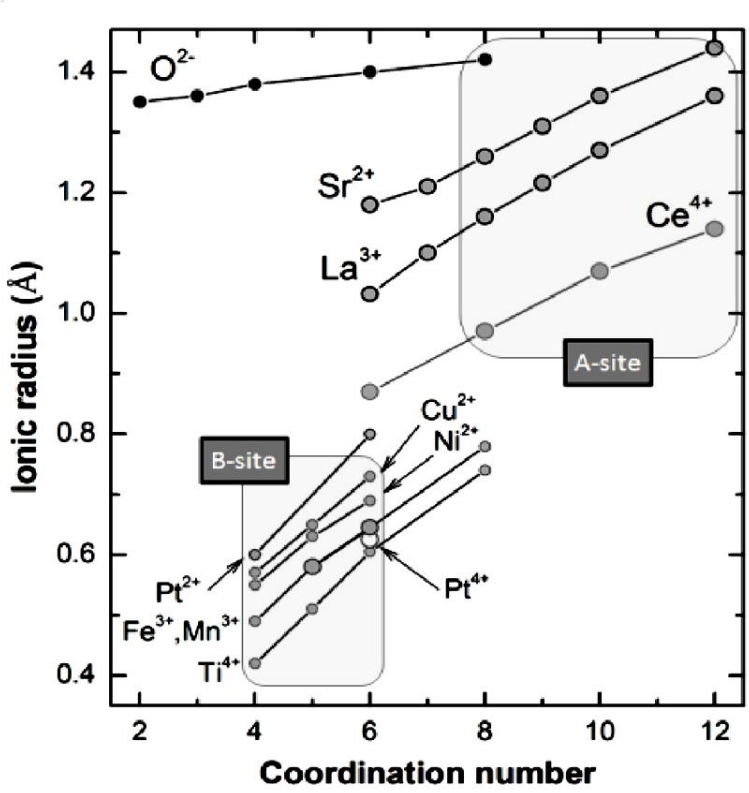

Figure 1-5 Relationship between ionic radii and coordination number for some representative A and B-site cations in perovskites [59, 60]

The size of the dopant itself can provide a very good prediction of which site a certain cation would occupy in the perovskite. However, in most of the cases, the dopant will still have a different volume compared to the cation being replaced. In addition, the size difference between the dopant and the site in the host lattice will cause distortion in the perovskite structure. The distorted perovskite structures normally display lower symmetry, caused by the size mismatch of the cations on the A or B site of the perovskite. If the chemical bonds in ABO_3 perovskite are viewed as purely ionic bonds, the way that perovskite accommodates the size mismatch can be illustrated by the difference between A-O and B-O bond lengths: tolerance factor (*t*).

$$t = \frac{r_A + r_O}{\sqrt{2}(r_B + r_O)} \qquad 1-2$$

r_A, r_B and r_O are the ionic radii of ions in the A, B and O sites of the perovskite which are acquired via X-ray diffraction at room temperature under atmospheric pressure [60]. It is worth pointing out that the tolerance factor is a measure of the extent to which the

perovskite deviates from the ideal perovskite structure. Therefore, it still applies to the perovskite even if there is no cation substitution in the perovskite. In the case where more than one type of cation is present in the same site, the average of their ionic radii will be used. Generally, the value of t is within the range $0.78 < t < 1.10$. When t is below this range, the structure of the metal oxide will become ilmenite [61]. In an ideal perovskite with cubic structure, $t = 1$, which means:

$$r_A + r_O = \sqrt{2}(r_B + r_O) \qquad 1-3$$

For $t > 1$, the A-site cations are larger than required. In this case, the BO_6 octahedra need to be expanded to make enough space for the A-site cations. As a result, the B-site cations shift away from the centre of the octahedra. The Ba^{2+} cation on the A-site of $BaTiO_3$ is fitted in the perovskite in this way (compared to $SrTiO_3$, in which case $t = 1$) and its ferroelectricity is increased as a result of the deformation (see Figure 1-6a). However, further distortion of the perovskite will lead to the generation of hexagonal polytypes in the perovskite structure [61-63]. For $t < 1$, the A-site cations are not large enough to fit in the perovskite with the 12-fold coordination. In this case, the perovskite will go through tilting and rotation of the BO_6 octahedra about one or more of the three axes of the octahedron (also known as octahedral tilting). As a result, the size and coordination number of the A-site is reduced, and the structure of the perovskite changes from cubic to lower symmetries [61, 64-69]. Normally, the degree of tilting in most of the perovskite is influenced by the temperature; increasing the temperature will reduce tilting in the perovskite. Therefore, it is quite common to see the structure of some perovskites change from non-cubic to cubic at high temperatures [64, 70-72].

In addition, it is worth pointing out that t is a very important indicator of the extent of the distortion of the perovskite structure but is not the only factor to be considered when deciding the properties of the perovskite. Since the value of t purely depends on the size of the ions in the perovskite, it cannot represent the effects of other factors which will also influence the property of the perovskite. These features include the covalent interactions between cations and anions, the nature of the cations on the A and B-site especially when there is more than one type of cations on each site, the amount of dopants, the coordination number of each cation, deficiencies in the perovskite, etc. [67,

73-75].

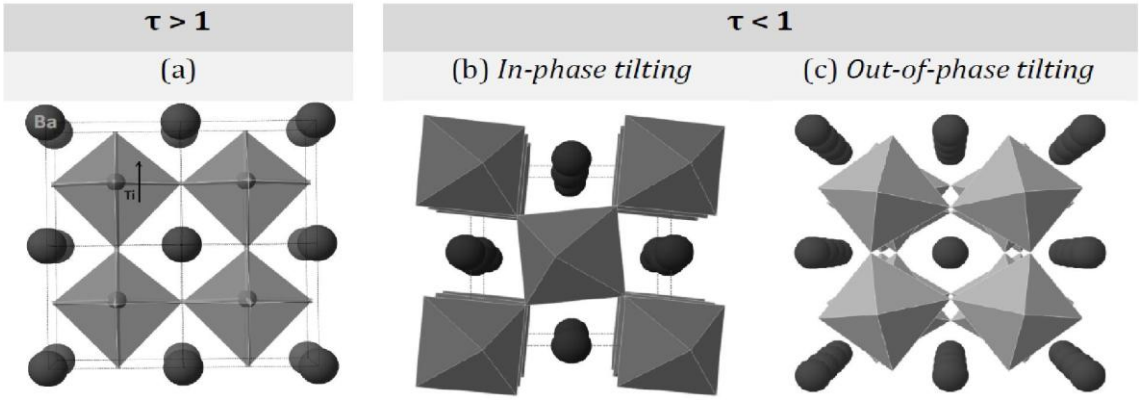

Figure 1-6 Different types of distortion in perovskites: (a) *t*>1, the BO_6 octahedra are expanded enabling the B-site cation to shift away from its symmetry centre; (b) *t*<1, in phase tilting in perovskite, BO_6 octahedra are tilting in the same direction as the neighbouring layer; (c) *t*<1, out-of-phase tilting in perovskite, BO_6 octahedra are tilting in the opposite direction as the neighbouring layer [59]

1.3.3 Non-stoichiometry in the perovskite

It is inevitable that certain amounts of defects will be present in the perovskite since they help to stabilize it by reducing its free energy. Meanwhile, the concentrations of the defects can be notably controlled and adjusted by substitution of other cations in the perovskite. As a result, the defect chemistry of the perovskite can be tailored to give a non-stoichiometric perovskite. The introduction of non-stoichiometry in the perovskite is achieved by replacing the parent cations with other cations of similar size but different valence. Depending on the valence of the dopant, the stoichiometry of the perovskite can be quite different after substituting new cations in the perovskite. The different possible non-stoichiometry of A-site and O-site in the perovskite is displayed in a Cartesian diagram in Figure 1-7, which is under the condition that the B-site of the perovskite is fully occupied [76]. The origin of the plot is defect free ABO_3 with O-site non-stoichiometry on the x-axis and A-site non-stoichiometry on the y-axis. Based on the graph, there are two possible scenarios for the perovskite to be non-stoichiometric on the A-site and O-site. When the molar ratio of A/B<1 and/or O/B<3, the perovskite is classified as sub-stoichiometric (deficient), examples of which include tungsten bronzes ($A_{0.6}BO_3$), brownmillerite structure $A_2B_2O_5$ ($A_nB_nO_{3n-1}$ series, $n = 2$), etc. (see quadrant **III**). When the molar ratio of A/B>1 and/or O/B>3, the perovskite is classified as super-stoichiometric (excess), examples of which include Ruddlesden-Popper phases

$A_{n+1}B_nO_{3n+1}$ ($n\geq1$), homologous series $A_nB_nO_{3n+2}$ ($n\geq4$), etc. (see quadrant **I**) [77-80].

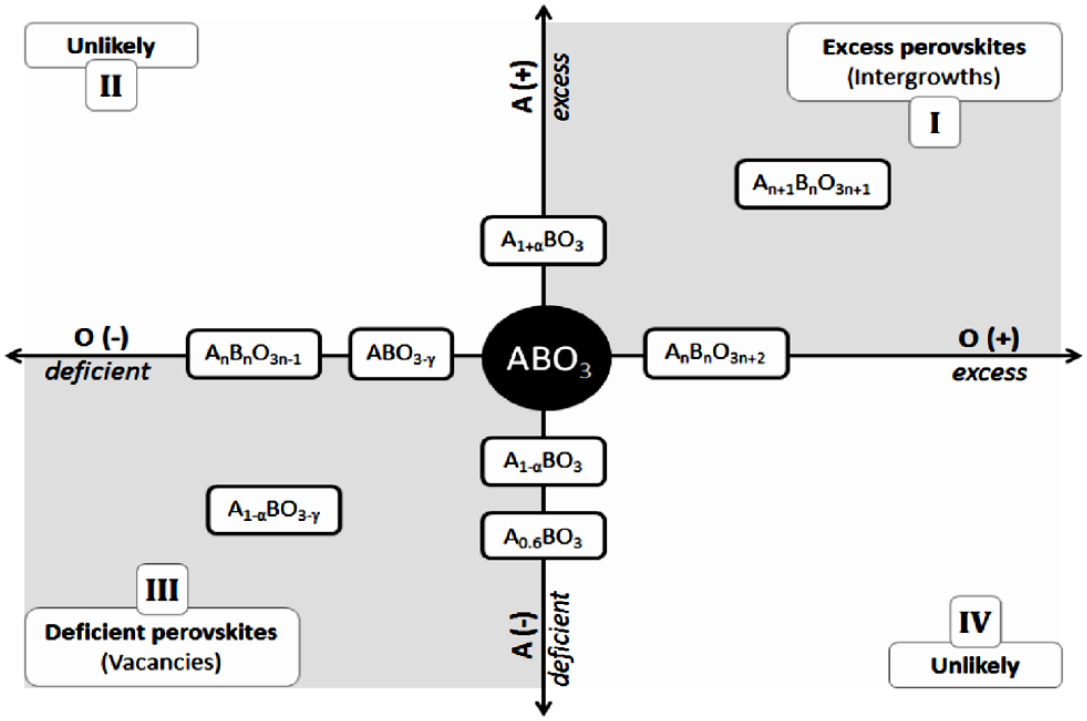

Figure 1-7 Schematic plot of non-stoichiometry of A-site and O-site of the perovskite in a Cartesian plane [76]

1.4 Exsolution of cations from the perovskite

1.4.1 Background on exsolution of cations from the perovskite

Phase segregation from the perovskite, which used to be viewed as an undesirable property, has recently become one of the most popular research topics. This is because the metal catalyst nanoparticles are segregated from the perovskite in such a way that they may serve as catalysts on the surface of the perovskite. As discussed earlier in section 1.3, incorporating the catalysts into the perovskite itself can promote electronic and ionic conductivity, as well as the catalytic activity of the perovskite. This is due to the different nature, charge and size of the catalyst cations compared to the cations in the host lattice. On top of that, it has been demonstrated that the doped metal catalyst can exsolve as nanoparticles from the perovskite upon reduction. This redox exsolution of the metal catalyst from the perovskite phenomenon is viewed as a phase segregation process in the current research [76, 81, 82]. The exsolved metal catalyst nanoparticles

can further improve the catalytic performance of the perovskite. In addition, the exsolved metal catalysts show higher stability compared to the traditional ones which were dispersed on the surface of substrate material using the impregnation method. What is more, in some cases, the redox exsolution of catalysts is even reversible, in which case the exsolved metal nanoparticles are able to diffuse into the perovskite lattice during oxidation and exsolve again during reduction. This special feature will magnificently prolong the life time of the catalysts [83, 84]. Therefore, exsolving the catalysts from the perovskite lattice is a very promising way of utilising catalyst in fuel cell reactions and lots of other reactions.

The research to date has proposed that, in order to enable the redox exsolution of the metal catalyst from the perovskite, the perovskite must be reduced to the degree that an adequate amount of oxygen is stripped from the perovskite until it reaches the limit of the perovskite. To balance the oxygen loss during the reduction, the perovskite will exsolve B-site catalyst cations in the lattice. The exsolved catalyst will be immediately reduced to metal and start nucleation on the surface of the perovskite where there are more crystal defects. The crystal defects on the perovskite surface will lower the surface energy of the lattice and favour the nucleation process. As the metal cations form crystals on the surface of the perovskite lattice, a compositional gradient will form, causing the neighbouring cations to diffuse to the surface. The metal cations in the bulk of the perovskite diffuse to the surface of the lattice in this way to sustain the growth of metal particles [81, 82, 85]. According to Horvath *et al.* [86], "the possible contributions to the segregation driving forces [are]:

a) The different vacancy-formation energies of the components
b) The elastic strain energy due to lattice distortion around a defect
c) The effect of the ambient atmosphere
d) The macroscopic electrostatic potential, which appears as a consequence of the locally non-stoichiometric charged species
e) The effect of surface energy
f) The energies due to the interactions between the defects"

Among all of the factors mentioned above, lattice defects play a very important role in the modification of many properties of perovskites and have become one of the most popular research topics over the last few decades [87]. For example the quantity of A-

site and oxygen deficiencies directly influences the ability of the material to transport oxygen and cations. They do so by minimising the collisions of ions as they diffuse through the lattice and providing hopping sites. In addition, due to the fact that stoichiometric composition is the most stable status for the perovskite, the existence of the A-site and oxygen vacancies will, therefore, promote the exsolution of catalyst cations on the B-sites in order to maintain the stability of the perovskite.

The perovskite series which have been studied with regard to metal catalyst exsolution from the B-site of the perovskite include titanate, ferrite and chromite or chromite-manganite. The metal catalysts which have been studied to show the redox exsolution property in the perovskite include Ni, Ru, Rh, Pd and Pt [76, 81-96]. In this thesis, the perovskite systems which are going to be studied are two of the most studied perovskite series, modified strontium titanate, $SrTiO_3$, and lanthanum chromite, $LaCrO_3$. More detailed discussion about them will be shown in the following section.

1.4.2 Exsolution from A-site deficient La substituted $SrTiO_3$ based perovskites

Due to the high conductivity, inherent redox stability, and excellent tolerance to sulphur and coking, La substituted $SrTiO_3$ (LST) have been extensively studied by many research groups. Zhou *et al* have reviewed the development of the material in detail [97]. The influence of the A-site deficiencies on the properties of $SrTiO_3$ based perovskite has been reviewed by Verbraeken *et al* [98]. In this section, we mainly focus on discussing the cation exsolution from A-site deficient La substituted $SrTiO_3$ based perovskite (LST_A). Slater *et al.* first reported LST perovskite with A-site deficiency $La_xSr_{1-3x/2}TiO_3$ as a potential anode material for SOFC [99]. Later, more studies on the LST_A perovskite series were carried out by a number of researchers. They obtained and reported promising results with a focus on adjusting the A-site deficiencies, incorporating other cations into the perovskite and depositing catalysts on the surface of the perovskite for fuel cell applications [76, 81, 85, 100-107].

Recently, it has been found that A-site deficiency could serve as a driving force for exsolving the catalyst cations on the B-site of the LST_A as nanoparticles, which further

improve the performance of the perovskite. Neagu *et al.* have incorporated different catalysts in $La_{0.4}Sr_{0.4}TiO_3$ with different catalyst, $La_{0.4}Sr_{0.4}M_{0.06}Ti_{0.94}O_{3-\gamma}$ (M = Mn, Fe, Ni, Cu) and observed nano particle exsolution after reducing the samples. The exsolved nanoparticles have been proven to significantly improve the electrocatalytic activity of the perovskite. In addition, the stability and surface structure of the perovskite can be further optimised by modifying the stoichiometry as exemplified by $La_{0.4+2x}Sr_{0.4-2x}Ni_xTi_{1-x}O_3$ and $La_{0.4+x}Sr_{0.4-x}Fe_xTi_{1-x}O_3$ [76, 85]. With half of its body confined inside the parent perovskite, the exsolved catalyst nanoparticles have stronger correlation with the surface of the substrate, and showed better stability and tolerance to coking compared to the catalyst deposited on the surface of the perovskite [81].

Yaqub *et al.* substituted the A-site of LST_A with a certain amount of Ca $La_{0.2}Sr_{0.25}Ca_{0.45}TiO_3$ ($LSCT_{A-}$) and incorporated Ni or Fe in the B-site of the perovskite to improve the conductivity of the parent perovskite. Apart from the increased conductivity, catalyst nano particle exsolution was also observed on the surface of the perovskite after reducing the samples, which agrees with the hypothesis that A-site deficiency would promote the exsolution of the B-site cations [108].

Li *et al.* incorporated Ni in A-site deficient titanate with the nominal molecular formula of $(La_{0.2}Sr_{0.8})_{0.9}(Ti_{0.9}Mn_{0.1})_{0.9}Ni_{0.1}O_{3-\delta}$ for the application of direct CO_2 electrolysis at high temperature. Exsolved Ni nanoparticles appeared on the surface of the perovskite after reduction and enhanced electrocatalytic activity was observed. In addition, the exsolved Ni catalysts have been shown to improve the electrochemical performance of the perovskite when being used as electrode material in fuel cells [109].

There is great potential in the application of exsolved catalysts on the surface of the perovskite with the help of A-site deficiency in $SrTiO_3$ based perovskite. More research still needs to be conducted to explore the possible applications of this concept.

1.4.3 Exsolution from $LaCrO_3$ based perovskites

Despite the fact that $LaCrO_3$ based perovskite materials exhibit very good stability and high electrical conductivity, the materials show very poor ionic conductivity as p-type semiconductors. Apart from depositing catalyst on the surface of the perovskite or

combining it with other metal oxides, the perovskite is doped with other cations on either A-site or B-site or both sites to improve its properties. The most common A-site dopants include Mg, Ca and Sr, among which Ca and Sr have a more profound influence on improving the properties of the $LaCrO_3$. Fergus has summarized the influence of different A-site dopants on the properties of $LaCrO_3$ [110]. Meanwhile, there are many transition metals which may be incorporated into the B-site in the $LaCrO_3$ based perovskite, such as Mn, Fe, Co, Ni, Cu, Ru, etc. [111]. There are many papers about doping the $LaCrO_3$ based perovskite with other transition metal cations in its lattice. In this section, we mainly focus on introducing the ones which has catalyst incorporated on their B-site and shows catalyst exsolution from its lattice under reducing conditions.

Kobsiriphat *et al.* substituted part of Cr with different amounts of Ru catalyst in the $LaCrO_3$ based perovskite, $La_{0.8}Sr_{0.2}Cr_{1-x}Ru_xO_{3-\delta}$ (LSCrRu), and observed Ru nano particle exsolution after reducing the perovskite. The density of the exsolved Ru particles is influenced by the proportion of Ru in the parent perovskite and the temperature, with higher Ru proportions and higher temperatures promoting more Ru particles to exsolve to the surface of the perovskite. In addition, higher temperatures also generated ruthenium particles of larger sizes. The exsolved Ru nanoparticles have been shown to exceptionally improve the electrical performance of the perovskite when compared to the perovskite with ruthenium catalyst simply deposited on the surface. In addition, the exsolved Ru nanoparticles have also shown very good stability throughout electrochemical tests [112, 113]. Later, the author also tried to incorporate Ni catalyst in the B-site of the perovskite, $La_{0.8}Sr_{0.2}Cr_{1-x}Ni_xO_{3-\delta}$ (LSCrNi). The exsolved Ni nanoparticles were 10 nm in diameter, which was larger than the exsolved Ru nanoparticles (less than 5 nm in diameter) under the same experimental conditions. In addition, the Ni nanoparticles agglomerated to 50 nm after reducing for an extended period of time; these proved less stable than the Ru nanoparticles. Although both catalysts improved the performance of the perovskite, the exsolved Ru catalyst nanoparticles showed better performance than Ni counterparts [82].

Bierschenk *et al.* incorporated different quantities of Pd catalyst into the B-site of the $LaCrO_3$ based perovskite, $La_{0.8}Sr_{0.2}Cr_{1-x}Pd_xO_{3-\delta}$ (LSCrPd) and observed Pd nano particle exsolution after reduction. The exsolved Pd nanoparticles were shown to

improve the performance of the perovskite at the beginning of fuel cell testing although later the performance of the perovskite started to degrade before finally stabilising. In addition, the Pd nano particle exsolution in this report was regenerative and showed redox stability, which helped solve the coarsening problem of the catalyst [114].

One of the most promising $LaCrO_3$ perovskite derivatives is $La_{0.75}Sr_{0.25}Cr_{0.5}Mn_{0.5}O_3$ (LSCM) which was first reported by Tao and Irvine [111]. Therefore, not surprisingly, there has been a great deal of research into the application and modification of this perovskite material. The modified LSCM perovskites which showed Ni nano particle exsolution phenomena were reported by Jardiel *et al.* and Papargyriou *et al*. According to the report from Jardiel *et al.*, the exsolved Ni catalyst helped to improve the catalytic activity and selectivity of the perovskite towards methane oxidation [115]. In the following report using perovskite as an electrode material for fuel cells, the perovskite was shown to be a very promising electrode material for fuel cells, although it still needed to be further improved for practical applications [116]. Meanwhile, Papargyriou *et al.* demonstrated that Ni catalyst exsolution helped to improve the reducibility and conductivity of the perovskite [117]. Monteiro *et al*. also reported that Ru could be incorporated into LSCM, and that it showed exsolution phenomena after reduction. The exsolved Ru nanoparticles have been shown to improve the electronic conductivity of the perovskite [88].

In addition to exsolving catalyst nanoparticles from stoichiometric LSCM substituted with catalyst, there are also reports showing the possibility of exsolving catalyst from A-site deficient LSCM doped with catalyst. Li *et al.* incorporated Cu into the A-site deficient LSCM, $(La_{0.75}Sr_{0.25})_{0.9}(Cr_{0.5}Mn_{0.5})_{0.9}Cu_{0.1}O_{3-\delta}$ and exsolved Cu nanoparticles from the perovskite. With the Cu nano particle exsolution, the catalytic activity for CO_2 electrolysis has been enhanced. Furthermore, the Cu nanoparticles have also been demonstrated to improve the electrochemical performance of the material [118]. Ruan *et al.* from the same research group later reported $(La_{0.75}Sr_{0.25})_{0.9}(Cr_{0.5}Mn_{0.5})_{0.9}Ni_{0.1}O_{3-\delta}$ exsolving Ni particles on the surface of the perovskite. The Ni nanoparticles improved the catalytic activity and electrochemical performance of the perovskite to a similar extent as the exsolved Cu catalyst in the previous report. The exsolved Ni catalyst is regenerative, which significantly prolonged the lifetime of the catalyst [119].

1.5 Impregnation method to improve the performance of perovskite

Impregnation, also called infiltration is a nanoscale engineering technique which deposit catalytically and/or electrochemically active nanoparticles onto a ceramic backbone via high temperature treatment. This technique has been widely studied in the application of heterogeneous catalysis and fabrications or modification of components in SOFC during the last 15 years [103, 120-126]. There are many comprehensive reviews about this subject; here we mainly focus on introducing the basic knowledge about this technique [126-130]. The process of impregnation is illustrated in Figure 1-8. First of all, a mechanically strong porous scaffold is prepared at high temperature (see Figure 1-8a). Then the precursor solution is infiltrated into the scaffold as shown in Figure 1-8b. The infiltrated skeleton then goes through thermal treatment which produces nanoparticles with two possible microstructures: disconnected individual particles (see Figure 1-8c), or a continuous thin layer of catalyst film (see Figure 1-8d) [129]. The loadings of the catalyst are normally in the range of 1-10 wt%, sometimes even higher depending on the application purpose of the catalyst. In general, the infiltration process has to be repeated at least a few times in order to reach the target loadings of the catalyst.

The infiltration technique is very useful in maximizing the triple phase boundary in SOFC due to the high surface areas of catalyst nanoparticles. In addition, it offers very high flexibility in choosing the catalyst to be deposited onto the scaffold ranging from single metal or metal oxide catalyst, metal catalyst alloys, perovskite oxide electrodes to the composites of the above components, etc. Compared to the high temperatures required for preparing backbone material, it requires much lower temperatures to decompose the precursor solution and form the desired phases, thus offering the possibility of inserting electrode materials which cannot be heated at high temperatures due to reasons such as low melting point [122, 127, 130-134].

Although the infiltration method is one of the most commonly used and effective ways of improving the performance and stability of the ceramic material in different applications, there are still a few challenges which remain: (a) the long-term microstructural and morphological stability because of the coarsening problem at high

temperature, (b) scalability for commercialisation purpose due to the high time and energy consumptions to reach certain amount of target loadings, (c) extra cost related to the process itself [129, 135]. The stability of the catalyst can be enhanced by controlling wettability of the precursor solution on the scaffold material [136]. The issues of scalability and extra cost of the technique can be significantly optimised by using a layer-by-layer assisted impregnation method, or using molten salts as a precursor for impregnation [137, 138]. Overall, the impregnation technique is still one of the most viable ways in which to modify the surface of perovskites for better performance.

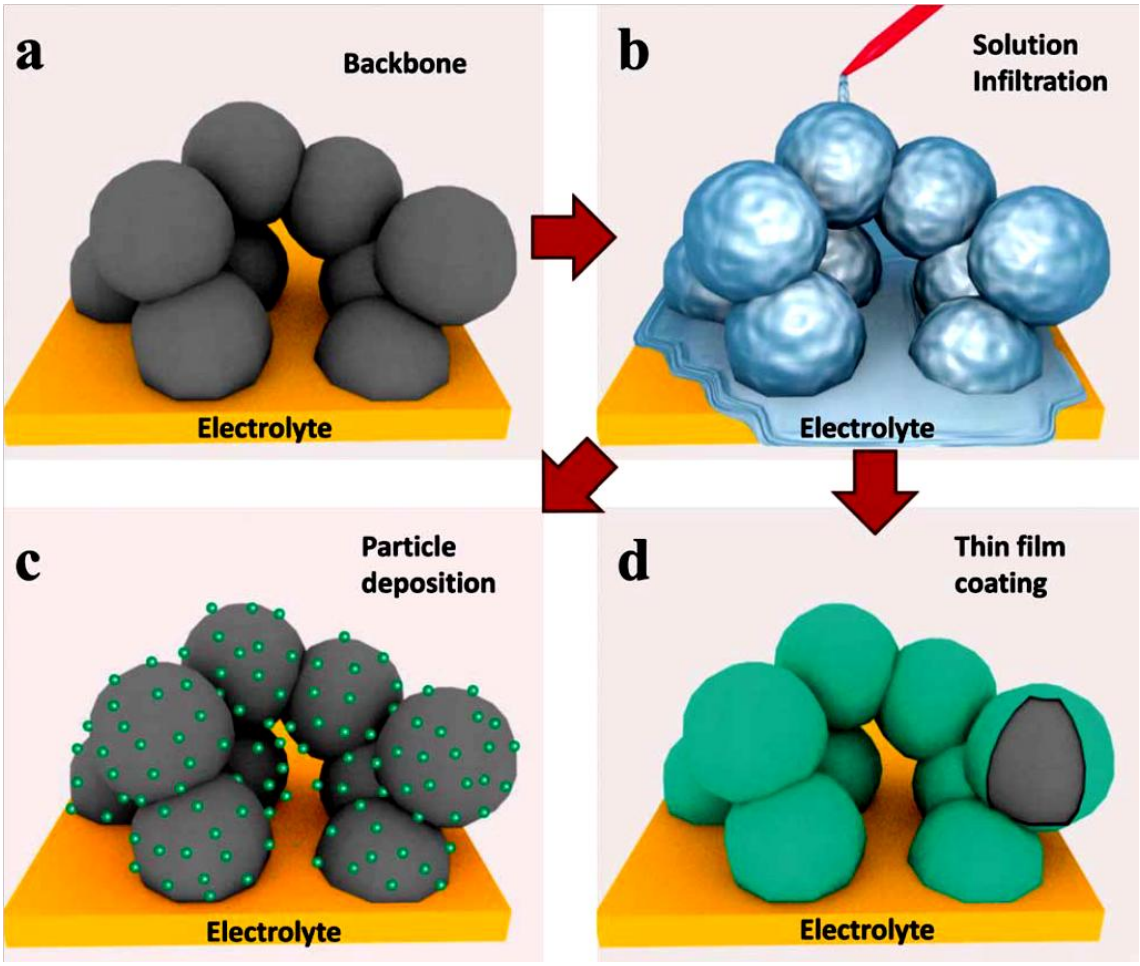

Figure 1-8 Schematic illustration of the impregnation procedure: (a) porous scaffold, (b)infiltration of scaffold with precursor solution, (c) catalyst forming discrete particles on the surface of infiltrated scaffold after thermal treatment, (d) catalyst forming a continuous thin film on the surface of infiltrated scaffold after thermal treatment [129]

1.6 Reverse water gas shift (RWGS) reactions

With the global warming issues caused by the increase of greenhouse gas emission into the atmosphere, CO_2 capture and sequestration has attracted a lot of attention as one of

the key strategies to resolve climate issues [139-141]. Among various methods to transform CO_2 into fuels, RWGS reaction is one of the most promising ways to achieve this goal. This technique has been known since 1914 and was first observed by Bosch *et al* [142]. However, more work is still needed to develop more cost-effective catalysts especially with the urgent need of overcoming the climate problems. A comprehensive review of the catalysts used for RWGS reaction, mechanisms and their results can be found in Ref [143]. In this section, we mainly focus on introducing the basic knowledge about this technique. The main reaction of RWGS reaction is shown below:

$$CO_2 + H_2 \leftrightarrow CO + H_2O,\ \Delta H^0_{298} = 42.1\ \text{kJ mol}^{-1} \qquad \text{Eq. 1-4}$$

Since the reaction is reversible, its maximum conversion rate and selectivity are controlled by a thermodynamic equilibrium. In addition, high working temperature is beneficial for a higher conversion rate of CO_2 to CO due to the fact this is an endothermic reaction. Depending on the type of catalyst, working temperature, ratios between reagent gases and etc, side reactions may also happen which would produce CH_4 (see Eq.1-5 and Eq. 1-6).

$$CO + 3H_2 \leftrightarrow CH_4 + H_2O,\ \Delta H^0_{298} = -206.5\ \text{kJ mol}^{-1} \qquad \text{Eq. 1-5}$$

$$CO_2 + 4H_2 \leftrightarrow CH_4 + 2H_2O,\ \Delta H^0_{298} = -165.0\ \text{kJ mol}^{-1} \qquad \text{Eq. 1-6}$$

Research has shown that certain degree of extra H_2 in the RWGS reaction gas mixture is also helpful in shifting the equilibrium towards the products [144-146]. The other method which helps to increase the CO_2 conversion rate is removing the product from the gas mixture [140].

Currently, there are mainly two types of catalysts which have been used for RWGS reactions. The first type of catalysts is metal nano particle catalysts distributed on various supports. The metal catalysts which are commonly used include Cu, Pt, Rh, Pd, Ni Fe, Cu and etc. The support materials for the metal catalysts are normally metal oxides which include CeO_2, Al_2O_3, ZnO, SiO_2, ZrO_2, TiO_2 and etc [147-157]. The other type of catalyst is metal oxide. The metal oxides which have been studied as catalysts

for RWGS consist of In_2O_3 doped with CeO_2 [158], Ga_2O_3 doped with CeO_2 [159], and perovskites [160-165]. Due to the fact that perovskite is able to tune its property by accommodating a wide range of cations on its A and B site, there is a great potential in exploring the material as a potential catalyst for RWGS reaction.

Chapter 2

Experimental Chapter

2.1 Solid state synthesis of A-site deficient titanates

The A-site deficient titanate based perovskite samples have been prepared by a solid state method reported by Neagu *et al* [100]. This section introduces the synthesis method for the most frequently used titanate based perovskite sample $La_{0.4}Sr_{0.4}Ga_xTi_{1-x}O_{3-x/2-\sigma}$ (x= 0.06, 0.10) perovskites. Most of the other titanate based perovskite samples were prepared based on this method with some small modifications. If there were any differences in the preparation method of other titanate based perovskite samples, details would be given in the corresponding chapter separately.

High purity raw materials (La_2O_3, $SrCO_3$, TiO_2, and Ga_2O_3) were first dried at different temperatures (300-800 °C). Stoichiometric amount of dried precursors were weighed while still hot before they were mixed with 0.1% of non-aqueous Hypermer KD-1 (polyester/polyamide copolymer) dispersant and acetone in a beaker. An ultrasonic probe (Hielscher UP200S) was then used at ~75% of maximum wave frequency and amplitude to break the agglomerates in the acetone mixture of the precursors and thoroughly homogenize it so that it became a fine suspension. The suspension was dried under stirring to evaporate the acetone and ensure its homogeneity. The dried mixture of the precursors was subsequently calcined in a crucible at 1000 °C for 12 h to decompose the carbonate and start the nucleation of the perovskite. The calcined powder was then milled for 2.5 h in a planetary ball mill at 200 rpm. After ball milling, the powder was pressed into dense pellets and fired for 12 h at 1400 °C. The sintered pellets were crushed and ball-milled for 1.5 h for making subsequent porous pellets.

2.2 Combustion synthesis of $LaCrO_3$ based perovskites

This section describes the combustion synthesis method of $La_{0.75}Sr_{0.25}Cr_{0.5}Mn_{0.5}O_3$ (LSCM), which was the most frequently used for $LaCrO_3$ based perovskites in this project. Other $LaCrO_3$ based perovskite samples were prepared based on this method. If there were any differences in the preparation method of other $LaCrO_3$ based perovskite samples, details would be given in the corresponding chapter separately.

Stoichiometric amounts of $La(NO_3)_3{\bullet}6H_2O$, $Sr(NO_3)_2$, $[Cr(H_2O)_6](NO_3)_3{\bullet}3H_2O$ and $C_4H_6MnO_4{\bullet}4H_2O$ were dissolved separately in de-ionized water before mixing them

together. Then glycine (NH_2CH_2COOH) was added to the solution mixture with the metal to glycine molar ratio of 1:1.18. The obtained solution was heated on a hot plate to keep the temperature at 80 °C for 4 h followed by evaporating the water at higher temperature. When the solution became viscous, the solution was transferred into a beaker which was heated on a hot plate at 250 °C to start the combustion process. For safety reasons, only a small amount of the viscous solution was transferred into the beaker each time. The viscous solution would start swelling first before the combustion began. Very fine dark brown to black coloured precursor powder was produced from the combustion synthesis. After the precursor powder was collected, it was mixed properly in a mortar and pestle to ensure homogeneity before being heated at 500 °C for 2 h to eliminate residual fuel traces (heating rate 2.5 °C/min). Finally, the powder was calcined at 1000 °C for 8 h to form the desired structure (heating rate 5 °C/min) [166].

2.3 Porous pellet preparation

To prepare porous perovskite pellets the ball-milled powder, pore-former and *Zschimmer-Schwarz DECOFLUX WB 41* (0.05g per 1g perovskite powder) were mixed thoroughly in acetone on a mortar with the pestle. The pore formers selected in the experiments were glassy carbon, graphite, rice starch, corn starch, flour, and sugar. The mixture was pressed into pellets by uniaxial pressing followed by firing slowly to high temperature. The ramp rate of the program was at 2 °C / min until 900 °C, to allow a slow burn-out of the carbon, and thus create pores in the ceramic bodies. Then the ramp rate was increased to 5 °C / min until 1300 °C followed by dwelling for 3-6 h to sinter the sample. After sintering, the sample was cooled down from 1300 °C to room temperature at the ramp rate of 5 °C / min.

2.4 Coating method of $La_{0.4}Sr_{0.4}Ga_xTi_{1-x}O_{3-x/2-\sigma}$ (x= 0.06, 0.10) perovskite with nickel catalyst

The coating process of $La_{0.4}Sr_{0.4}Ga_xTi_{1-x}O_{3-x/2-\sigma}$ (x= 0.06, 0.10) perovskite with nickel catalyst via impregnation method is shown in this part. When $La_{0.4}Sr_{0.4}Ga_xTi_{1-x}O_{3-x/2-\sigma}$ (x= 0.06, 0.10) perovskites were coated with other catalysts, this procedure was modified correspondingly according to the properties of the catalyst. Further details can

be found in corresponding chapters.

The Ni^{2+} catalyst containing solution was prepared by dissolving $Ni(NO_3)_2 \cdot 6H_2O$ and 1wt% Cetyl-triammonium bromide (CTAB) in ethanol. The coating procedure for the porous pellet involved impregnating the reduced porous pellets with the catalyst precursor containing solution. In the daytime, the impregnated pellets were heated at 250 °C for 0.5 h before the next impregnation. After that, the samples were fired at 400 °C for 4 h to thoroughly decompose the nitrate to the corresponding oxide. The above procedure was repeated until the target loadings of catalysts on the perovskite were achieved. Then the samples were fired at higher temperatures (1100-1300 °C) to promote the doping of the catalyst into the perovskite.

2.5 Coating method of $La_{0.75}Sr_{0.25}Cr_{0.5}Mn_{0.5}O_3$ (LSCM) with ruthenium catalyst

This section presents the coating procedure of LSCM perovskite with ruthenium catalyst. When LSCM perovskite was coated with palladium catalyst, similar method was used with different heating program. Details will be shown in the later chapter.

The coating procedure was carried out by mixing the LSCM with an appropriate amount of ruthenium nitrate solution (1.08 wt% Ru and 1 wt% CTAB in ethanol) for 18 h at 160 rpm in a horizontal ball mill. The milling balls used in the experiment was zirconia balls with 10 mm diameters. The obtained mixture was dried on a hot plate under stirring to maintain the homogeneity of the suspension. The dried powder was then heated at 400 °C for 2 h to completely decompose the ruthenium nitrate before being transferred to the VT-XRD sample holder.

2.6 Reduction

Depending on the sample, reduction was conducted at different temperatures under a controlled atmosphere 5% H_2/Ar in a tubular furnace. Details of the heating program will be given separately in each chapter.

2.7 Powder X-ray diffraction

2.7.1 Powder X-ray diffraction and Bragg's law

The crystal structures and phase purity of samples have been studied on a STOE X-ray diffractometer with a Cu-Kα X-ray source at room temperature, which is one of the most frequently used techniques for characterizing solids in solid state chemistry. It has the advantages of being non-destructive and only requiring a small quantity of sample. The general procedure of X-ray diffraction is illustrated in Figure 2-1.

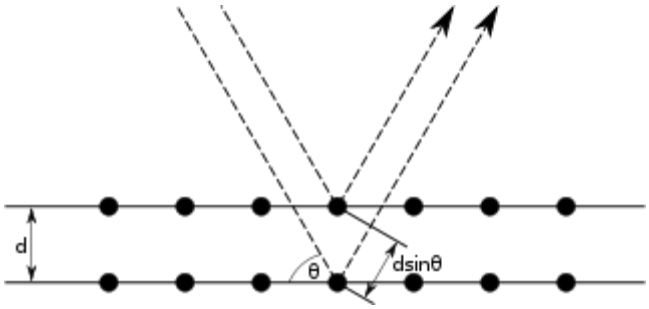

Figure 2-1 Schematic diagram of deviation of Bragg's law

The principle of this technique can be described by Bragg diffraction, which follows Bragg's law:

$$2d\ sin\theta = n\lambda \qquad \text{Eq.2-1}$$

where d is the distance between the atomic layers in the crystals, θ is the incident angle, n is an integer, and λ is the wavelength of the incident X-ray beam. The monochromatic beams of X-rays are incident upon successive crystallographic planes of the crystalline material, and are subsequently scattered from lattice planes separated by the interplanar distance d. When the waves are in phase, the path difference between them is equal to 2dsinθ, where θ is the scattering angle. Since the intensity of scattered waves is a function of the scattering angle, measuring it can provide a diffraction pattern of the sample. All X-ray diffraction patterns of the samples were collected in the range 2θ = 10°- 90° in air. The XRD patterns obtained were analysed using STOE Win XPOW software so as to obtain the information of the crystal structures and cell parameters.

2.7.2 Rietveld refinement method

For some samples, their XRD patterns were analysed by GSAS software using Rietveld refinement method. The Rietveld refinement approach involves establishing a hypothetical model with trial structural parameters and matching it with the actual XRD pattern by minimizing their differences with a least square method. Diffraction peaks were fitted using a pseudo-Voigt profile. Factors which were refined in this process involved scale factor, background polynomial parameters, zero shift, peak profile parameters u, v, w and η (Lorentzian–Gaussian distribution), unit cell parameters, atomic positions, site occupancies and thermal factors. The initial unit cell parameters were decided according to the XRD studies of samples with similar composition. All models were refined to convergence with the best fits and stability of the refinement process.

2.8 *In-Situ* variable temperature X-ray diffraction (VT-XRD) sample preparation

The VT-XRD instrument used in the experiment was PANalytical Empyrean using Mo X-ray tube with β–filter (Mo Kα1, 2) and an X'celerator RTMS detector. To perform the high temperature experiments, Anton Paar HTK1200N stage (room temperature - 1200 °C) in capillary was used. The VT-XRD was used for studying the in situ structural change of $La_{0.4}Sr_{0.4}Ga_{0.1}Ti_{0.9}O_{2.95-\sigma}$ (LSGT10) perovskite and $La_{0.75}Sr_{0.25}Cr_{0.5}Mn_{0.5}O_3$ (LSCM) when they were coated with ruthenium catalyst at high temperatures. The heating program and sample preparation method of LSGT10 perovskite samples are shown in this section. Different experiment procedure was used for LSCM perovskite samples and details will be shown in later chapter.

The investigation of the structural change of ruthenium impregnated $La_{0.4}Sr_{0.4}Ga_{0.1}Ti_{0.9}O_{2.95-\sigma}$ (LSGT10) perovskite when it was coated at different temperatures in air was carried out by crushing the pellet into powder before loading it onto the sample holder on the heating stage of the instrument. A platinum foil was placed between the sample holder and the sample since the perovskite sample may react with the sample holder (Al_2O_3). The sample was heated at a ramp rate of 10 °C/min in

air. The data were collected at various temperatures from room temperature to 1100 °C at 2θ range of 10°-50°. The blank sample, as prepared LSGT10, was also studied in the form of powder following the same collection parameters as the ruthenium coated LSGT10 in VT-XRD instrument.

2.9 Scanning electron microscope (SEM)

The morphologies of the samples were studied using either a JEOL JSM-5600 Scanning Electron Microscope (SEM) or JEOL JSM-6700 field emission scanning electron microscope (FEG-SEM). The basic principle of SEM is shown in Figure 2-2. In the vacuum chamber, a tungsten filament or a field emission gun generates a high energy beam of electrons which is subsequently accelerated by a high voltage. The apertures and electromagnetic lenses in the microscope column system then converges the accelerated electron beam to a thin beam of electrons as the beam accelerated down the length of the microscope. After reaching the sample, the beam scans the surface of it by means of scan coils so that the secondary electrons which are emitted from the specimen can be collected by a suitably-positioned detector to form an image showing the morphology of the sample.

2.10 Particle size analysis

The particle size analysis of the perovskite sample was carried out by measuring the individual size of each perovskite particle on the SEM images. The software used to measure the size of the perovskite particles was ‘‘Image-Tool’’. Over 5000 particles were measured to ensure the statistical validity of the experiment.

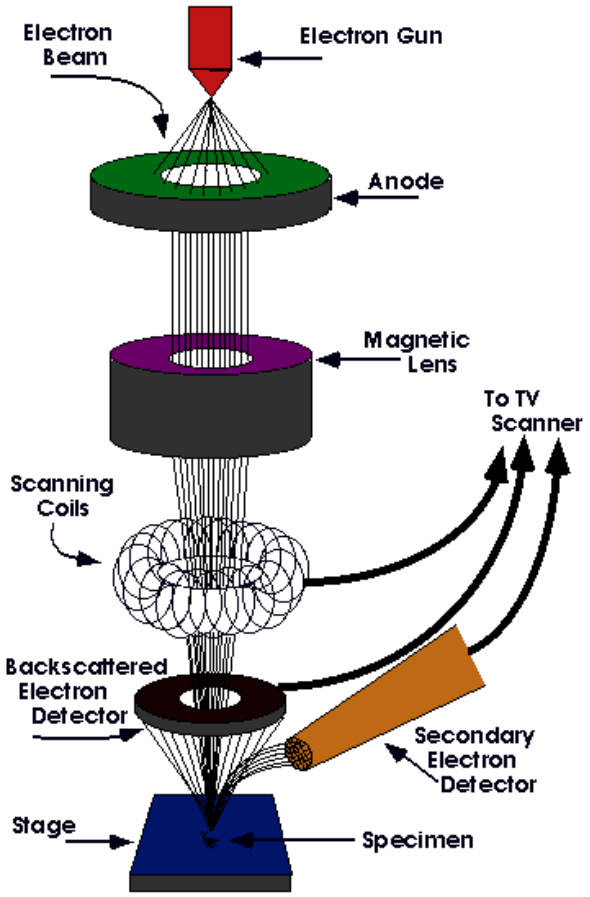

Figure 2-2 Schematic diagram of SEM [167]

2.11 Transmission electron microscopy (TEM)

When the samples were smaller in particle size or there were nanoparticles on the surface of the samples which were difficult to identify using SEM, TEM (Jeol JEM-2011) was used to study the morphologies of the samples. The principle of TEM is similar to that of SEM apart from the fact that the SEM is based on scattered electrons while TEM is based on transmitted electrons. The principle of TEM is illustrated in Figure 2-3. The beam of electrons is generated by the electron gun in a vacuum chamber which is then focused into a thin, coherent beam through condenser lenses. The electrons then travel through the specimen and eventually generate an image. The image is focused by objective lens and then magnified by intermediate lens and projector lens before hitting the fluorescent screen at the bottom of the microscope for users to see.

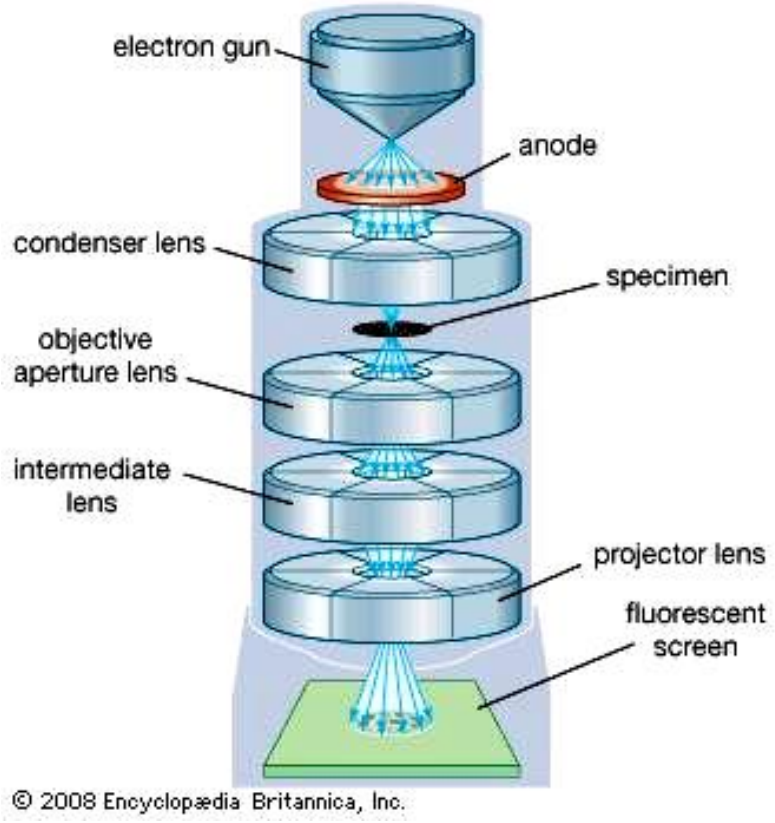

Figure 2-3 Schematic diagram of TEM [168]

2.12 Energy-dispersive X-ray spectroscopy

The composition of certain samples was studied using Energy-dispersive X-ray spectroscopy (EDS, EDX, or XEDS) on either SEM instrument or TEM instrument. This analytical technique is based on the characteristic X-ray spectra emitted by the elements in the sample. When a high energy electron beam hits the sample, an electron in an inner shell of the element may be excited and leave the shell. The electron hole left by the electron is filled by an electron from an outer shell which is higher in energy. The energy difference between two shells is liberated in the form of an X-ray which is then detected by an energy-dispersive spectrometer and presented in the form of X-ray emission spectrum.

2.13 Thermo-gravimetric analysis

The weight change of a sample under various heating temperatures and atmospheres was studied by thermo-gravimetric analysis (TGA). Depending on the sample, the thermo-gravimetric analysis was carried out either in a Netzsch STA 449C instrument or

in a tube furnace manually.

2.13.1 *In situ* thermo-gravimetric analysis in Netzsch STA 449C

The TGA study of LSCM perovskite coated with ruthenium catalyst was conducted in Netzsch STA 449C. Samples were tested in the form of fine powder weighing between 100-110mg in an alumina crucible. Samples were heated at a fixed ramp rate of 10°C/min. The heating program of samples in the TGA is shown below. First of all samples were heated in air from room temperature to a selected high temperature which was based on VT-XRD experiment results. After dwelling at high temperature for 11h, samples were cooled down to room temperature in air before switching the atmosphere to 5% H_2. Samples were then heated from room temperature to the same high temperature in 5% H_2 for 20h before finally cooling down to room temperature. The data were collected and analysed via Proteus thermal analysis software.

2.13.2 Thermo-gravimetric analysis for Ga loss measurement

Thermo-gravimetric analysis was conducted in a tube furnace in order to investigate the amount of Ga loss from $La_{0.4}Sr_{0.4}Ga_xTi_{1-x}O_{3-x/2-\sigma}$ (x= 0.06, 0.10) under reducing atmosphere. According to the method described in chapter 2.3, porous pellets having a mass around 1g were prepared first. Then the porous pellets were reduced in 5% H_2 at different temperatures (900-1000 °C) for 8 h to deprive both oxygen and Ga from the perovskites. After measuring the weight loss of the samples, the same samples were oxidized in air at the same temperature to refill the oxygen vacancies in the perovskites. The difference between the mass loss during the reduction and the mass gain during the re-oxidation was calculated as the amount of Ga loss [100].

The method to calculate the amount of Ga loss according to the Ga loss measurement experiment is shown below. The stoichiometry change of Ga and O caused by Ga and O loss on reduction is expressed as ζ and δ respectively in $La_{0.4}Sr_{0.4}Ga_{x-\zeta}Ti_{1-x}O_{3-\gamma-\delta}$ series. ζ and δ are usually expressed in Ga and O atoms per formula unit of perovskite (at/fu). The amount of oxygen restored during the re-oxidation equals to δ. Two assumptions were made to simplify the calculation of ζ and δ. First of all, the charge compensation needed for eliminating ζ Ga cations was neglected based on the expectation of low ζ

values. For the same reason, the molar weight was assumed not to be influenced by oxygen loss. The perovskite samples weights and their corresponding molar weights in each stage of Ga are expressed as m_i, μ_i (i = 1, 2, 3) (see Figure 2-4).

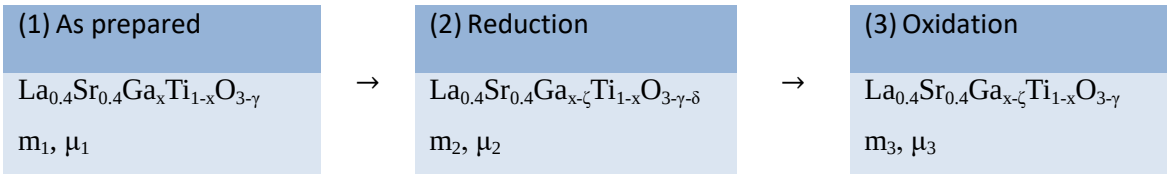

Figure 2-4 Schematic illustration of the change of various parameters in the redox cycle [169]

According to the assumptions, the moles of perovskite remained constant throughout the redox cycle. Therefore,

$$\frac{m_1}{\mu_1} = \frac{m_2}{\mu_2} \quad \text{Eq. 2-1}$$

$$\frac{m_2}{\mu_2} = \frac{m_3}{\mu_3} \quad \text{Eq. 2-2}$$

With proportions, the above equations can be written as:

$$\frac{\mu_2 - \mu_1}{\mu_1} = \frac{m_2 - m_1}{m_1} \quad \text{Eq. 2-3}$$

$$\frac{\mu_3 - \mu_2}{\mu_3} = \frac{m_3 - m_2}{m_3} \quad \text{Eq. 2-4}$$

After introducing the atomic weights of Ga (M_{Ga}) and O (M_O), together with ζ and δ, Eq. 2-3 and Eq. 2-4can be extended as below:

$$\frac{-(\zeta \cdot M_{Ga} + \delta \cdot M_O)}{\mu_1} = \frac{m_2 - m_1}{m_1} \quad \text{Eq. 2-5}$$

$$\frac{\delta \cdot M_O}{\mu_1 - \zeta \cdot M_{Ga}} = \frac{m_3 - m_2}{m_3} \quad \text{Eq. 2-6}$$

The above equations can be solved since ζ and δ are the only two unknowns in Eq. 2-5 and Eq.2-6. After solving the equations, ζ and δ can be expressed as below:

$$\zeta = \frac{\mu_1}{M_{Ga}} \cdot \frac{m_1 - m_3}{m_1} \quad \text{Eq. 2-7}$$

$$\delta = \frac{\mu_1}{M_O} \cdot \frac{m_3 - m_2}{m_1} \quad \text{Eq. 2-8}$$

According to Eq.2-7 and Eq.2-8, the amount of Ga loss and oxygen loss during the reduction at different temperatures can be calculated for $La_{0.4}Sr_{0.4}Ga_xTi_{1-x}O_{3-x/2-\sigma}$ (x= 0.06, 0.10) perovskites [169].

2.14 Reverse water gas shift reaction (RWGS)

RWGS reactions were conducted as a quick way to investigate the influence of the catalyst coating on the performance of the perovskite. All LSGT10 perovskite based samples were ball milled for 5 h in a planetary ball mill at 200 rpm to obtain uniform powder. The procedure of the catalysis tests is shown in Figure 2-5. Samples were placed on a fixed quartz wool bed in the form of powder in a quartz reactor (8 mm internal diameter and 210 mm length). The height of the catalysts bed was fixed at 2mm. First of all, the sample was heated from room temperature to 900 °C at a heating rate of 5 °C/min in a continuous Ar flow (20ml/min). Then the gas flow was switched to a reagent gas mixture (ratio H_2: CO_2 = 3:1) with a fixed total flow rate of 20ml/min. The mass flow of the gas mixture was not influenced by the catalytic bed. A cold trap filled with dry ice was used to remove the water from the outlet gas mixture before flowing into the gas chromatograph to monitor the content of the gas. Samples were kept at 900 °C for 300 min before cooling down to room temperature.

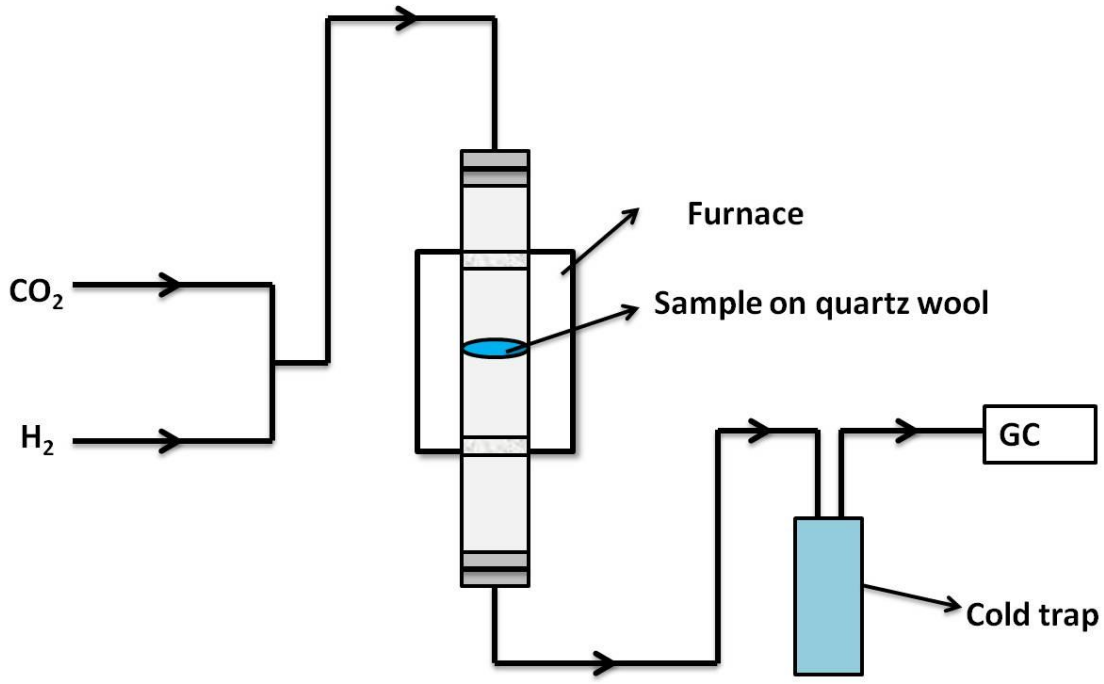

Figure 2-5 Schematic diagram of RWGS catalysis test procedure

Chapter 3

Coating $La_{0.4}Sr_{0.4}Ga_xTi_{1-x}O_{3-x/2}$ (LSGT) with nickel catalyst

3.1 Introduction

One of the most common ways of improving the performance of electrode materials in fuel cells is impregnating the micro-structured perovskite with catalysts. Since the metal or metal oxide catalysts produced by this method are all nano-size particle, this technique has been proven to be effective in increasing the Triple Phase Boundaries (TPB), the interface between the electrolyte, the electrode and the gas fuel, for the catalytic reaction in fuel cells. However, the stability of the catalysts is a major challenge for long term applications since they will agglomerate during the operation of the fuel cell, causing the fuel cell performance to degrade [122, 124-126, 130, 132, 170].

Another way of improving the performance of electrode materials in fuel cells is by doping the perovskite material with other catalysts [102, 171-177]. However, doping the perovskite material still requires a reasonably large amount of catalysts, which makes the cost of the fuel cell quite high, especially when using PGM elements. Another problem with doping is that only a fraction of the catalyst is able to exsolve to the surface of the perovskite and catalyses the electrode reaction, while a large quantity of the doped catalyst remains in the bulk of the structure due to its high stability.

It would be ideal to develop a core-shell structure which keeps the catalysts anchored to the surface of the perovskite without agglomeration during the electrochemical reaction. To achieve this goal, the perovskite will first be coated with catalyst, followed by further firing to dope the catalyst into the surface layer of the perovskite. The surface-doped perovskite is then reduced in 5% H_2 to exsolve catalysts to the surface to take part in the catalysis reaction. Since the exsolved catalysts are normally anchored on the perovskite, the problem of catalyst agglomeration in the traditional impregnation method can be avoided. In addition, most of the catalyst is doped only in the surface layer of the perovskite. Compared to the traditional doping method, the amount of catalyst required is much less and the catalyst is more efficiently utilized.

The perovskite material chosen in the experiment was Ga doped strontium titanate $La_{0.4}Sr_{0.4}Ga_xTi_{1-x}O_{3-x/2}$ (LSGT) which was first reported by Neagu *et al* [100]. It has

been previously reported that when LSGT was reduced in a reducing atmosphere for the first time, surface Ga loss was observed. This leaves a Ga depleted layer on the surface of the perovskite grains due to the natural volatility of Ga at low pO_2 at high temperatures. There was no further Ga loss observed from LSGT perovskite even if more redox cycles were carried out [100, 178-180]. If the Ga depleted layer can be preserved by using a fast cooling process, it means that the LSGT would also become slightly B-site deficient. The B-site deficiency would be beneficial for the catalysts to be doped in the surface of the LSGT perovskite since the perovskite will naturally tend to form the ABO_3 stoichiometry to maintain its stability. By filling the Ga vacancies on the B-sites of the reduced LSGT perovskites with the same amount of other catalysts, while keeping its A-site deficiency, the perovskite should be able to exsolve the surface doped catalyst under a reducing atmosphere since the A-site deficiency would promote exsolution of the atoms on B-site [100]. Since it might be difficult to preserve the B-site vacancies in the perovskite, the other possible way of viewing the Ga depleted layer in the perovskite is viewing it as a stoichiometry rearrangement after reduction (see Eq 3-1) [76].

$$A_{1-\alpha}BO_{3-\delta} \xrightarrow{\text{Reduction}} (1-\alpha)ABO_{3-\delta'} + \alpha B \qquad \text{Eq. } 3-1$$

Instead of maintaining B-site vacancies in the Ga-depleted layer, the stoichiometry of the surface of the perovskite could become the more stable ABO_3. Coating other catalyst into the LSGT perovskite from its surface can then be viewed as the reverse process of Eq.3-1 (see Eq. 3-2).

$$(1-\alpha)ABO_{3-\delta} + \alpha B'O \xrightarrow{\text{Oxidation}} A_{1-\alpha}BB'_{\alpha}O_{3-\delta'} \qquad \text{Eq. } 3-2$$

In this case, the A-site vacancies are still conserved and the perovskite surface doped with catalyst should still be able to exsolve the catalyst from the B-site.

Ni has been widely used as a fuel oxidation catalyst in fuel cells. Apart from the traditional way of simply mixing the Ni catalyst with the electrode material, doping Ni in the perovskite has become very popular in the last few decades. Ni catalysts were firstly chosen to investigate the assumption of the experiment since Ni atoms are very mobile and have a good chance of entering the perovskite lattice [181]. In addition, it has been proven that it is possible to exsolve the doped Ni catalyst as nano-particles to the surface of the doped material through the control of non-stoichiometry [76, 82, 172,

182, 183]. Thermogravimetric analysis (TGA) was conducted to investigate the amount of Ga loss under different conditions. The structure change of the perovskite was investigated by X-ray Powder Diffraction (XRD). The surface characteristics and chemical compositions were examined by Scanning Electron Microscopy (SEM) and Energy-dispersive X-ray spectroscopy (EDS, EDX, or XEDS).

3.2 Experimental Section (Reduction)

There were two types of reduction in this experiment. The first type was to lose the Ga on the surface of the perovskite so as to generate B-site vacancies for other catalyst to replace by coating. The temperature range for this type reduction was 900-1000°C. The reduction time was 8h. The second type of reduction was to exsolve the catalyst which was doped into the perovskite from the surface. This was carried out at 930°C for 30h. This was mentioned as 2nd reduction in the thesis.

3.3 The influence of reduction temperature and the content of Ga in LSGT on Ga loss

It was mentioned earlier that LSGT will lose Ga from an outer shell on its first reduction and no more Ga loss would happen even if after more redox cycles treatment [100]. The amount of catalyst targeted to be coated onto the perovskite is equal to the amount of Ga loss during the first reduction under the given experimental conditions. Therefore, it is essential to establish the amount of Ga lost from the perovskite under different experiment conditions. Perovskite samples with different amounts of Ga dopant, $La_{0.4}Sr_{0.4}Ga_{0.06}Ti_{0.94}O_{2.97}$ (LSGT06) and $La_{0.4}Sr_{0.4}Ga_{0.1}Ti_{0.9}O_{2.95}$ (LSGT10), were chosen to study the influence of Ga content on the amount of Ga loss under different reduction temperatures (900-1000 °C).

According to the method described in Chapter 2.13.2, the obtained Ga losses from perovskites under different reduction temperatures are plotted in Figure 3-1. Although the amounts of the Ga losses from the reduction of the perovskite materials is different from what has been reported by Neagu *et al* [100], possibly due to differing morphologies, the main trends remain the same with regard to the change of reduction

temperature and Ga content. It can be noted that, in general, Ga loss increases as the amount of Ga dopant and reducing temperature increase. However, for LSGT06, the Ga loss at 950 °C is the same as that at 1000 °C. This may be due to the fact that only the Ga ions which are on the perovskite surface are volatile enough to leave the perovskite at these temperatures. In addition, the Ga loss is accompanied by O loss which also kinetically hindered the Ga diffusion to the surface. The Ga depleted layer will further prevent the Ga ions in the bulk from diffusing to the surface of the perovskite since the Ga ions in the bulk require more energy than the experimental condition could provide to diffuse to the surface of the perovskite. At 950 °C, all of the Ga on the surface has escaped from the perovskite and increasing the temperature will not promote more Ga escaping out of the LSGT06 [100, 180]. As a result, samples which were reduced at 900 °C and 950 °C were chosen for the following Ni^{2+} coating experiment. The amount of Ni^{2+} catalyst to be coated on the perovskite is listed in Table 3-1. Typically, sufficient amounts of Ni^{2+} were added to each sample to compensate for the Ga loss during the first reduction.

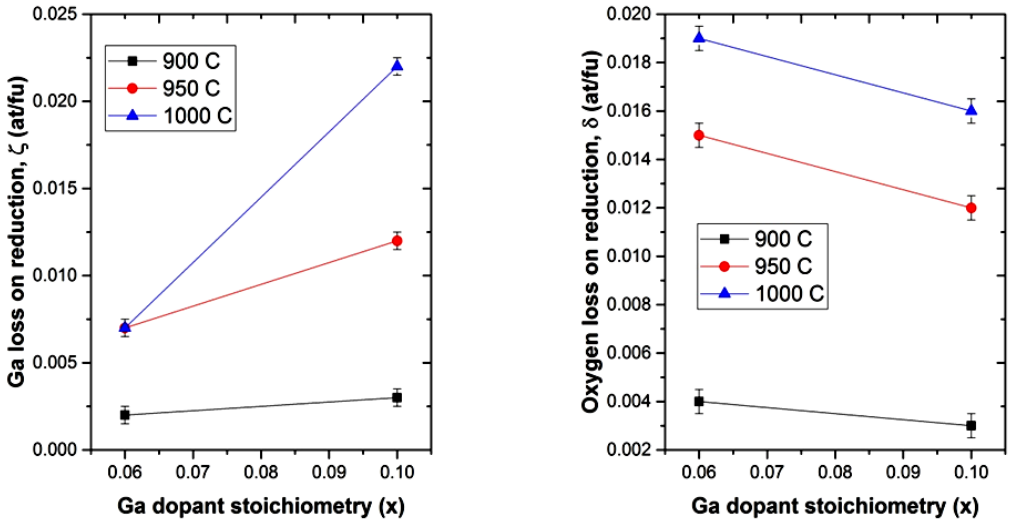

Figure 3-1 Ga and O loss of LSGT06 and LSGT10 (LSGT06, x=0.06; LSGT10, x=0.1) after first reduction in 5% H_2 at different temperatures (900 ºC, 950 ºC, 1000 ºC)

Ni loading per mole of perovskite after reduction pre-treatment at different temperatures /mol	900 °C	950 °C
LSGT06	0.002	0.007
LSGT10	0.003	0.012

Table 3-1. The amounts of Ni^{2+} catalyst coated onto $La_{0.4}Sr_{0.4}Ga_{x-\zeta}Ti_{1-x}Ni_yO_{3-\gamma-\sigma}$ (x= 0.06, 0.10) which were first reduced at different temperatures.

3.4 The influence of coating temperature on the crystal structure of Ni^{2+} coated LSGT

The catalyst nano-particles generated by the traditional infiltration method are only deposited on the surface of the substrate material. During the operational process, the performance of the material will deteriorate due to the agglomeration of the catalysts [184]. To promote the catalyst dissolving in the perovskite, higher firing temperatures are required. After the samples were coated with Ni^{2+} catalysts *via* the infiltration method, higher firing temperatures were applied to the samples.

Figure 3-2 shows the XRD patterns of LSGT10 coated with Ni^{2+} at different temperatures when it was first reduced at 900 °C and 950 °C, respectively. It is worth pointing out that in order to show the 2nd phases more obviously, the XRD data was presented in the form of square root of the peak intensities in Figure 3-2. According to Figure 3-2a, there were no significant changes in the XRD patterns of LSGT10 between when it was first reduced at 900 °C and when it was coated with the Ni^{2+} catalyst afterwards. This may be due to the fact that the amount of Ni^{2+} coated onto the perovskite was not high enough to cause any change. However, when LSGT10 was first reduced at 950 °C, after coating it with Ni^{2+} at 1200 °C, a second phase of NiO and an unknown species were observed in the XRD pattern (see Figure 3-2b). The reason NiO was not observed in the XRD pattern when the sample was coated at 1100 °C may be because the NiO was not crystallized enough at that temperature. When the sample was coated and treated at 1300 °C, small amount of 2nd phase with a possible spinel structure showed up in the XRD pattern (see Figure 3-2). The formation of the 2nd phase could be a result of lattice decomposition through solid state reaction. Both LSGT06 and LSGT10 displayed similar changes in their XRD patterns with respect to varying coating temperatures, so the XRD patterns of LSGT06 corresponding to different experimental treatment is not introduced in detail and is only shown at the end of this chapter for reference (see Figure 3-16).

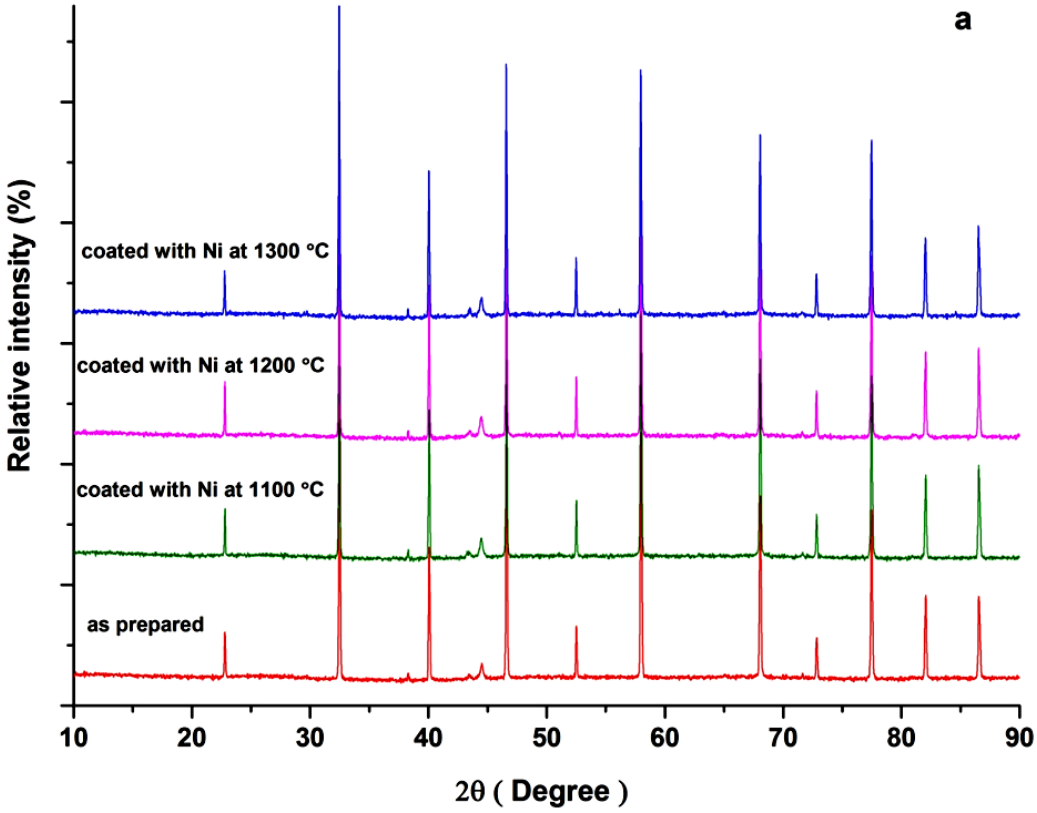
a
Relative intensity (%)
coated with Ni at 1300 °C
coated with Ni at 1200 °C
coated with Ni at 1100 °C
as prepared
10
20
30
40
50
60
70
80
90
2θ (Degree)

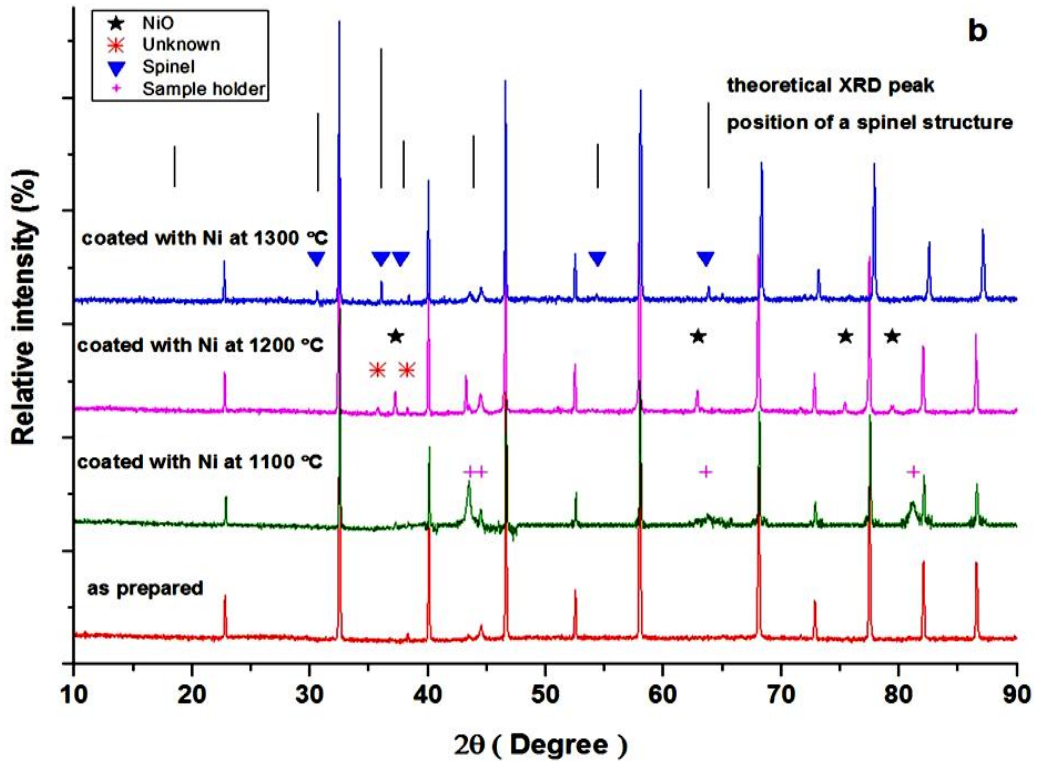
b
NiO
Unknown
Spinel
Sample holder
theoretical XRD peak
position of a spinel structure
Relative intensity (%)
coated with Ni at 1300 °C
coated with Ni at 1200 °C
coated with Ni at 1100 °C
as prepared
10
20
30
40
50
60
70
80
90
2θ (Degree)

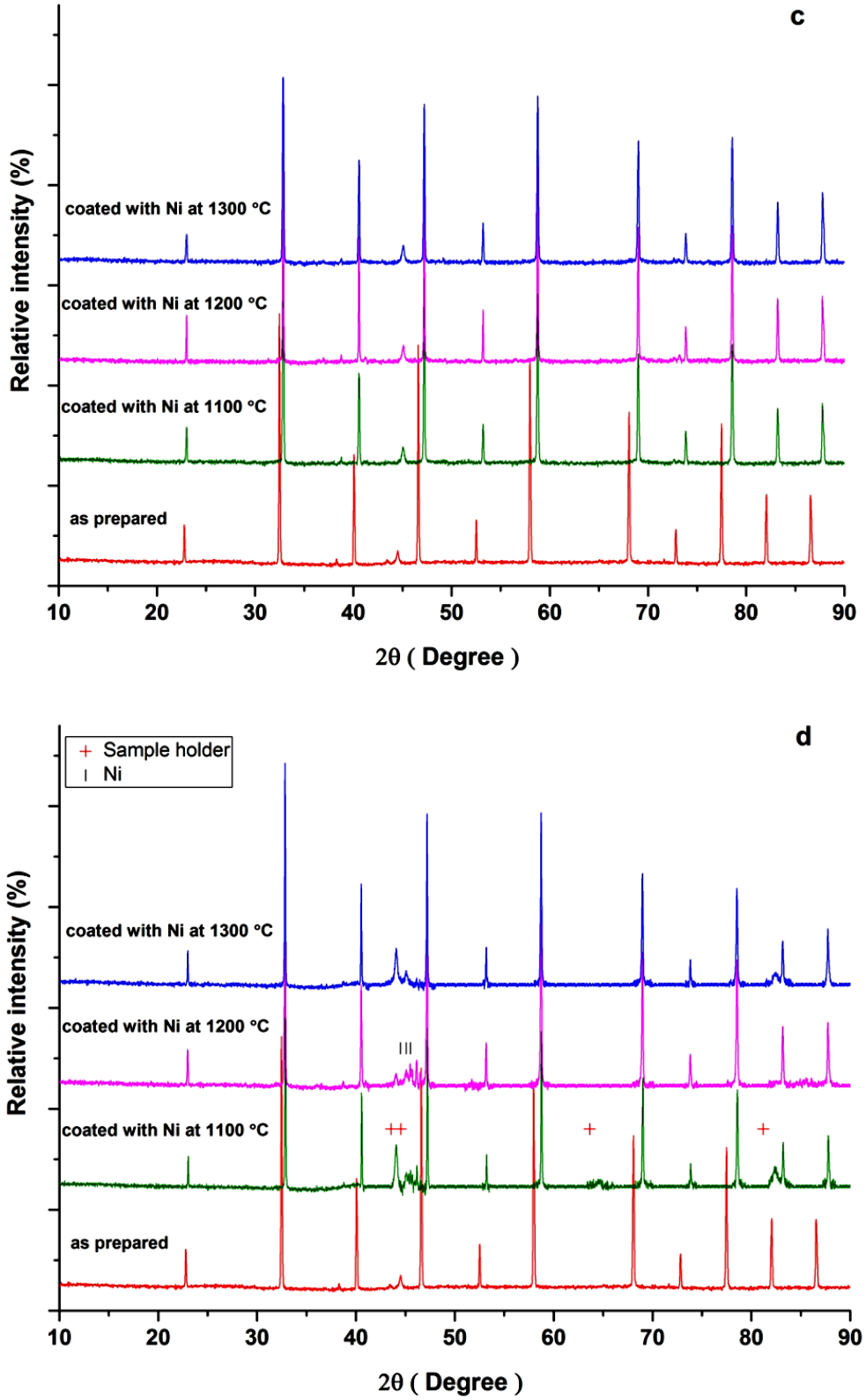

Figure 3-2 XRD patterns of LSGT10 at different stages of treatment, a. LSGT10 1st reduced at 900 °C then coated with Ni^{2+} catalyst at different temperatures, b. LSGT10 1st reduced at 950 °C then coated with Ni^{2+} catalyst at different temperatures, c. LSGT10 1st reduced at 900°C then coated with Ni^{2+} catalyst at different temperatures after 2nd reduction, d. LSGT10 1st reduced at 950°C then coated with Ni^{2+} catalyst at different temperatures after 2nd reduction

After the 2nd reduction, the 2nd phase was not apparent in the XRD patterns of the samples which were first reduced at 900 °C (see Figure 3-2c). There were no obvious changes in the XRD patterns for the samples first reduced at 900 °C, possibly also due to the fact that the amount of Ni^{2+} used for coating the perovskite was not high enough to be detected by XRD. However, Ni was detected for the coated samples which were first reduced at 950 °C when they were coated at 1100 °C and 1200 °C (see Figure 3-2d). The presence of Ni for the samples which were coated at 1100 °C and 1200 °C should be due to the reduction of NiO.

The unit cell volumes of LSGT06 and LSGT10 when subjected to different experimental treatments were plotted against different coating temperatures (Figure 3-3). Both LSGT06 (a = 7.78366 (17), b = 5.50221 (13), c = 5.50038 (14), β = 90.0443 (15), V = 235.567(10)) and LSGT10 (a = 7.78484 (12), b = 5.50326 (10), c = 5.50145 (8), β = 90.0716 (9), V = 235.693 (6)) showed monoclinic structures and both samples retained their structures throughout the experiment. Generally, the unit cell volumes of LSGT06 and LSGT10 pre-reduced at 900 °C were smaller than those which were first reduced at 950 °C. This is expected since the unit cells of the titanates would expand on reduction. When samples were reduced at higher temperature, they would be further reduced thus leading to more expansion of the unit cells. For LSGT06 and LSGT10 pre-reduced at 900 °C, the unit cell volumes of both perovskites decreased as the coating temperature increased. This is not surprising since the samples were reduced first leading to expanded unit cells, and oxidizing them would reversely decrease the size of their unit cells. The higher oxidizing temperatures are, the smaller the titanate unit cells would become as what was observed in the experiment. However, the changes of the unit cell volumes showed the opposite trend for the perovskites which were first reduced at 950 °C.

The reasons for the change of the unit cell volumes of the sample being so different could be due to the fact that at different reduction temperatures, the perovskite lost different amounts of Ga and O, which lead to very different deficiencies in the perovskite. The perovskites which were first reduced at 950 °C lost more Ga and O than those at 900 °C. Therefore more B-site and O deficiencies were expected from the samples which were reduced at 950 °C. The radius of six-fold coordinated Ni^{2+} is 0.69 Å, which is bigger than those of 6-fold coordinated Ti^{4+} (0.605Å) and Ga^{3+} (0.62Å) [60].

The expansion of the unit cells of the samples which were first reduced at 950 °C could be an indicator that Ni^{2+} may have entered the unit cell of the perovskite.

After 2nd reduction, the unit cell volumes of both samples increased by around 0.3% on average. It is worth noting that, after the 2nd reduction, the unit cell volumes of LSGT10 which were first reduced at 950 °C became smaller than those first reduced at 900 °C. This could be due to the fact that the samples had lost more oxygen in the pre-reduction treatment at 950 °C than the ones which were first reduced at 900 °C. In addition, more nickel catalysts were doped into the samples which were first reduced at 950 °C. This means more vacancies would be left in the lattice after nickel catalysts exsolved from the bulk material leading to a smaller unit cell.

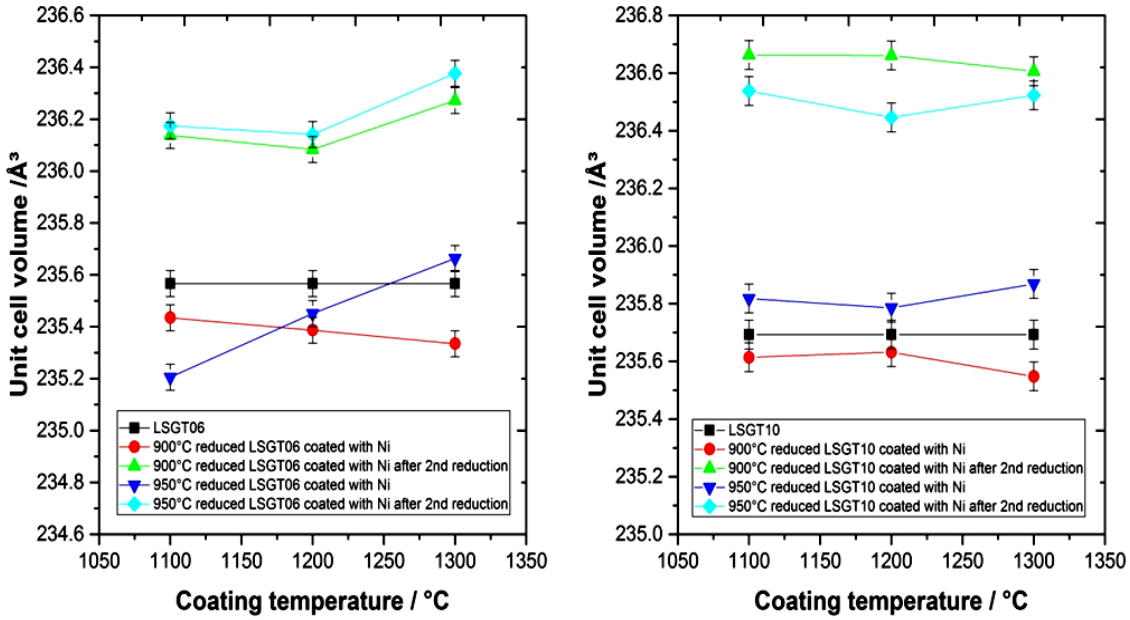

Figure 3-3 Unit cell volumes of LSGT06 and LSGT10 as a function of coating

3.5 The influence of coating temperature on the morphology of Ni^{2+} coated LSGT

The morphology of the pellet samples was studied by FEG-SEM before each treatment throughout the experiment. After LSGT10 was firstly reduced at 900 °C (Figure 3-4b) and 950 °C (Figure 3-4c) in 5% H_2, the surfaces of the grains look the same as they did before they were reduced (Figure 3-4a). However after coating the pellets with Ni^{2+} catalyst, the grain surface of the samples may look very different depending on the coating temperature.

Samples which were first reduced at 950 °C followed by coating Ni^{2+} catalysts at 1100 °C (Figure 3-6a) and 1200 °C (Figure 3-6b) showed a lot of NiO particles on the surfaces of the grains, as can be clearly seen from both SEM pictures. When the sample was coated with nickel at 1100 °C, NiO particles were distributed evenly in the form of nanoparticles with the size range of mostly below 120 nm on the surface of the perovskite. As the coating temperature became higher, the NiO particles on the surface of the perovskite became more crystallized and grew much bigger (200-600 nm). This is supported by the XRD results discussed earlier. Nevertheless, the surfaces of the grains of the sample which was coated with Ni catalyst at 1300 °C were clean (Figure 3-6c). They looked the same as that of the as prepared pellet, and it seemed that all the Ni^{2+} catalyst had diffused inside the perovskite. After reducing the sample in 5% H_2 at 930 °C for 30 h after coating, the exsolution of Ni particles on the surface of the grain can be seen. There were two size ranges (20-50 nm and 100-200 nm) of the Ni particles observed for the samples which were coated at 1100 °C (Figure 3-8a) and 1200 °C (Figure 3-8b). The larger Ni particles look similar to the result of normal impregnation, meaning that they did not enter the perovskite. The smaller particles might be a result of impregnation, as they are known to form during the impregnation process [185]. Another possible reason for the presence of smaller Ni particles is that some of the catalyst has diffused into the perovskite and then exsolved.

The sizes of catalyst particles observed from the sample which was fired at 1300 °C (Figure 3-8c) were all within the range of 20-50 nm. This means that all of the catalyst particles on the surface of the 1300 °C coated sample were formed by exsolution from the perovskite. This confirms that the Ni^{2+} had fully diffused into the perovskite upon firing in air and successfully exsolved to the surface of the perovskite after reduction.

The morphology of the samples which were first reduced at 900 °C after coating at different temperatures and subsequent 2^{nd} reduction in 5% H_2 are shown in Figures 3-5 and 3-7, respectively. The change of the morphology of the samples corresponding to different coating temperatures was similar to that of the samples which were first reduced at 950 °C, but with lower amounts of catalyst since they show less Ga loss. As for the LSGT06 perovskite pellets, their morphology was similar to that of LSGT10, but with less catalyst on the surface after the same treatments.

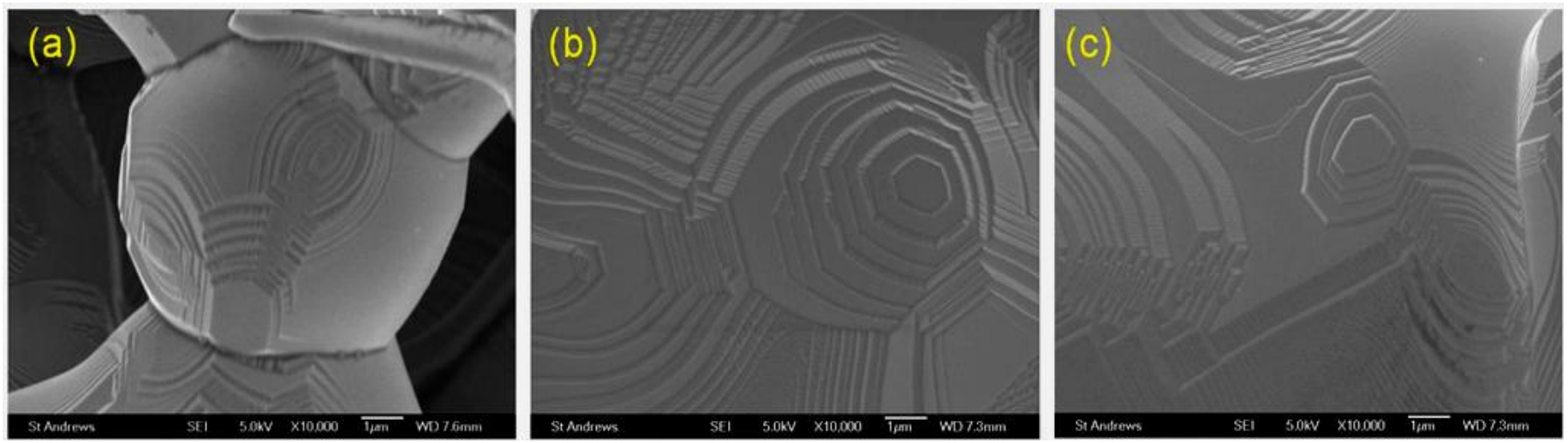

Figure 3-4 SEM images of LSGT10 before catalyst coating: (a) as prepared LSGT10 pellet, (b) LSGT10 after 1st reduction in 5% H2 at 900 °C, (c) LSGT10 after 1st reduction in 5% H2 at 950 °C

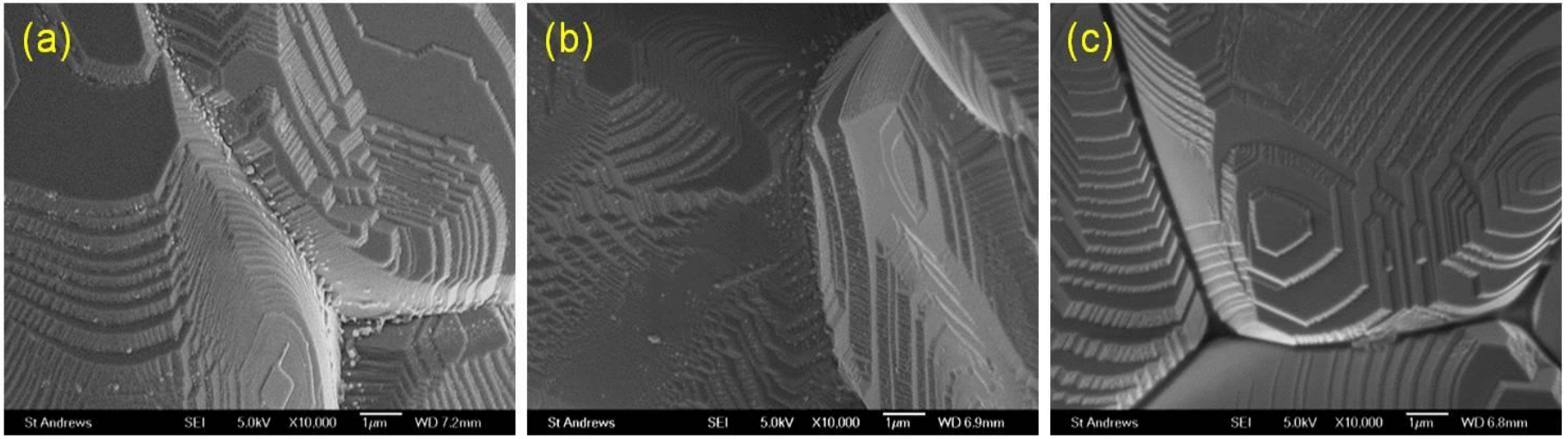

Figure 3-5 SEM images of 900 °C 1st reduced LSGT10 then coated with Ni at different temperatures: (a) coated with Ni at 1100 °C, (b) coated with Ni at 1200 °C, (c) coated with Ni at 1300 °C

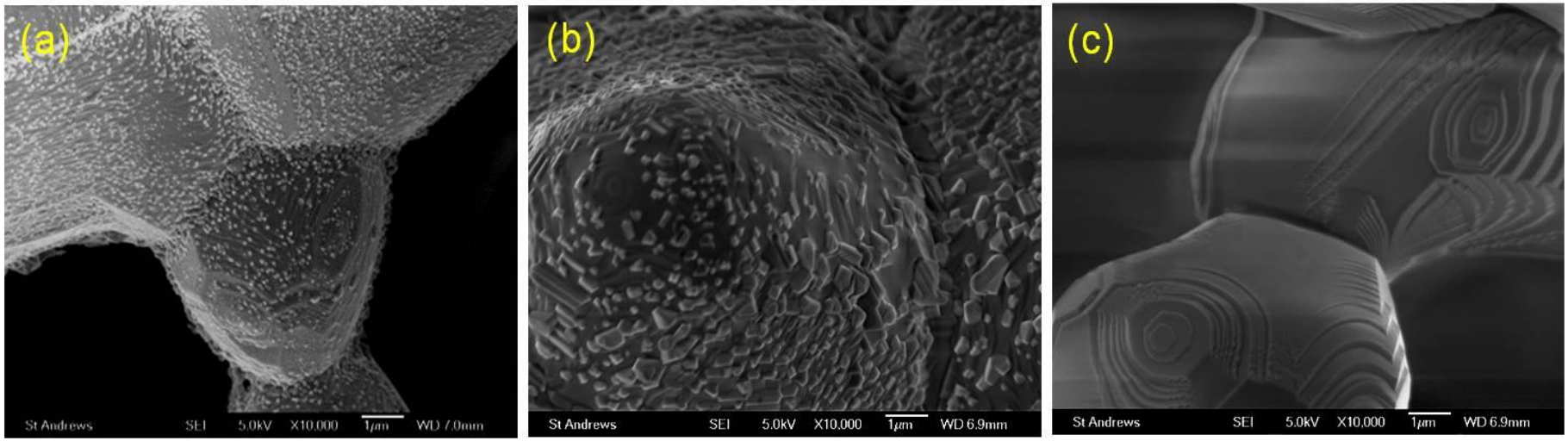

Figure 3-6 SEM images of 950 °C 1st reduced LSGT10 then coated with Ni at different temperatures: (a) coated with Ni at 1100 °C, (b) coated with Ni at 1200 °C, (c) coated with Ni at 1300 °C

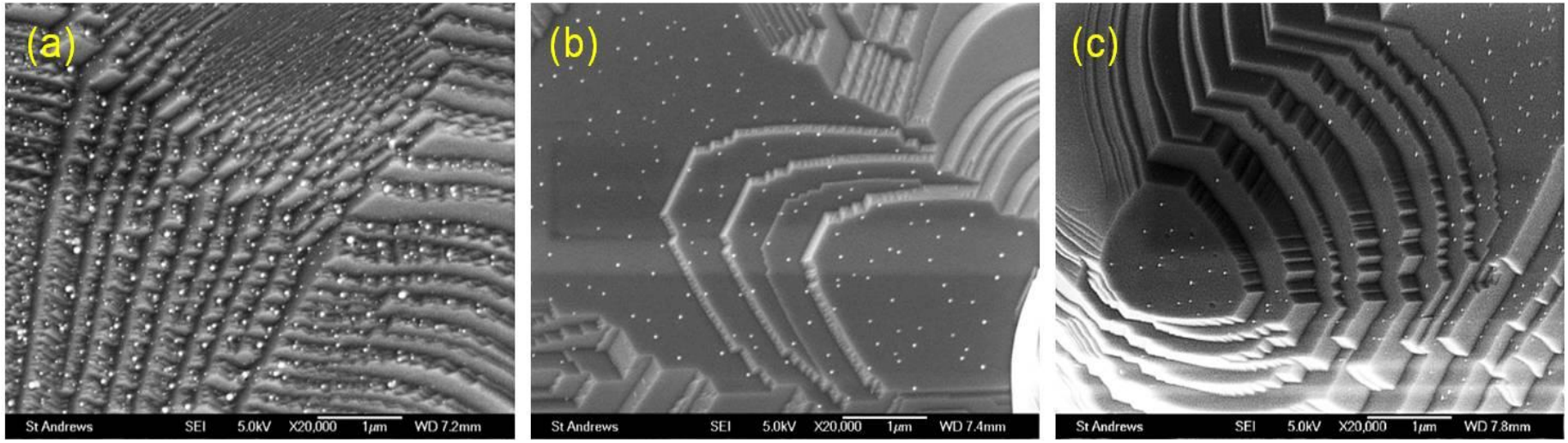

Figure 3-7 SEM images of 900 °C 1st reduced LSGT10 then coated with Ni after 2nd reduction for 30 h: (a) coated with Ni at 1100 °C, (b) coated with Ni at 1200 °C, (c) coated with Ni at 1300 °C

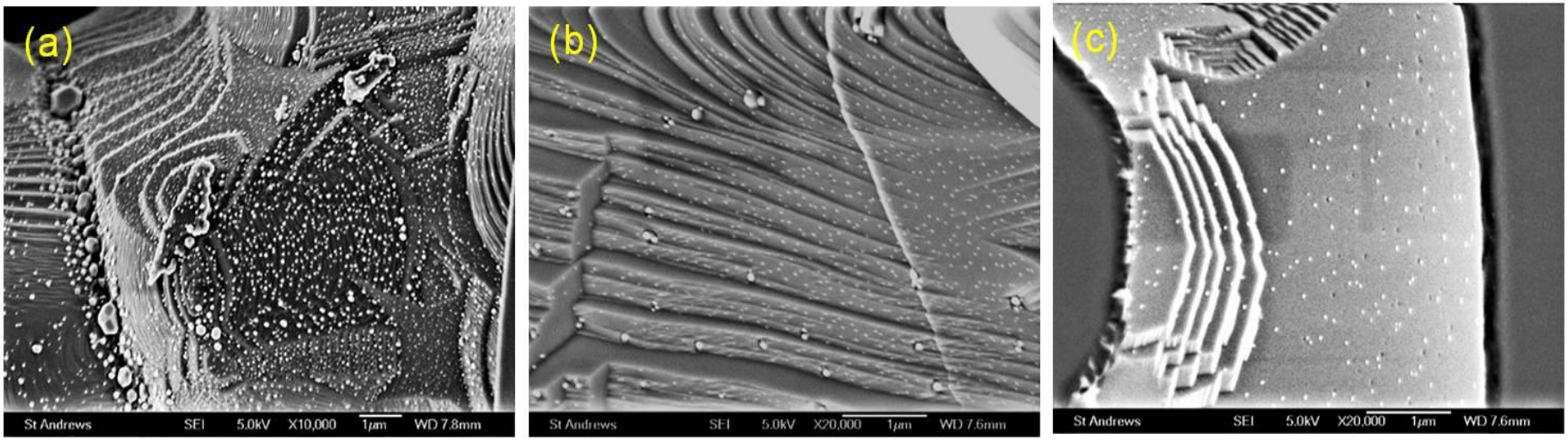

Figure 3-8 SEM images of 950 °C 1st reduced LSGT10 then coated with Ni after 2nd reduction for 30 h: (a) coated with Ni at 1100 °C, (b) coated with Ni at 1200 °C, (c) coated with Ni at 1300 °C

3.6 The influence of pore formers on the properties of LSGT

The phenomenon of Ga loss from LSGT in a reducing atmosphere only happens on the surface of the perovskite. The microstructure and specific surface area of the LSGT have an influence on the amount of Ga loss. As the catalyst will be coated on the surface of the porous pellets, it is important to ensure that the pellets have high porosity and uniformly distributed pores. A small size difference between the ball-milled perovskite powder and the pore formers is helpful in making porous perovskite pellets with uniformly distributed pores. However, there are other factors that may also influence the microstructure of the perovskite. A few well-known pore formers - namely glassy carbon, graphite, rice starch, corn starch, and sugar - have been chosen to optimize the microstructure of the LSGT perovskite. Their influence was evaluated on the porosity, the pore shape and distribution of the LSGT, as well as the effect on its reducibility [186-189].

3.6.1 The morphologies of different pore formers

To obtain optimum scaffolds for catalyst coating, the sizes and morphologies of different potential pore formers were examined by FEG-SEM (see Fig 3-9). According to Fig 3-9a and Fig 3-9b, rice starch and corn starch have very similar, well-defined shapes, although their dimensions differ from one another. The corn starch particles are clearly much larger than the rice starch particles. Sugar (see Figure 3-9c) shows lamellar morphology which is similar to graphite (see Figure 3-9d). Glassy carbon, as the other inorganic pore former, has a perfectly spherical shape (see Figure 3-9e).

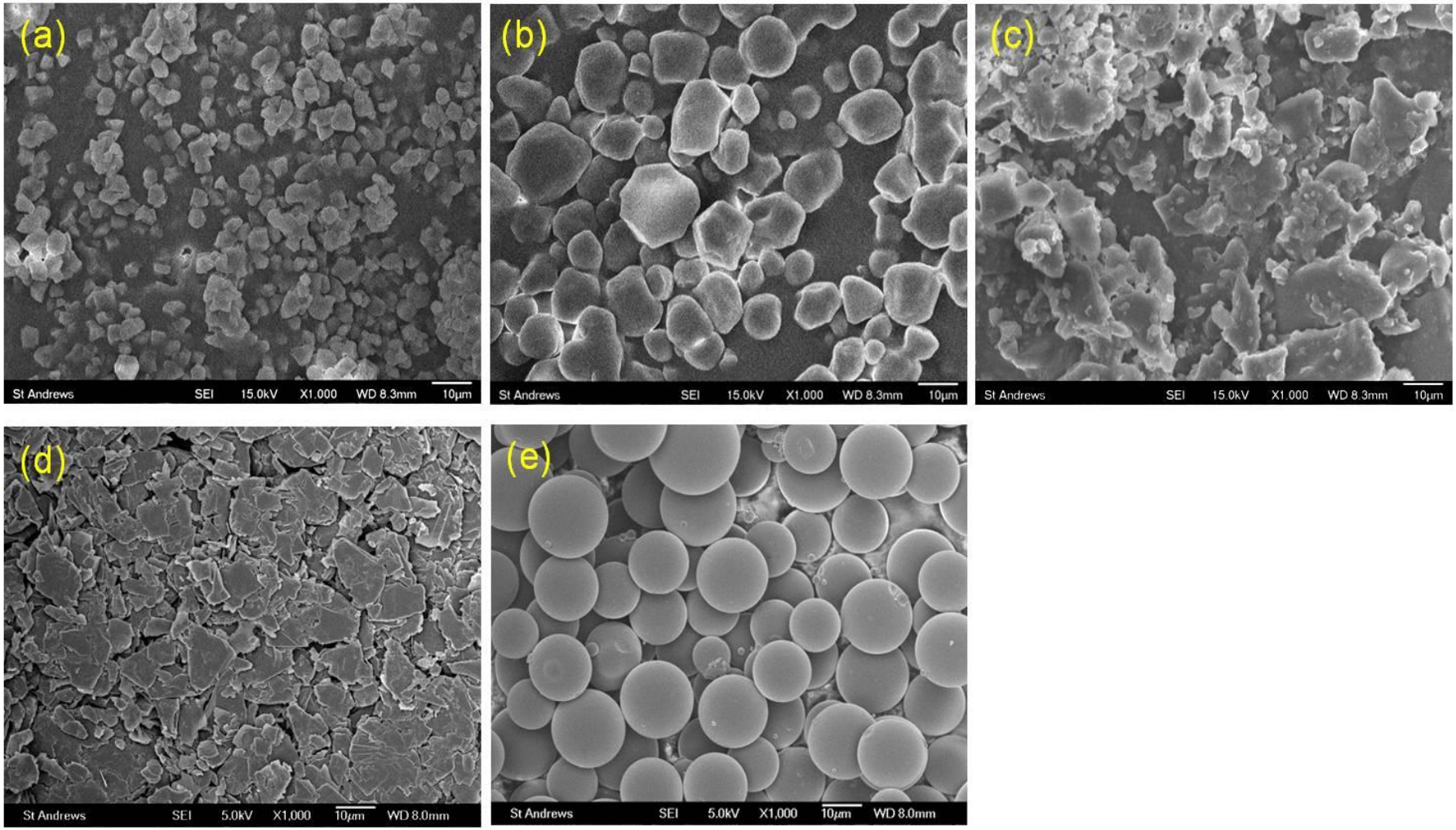

Figure 3-9 SEM micrographs of different types of pore formers: a. rice starch, b. corn starch, c. sugar, d. graphite, e. glassy carbon

3.6.2 The effect of different pore formers on the purity of LSGT pellets

The powder used to study the influence of the pore formers on the perovskite purity was $La_{0.4}Sr_{0.4}Ga_{0.1}Ti_{0.9}O_{3-\gamma}$ (LSGT10). The amount of each pore former used to make porous pellets was 15wt% (relative to perovskite powder). After making porous pellets and sintering at 1300 °C with different pore formers, X-ray diffraction was used to check if there were any impurities brought in by the pore formers. Most of the materials did not produce other phases when functioning as pore formers. However, an unknown 2nd phase was detected from the XRD pattern of the pellet which used rice starch as the pore former (see Fig 3-10). Since clean surfaces are very important for the coating procedure, the rice starch was rejected as a pore former for further studies.

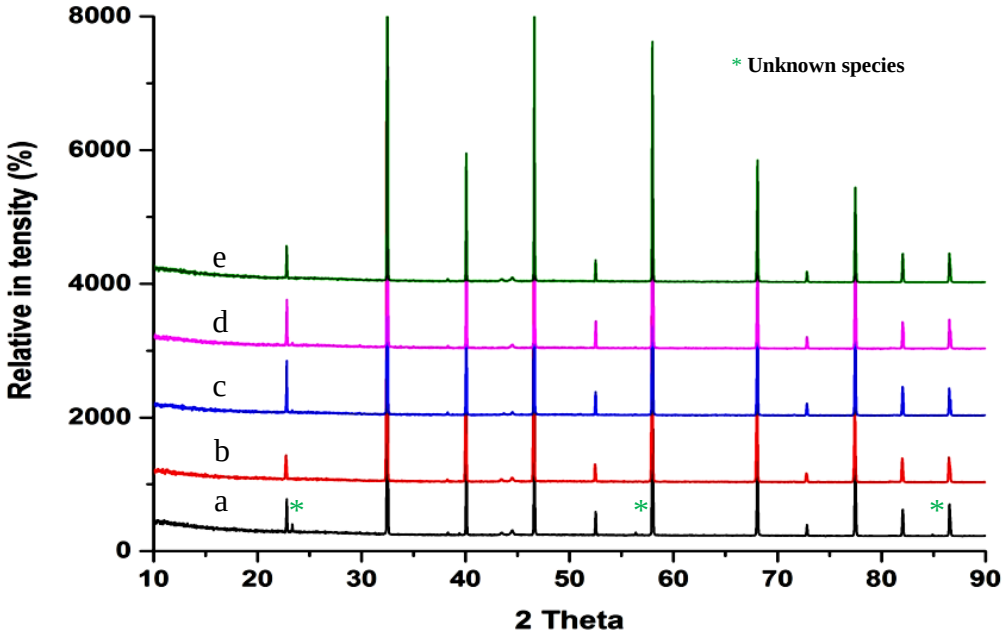

Figure 3-10 XRD patterns of LSGT10 pellets made with different pore formers by sintering at 1300 °C: a. rice starch, b. corn starch, c. sugar, d. graphite, e. glassy carbon

3.6.3 The effect of different pore formers on the porosity of LSGT10 pellets

The sintered porous pellets using different pore formers were also examined by SEM to check the porosities of the perovskites (see Fig 3-11). From the SEM images, the porosities of the perovskite generated by different pore formers are in the order of graphite < sugar < corn starch < glassy carbon. This suggests that the shape of the pore former influences the shape of the pores. It seems that pore formers with bulkier 3-dimensional shapes tend to make perovskites with better porosities, compared to those with flatter, more 2-dimensional shapes, i.e. graphite.

The porosities of the porous pellets were measured by comparing the densities of the pellets with the theoretical densities of the samples. The results are plotted in the graph shown in Fig 3-12. The trend in relative densities corresponded to the above SEM results. The sample which used graphite as the pore former exhibited the lowest porosity and the sample using glassy carbon as the pore former showed the highest porosity. The relative porosities of the samples using corn starch and sugar as pore formers were between the other two, while sugar made the perovskite slightly more porous than did the corn starch.

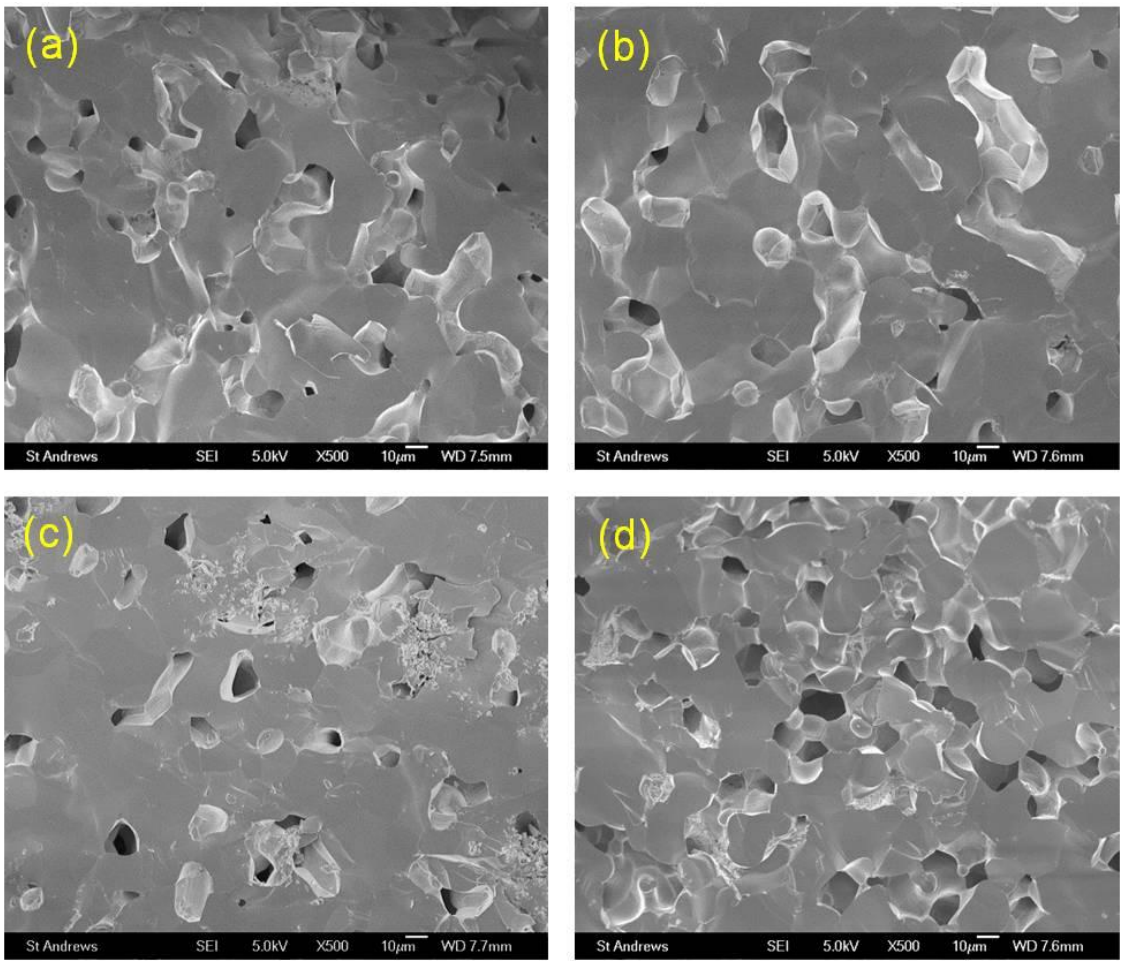

Figure 3-11 SEM micrographs of sintered LSGT10 pellets made with different pore formers: a. corn starch, b. sugar, c. graphite, d. glassy carbon

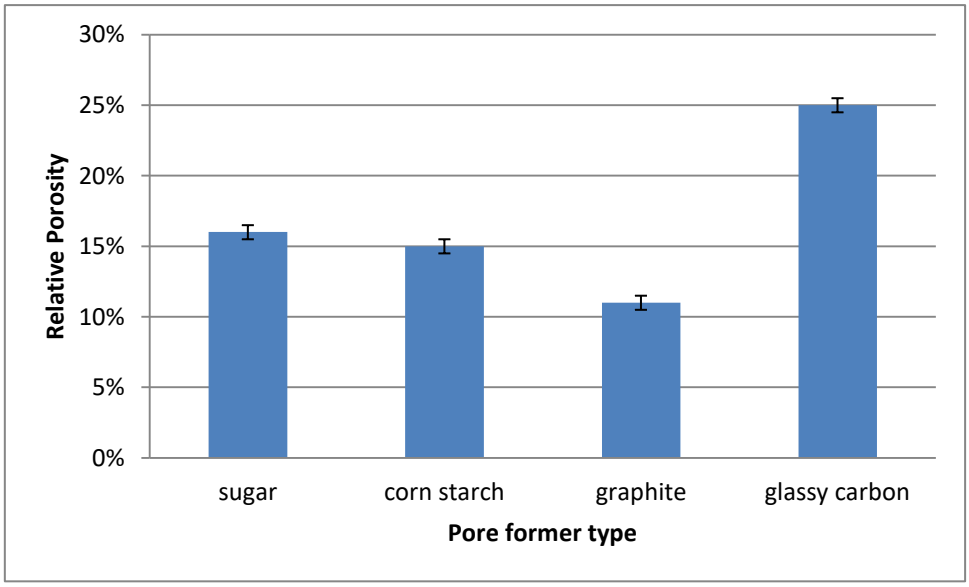

Figure 3-12 Relative porosity of LSGT10 pellets using different pore formers

3.6.4 The effect of different pore formers on the amount of Ga loss and reducibility of LSGT10 pellets

The amount of catalyst to be coated onto the perovskite depends purely on the amount of Ga loss after the perovskite pellets were reduced for the first time. Therefore, it is very important to evaluate the influence of the different pore formers on the amount of Ga loss during the 1st reduction.

The amounts of Ga and oxygen losses for each sample during the first reduction are listed in Table 3-2. From Table 3-2, it can be noted that the amount of Ga and oxygen losses during the first reduction was largest from the more porous sample which employed glassy carbon as the pore former. LSGT10 using sugar or corn starch as pore formers showed similar magnitudes of both Ga and oxygen loss, while the reducibility of the perovskite was higher when corn starch served as the pore former. Interestingly, the quantity of Ga and oxygen loss was negligibly negative when graphite was used as the pore former. One possible explanation could be that the porosity of the pellet was low and not continuous enough to allow the H_2 to travel properly through every pore in the pellet and effectively reduce the sample. It is well known that graphite flakes lead to a horizontal type of porosity that might lack interconnectivity. At the same time, due to the insufficient gas flow, the moisture brought in by the hydrogen may have been trapped in the pores, resulting in an increase in the mass of the sample. It seemed that the sample which used glassy carbon as the pore former showed the best reducibility compared to the others.

Pore Former	Corn starch	Sugar	Graphite	Glassy carbon
Ga loss at/fu	0.0032	0.0022	-0.0002*	0.0121
O loss at/fu	0.0065	0.0048	-0.0012*	0.0116

Table 3-2. Ga and O loss of LSGT10 pellets made with different pore formers during the first reduction; *: negative values of Ga and O loss mean that the sample gained weight during the reduction treatment

The above hypothesis was supported by checking the appearance of the samples after

each stage (see Fig 3-4). The porous samples all looked the same in colour after being fired in air, and turned dark grey after reduction in 5% H_2. However, the samples reacted differently after re-oxidation. After re-oxidation, the samples which used corn starch or glassy carbon as pore formers looked almost the same as the as prepared pellets. Meanwhile, the samples which used sugar or graphite as pore formers showed some grey areas after re-oxidation, especially the one which used graphite as the pore former. This suggested that, under the given reaction conditions, the porosities in the above two samples were not high enough to ensure complete reduction and re-oxidation of the perovskite pellets.

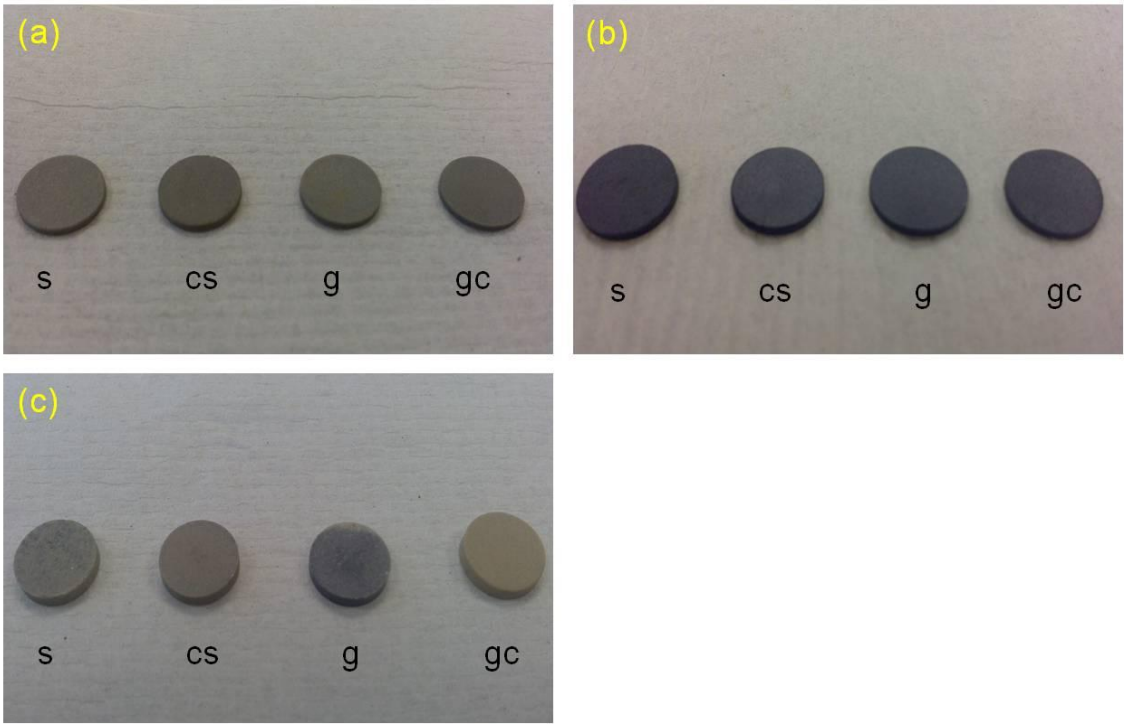

Figure 3-13 LSGT10 pellets made with different pore formers (sugar (s), corn starch (cs), graphite (g), glassy carbon (gc)) after each stage treatment: a. as prepared (oxidation), b. after reduction, c. after re-oxidation

By comparing all of the different aspects, it can be concluded that glassy carbon as the pore former provided the best porosity under these experimental conditions. However, considering the cost of the material, the corn starch was chosen as the pore former for making porous pellets since it also provided relatively good porosity for the perovskite.

3.6.5 Optimization of the porosities of LSGT pellets using corn starch as the pore former

The corn starch provided relatively good porosity compared to the other pore formers. However, the porosity of the sample still needs to be improved when it is being used for catalyst coating. Hence, it is necessary to optimize the conditions of making porous perovskite pellets. In order to achieve higher porosity, different fractions of corn starch were used for making porous pellets, in order to assess the influence of the quantity of pore former on the porosity and Ga loss of LSGT10 pellets under reducing atmospheres (see Figure 3-14 and Figure 3-15).

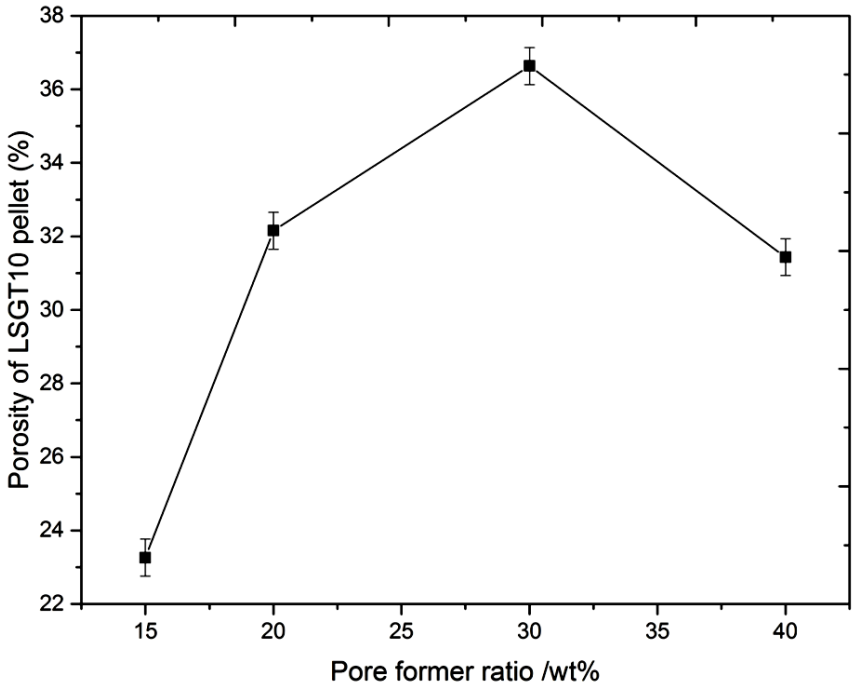

Figure 3-14 Porosity of LSGT10 pellet as a function of pore former content

The porosities of LSGT10 pellets were measured with respect to the amount of corn starch pore former, as shown in Figure 3-14. The porosities of the samples generally increased with the quantity of the pore former. However, when the pore former exceeded 30 wt%, the porosity of the sample started to decrease. This may be because the sizes of the pores created by the excess pore former were too large for the perovskite to support. As a result, the perovskite support collapsed in the process of forming the porous structure, leading to lower porosity. According to Figure 3-15, maximum Ga loss was achieved when 20 wt% of pore former was used. The same phenomenon also

happened with oxygen loss on reduction. Combining these results with the good porosities also attained, 20 wt% of pore former was chosen for making porous pellets in later experiments.

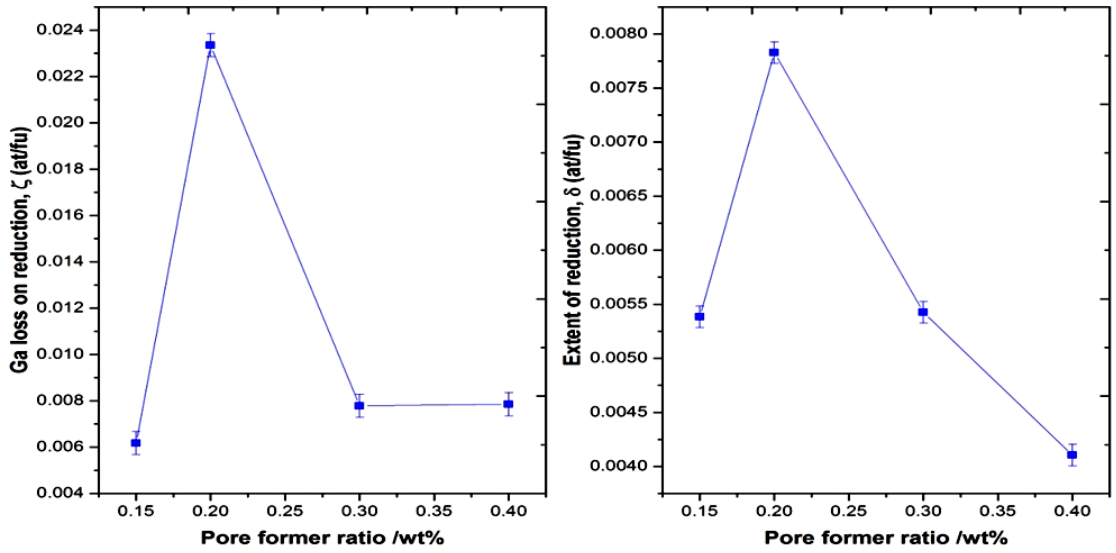

Figure 3-15 Ga loss and extent of reduction of perovskite as a function of pore former content

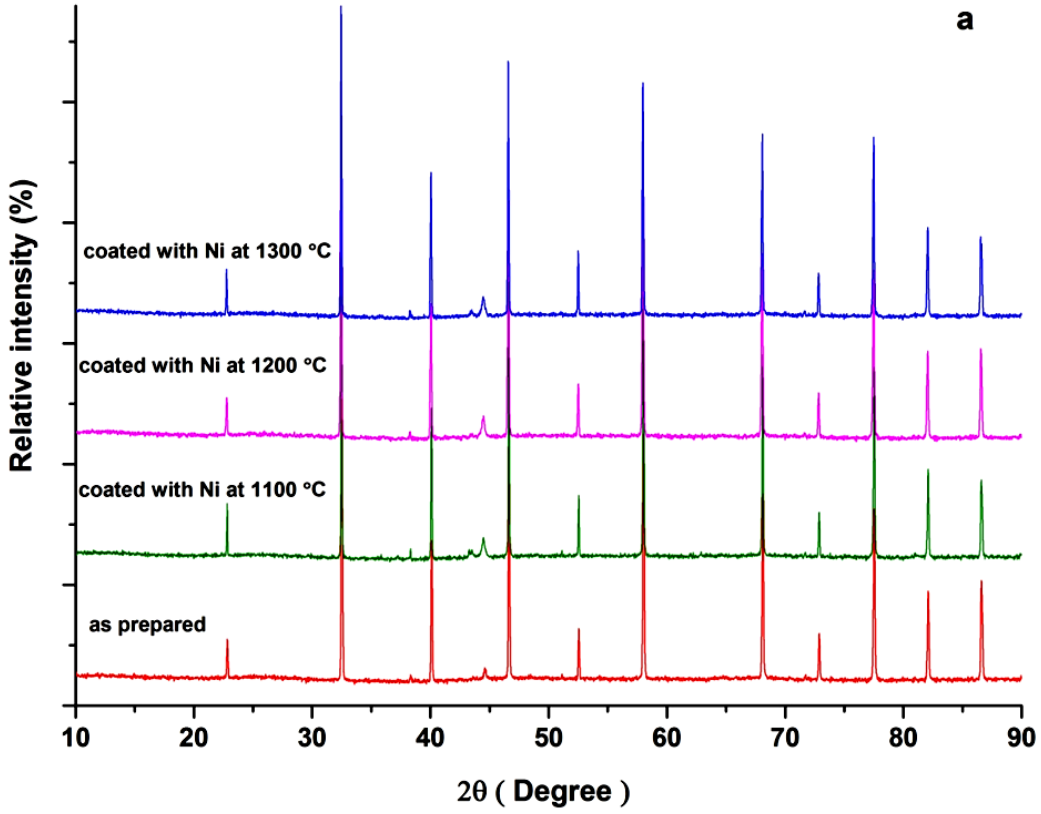

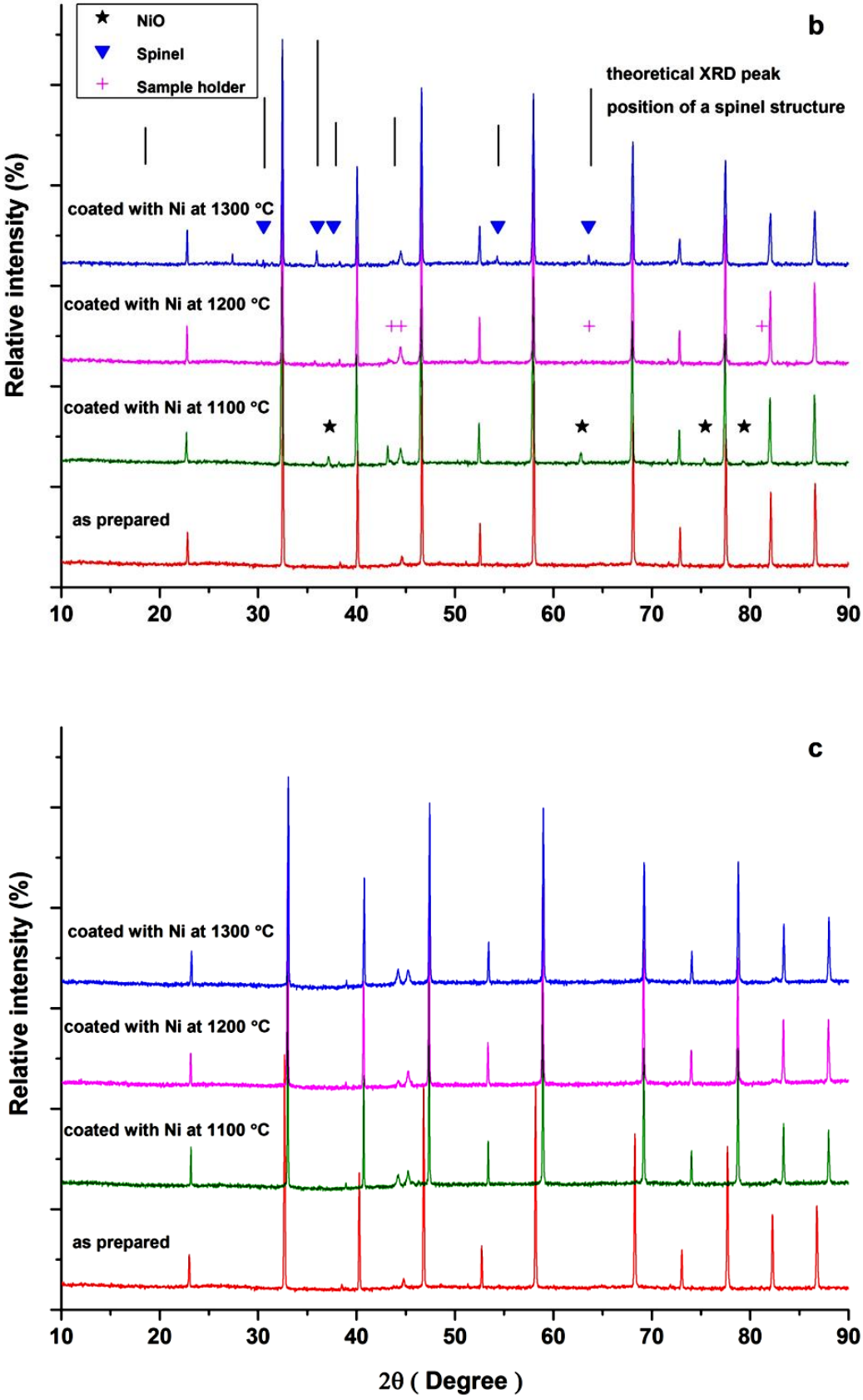
b
NiO
Spinel
Sample holder
theoretical XRD peak
position of a spinel structure
coated with Ni at 1300 °C
coated with Ni at 1200 °C
coated with Ni at 1100 °C
as prepared
Relative intensity (%)
10
20
30
40
50
60
70
80
90
c
coated with Ni at 1300 °C
coated with Ni at 1200 °C
coated with Ni at 1100 °C
as prepared
Relative intensity (%)
2θ (Degree)

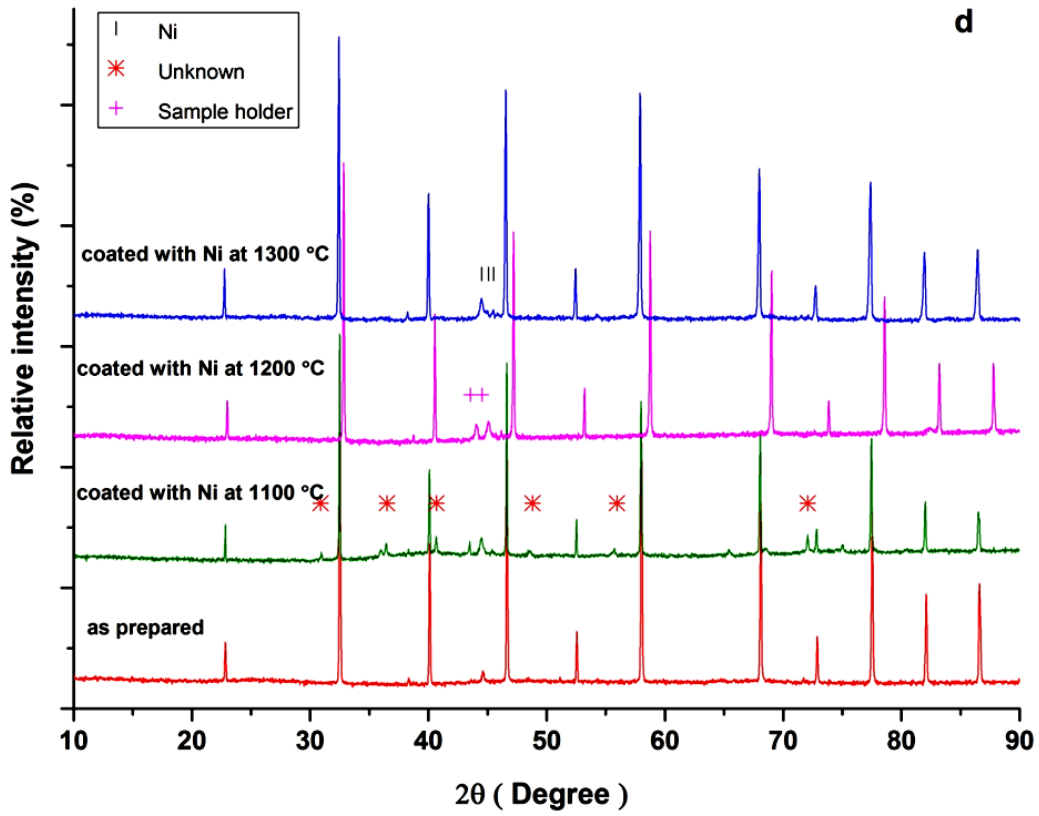

Figure 3-16 XRD patterns of LSGT06 at different stages of treatment, a. LSGT06 1st reduced at 900 °C then coated with Ni^{2+} catalyst at different temperatures, b. LSGT06 1st reduced at 950 °C then coated with Ni^{2+} catalyst at different temperatures, c. LSGT06 1st reduced at 900°C then coated with Ni^{2+} catalyst at different temperatures after 2nd reduction, d. LSGT06 1st reduced at 950°C then coated with Ni^{2+} catalyst at different temperatures after 2nd reduction

3.7 Conclusions

The Ni^{2+} catalyst has been successfully coated into the LSGT06 and LSGT10 perovskite at 1300 °C with the preliminary reduction treatment. It seemed that the reduction pre-treatment provided the perovskite with a Ga-depleted surface layer so that vacancies were made for nickel catalyst to be doped into the surface of the perovskite. There might be some Ni^{2+} diffused into the perovskite even at lower temperatures (1100 °C and 1200 °C). However, either the firing time was not long enough or the temperature was not high enough to provide a sufficient driving force and, as a result, most of the NiO particles remained on the surface of the perovskite grains in the form of angular shaped particles. In addition, NiO particles grew much bigger as the coating temperature increased from 1100 °C to 1200 °C. When the sample was coated at 1300 °C, the surface of the sample was clear and there was no NiO particles observed. After 2nd

reduction, the Ni exsolution can be observed on the surface of the perovskite grains in the form of spherical nanoparticles. This is the first demonstration of a catalyst coating diffusing into a Ga doped strontium titanate material and then exsolving under a reducing atmosphere. If other catalysts can be coated into the perovskite in the same way, the cost of using catalysts may be greatly reduced. Since LSGT10 showed more gallium loss which allowed for more catalysts coating loading than LSGT06, LSGT10 was chosen for the investigation of surface coating the perovskite with other catalysts.

A few well-known pore formers - namely glassy carbon, graphite, rice starch, corn starch, and sugar - were chosen to optimize the microstructure of the LSGT perovskite. Using the same amount of pore former, glassy carbon produced the highest porosity sample, while graphite provided the sample with the lowest porosity. Corn starch provided the perovskite with slightly lower porosity than sugar. However, according to the redox experiment which quantified the Ga loss during the reduction, the pores produced by corn starch had better connectivity. Considering the cost of making the samples, corn starch was chosen as the pore former for later experiments.

Chapter 4

Investigation of incorporating or coating palladium catalyst into the A-site deficient titanates

4.1 Introduction

Noble metals have been widely used as catalysts in fuel cells. In proton exchange membrane (PEM) fuel cells, Pt was one of the main catalysts being used in its catalyst layer. The cost of the fuel cell had been hugely reduced by decreasing the loadings of Pt from 4mg/cm^2 to 0.4mg/cm^2. However, the commercialization of the fuel cell was still difficult due to the high price of the Pt itself [22, 190]. Pd has proven to be one of the most likely replacements of Pt as the catalyst in fuel cells due to its higher abundance in earth and lower price in comparison to Pt [191-193]. However, the price of Pd is still very high, which limits its commercial applications in fuel cell, especially PEM fuel cells. A lot of effort has been made to produce Pt or Pd containing catalysts which show high activity and stability with lower amounts of catalyst required. This includes doping Pd into other materials [174, 194, 195], alloying Pd with other catalysts to form core-shell structures [192, 196-198], optimizing the size of the Pd particles through control of synthetic methods [197, 199], etc. The previous chapter has also verified the possibility of surface doping a Ni catalyst with the help of preliminary reduction treatment. Hence, it is worth investigating the possibility of surface doping Pd into the LSGT perovskite to decrease the amount of Pd needed.

In addition, it has been reported that Pd can be incorporated into the perovskite and exsolve afterwards as nano-particles on the surface of the material. In these reports, Pd cations normally occupy the B-site of the perovskite and showed reversible properties during the redox cycle. Doping the Pd into the perovskite can efficiently reduce the agglomeration phenomenon which normally leads to the deterioration of the catalysts [83, 92, 93]. The state of the art method of doping Pd into lanthanum-based perovskite typically involves doping the Pd into $LaMO_3$ (M = Mn, Co, Fe, Ga, etc.) with A-site fully occupied [173, 174, 194-197, 200]. However, few reports currently exist which describe doping A-site deficient perovskite or lanthanum titanate based perovskite with Pd catalysts. Combined with the results from the previous chapter, the possibility of incorporating the palladium into a lanthanum gallium doped strontium titanate with the nominal molecular formula of $La_{0.4}Sr_{0.4}Ti_{0.9}Ga_{0.077}Pd_{0.023}O_{3-\delta}$ was investigated. The experimental conditions of coating the palladium into the surface of LSGT10 perovskite which was first reduced at 950 °C were then explored.

In order to understand the mechanism of Pd doping in the A-site deficient titanate based perovskite, the doping of $Pd^{2+/3+/4+}$ into other A-site deficient titanates $A_{1-\alpha}Ti_{0.97}Pd_{0.03}O_{3-\delta}$ was also investigated. In order to substitute the cations in the solid solutions with the other cations, the size of the replacement cations should be similar to the cations that are going to be replaced. In addition, the coordination number (CN) of the cations is also very important in forming a solid solution since it will influence the size of the cations. Figure 4-1 shows a chart of ionic radii against coordination number for the cations involved in the study [58]. According to the graph, there are three possible metal valences that may be incorporated into the perovskite. In this experiment, the valences of the palladium doped in the A-site deficient titanates were assumed to be 2+ and 4+. The molecular formula design was based on the A-site deficient series $La_xAe_{1-3x/2}TiO_{3-\delta}$ (Ae-alkaline earth, A-site deficiency $\alpha=x/2$) reported by Slater and Irvine *et al* [99]. Two assumptions were made when designing the molecular formula of the perovskite. The molecular formulae of Pd doped A-site deficient titanates and their abbreviations are listed in Table 4-1. The assumed valence of the palladium cations in the perovskites were also listed in the table.

Nominal molecular formula of Pd doped perovskite	Abbreviation of the Pd doped perovskite	Assumed valence of Pd in the perovskite
$La_{0.14}Ca_{0.76}Ti_{0.97}Pd_{0.03}O_{2.94}$	LCPT01	2+
$La_{0.14}Sr_{0.76}Ti_{0.97}Pd_{0.03}O_{2.94}$	LSPT01	2+
$La_{0.4}Sr_{0.4}Ti_{0.97}Pd_{0.03}O_3$	LSPT02	4+
$La_{0.6}Sr_{0.1}Ti_{0.97}Pd_{0.03}O_3$	LSPT03	4+

Table 4-1 The abbreviations of the palladium doped perovskite and the valence of the doped palladium cations in the experimental plan assumption

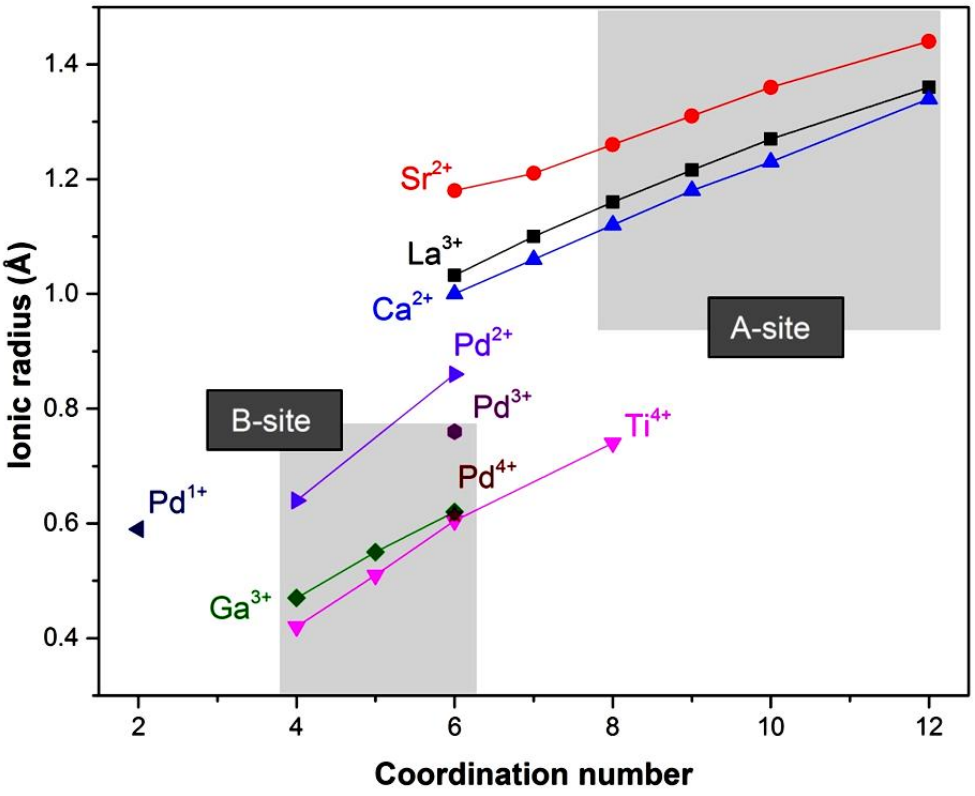

Figure 4-1 Ionic radii vs. coordination number for palladium cations and cations in the perovskite. The characteristic regions for A and B-site cations are emphasized and labelled. The effective ionic radii are from Shannon [58, 60]

In the first assumption, palladium cations adopt square planar coordination (IVSQ) with the valence of 2+ in the perovskite. In this case, the CN of Pd^{2+} in the perovskite is 4. The molecular formula is designed to have two oxygen vacancies for each palladium dopant. Therefore, the general molecular formula based on this assumption became $La_{x+a}Ae_{1-3x/2+b}Pd_yTi_{1-y}O_{3-2y}$ (Ae=Ca, Sr). In order to fix the stoichiometry of oxygen at 3-2y, the stoichiometry of the A-site of the perovskite was balanced by adjusting the ratio of cations on the A-site (see Equation 4-1):

$$(x + a) + \left(1 - \frac{3x}{2} + b\right) = x + \left(1 - \frac{3x}{2}\right) \qquad \text{Eq. } 4-1$$

Combining with the charge balance equation (see Equation 4-2),

$$3\bullet(x + a) + 2\bullet(1 - 3x/2 + b) + 2y + 4\bullet(1-y) = 2\bullet(3-2y) \qquad \text{Eq. } 4-2$$

The relationship between a, b and y was found out to be

$$\begin{cases} a = -2y & \text{Eq. } 4-3 \\ b = 2y & \text{Eq. } 4-4 \end{cases}$$

By inserting equations Eq.4-3 and Eq4-4 into the general molecular formula $La_{x+a}M_{1-3x/2+b}Pd_yTi_{1-y}O_{3-2y}$, the molecular formula then became

$$La_{x-2y}M_{1-3x/2+2y}Pd_yTi_{1-y}O_{3-2y}$$

Sample LCPT01 and LSPT01 were based on the above molecular formula. One of the reasons for choosing calcium as one of the cations on the A-site of the perovskite was the fact that Ca leads to less perovskite surface structuring compared to Sr, which is known for forming the A-site rich surfaces (Ruddlesden–Popper phases ($A_{n+1}B_nO_{3n+1}$)) due to the mismatch of cation sizes and compensating the charges, therefore, hindering the exsolution of nanoparticles [201-203]. In addition, calcium helps with cation diffusion due to its smaller ionic radius which could be helpful for the exsolution of palladium cations to the surface of the perovskite.

The second assumption is that the Pd cations adopt octahedral coordination with the valence of 4+ in the perovskite. The reason of assuming Pd to be 4+ in the perovskite is that A-site deficiency in the perovskite is known to lead to B-site cations in the highest oxidation state [76, 101]. Different A-site deficiencies were selected in order to see the influence of the A-site deficiencies on the Pd doping in the titanate based perovskite. Samples LSPT02 and LSPT03 were chosen based on this assumption.

4.2 Experimental Section

4.2.1 Solid state synthesis of Pd containing titanate

The Pd doped A-site deficient titanates, both with and without Ga, were synthesized by the same solid state method as described for LSGT (see Chapter 2.1). The palladium source in the synthesis process was Pd $(NO_3)_2$ in nitric acid solution and it was added in the deionised water before the other solid powder mixture went through the ultrasonic probe.

4.2.2 Coating LSGT10 with palladium catalyst

Pd was coated into the LSGT10 perovskite pellets via the same method of coating Ni^{2+} (see Chapter 2.4). The as prepared LSGT10 pellets were reduced at 950 °C first. After the samples were impregnated with Pd $(NO_3)_2$ solution, they were either fired in air or in O_2 for 1-24 h before the 2nd reduction.

4.2.3 Reduction of the samples

In this chapter, the reductions of all the perovskite samples after they were doped or coated with catalyst were carried out in 5% H_2/Ar at 930 °C for 30 h in the tube furnace. Each coated sample was reduced in the form of a pellet while the doped samples were reduced in the form of powder.

4.3 The investigation of incorporating palladium into the bulk surface of LSGT10

4.3.1 Solid state synthesis of $La_{0.4}Sr_{0.4}Ti_{0.9}Ga_{0.077}Pd_{0.023}O_{3-\delta}$

In order to coat palladium into LSGT10, it is worth investigating first whether or not it is possible to dope palladium into the titanate. Hence, perovskite with the nominal molecular formula of $La_{0.4}Sr_{0.4}Ti_{0.9}Ga_{0.077}Pd_{0.023}O_{3-\delta}$ (LSGTP) was prepared by solid state method. The amount of palladium in the LSGTP equals to the amount of Ga loss of LSGT10 when it was first reduced at 950 °C. The as prepared LSGTP perovskite then went through reduction in 5% H_2/Ar to investigate the potential exsolution of the palladium particles. The XRD patterns of the LSGTP before and after it was reduced are shown in Figure 4-2. According to Figure 4-2, single phase of LSGTP with the monoclinic structure has been achieved by the solid state synthesis method. After reduction, the perovskite retained its main structure with small amount 2nd phase which might be Pd_5Ga_3 in the XRD result. The unit cell parameters of the perovskite before and after reduction are listed in Table 4-2. There is a slight increase in unit cell volume upon reduction due to reduction of Ti^{3+} to Ti^{4+}.

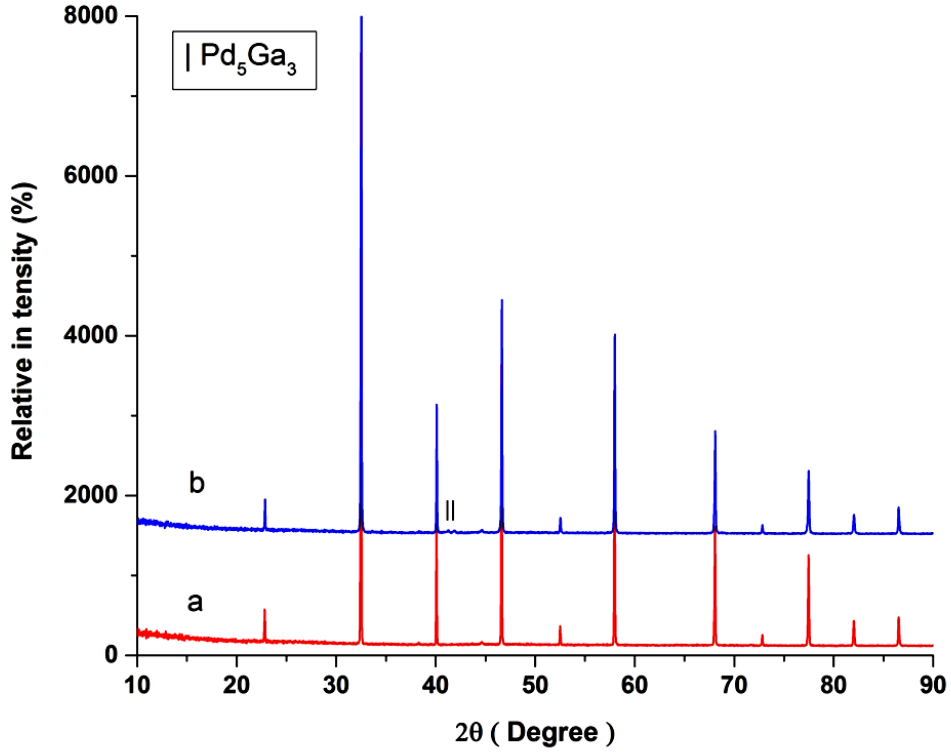

Figure 4-2 XRD patterns of LSGPT: a. as prepared LSGPT, b. LSGPT after reduction

Treatment of LSGTP	Space group	Unit cell parameters (Å)	β (°)	Unit cell volume (Å^3)
As prepared	I2/a	a=7.7775 (6) b=5.5012 (5) c=5.50737 (25)	90.038 (3)	235.63 (4)
After reduction	I2/a	a=7.7797 (6) b=5.50451 (24) c=5.5038 (3)	90.085 (6)	235.69 (4)

Table 4-2 Unit cell parameters of LSGPT under different experimental treatment

The morphology of the LSGPT before and after reduction was examined by SEM (Figure 4-3). There were some "cauliflower" shaped palladium oxide particles on the surface of the as prepared LSGPT sample, probably produced by agglomeration of initial small Pd particles, indicating that there might be small amount of palladium not doped into the perovskite [204]. After reduction, palladium nano particle exsolution was observed on the surface of the perovskite. At the same time, some particles which were

a few microns in size with well defined shape were also observed on the surface of the perovskite. To confirm the composition of the big particles on the surface, the sample was examined by EDX. According to the EDX result shown in Figure 4-4, the large particles on the surface of the perovskite mainly consisted of Pd and Ga. Combined with the XRD result, it can be confirmed that these particles are likely to be Pd_5Ga_3 alloy. The formation of the Pd_5Ga_3 may be due to the fact that Ga is volatile and would leave the perovskite during the first reduction as has been reported [100]. Although, the perovskite was doped with Pd, the bulk material still maintained the same structure as the non-doped LSGT. As a result, Ga would escape the perovskite during reduction and alloy with the non-doped palladium on the surface of the sample.

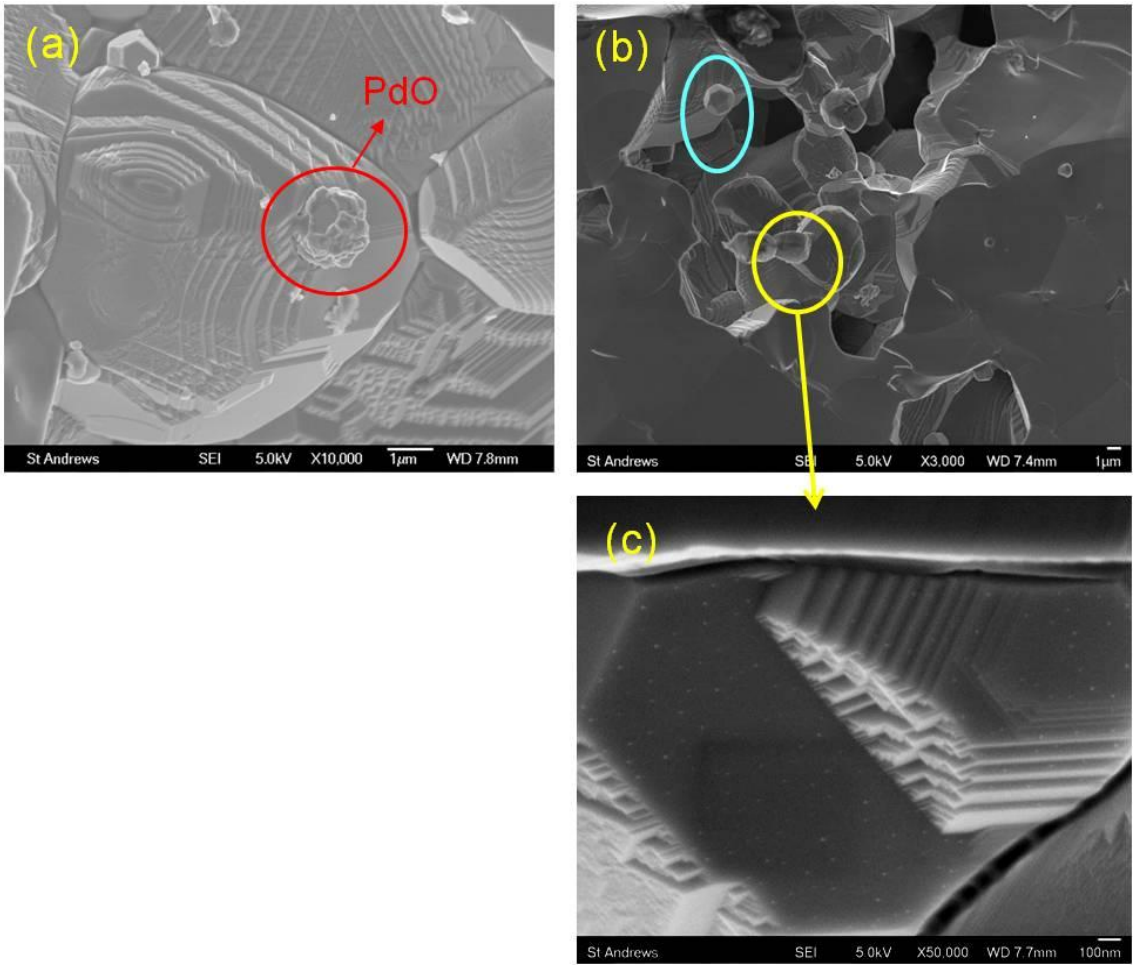

Figure 4-3 SEM images of LSGPT: a. as prepared LSGPT, b. LSGPT after reduction, c. nano particle exsolution from reduced LSGPT

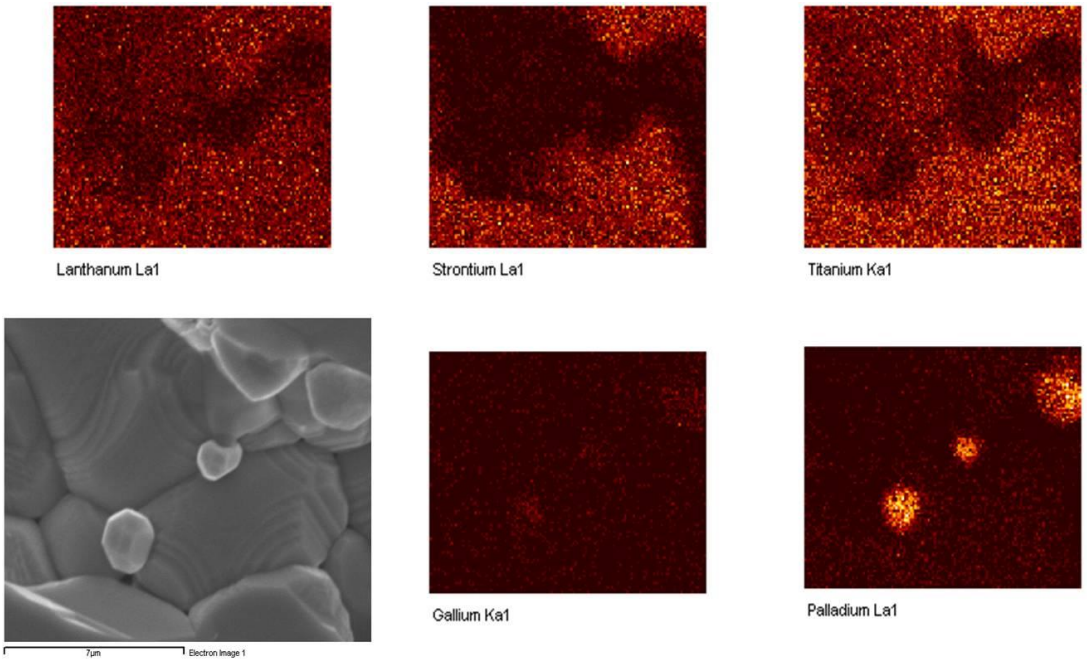

Figure 4-4 EDX of LSGPT after reduction

4.3.2 Surface coating palladium into4 the LSGT10

Although not all the palladium had been successfully incorporated into the LSGT perovskite, it was proven that it is possible to introduce palladium into the perovskite and exsolve it afterwards. To surface coat palladium into the reduced LSGT10, the experimental conditions may need to be altered to promote more palladium being doped into the LSGT10 from the surface. At first, palladium was coated into the perovskite following the same method as nickel coating LSGT10. However, there was a very obvious peak of PdO in the XRD pattern of the palladium coated LSGT10 (see Figure 4-6a). In addition, many palladium oxide particles were observed on the surface of LSGT10 from the SEM (see Figure 4-5a). Therefore, a longer firing time was applied to promote more palladium diffusing into the perovskite. After the sample was fired for an extended time, there was no PdO peak apparent in the XRD patterns. The density of PdO particles became smaller but their particle size became larger (see Figure 4-5b). However, no exsolved nanoparticles were observed after reduction (see Figure 4-5c). This may be due to the fact that palladium oxide particles had agglomerated into clusters on the surface of the perovskite instead of dissolving into the perovskite during the heating. After palladium nitrate was impregnated onto the surface of the reduced LSGT10, it would decompose and form PdO under heating. Although LSGT10 was reduced earlier to make Ga-depleted layer for palladium to diffuse into the perovskite,

Pd^{2+} from PdO may still be too large to fit into the B-site of LSGT when its coordination number is six (see Figure 4-1). Hence, the sample was fired in oxygen to promote further oxidation of the palladium to make it fit in the B-site of the LSGT10 perovskite.

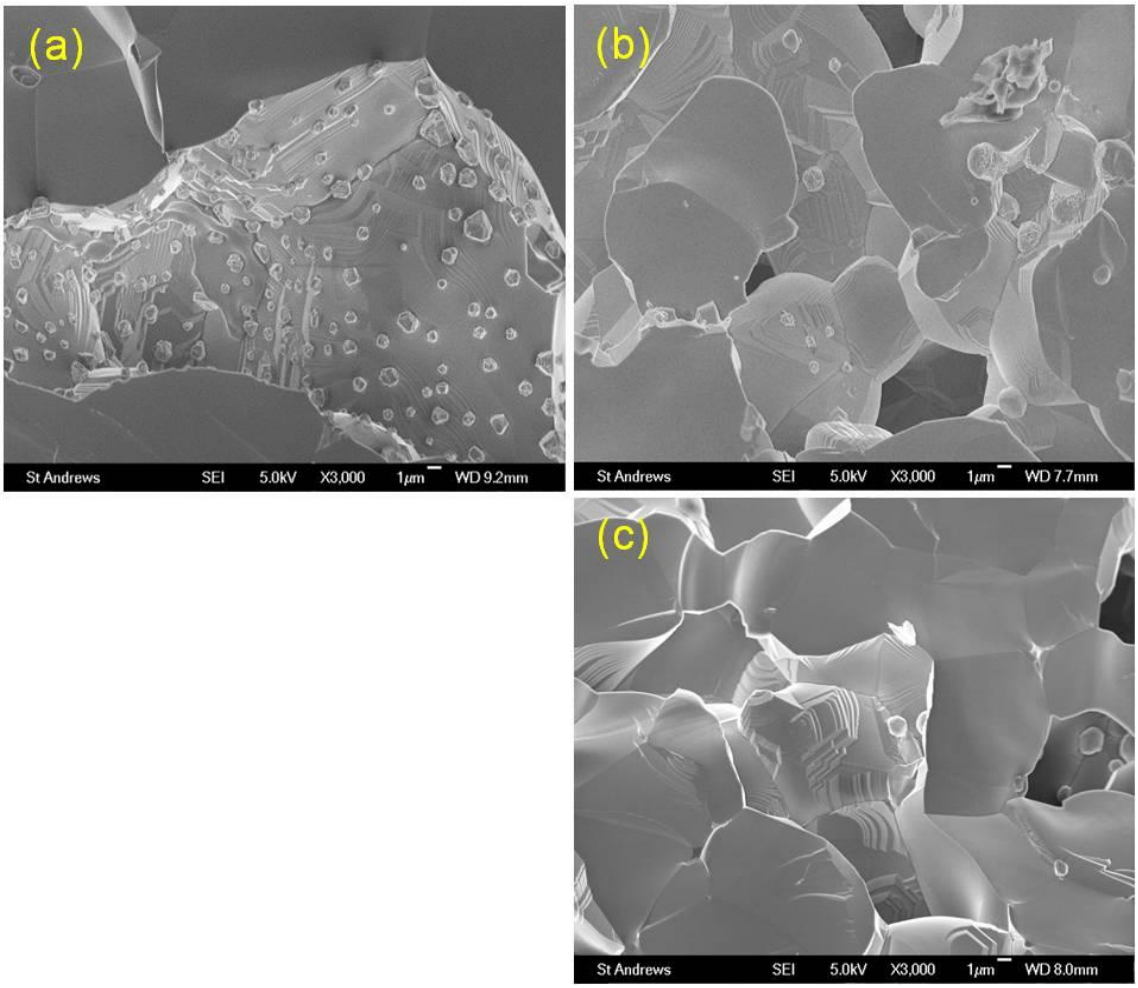

Figure 4-5 SEM images of 950°C reduced LSGT10 coated with palladium in air: a. fired at 1300°C for 1h, b. fired at 1300°C for 3h, c. after reduction for 30h

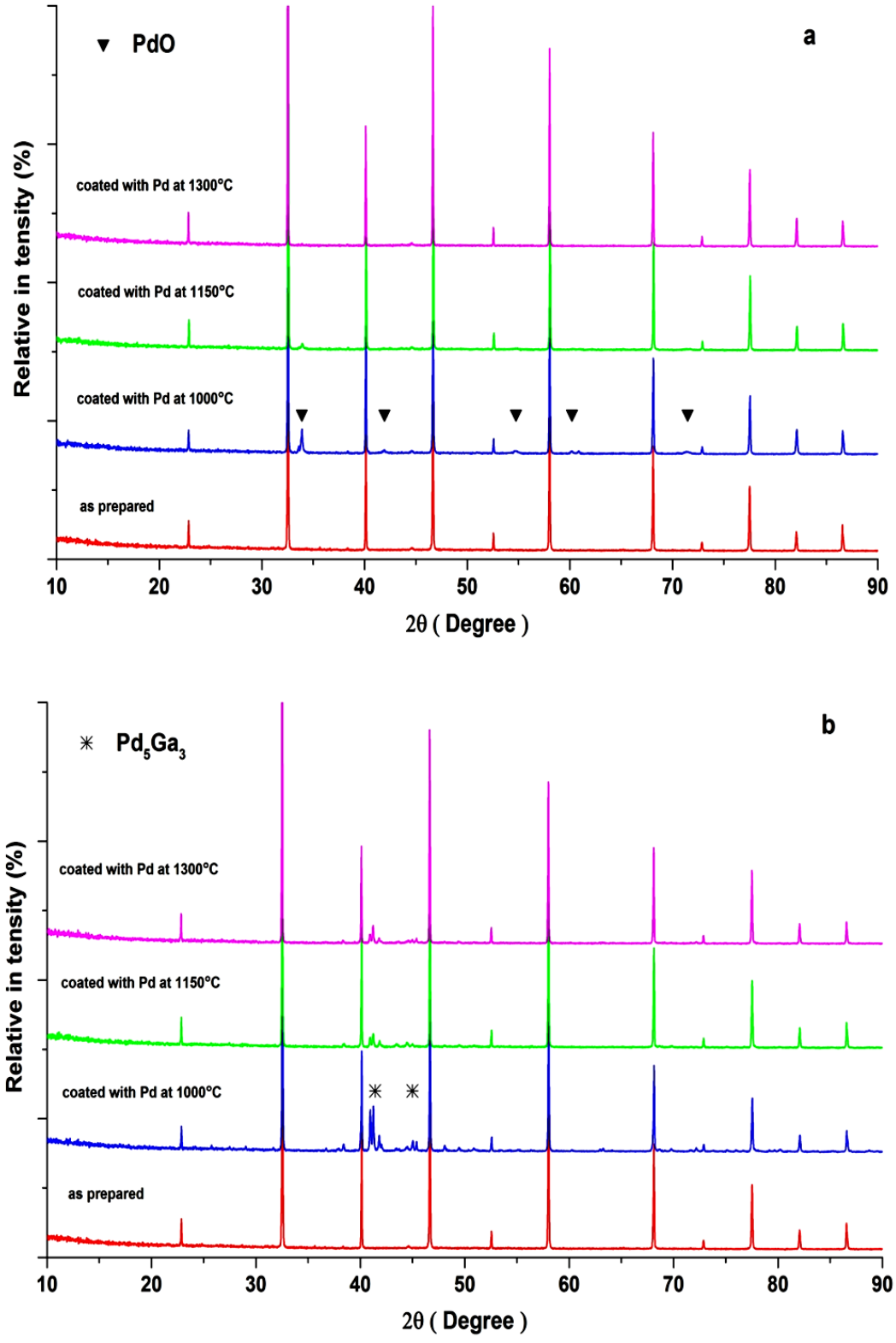

Figure 4-6 a. XRD patterns of 950 °C reduced LSGT10 coated with palladium in O_2 for 12 h at different temperatures, b. XRD patterns of LSGT10 coated with palladium in O_2 for 12 h at different temperatures after reduction

When the sample was heated in oxygen, a longer firing time of 12 h was applied to give the palladium more time to dissolve into the perovskite. In addition, different firing

temperatures were investigated in relation to the longer firing time. The XRD patterns of the samples are shown in Figure 4-6. As the firing temperature increased, the peak intensities of the PdO second phase decreased. After reduction, Pd_5Ga_3 also appeared as the 2nd phase in the XRD patterns. Figure 4-7 shows the change of the unit cell volumes of the sample after it was coated with palladium. According to the graph, the unit cell of the perovskite shrank as the coating temperature increased. By comparing the radii of palladium cations with different valences and coordination numbers from Figure 4-1, it is easy to find out that 6-fold coordinated Pd^{4+} is the only option which has a smaller radius than 6-fold coordinated Ga^{3+} (0.615 Å vs. 0.62 Å) [60]. This may indicate that palladium was diffusing into the perovskite as six-fold coordinated Pd^{4+}. Another possible explanation for the unit cell contraction may be due to Ga evaporation and perovskite re-equilibration by creating oxygen vacancies.

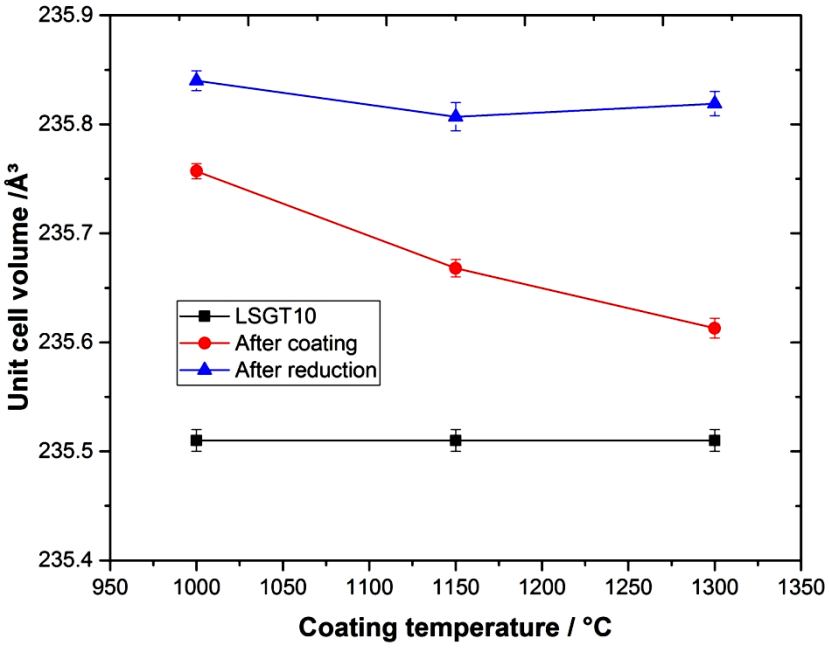

Figure 4-7 The change of unit cell volumes of LSGT10 as a function of coating temperature after it was coated with palladium in O_2 for 12h

The SEM images of the morphologies of the LSGT10 samples coated with palladium at different temperatures are shown in Figure 4-8. At the lower coating temperature of 1000 °C, the catalyst particles were distributed all over the surface of the perovskite, which looked the same as the normal impregnation result (see Figure 4-8a). After reduction, there was no obvious change on the surface of the perovskite (see Figure 4-9a). As the coating temperature increased, the Pd catalyst particles started to agglomerate into bigger particles. After reduction, the PdO particles on the surface of

the perovskite changed from cauliflower shape to a well-defined geometric shape. It is worth noting that much less palladium catalyst was observed on the surface of the perovskite when the sample was fired at 1300 °C (see Figure 4-8c). The catalyst on the surface of the perovskite looked to be partly dissolving in the perovskite. After reduction, exsolution of Pd particles was observed on the surface of the sample (see Figure 4-9c). At the same time, some particles were present on the surface of the perovskite, with shapes similar to those which appeared in the sample coated at 1200 °C. Examining the sample by EDX (see Figure 4-10), the composition of the big particles was Pd_5Ga_3, which corresponds to the result of the XRD analysis. The same particles were also observed in the sample which was coated at 1300 °C after they were reduced.

One possible explanation accounting for the formation of Pd_5Ga_3 may be that, after the perovskite was coated with palladium, it was heated at high temperature and the perovskite reorganised its structure to maintain its stability. At the same time, the Ga^{3+} cations diffused from the bulk of the perovskite to the surface [100]. When the samples were then reduced, apart from the doped palladium exsolving from the perovskite as nanoparticles, the gallium at the surface of the perovskite also started evaporating from the sample and alloyed with the un-dissolved palladium on the surface of the perovskite. The evaporation of gallium from the perovskite should be faster than the palladium exsolution from the perovskite since the gallium would have alloyed with the exsolved palladium nanoparticles as well.

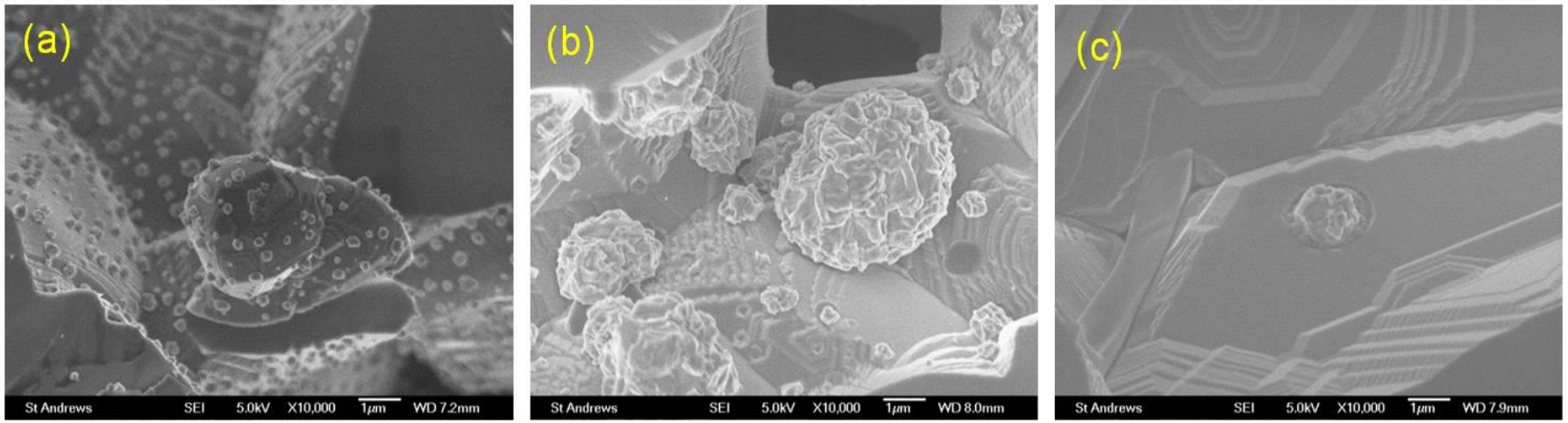

Figure 4-8 SEM images of 950 °C reduced LSGT10 coated with palladium in O_2 at different temperatures for 12h, a. coated with palladium at 1000 °C, b. coated with palladium at 1150 °C, c. coated with palladium at 1300 °C

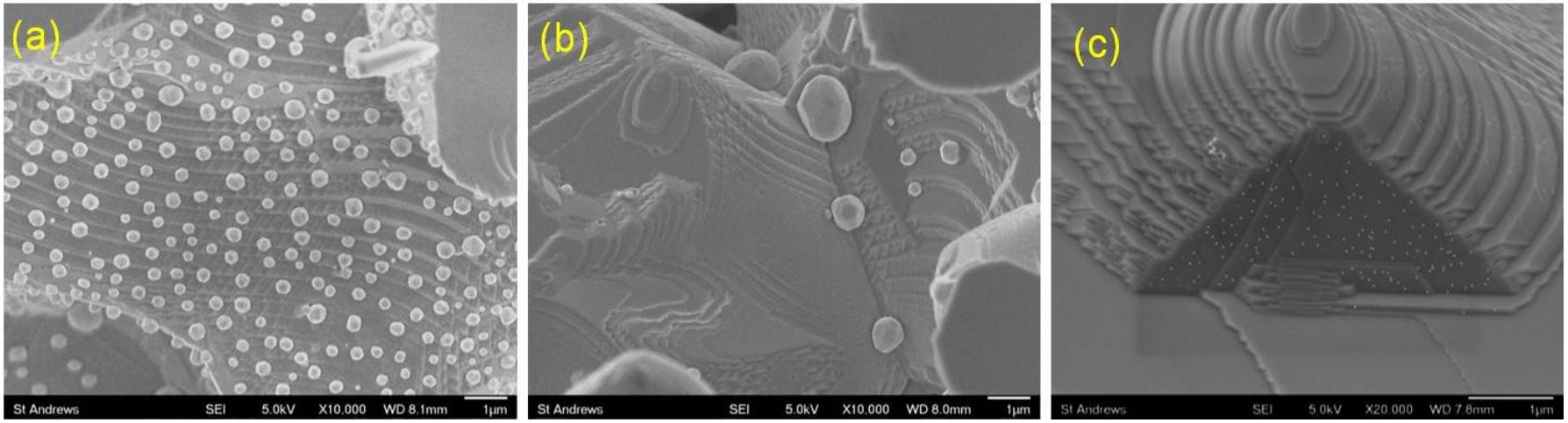

Figure 4-9 SEM images of 950 °C reduced LSGT10 coated with palladium in O_2 at different temperatures for 12 h after 2nd reduction for 30h, a. coated with palladium at 1000 °C, b. coated with palladium at 1150 °C, c. coated with palladium at 1300 °C

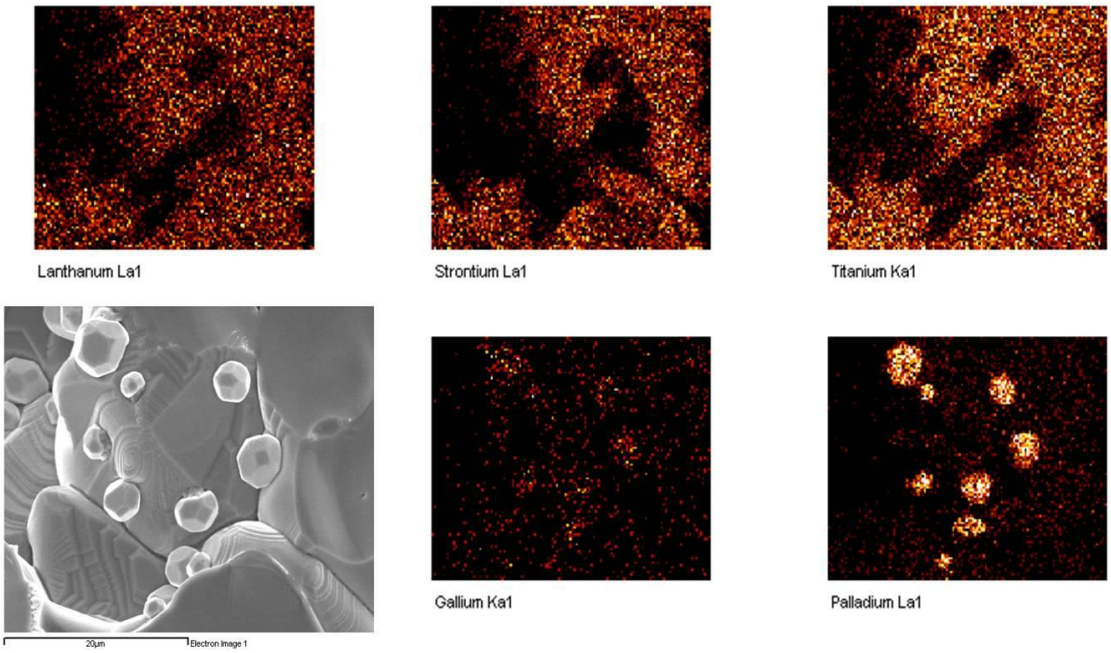

Figure 4-10 EDX of 950 °C reduced LSGT10 coated with palladium in O_2 at 1300 °C for 12 h which was reduced for 30h afterwards

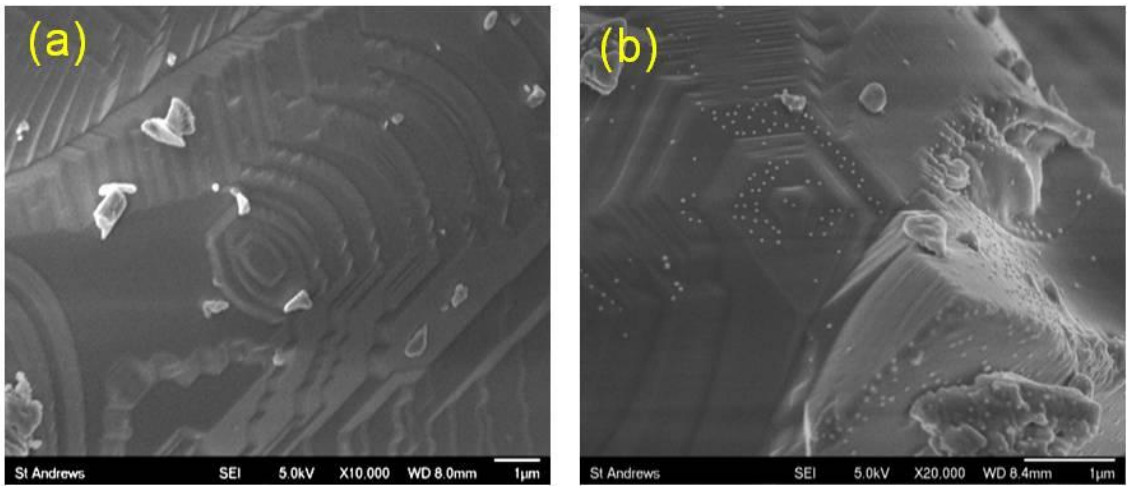

Figure 4-11 SEM images of 950 °C reduced LSGT10 : a. fired in O_2 at 1300 °C for 24h, b. coated with palladium O_2 at 1300 °C for 24 h after reduction

It seems that, for the sample which was coated at 1300 °C in O_2 for 12 h, the palladium oxide on the surface was in the process of dissolving into the perovskite. Therefore, a longer firing time of 24 h was applied to see if this would enhance the diffusion of the palladium catalyst into the perovskite. For comparison, non-coated LSGT10 perovskite was also heated at 1300 °C in O_2 for 24 h. The morphologies of the samples after reduction were studied by SEM as shown in Figure 4-11. After reduction, more exsolved nano-particles showed up on the surface of the palladium coated sample (see Figure 4-11b). By contrast, the surface of the blank sample was clear, which further

supports the hypothesis that the content of the exsolved particles was palladium (see Figure 4-11a).

4.4 LCPT01 & LSPT01 based on IVSQ coordination assumption

Li *et al* have demonstrated that the Pd^{2+} was successfully incorporated into the B-site of the $BaCe_{1-x}Pd_xO_{3-\delta}$ perovskite with square planar four coordination environment [123]. According to Figure 4-1, when the palladium ion (Pd^{2+}) is adopting a square planar 4-coordinate geometry on the B-site of the perovskite, it is possible for Pd^{2+} to substitute the titanium on the B-site to stabilize the perovskite. In order to find out whether the Pd^{2+} ion may indeed be doped in A-site deficient titanate, solid samples with the chemical formulae of $La_{0.14}Ca_{0.76}Ti_{0.97}Pd_{0.03}O_{2.94}$ (LCPT01) and $La_{0.14}Sr_{0.76}Ti_{0.97}Pd_{0.03}O_{2.94}$ (LSPT01) were synthesized by solid state methods and characterised as shown below.

4.4.1 LCPT01

The XRD patterns of the as prepared LCPT01 and the sample after it was reduced are shown in Figure 4-12. The first thing to notice by checking Figure 4-12 is that the sample did not form a single phase and there were very obvious Pd peaks showing up in the XRD patterns even before the sample was reduced. This indicates that not all palladium catalysts were doped into the perovskite lattice. Since there was very small difference in the intensities of the Pd peaks between the as prepared sample and after it was reduced. It was difficult to decide whether or not more palladium catalyst exsolved from the LCPT01 perovskite after it was reduced according to the XRD results. With the Rietveld refinement, it seemed that the proposed orthorhombic model fitted well for the LCPT01 perovskite sample (see Figure 4-13). The unit cell parameters of the reduced sample were calculated based on the same model using the same method. The unit cell parameters of the perovskite samples before and after reduction are listed in Table 4-3. After reduction, there was no obvious change on the structure of the perovskite and the unit cell volume of the LCPT01 had increased by 0.03%.

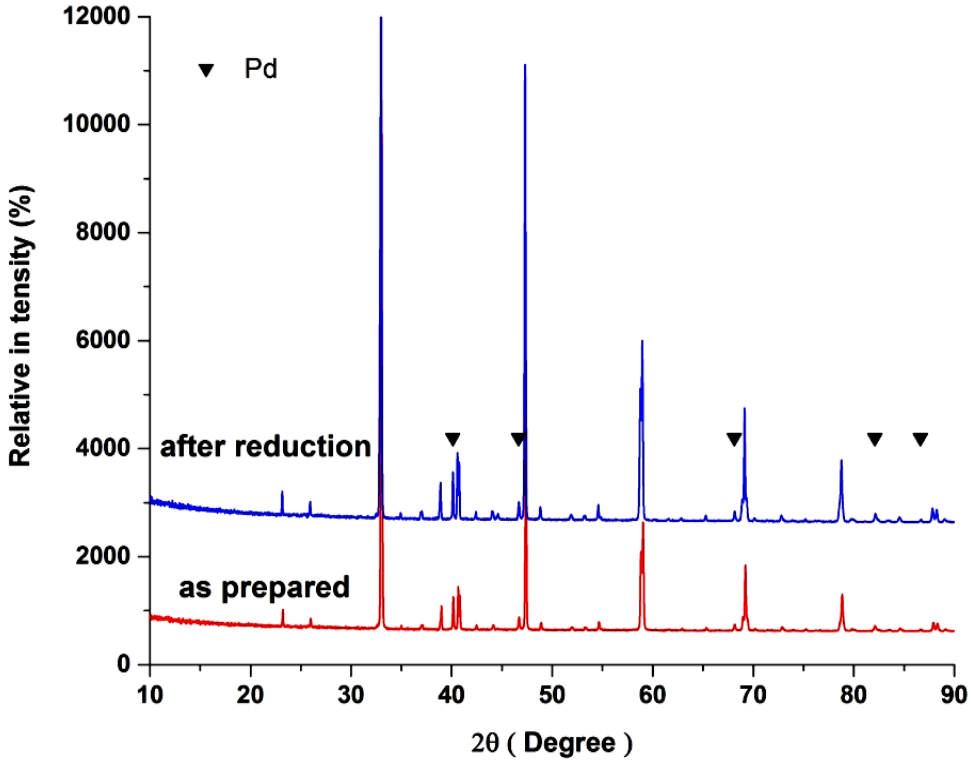

Figure 4-12 XRD patterns of as prepared LCPT01 and after it was reduced

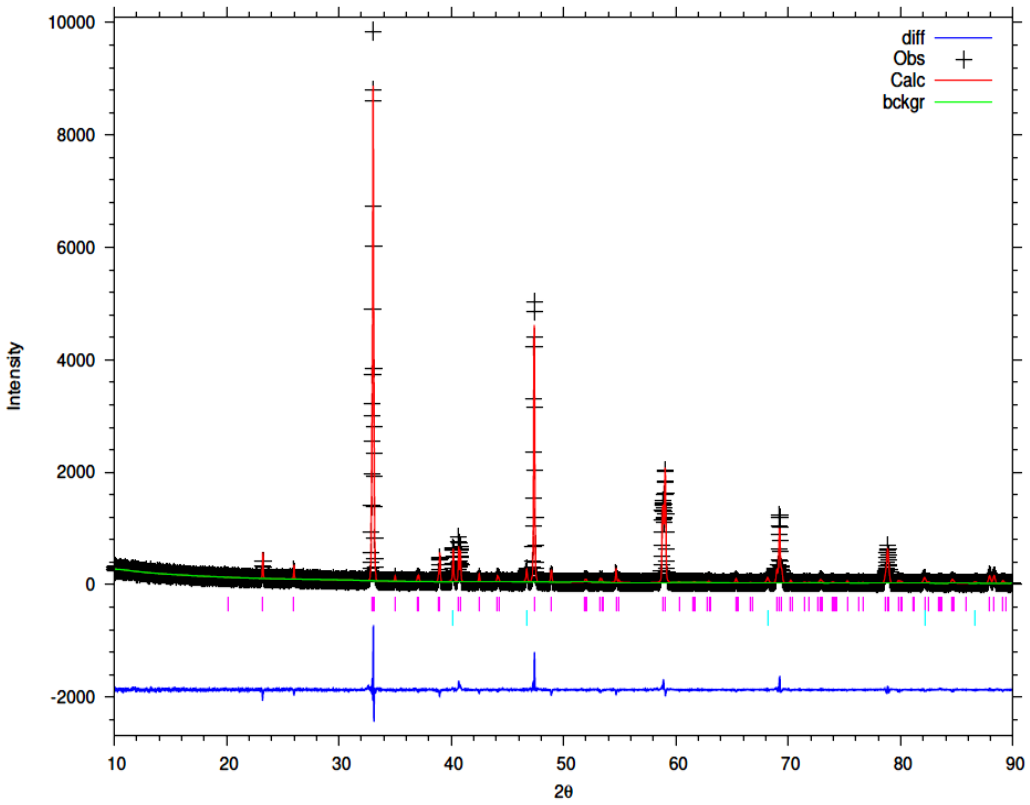

Figure 4-13 Rietveld refinement of as prepared LCPT01

Perovskite	Space group	Unit cell parameters (Å)	Unit cell volume (Å^3)	Rietveld fit parameters	2nd phase
LCPT01 as prepared	Pbnm	a = 5.41648(8) b = 5.44630(8) c = 7.67675(13)	226.463(6)	R_{wp} = 11.07%, R_p = 8.7%, χ^2 = 1.51	Pd
LCPT01 after reduction	Pbnm	a = 5.41811(7) b = 5.44803(7) c = 7.67957(11)	226.686(5)	R_{wp} = 10.88%, R_p = 9.01%, χ^2 = 1.51	Pd
LSPT01 as prepared	P m-3m	a = 3.901165(23)	59.3722(6)	R_{wp} = 13.78%, R_p = 10.3%, χ^2 = 2.83	TiO_2
LSPT01 after reduction	P m-3m	a = 3.901433(21)	59.3844(6)	R_{wp} = 15.13%, R_p = 10.99%, χ^2 = 3.44	TiO_2, Pd
LSPT02 as prepared	P m-3m	a = 3.890801(22)	58.9002(6)	R_{wp} = 9.99%, R_p = 7.57%, χ^2 = 3.82	PdO
LSPT02 after reduction	P m-3m	a = 3.892483(26)	58.9767(7)	R_{wp} = 13.22%, R_p = 9.74%, χ^2 = 2.59	N/A
LSPT03 as prepared	Pmmm	a = 3.88016(5) b = 3.87114(4) c = 7.78778(9)	116.9776(23)	R_{wp} = 14.06%, R_p = 10.50%, χ^2 = 2.744	$La_2Ti_2O_7$
LSPT03 after reduction	Pmmm	a = 3.88013(4) b = 3.87087(4) c = 7.79021(9)	117.0047(23)	R_{wp} = 14.80%, R_p = 10.69%, χ^2 = 3.08	$La_2Ti_2O_7$

Table 4-3 Unit cell parameters of palladium doped A-site deficient titanate under different experimental treatments

The morphology of the as prepared LCPT01 is shown in Figure 4-14a. The morphology of the sample after reduction at 930 °C for 30 h is shown in Figure 4-14b. Compared to Figure 4-14a, there were many nanoparticles apparent on the surface of the reduced perovskite. In addition, there was more than one type of nano particle present on the surface: angular shaped particles (see Figure 4-14b1); triangular and spherical shaped particles (see Figure 4-14b2). It was difficult to identify the composition of all the

nanoparticles mentioned above, but it is likely that they are palladium particles with different shapes [205]. In addition, according to the result of TEM, it can be certain that one type of the nanoparticles is definitely palladium (see Figure 4-15).

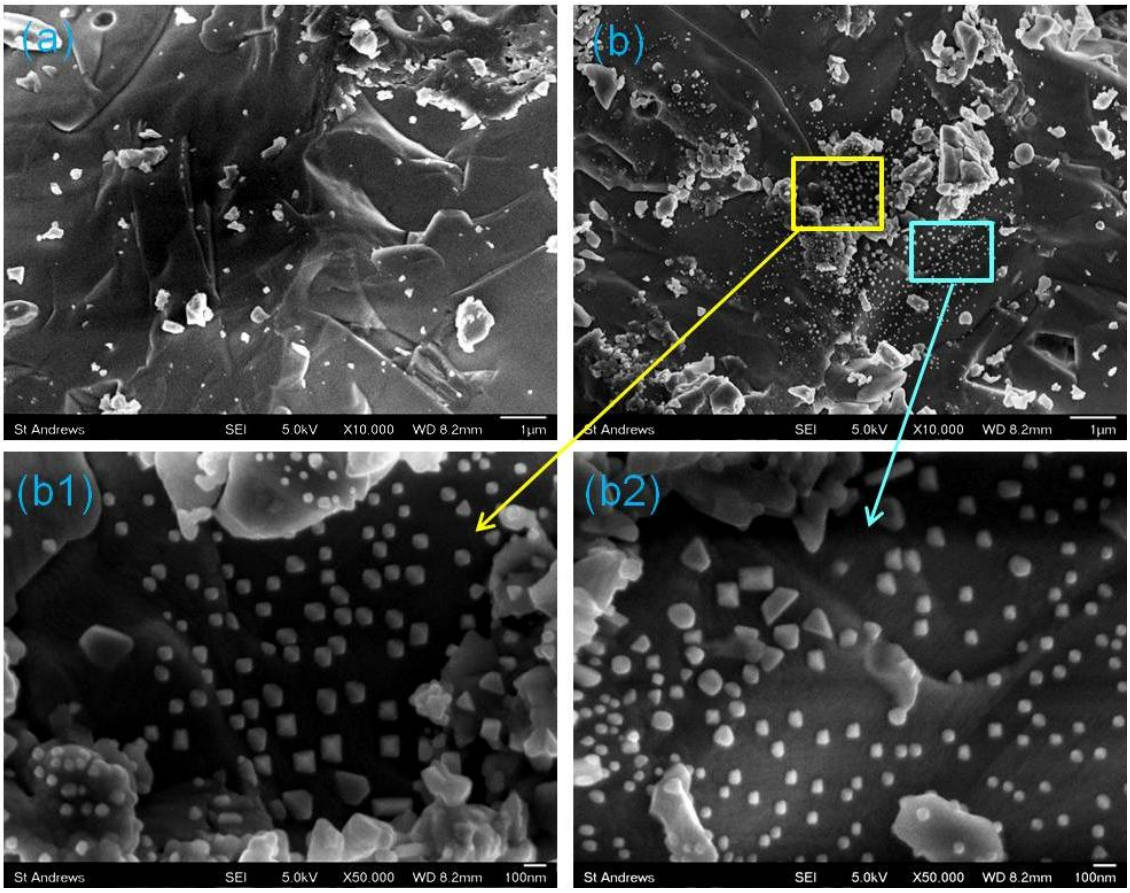

Figure 4-14 SEM images of LCPT01: a. as prepared LCPT01, b&b1&b2. reduced LCPT01

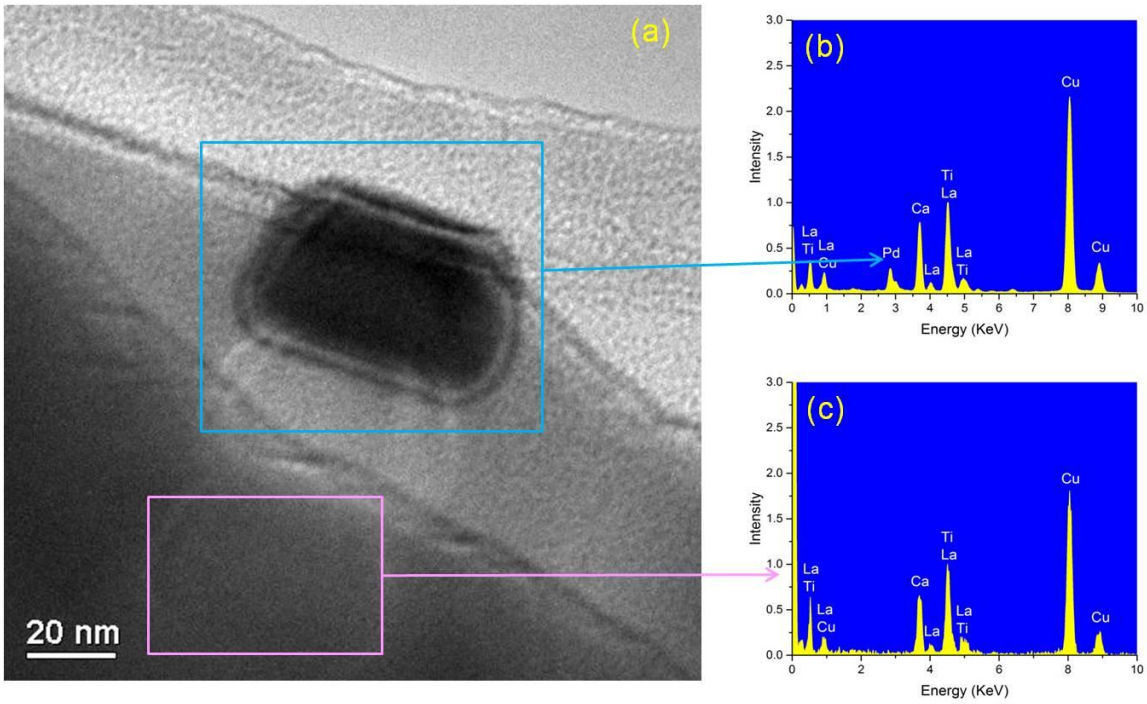

Figure 4-15 TEM and EDX of reduced LCPT01: a. TEM of reduced LCPT01, b. EDX of palladium particles from reduced LCPT01, c. EDX of the bulk of reduced LCPT01

The particles with angular shapes were generally larger (50-200 nm) than the spherical ones (10-50 nm). The shape of the nanoparticles is controlled by the internal structure of the seed and the growth rate of different crystallographic planes. Therefore, if the seeds of all the palladium nanoparticles in this experiment were the same, the presence of the nanoparticles on the surface of the perovskite with different shapes may be a result of the differing growth rates of the various crystallographic planes. Alternatively, if the seed structures of the palladium nanoparticles were different, it would not be surprising that the nanoparticles had different shapes from one another. The possible reasons for the formation of different palladium seed structures in this experiment may be due to the fact that, when the sample was being reduced, it was in the form of powder, which was prepared by crushing the sintered perovskite pellets. Using this technique, it was unavoidable that different surfaces of the perovskite would be exposed to the reducing atmosphere during reduction. Therefore, when the nano crystals were growing on the surface of the perovskite, different crystal growing thermodynamics would be favoured by different surfaces due to their differing surface energies. As a result, different types of nano crystal seeds may have been generated [205, 206].

4.4.2 LSPT01

Figure 4-16 shows the XRD patterns of as prepared LSPT01 and after it was reduced. Different from LCPT01, the sample basically formed single phase with traces of TiO_2 showing up in the XRD patterns. After LSPT01 was reduced in 5% H_2, there were a few 2nd phase peaks showing up in the XRD pattern and they were especially obvious at around 40 degrees (see Figure 4-16). The 2nd phase peaks are very likely to be Pd metal according to their position. However, due to the fact that the intensities are not very strong, further characterization needs to be carried out in order to confirm it. With Rietveld refinement, it seemed that the proposed cubic model fitted well for the LSPT01 perovskite sample (see Figure 4-17). After reduction, there was no obvious change in the structure of the perovskite, and the unit cell parameters of the reduced sample were calculated based on the same model using the same method. The unit cell parameters of the perovskite samples before and after reduction are shown in Table 4-3. After reduction, the unit cell volume of the sample had increased by 0.02%.

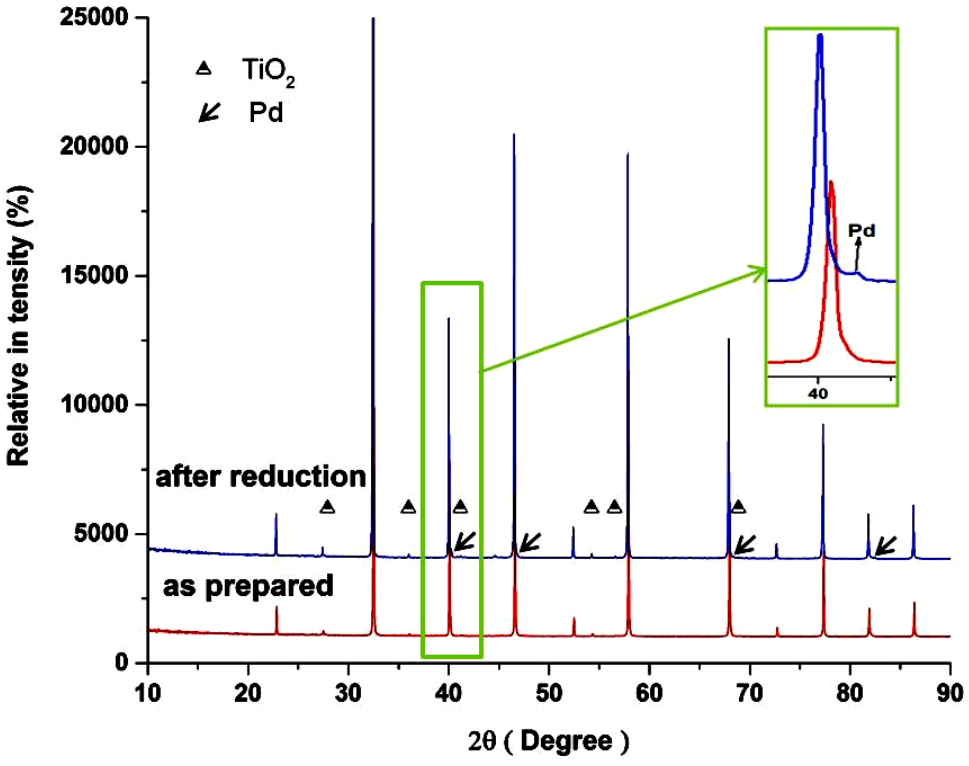

Figure 4-16 XRD pattern of as prepared LSPT01 and after it was reduced.

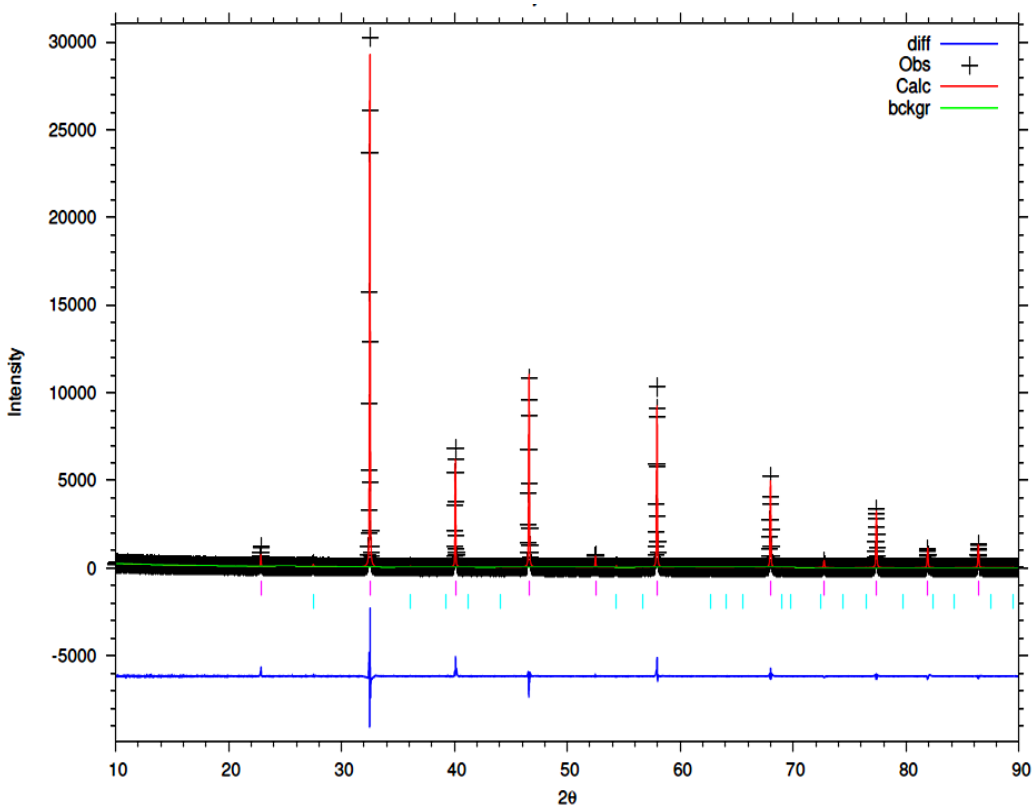

Figure 4-17 Rietveld refinement of as prepared LSPT01

Figure 4-18 shows the surface of as prepared LSPT01 and after it was reduced. Compared to the surface of the as prepared LSPT01, there were many nanoparticles with the size range of 5-20 nm on its surface after the sample was reduced. According to the TEM and EDX analysis as shown in Figure 4-19, it can be confirmed that the nanoparticles on the surface of the reduced LSPT01 are Pd nanoparticles. This suggests that the 2nd phase peak observed in the reduced LSPT01 should belong to Pd metal. Since there was no sign of palladium or palladium oxide in the XRD pattern of the as prepared LSPT01, this strongly suggested that the palladium was incorporated in the perovskite and exsolved after reduction. Most of the nanoparticles were spherical in shape, while a much smaller ratio of them were angular in shape in comparison to the nanoparticles observed for the reduced LCPT01. The reasons for the formation of differently shaped nanoparticles should be the same as that for LCPT01, which was explained earlier. The fact that the nanoparticles observed from LCPT01 were larger than those from LSPT01 may be due to the fact that calcium has a weaker surface structuring effect compared to strontium. Meanwhile, as previously mentioned, the smaller ionic radius of calcium will help with cation diffusion. As a result, it is easier for the doped palladium in LCPT01 to diffuse to the surface of the perovskite and grow

relatively larger [201].

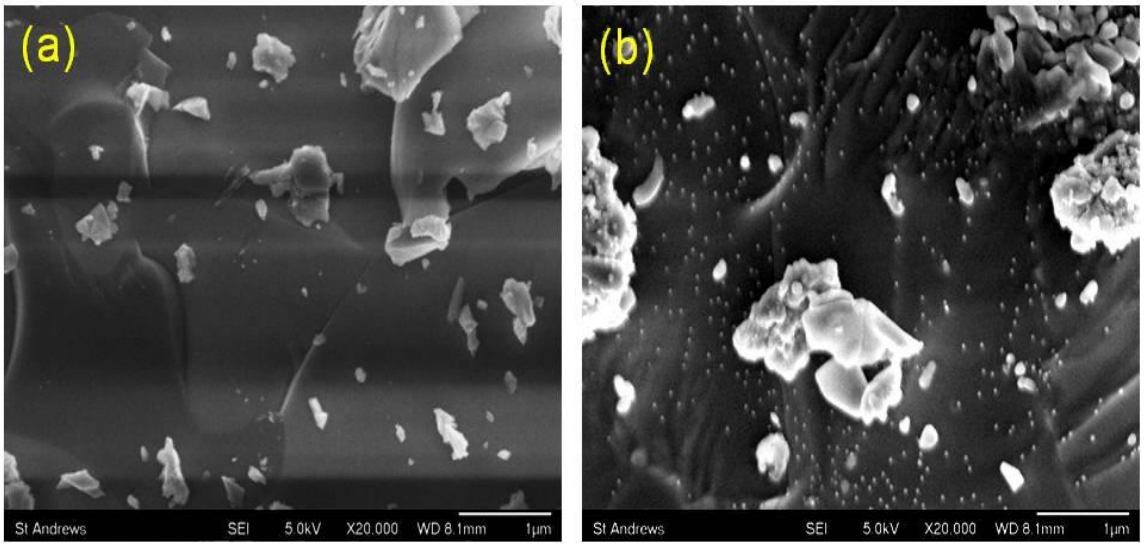

Figure 4-18 SEM images LSPT01: a. as prepared, b. after reduction

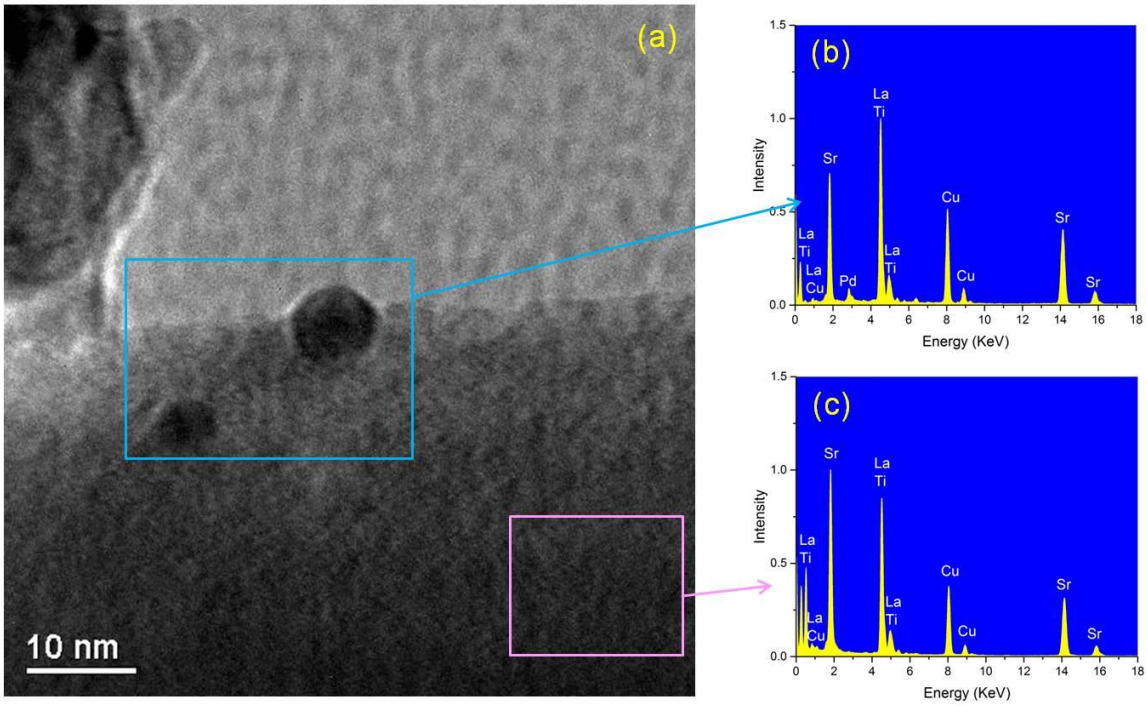

Figure 4-19 TEM and EDX of reduced LSPT01: a. TEM of reduced LSPT01, b. EDX of palladium particles from reduced LSPT01, c. EDX of the bulk of reduced LSPT01

4.5 LSPT02 & LSPT03 based on A-site deficiency assumption

Another two possible situations in which palladium may be incorporated in A-site deficient titanate are if Pd^{3+} or Pd^{4+} cations occupy octahedral 6-fold coordination

geometries. Since A-site deficiencies are known *for oxidizing the cations on the B-site*, it was assumed that the palladium cations on the B-sites of the perovskites in this experiment would be oxidized to 4+ [76, 101]. In order to confirm that whether A-site deficiency would help oxidizing the palladium, promoting its incorporation into the perovskite, samples with the chemical formulae of $La_{0.4}Sr_{0.4}Ti_{0.97}Pd_{0.03}O_3$ (LSPT02) and $La_{0.6}Sr_{0.1}Ti_{0.97}Pd_{0.03}O_3$ (LSPT03) were prepared and characterized as shown below.

4.5.1 LSPT02

The XRD patterns of as prepared LSPT02 and reduced LSPT02 are shown in Figure 4-20. According to the XRD patterns, the sample was basically single phase with a weak 2^{nd} phase peak in the showing up as prepared LSPT02. After the sample was reduced, the 2^{nd} phase peak disappeared. According to the peak position, the 2^{nd} phase peak might belong to PdO. In that case, it would not be surprising that the peak disappeared after reduction since the PdO would have been reduced to Pd metal whose peak position would overlap with some of the XRD peaks of the sample. However, further characterization still needs to be conducted in order to verify it. The cubic model seemed to fit well for the as prepared LSPT02 with Rietveld refinement (see Figure 4-21). The XRD pattern of the reduced LSPT02 was also refined by the same model since there was no obvious change in its structure. According to the unit cell parameters of the sample throughout the experiment, the unit cell volume of the sample increased by 0.13% (see Table 4-3).

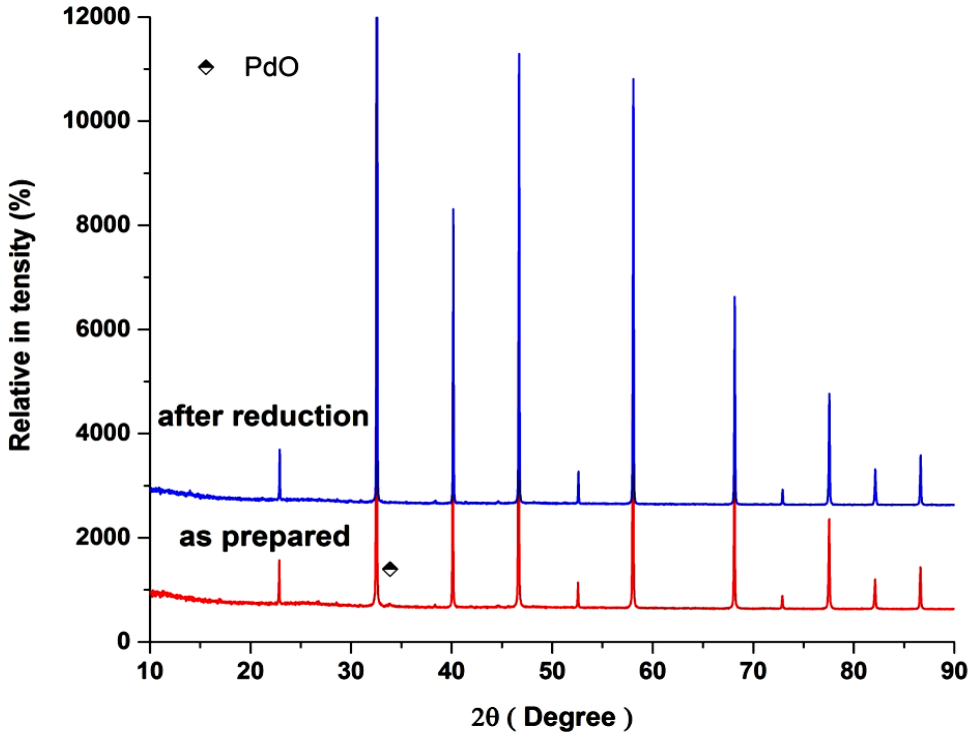

Figure 4-20 XRD pattern of as prepared LSPT02 and after it was reduced

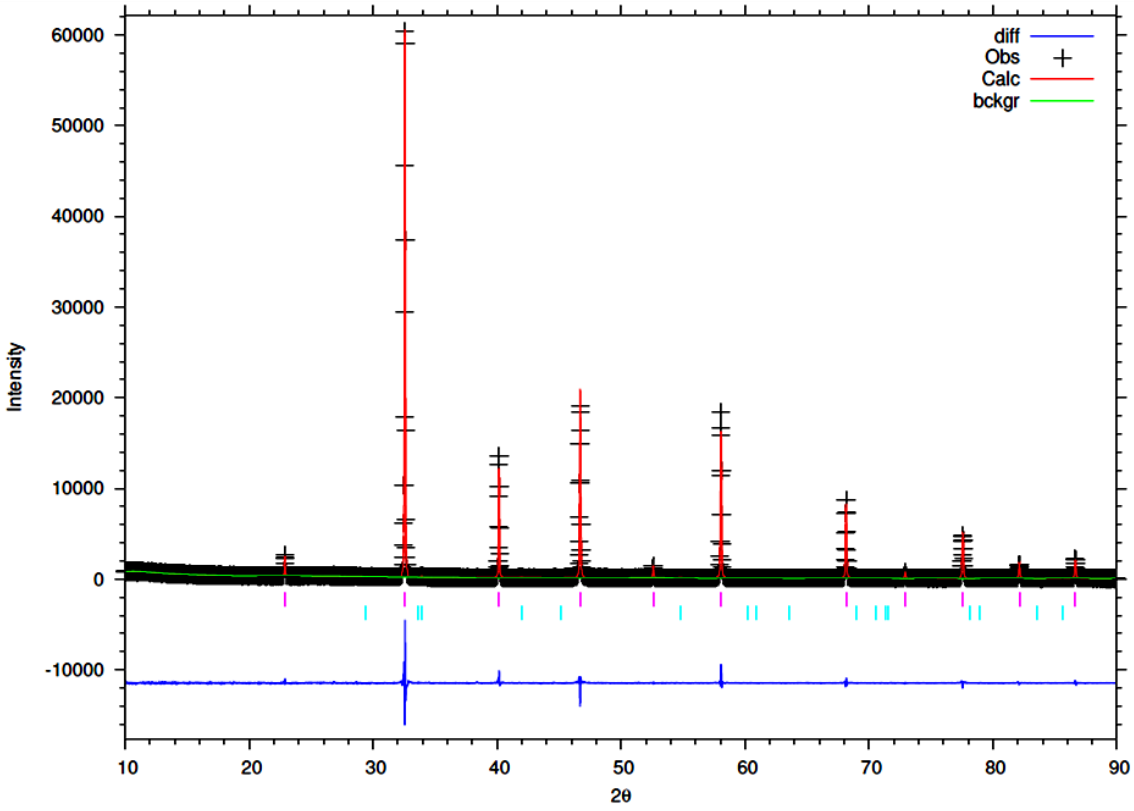

Figure 4-21 Rietveld refinement of as prepared LSPT02

Since the peaks of palladium could overlap with the peaks of the perovskite, it was difficult to confirm whether or not the palladium had exsolved. In order to find out if

any palladium particles had exsolved from the perovskite after reduction, the sample was analysed more closely by SEM (see Figure 4-22). Compared to Figure 4-22a, there was no nano particle exsolution observed in Figure 4-22b, which is in agreement with the XRD result. Hence, it can be confirmed that the incorporated palladium particles did not exsolve from the perovskite after reduction. The explanation for this behaviour may be due to the fact that the perovskite underwent surface A-site enrichment, as has been reported for many perovskites [86, 207, 208]. The A-site surface enrichment may have developed during the firing process and then acted as a barrier to hinder the exsolution of B-site cations [76]. As a result, the palladium on the B-site would have been unable to exsolve to the surface of the perovskite.

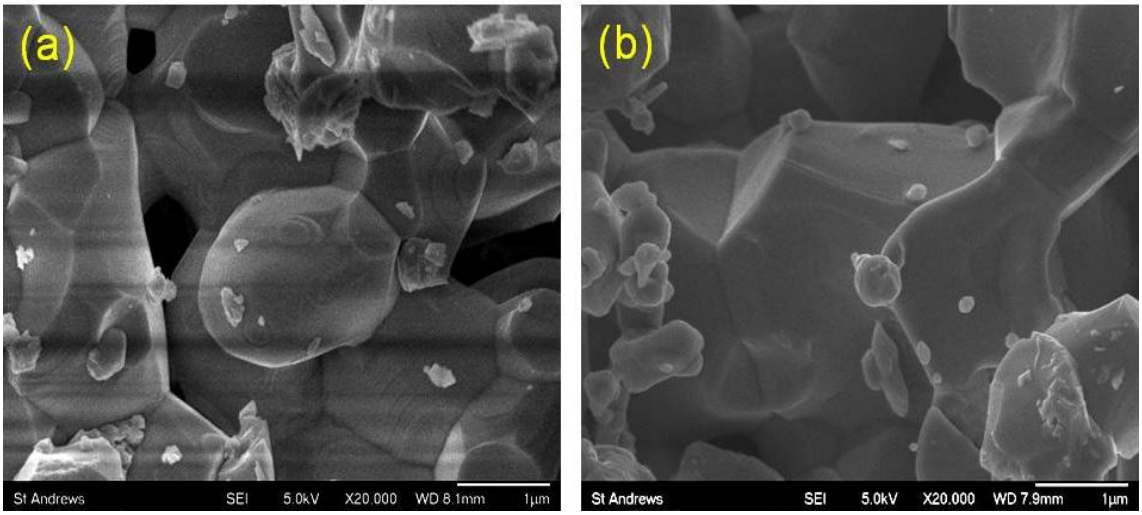

Figure 4-22 SEM images LSPT02: a. as prepared, b. after reduction

4.5.2 LSPT03

Figure 4-23 shows the XRD patterns of as prepared LSPT03 and after it was reduced. During the synthesis of LSPT03, it seemed that the perovskite was unable to accommodate the high amount of A-site deficiency since the as prepared sample was obviously not single phase according to its XRD pattern. There were very apparent second phase peaks which might belong to $La_2Ti_2O_7$ present in the XRD patterns of the samples (see Figure 4-23). After the sample was reduced, the 2nd phase was still present in its XRD pattern and there was no obvious change observed. It was difficult to decide whether or not palladium was incorporated into the perovskite lattice since the peaks of Pd overlapped with some of the peaks of the sample. More experiments need to be

carried out in order to find out the answer. Although the sample was not single phase, an attempt was still made to calculate its unit cell parameters with the Rietveld refinement method (see Figure 4-24). The orthorhombic model seemed to provide a reasonable fit for the sample and the unit cell parameters of the reduced sample were also calculated based on the same model. According to the unit cell parameters of the sample shown in Table 4-3, the unit cell volume of the sample had increased by 0.02% after reduction.

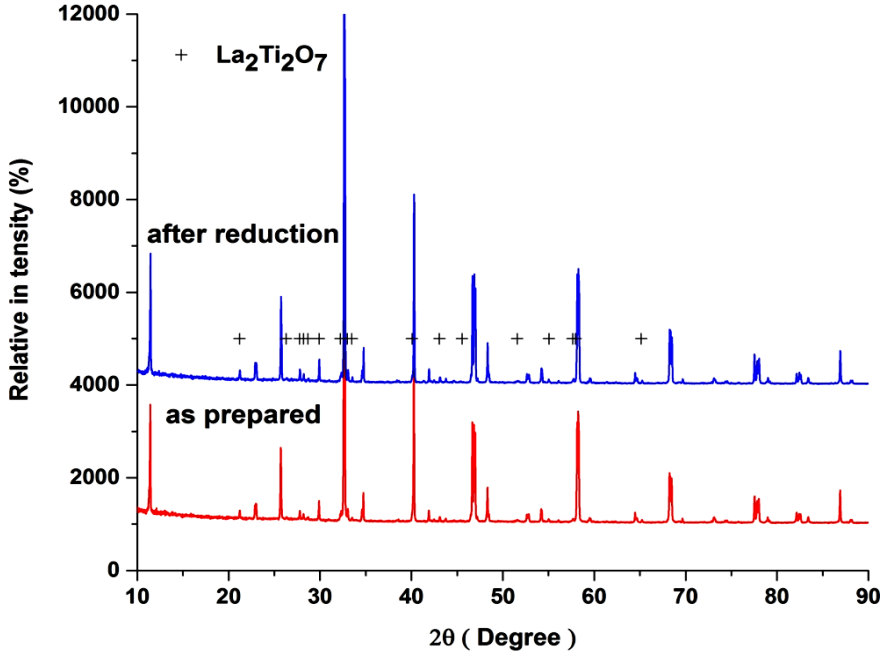

Figure 4-23 XRD pattern of as prepared LSPT03 and after it was reduced

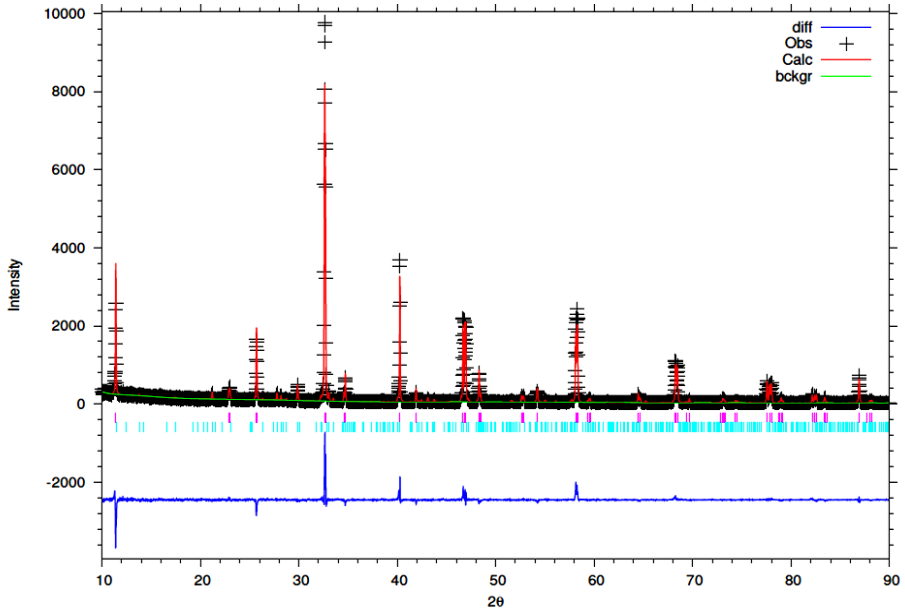

Figure 4-24 Rietveld refinement of as prepared LSPT03

After studying the surface of the sample by SEM, it was found out that there were nanoparticles (5-20 nm) present on the surface of the perovskite after reduction (see Figure 4-25b). The composition of the nanoparticles was confirmed to be palladium through TEM and EDX analyses, as shown in Figure 4-26. This suggests that the palladium catalyst was incorporated into the LSPT03 lattice although the sample was not pure phase. Despite the fact that LSPT02 and LSPT03 both are A-site deficient perovskite, only the palladium incorporated in the sample LSPT03 managed to exsolve to the surface of the perovskite after reduction. In order to find out the reason for this behaviour, the stoichiometry of both samples was compared and it was found that LSPT03 is more A-site deficient than LSPT02 which should provide a greater driving force for the exsolution of B-site cations since A-site deficient perovskites are known for promoting the segregation of B-site cations. Overall, it seemed that the stoichiometry of LSPT03 was more favourable for the exsolution of B-site cations when compared to LSPT02.

Another possible explanation is that A-site deficiency could not provide enough driving force for oxidizing the palladium cations to 4+, and thus they were unable to fit in the B-site. Palladium was doped into the LSPT03 in the form of Pd^{2+} in square planar 4-fold coordination. The molecular formula of the synthesized LSPT03 then became $La_{0.6}Sr_{0.1}Ti_{0.97}Pd_{0.03}O_{2.97}$, which was even more oxygen deficient than the originally planned formula. The perovskite may not have been able to accommodate so many A-site vacancies and oxygen vacancies at the same time, and so would have started to reorganize its structure to maintain its stability. This explains why so much $La_2Ti_2O_7$ was observed in the XRD pattern and corresponds well with the fact that there was no palladium exsolution observed from LSPT02 after it was reduced. As for LSPT02, the reason why there was little 2^{nd} phase observed may be because it was less A-site deficient and more thermodynamically favourable to form the single phase perovskite.

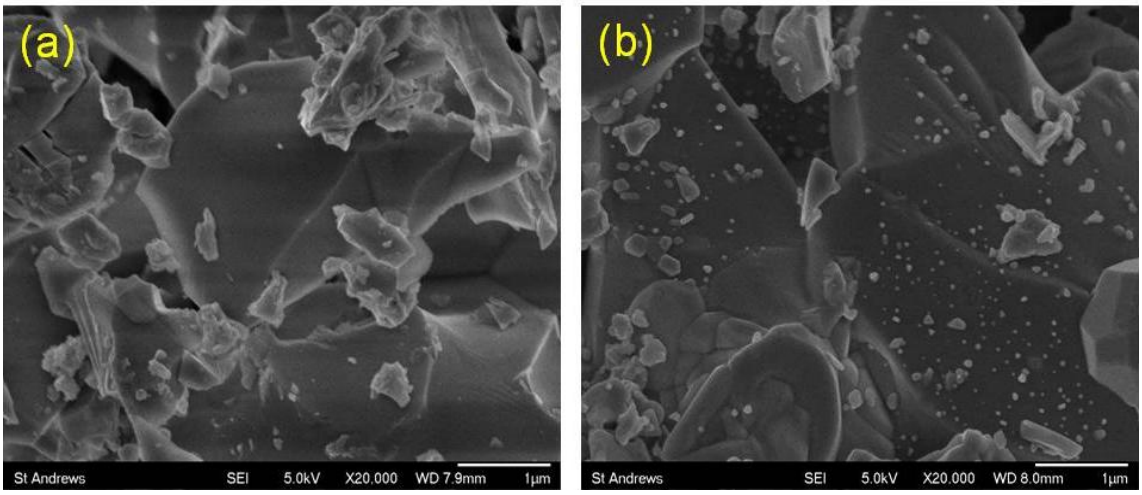

Figure 4-25 SEM images LSPT03: a. as prepared, b. after reduction

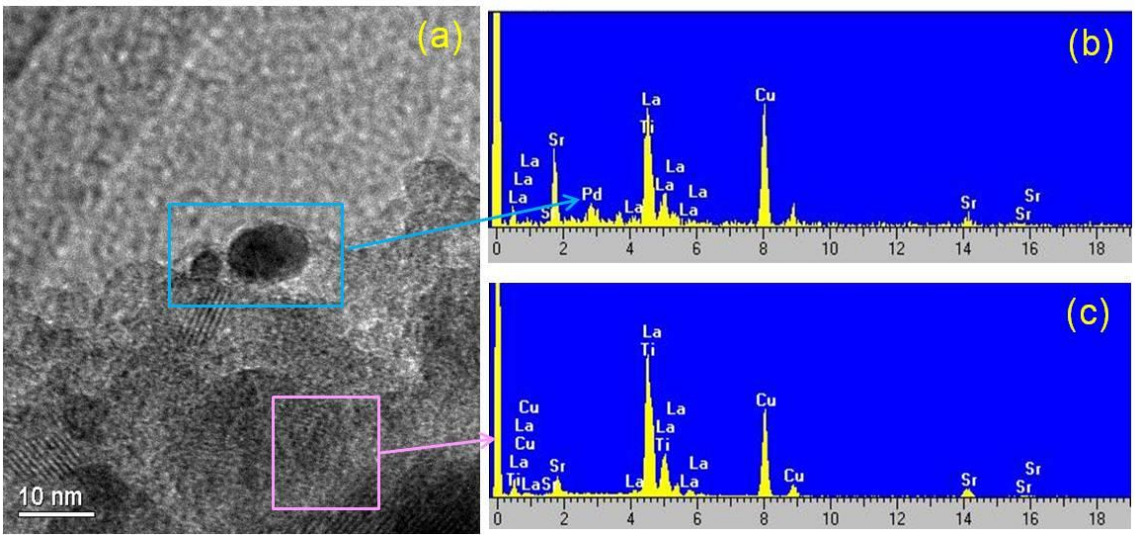

Figure 4-26 TEM and EDX of reduced LSPT03: a. TEM of reduced LSPT03, b. EDX of palladium particles from reduced LSPT03, c. EDX of the bulk of reduced LSPT03

4.6 Discussion and Conclusions

LSGPT was prepared in order to investigate the possibility of doping palladium into the LSGT and exsolve it afterwards by reduction. According to the XRD analysis of the product, a single phase of LSGPT had been achieved and Pd_5Ga_3 was generated after reduction. However, the SEM result showed that there was a small amount of PdO in the as prepared LSGPT. This may not have appeared in the XRD pattern if the PdO had poor crystalline or small particle size. Apart from Pd_5Ga_3 particles, palladium nanoparticles were also observed by SEM, thus confirming the possibility of doping palladium into the LSGT perovskite and exsolving it afterwards.

After confirming the possibility of incorporating palladium into the LSGT perovskite,

LSGT10 with reduction pre-treatment was coated with palladium catalyst in air. However, palladium did not dissolve into the perovskite even with an extended firing time. The sample was then coated with palladium in oxygen with a longer firing time at different temperatures (1000-1300 °C). Similar to nickel coating LSGT10, the intensities of the coated catalyst peaks decreased as the firing temperature increased. At 1300 °C, the intensities of the PdO XRD peaks were very small. According to the SEM images of the sample coated at 1300 °C, it seemed that palladium oxide was largely dissolved into the perovskite. To ensure that all of the palladium may be incorporated into the surface of the perovskite, a longer firing time in oxygen was applied to the sample. At the same time, non-coated LSGT10 was fired together with the coated sample for the purpose of comparison. According to XRD and SEM analyses, there was no obvious difference between the palladium coated samples which were fired for different lengths of time. However, after reduction, it was very obvious that there was more nano particle exsolution from the sample which had been heated in oxygen for a longer period. No nano particle exsolution or any other 2^{nd} phase was observed from the blank sample, confirming that the exsolved nanoparticles from the palladium coated sample were palladium rather than other elements in the perovskite. This proved that the palladium did diffuse into the LSGT10 perovskite on oxidation and exsolve after reduction.

In order to understand the mechanism of palladium incorporation in the A-site deficient titanate, LCPT01, LSPT01, LSPT02 and LSPT03 samples with different stoichiometry were prepared and studied based on different assumptions. LCPT01 and LSPT01 were prepared based on the assumption that Pd^{2+} was incorporated in the perovskite with square planar 4-fold coordination environments. When the experiment was designed, each palladium cation was coupled with 2 oxygen vacancies in the perovskite. If palladium was doped in the perovskite in this way, LCPT01 and LSPT01 should both be single phase after synthesis. Palladium was successfully doped into LSPT01 with a very small amount of rutile as 2^{nd} phase. However, in the case of LCPT01, it was found that not all of the palladium had been incorporated as originally designed. The reason for this phenomenon might be due to the fact that the calcium cations on the A-site of LCPT01 are smaller than the strontium cations in LSPT01. Therefore, the host matrix of LCPT01 was smaller than that of LSPT01 and there was limited space available for the palladium to fit into the perovskite in LCPT01.

The other assumption about the mechanism of palladium doping the A-site deficient titanate was that the A-site deficiency would oxidize the palladium to higher valence, and therefore the palladium cations would be able to fit into the B-site of the perovskite with octahedral 6-fold coordination. LSPT02 and LSPT03 were prepared to investigate this assumption. The experiment results suggested that not all of the palladium was doped into the LSPT02 and the doped palladium was unable to exsolve to the surface of the perovskite after reduction. As for LSPT03, it seemed that palladium was incorporated into the perovskite lattice at the sacrifice of re-organizing the composition of the perovskite.

There is a possibility that palladium did go inside the lattice of the perovskite with the aid of A-site deficiency oxidation. In this case, it seemed that perovskite was not able to host that amount of A-site vacancies, and so the perovskite was not stable enough to maintain its structure and $La_2Ti_2O_7$ was generated as a 2nd phase instead. In this case, the A-site deficiencies of the perovskite might be lower than originally planned, which suggested that palladium might not require so many A-site deficiencies to be oxidized to higher valence. However, according to the report from Battle *et al* [209], $La_{0.6}Sr_{0.1}TiO_3$ is a stable phase which means that LSPT03 should be single phase if A-site deficiencies did oxidize palladium to higher valence. Another possible explanation for the experimental result is that the A-site deficiency was not able to oxidize the palladium to 4+ to allow it to fit into the B-site. The palladium was doped into the perovskite lattice with the square planar 4-fold coordination instead. In this case, more oxygen vacancies would have been introduced into the perovskite. It seemed that perovskite was still not able to accommodate so many A-site and oxygen deficiencies at the same time and reorganised its structure, generating the 2nd phase in the end.

By comparing the results of the experiments testing these two assumptions, it seems that it is more likely for palladium to be doped into the A-site deficient perovskite when it adopts the square planar 4-fold coordination in the perovskite. In addition, there might also be a minimum size requirement for the size of the host lattice for the palladium to fit in.

Chapter 5

Coating $La_{0.4}Sr_{0.4}Ga_xTi_{1-x}O_{3-x/2-\sigma}$ (LSGT) with ruthenium catalysts

5.1 Introduction

Ruthenium has been widely used as a catalyst in many areas such as water electrolysis, catalysed oxygen evolution reactions, gas reformation, etc. [210-215]. It is also a very good candidate for replacing the noble metals in certain areas so as to decrease the cost in practical applications, especially in PEM fuel cells [21, 33, 34, 214, 216-218]. In the previous two chapters, it was proven possible to dope nickel and palladium catalysts into the surface of reduced LSGT10 perovskite. It is also worthwhile to investigate the possibility of doping ruthenium into the perovskite surface. However, the boiling point of ruthenium oxide (RuO_2) is 1200 °C. Above this temperature, the oxide will sublime. As a result, one of the biggest challenges of coating the ruthenium catalyst into the perovskite is to stabilize it, due to its instability at high temperatures [219]. However, the ruthenium oxide may not sublime at high temperatures if it is incorporated into the perovskite as the dopant at the beginning of the synthesis [210, 215, 220]. Whether or not it is possible to get ruthenium oxide diffused into the LSGT10 perovskite lattice from the surface before the catalyst starts to sublime still remains a challenge.

In order to find out the answer to the above question, different firing temperatures and atmospheres were used when coating ruthenium into the reduced LSGT10 perovskite. Before coating the ruthenium into the reduced LSGT10 perovskite, perovskite with a nominal formula of $La_{0.4}Sr_{0.4}Ti_{0.9}Ga_{0.077}Ru_{0.023}O_{3-\delta}$ (LSGRT) was prepared by the solid state method to explore the possibility of doping ruthenium into the A-site deficient titanate and exsolving it afterwards. Then VT-XRD was used to investigate the structural change of ruthenium impregnated LSGT10 perovskite at different temperatures so as to find out the temperature at which ruthenium would enter the perovskite lattice from its surface in air. Since the highest firing temperature the VT-XRD instrument could be programmed to was 1100 °C, the changes in the structure and morphology of the ruthenium coated perovskite at higher temperature were investigated by firing the samples in the furnace in air followed by XRD and SEM at room temperature. After the samples were fired at high temperatures to coat ruthenium into the perovskite, they were reduced in 5% H_2 to allow the exsolution of the ruthenium which had been LSGT10 perovskite at high temperatures to exclude the possibility of ruthenium oxide volatilization when coating the sample in air.

5.2 Experimental Section

5.2.1 Solid state synthesis of LSGRT

The LSGRT was synthesized via the same solid state method as LSGT, which was mentioned in Chapter 2.1. It is worth noting that the ruthenium source in the synthesis process was ruthenium nitrate in nitric acid solution and it was added into a beaker before the addition of the other dried solid powder mixture. The mixture of all the components then went through an ultrasonic probe following the same solid synthesis procedure as LSGT.

5.2.2 Coating LSGT10 with ruthenium catalyst

Ruthenium was coated into the LSGT10 perovskite pellets via the same method of coating Ni^{2+} into the LSGT10 perovskite (see Chapter 2.4). The as prepared LSGT10 pellets were first reduced at 950 °C in 5% H_2. After the samples were impregnated with ruthenium nitrate, they were fired at different temperatures. In the cases where the coating atmosphere was air, firing temperatures between 1000 °C – 1300 °C were employed for 6 h to allow the impregnated ruthenium to diffuse into the perovskite. Where the coating atmosphere was 5% H_2, the samples were fired at 1000 °C or 1300 °C for 12 h.

5.2.4 Reduction

In this chapter, the reduction of most of the samples after they were doped or coated with ruthenium catalyst was carried out in 5% H_2 at 930 °C for 30 h in the tube furnace for the purpose of studying normal exsolution. However, when the samples were reduced at higher temperatures (1000 °C or 1300 °C) with the purpose of exsolving ruthenium particles, they were reduced in a tube furnace in 5% H_2 for 20 h.

5.3 Ru containing perovskite synthesis investigation

The XRD patterns of the as prepared LSGRT and the sample after it was reduced are

displayed in Figure 5-1. A single phase of LSGRT was obtained according to the XRD result. The incorporation of ruthenium into the perovskite did not dramatically change the lattice structure of the perovskite. There was no 2nd phase observed from the synthesized sample which indicated that ruthenium was successfully doped into the perovskite. This is not surprising since the ionic radius of ruthenium (Ru^{4+} = 0.62 Å, CN=6) is close to that of titanium (Ti^{4+} = 0.605 Å, CN=6). After reduction, no obvious structural change or 2nd phase was discovered from the XRD pattern either. It is difficult to decide whether or not ruthenium had exsolved from the perovskite since the amount of ruthenium added in the perovskite was quite small. If the ruthenium had exsolved from the perovskite, depending on the amount of ruthenium exsolution, it might be below the detection limit of the XRD equipment and may not show up in the XRD result. Another characterization technique was required to clarify the results. After refining the unit cell, the unit cell parameters of LSGRT are shown in Table 5-1. As a result of reduction, the unit cell volume of the perovskite was increased by 0.12%. Compared to LSGPT whose unit cell volume was increased by 0.03% (see Chapter 4), it seemed that the addition of ruthenium dopant into the perovskite increased its reducibility. This hypothesis is supported by recent reports which have demonstrated that ruthenium would generate rotational and Jahn−Teller distortions in the perovskite structure leading to the distortions of the oxygen and La-O coordination and weaker metal-oxygen bonds. As a result, the anionic mobility was increased thus improving the reducibility of the perovskite [221, 222]. This could have been better verified if there was experimental data of the unit cell volume change of the undoped LSGT10 under the same reduction condition. Unfortunately, it was not possible to obtain the data due to the time limitation.

In order to see if any ruthenium particles had exsolved from the perovskite, the morphology of the perovskite was studied by SEM as shown in Figure 5-2. The surface of the as prepared perovskite was clean after synthesis according to Figure 5-2a. However, after reduction, there was no sign of nanoparticles on the surface of the perovskite grains either (see Figure 5-2b). In nickel or palladium coated or doped LSGT perovskite, the exsolution of the corresponding catalyst nanoparticles were observed after the samples were reduced in 5% H_2. However, in the case of the ruthenium dopant, there was no sign of ruthenium exsolution from the perovskite after reduction. One possible explanation was that the ruthenium was very stable in

the perovskite lattice and so it requires a greater driving force in order to be separated from the perovskite lattice. The ionic radii of different cations in various possible coordination environments are compared in Figure 5-3. In the nickel coated sample, the valence of nickel was assumed to be 2+ with a 6-fold octahedral coordination environment, the same as when it was doped in another A-site deficient strontium titanate with a similar structure and composition [76]. While in the palladium doped sample, according to the previous chapter, palladium should be 2+ with a square planar coordination environment. As for LSGRT, the ruthenium was assumed to be 4+ with a 6-fold octahedral coordination environment since RuO_2 is the only stable form compared to all of the other ruthenium oxides [223]. According to Figure 5-3, the radius of Ru^{4+} (CN = 6) is the closest to that of Ti^{4+} (CN = 6). Therefore, it is more stable in the perovskite lattice compared to Ni^{2+} (CN = 6) and Pd^{2+} (IV SQ). As a result, ruthenium did not exsolve from the LSGRT perovskite after reduction.

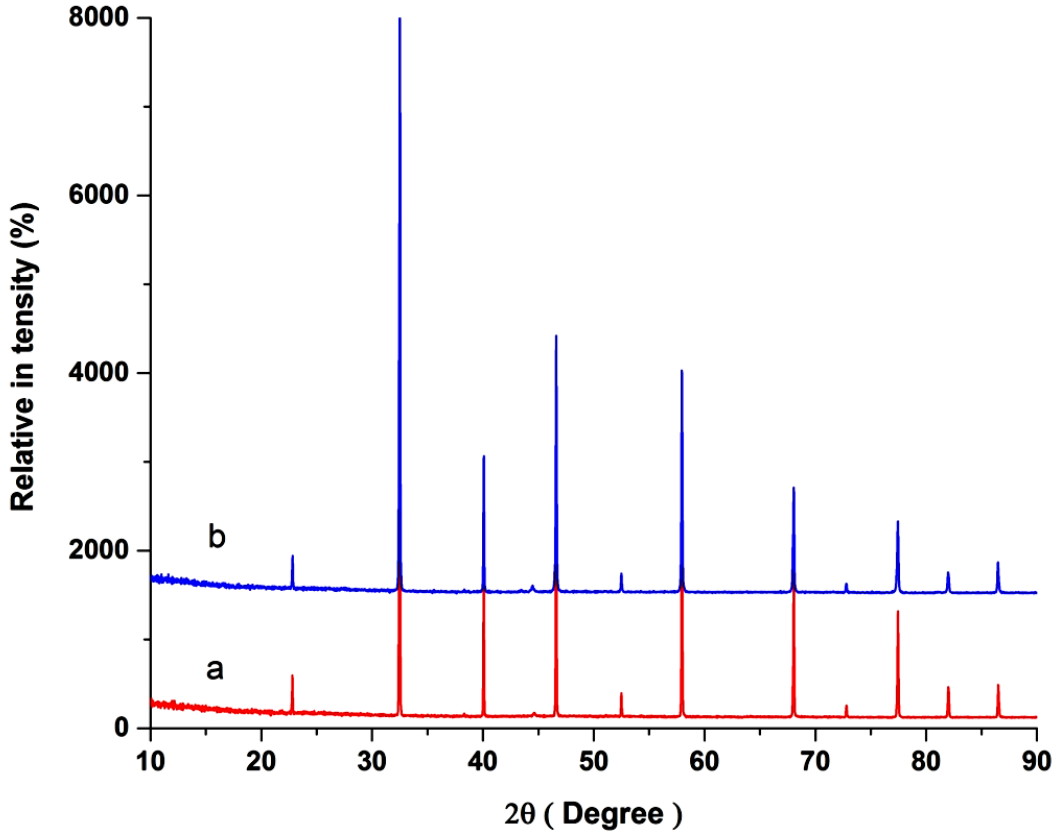

Figure 5-1 XRD patterns of LSGRT: a. as prepared LSGRT, b. LSGRT after reduction

Treatment of LSGRT	Space group	Unit cell parameters (Å)	β (°)	Unit cell volume (Å^3)
As prepared	I2/a	a=7.7839 (5) b=5.5046 (3) c=5.5031 (4)	90.098 (6)	235.79 (4)
After reduction	I2/a	a=7.7861 (6) b=5.5068 (3) c=5.5060 (3)	90.063(6)	236.08 (4)

Table 5-1 Unit cell parameter of LSGRT under different experimental treatment

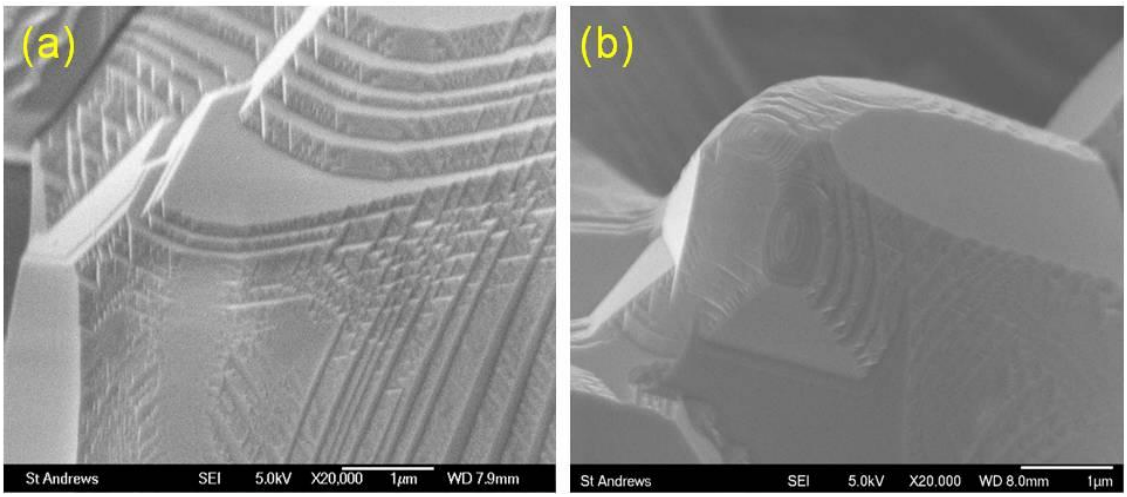

Figure 5-2 SEM images of LSGRT under different experimental treatment: a. as prepared LSGRT, b. reduced LSGRT

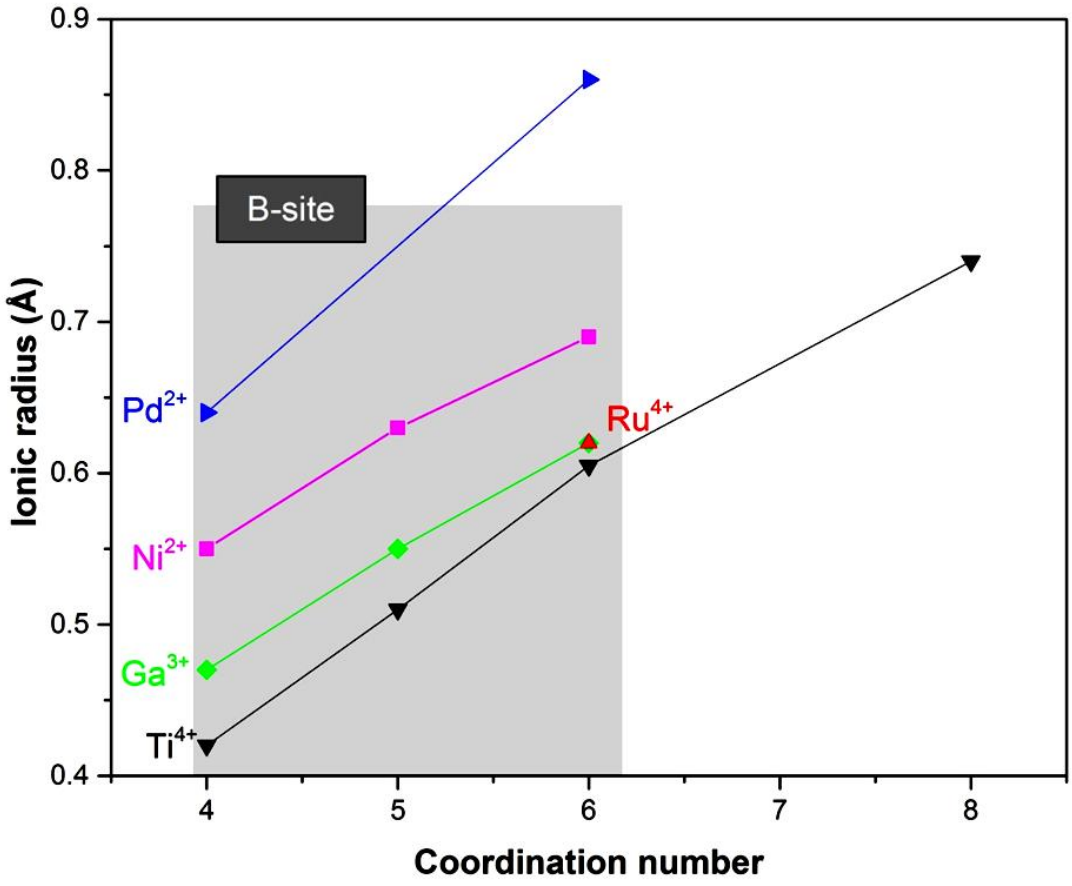

Figure 5-3 Ionic radii vs. coordination number for ruthenium cations and other possible cations on the B-site of perovskite. The characteristic regions for B-site cations are emphasized and labelled. The effective ionic radii are from Shannon [60]

5.4 Investigation into coating LSGT10 with ruthenium

Even if no ruthenium exsolution was observed from the reduced LSGRT, the possibility of ruthenium entering the lattice of the LSGT perovskite has been proven. Coating ruthenium into the reduced LSGT10 would be carried out at lower temperatures. Therefore, if the ruthenium can be doped into the perovskite from the surface, it should be less stable than the ruthenium cations in LSGRT since the ruthenium would only exist in the surface part of the perovskite. The chance of ruthenium exsolving from the ruthenium coated perovskite should be thus higher. Therefore, the possibility of coating ruthenium into the LSGT10 perovskite and exsolving it from LSGT10 afterwards was explored in this section.

5.4.1 In-situ VT-XRD investigation of LSGT10 coated with ruthenium catalyst at different temperatures in air

Since the volatilization of RuO_2 will happen when it is heated above 1200 °C [219], it is worth investigating the temperature at which the ruthenium will start entering the lattice of the LSGT10 perovskite. In order to answer this question, in-situ VT-XRD was carried out on 950 °C reduced LSGT10 which had been impregnated with ruthenium. For the purpose of comparison, as prepared LSGT10 was also studied by VT-XRD following the same heating procedure as the ruthenium coated sample. Figure 5-4 shows the in-situ XRD patterns of ruthenium coated LSGT10 which have been heated at different temperatures. The VT-XRD patterns of as prepared LSGT10 are not shown here since they are very similar to that of ruthenium coated LSGT10. According to the XRD patterns of the sample, there was no sign of RuO_2 or any other 2nd phase showing up throughout the heating procedure. As the heating temperature increased, the XRD patterns of the sample started shifting towards the left, which should be caused by the thermal expansion of the perovskite lattice.

It is notable that RuO_2 was not observed in the VT-XRD patterns even at room temperature. In order to exclude the likelihood of RuO_2 evaporating even during the impregnation at low temperature, the sample which was impregnated with ruthenium at low temperature was studied by the Cu-Kα X-ray source XRD and SEM at room temperature. According to the XRD result, very obvious peaks of RuO_2 were observed (see Figure 5-7a). Meanwhile, the SEM result also agreed with the XRD result since very obvious RuO_2 particles can be seen on the surface of the perovskite grains after impregnation (see Figure 5-5). Therefore, the fact that RuO_2 was not present in the VT-XRD even at room temperature was not caused by material loss during the impregnation stage.

One possible explanation for this absence may be due to the fact that the resolution of the VT-XRD instrument (Mo-Kα X-ray source) was not as high as the instrument which used Cu-Kα X-ray source. In addition, laboratory X-ray sources are generally not as intense as other X-ray sources e.g. synchrotron X-ray sources. Therefore, their penetration depth depends on the mass absorption coefficient of the sample and the

incident angle of the X-ray beam. The high atomic number elements have higher mass absorption coefficient compared to the elements with lower atomic number [224, 225]. Therefore, the way the sample was prepared may also contribute to the absence of RuO_2. In order to make sure that the surface of the sample was flat even at high temperatures throughout the experiment, the sample was crushed from a porous pellet into powder. The impregnation procedure at low temperature only provided a layer of RuO_2 particles, which acted like a shell, lying on the surface of the perovskite grains. When the sample was crushed into powder, the shell was also broken and not able to cover every side of the perovskite grains anymore. Instead, a large proportion of the bulk of the LSGT10 perovskite was exposed to the X-ray beam during scanning due to the random distribution of the particles in the sample powder. Obviously lanthanum in the bulk material is higher in atomic number than ruthenium. Other elements in LSGT10 also have relatively high atomic numbers which meant a strong absorption of the X-ray. This may lead to a full absorption of X-ray before it reached the RuO_2. As a result, it was not present in the VT-XRD patterns.

After refining the VT-XRD results of the samples, the changes in the unit cell volumes of the perovskites at different temperatures are shown in Figure 5-6. According to the graph, the unit cell volume of ruthenium coated LSGT10 was similar to that of the as prepared LSGT10 at room temperature before the samples were heated in air. As the samples were heated at high temperatures, the unit cell volume of ruthenium coated LSGT10 was always larger than that of as prepared LSGT10. There was no obvious difference in the trend of the unit cell volume change between both samples until when the temperature was increased to 1100 °C. The unit cell volume of ruthenium coated LSGT10 became smaller with time when the sample was heated at 1100 °C for the first 6 h. It seemed that 6 h was enough for the sample to reorganize its structure, since there was a very small difference in the size of the unit cell when the sample was heated for 8 h compared to when the sample was heated for 6 h. The unit cell volume of the as prepared LSGT10 remained basically the same even when the sample was heated for longer. Interestingly, when the samples were cooled down, the unit cell volume of the ruthenium coated sample became smaller than that of the as prepared LSGT10.

The ruthenium coated LSGT10 perovskite unit cell may have been larger than that of as prepared LSGT10 at high temperatures due to the fact that the former was reduced at

950 °C before coating. The unit cell of the LSGT10 perovskite was, therefore, increased by the initial reduction pre-treatment. The later firing treatment including ruthenium impregnation and VT-XRD could not provide enough driving force for the perovskite to reorganize its structure. When the coating temperature was increased to 1100 °C, it seemed that the temperature was high enough for the sample to reorganize its structure. However, there was still not a strong enough driving force for ruthenium to enter the perovskite. As a result, the perovskite restructured itself to accommodate the oxygen and Ga deficiencies from the pre-treatment, which lead to the shrinkage of the unit cell at 1100 °C and after the sample was cooled down.

Alternatively, the ruthenium may have entered the perovskite at 1100 °C. Since the X-ray analysis only scanned the surface of the sample, the information collected by the instrument was only able to reflect the structural change on the surface of the sample. However, the ruthenium may not have had enough energy to diffuse to the other side of the perovskite powder particles, and thus was unable to change the structure of the perovskite and be detected by XRD. The surface of the sample which was exposed to the X-ray would still reorganise its structure to accommodate the deficiencies in the perovskite. Consequently, the shrinkage of the unit cell of the sample at 1100 °C and after it cooled down to room temperature was observed from the XRD results.

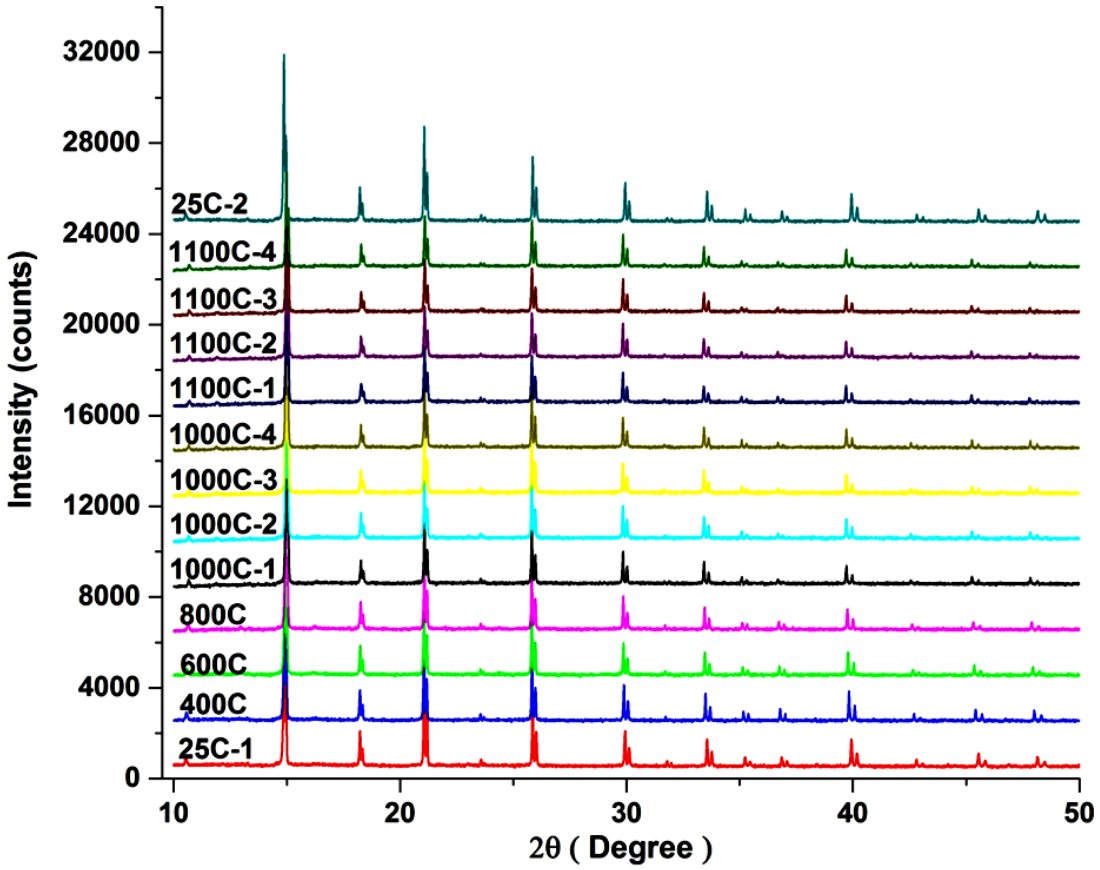

Figure 5-4 The *in situ* VT-XRD patterns of LSGT10 perovskite pre-coated with ruthenium during heating stage from room temperature to 1100 °C

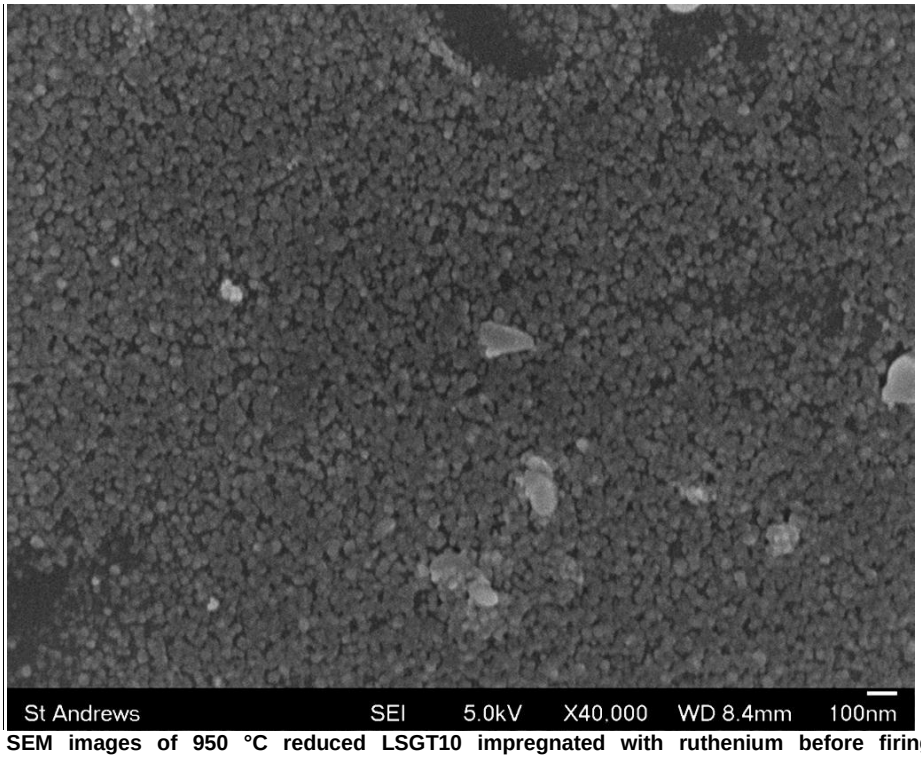

Figure 5-5 SEM images of 950 °C reduced LSGT10 impregnated with ruthenium before firing at high temperatures

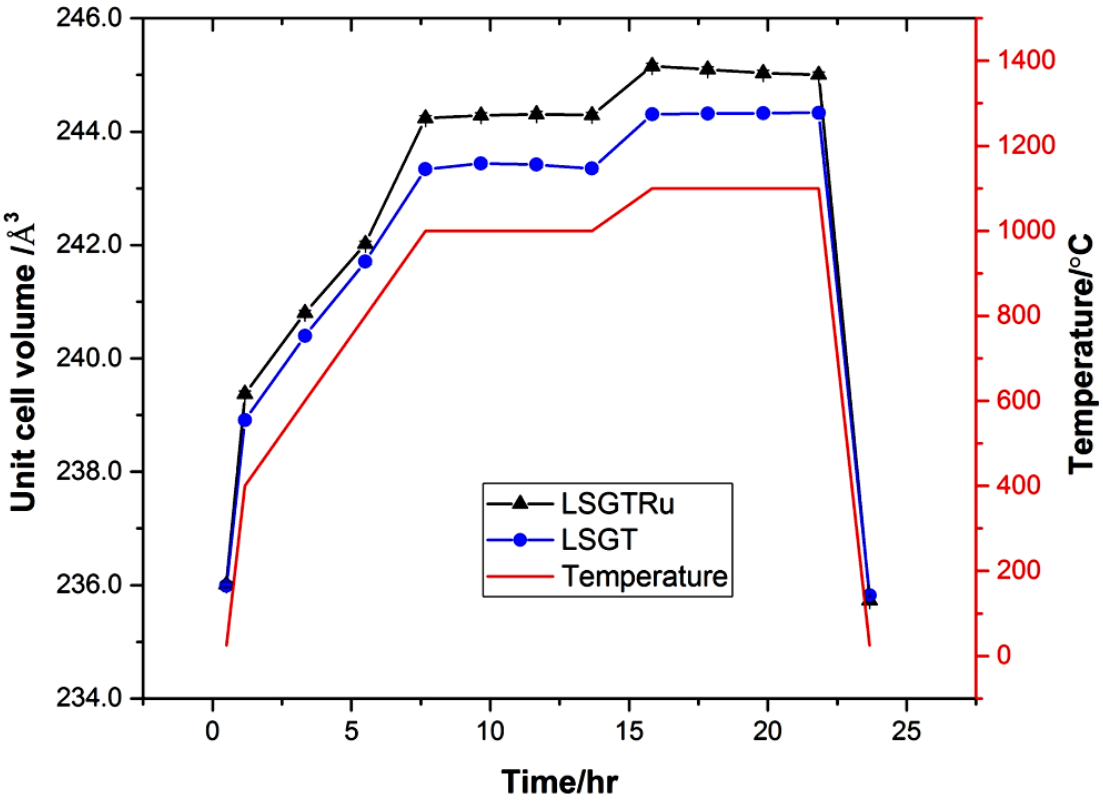

Figure 5-6 The change of unit cell volumes of 950 °C reduced LSGT10 coated with ruthenium and as prepared LSGT10 at different temperatures in VT-XRD

5.4.2 Investigation of LSGT10 coated with ruthenium catalyst at higher temperatures in air

Since it is difficult to tell if ruthenium had entered the perovskite lattice at high temperatures via VT-XRD, the samples were instead heated in air at different temperatures in the form of pellets. Based on the result from VT-XRD, heating for 6 h was enough for the ruthenium to enter the perovskite lattice and for the sample to restructure itself. A STOE X-ray diffractometer with a Cu-Kα X-ray source was used for studying the structural changes of the samples at room temperature.

The XRD patterns of the samples coated with ruthenium at different temperatures are shown in Figure 5-7. According to Figure 5-7a, very obvious RuO_2 peaks were observed when the sample was impregnated with ruthenium at low temperature. As the samples were fired at higher temperatures, the intensities of the peaks of RuO_2 decreased dramatically, even at 1100 °C. At 1200 °C and 1300 °C, no RuO_2 peaks can be observed.

After reduction, there was no 2nd phase observed in the XRD (see Figure 5-7b). It is difficult to identify whether ruthenium had exsolved from the perovskite from the XRD patterns since the most intense XRD peaks of ruthenium metal overlapped with the peaks of the sample holder under these experimental conditions.

Figure 5-8 shows the unit cell volume change of the 950 °C reduced LSGT10 perovskite when it was coated with ruthenium at different temperatures. According to the graph, the unit cell of LSGT10 shrank as the firing temperature increased. Since the 6-fold coordinated Ru^{4+} has the same cation radius as 6-fold coordinated Ga^{3+} (see Figure 5-3), the fact that the unit cell parameter became smaller at higher temperatures indicated that the ruthenium may have gradually entered the perovskite at higher firing temperatures. Alternatively, it may be a result of the LSGT10 perovskite being oxidized and re-organising its structure after heating at high temperatures. However, the unit cell volume of the sample which was coated at 1300 °C was still larger than that of the as prepared LSGT10. If ruthenium did not enter the perovskite lattice, the unit cell volume of the perovskite should be either the same as the as prepared LSGT10 perovskite or smaller, since it lost Ga during the reduction pre-treatment leaving the perovskite with less cations on the B-site and therefore smaller unit cells. On that basis, it seems more plausible that ruthenium had entered the perovskite lattice from its surface at high temperatures. The fact that the unit cell volumes of the samples were higher than that of the as prepared LSGT10 may be caused by the fact that Ru^{4+} has higher valence than Ga^{3+}. Therefore, the perovskite which was doped by Ru^{4+} on the surface required more oxygen ions to compensate for the extra charge. Assuming that all the ruthenium had replaced the Ga^{3+} cations lost on the surface of the perovskite, the molecular formula of the perovskite then became $La_{0.4}Sr_{0.4}Ti_{0.9}Ga_{0.077}Ru_{0.023}O_{2.962}$ versus that of the LSGT10 ($La_{0.4}Sr_{0.4}Ti_{0.9}Ga_{0.1}O_{2.95}$). It is therefore obvious that, after the ruthenium had filled in the gallium cation vacancies, the perovskite gained more oxygen, leading to a larger perovskite unit cell.

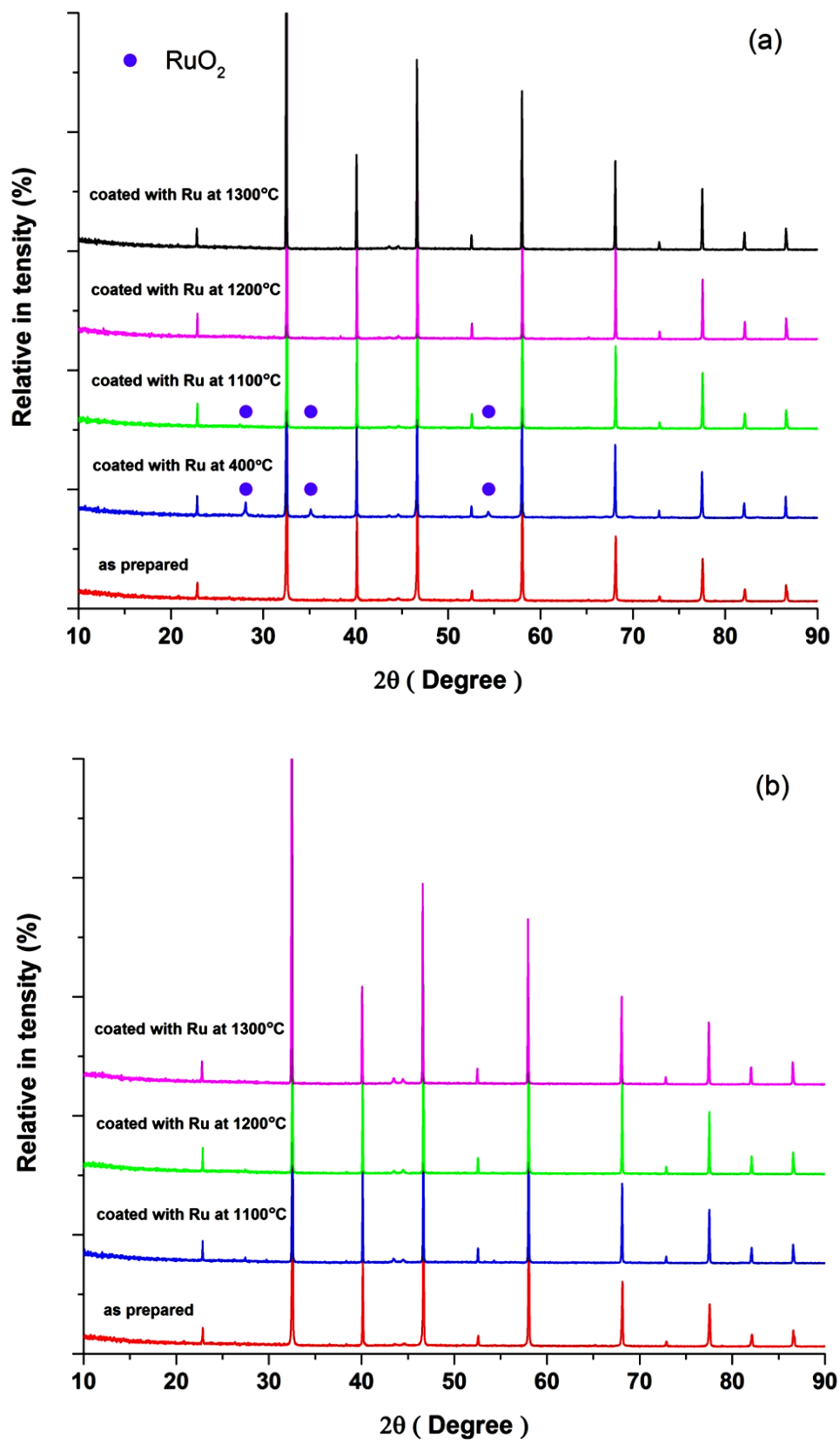

Figure 5-7 a. XRD patterns of 950 °C reduced LSGT10 coated with ruthenium in air for 6 h at different temperatures, b. XRD patterns of 950 °C reduced LSGT10 coated with ruthenium in air for 6 h at different temperatures after reduction for exsolution

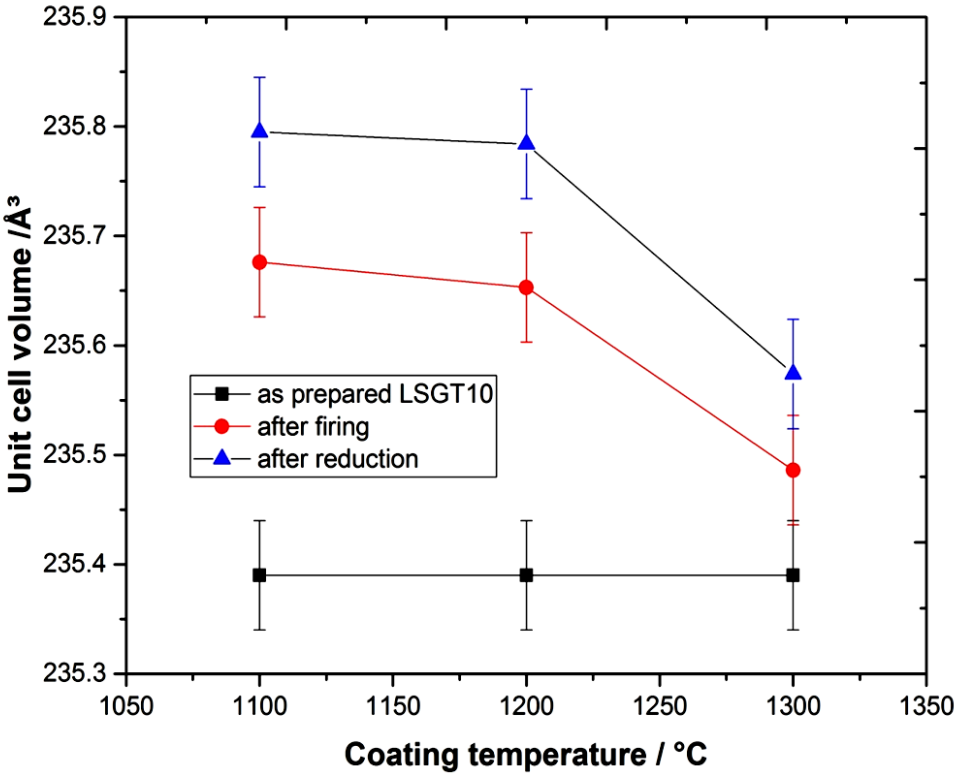

Figure 5-8 The change of unit cell volumes of 950 °C reduced LSGT10 as a function of coating temperature after it was coated with ruthenium in air for 6 h

The morphologies of the 950 °C reduced LSGT10 perovskite coated with ruthenium at different temperatures are shown in Figure 5-9. Compared to the ruthenium dioxide particles observed from the sample which was impregnated with ruthenium at low temperature (see Figure 5-5), the ruthenium dioxide particles on the surface of the sample which was coated with ruthenium at 1100 °C are much bigger (see Figure 5-9a). Unlike the nickel or palladium coated LSGT10, the ruthenium had already started to agglomerate even when the sample was coated at 1100 °C. In addition, it seemed that there were fewer ruthenium dioxide particles left on the surface of the perovskite grains compared to when the LSGT10 perovskite was coated with nickel or palladium catalysts. At 1200 °C, there were basically no ruthenium oxide particles apparent on the surface of the perovskite (see Figure 5-9b). As the heating temperature increased, the surface of the perovskite was free of ruthenium oxide particles (see Figure 5-9c). Figure 5-10 shows the morphologies of the 950 °C reduced LSGT10 perovskite coated with ruthenium at different temperatures after reduction. Similar to LSGRT, there were no ruthenium nanoparticles observed from the samples which were coated at different temperatures.

There are two possible explanations why no ruthenium nano particle exsolution was observed after exsolution reduction. The first one is based on the assumption that ruthenium was successfully doped into the LSGT10 perovskite from its surface. In this case, the ruthenium may have diffused into the bulk of the LSGT10 perovskite due to the longer heating time compared to that of the nickel coating procedure. So the ruthenium was stabilized in the lattice of the perovskite and unable to exsolve after reduction due to its closer ionic radius to Ti^{4+} (CN = 6) compared to that of Ni^{2+} (CN = 6) and Pd^{2+} (IVSQ) (see Figure 5-3). The other possible explanation is based on the assumption that ruthenium was not doped into the LSGT10 perovskite from its surface. It has been reported that RuO_2 would start losing weight even at 1050 °C, and it is possible that RuO_2 started to evaporate when the sample was heating at high temperatures before it was able to enter the perovskite lattice [219]. As a result, the ruthenium was not doped into the surface of the perovskite and evaporated instead. More experiments have been carried out to address this issue and will be explained in later sections.

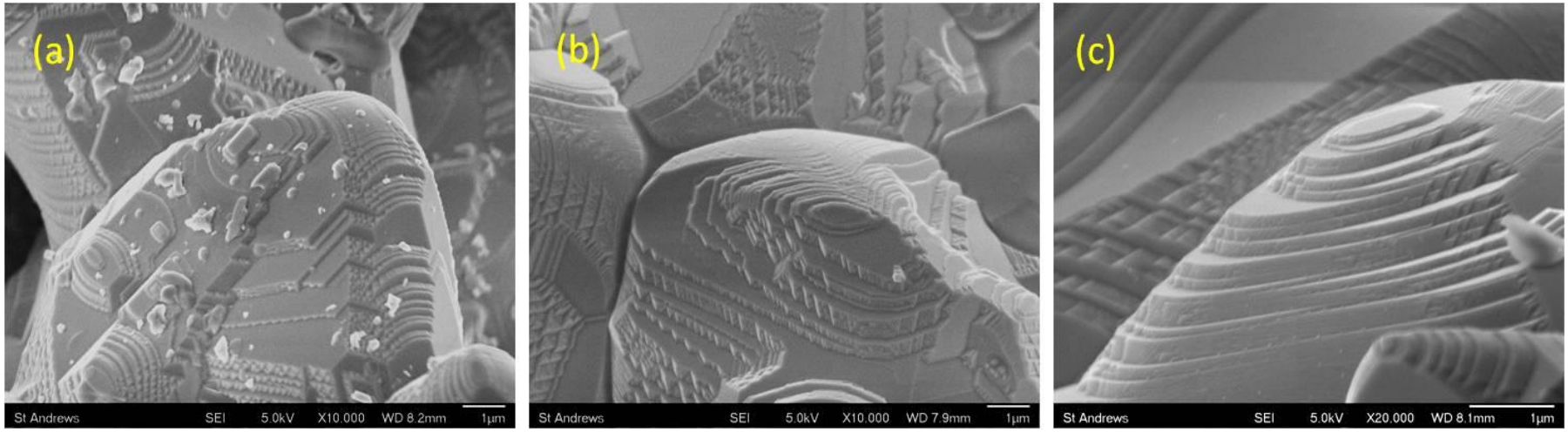

Figure 5-9 SEM images of 950 °C reduced LSGT10 coated with ruthenium in air for 6 h at different temperatures, a. coated with ruthenium at 1100 °C, b. coated with ruthenium at 1200 °C, c. coated with ruthenium at 1300 °C

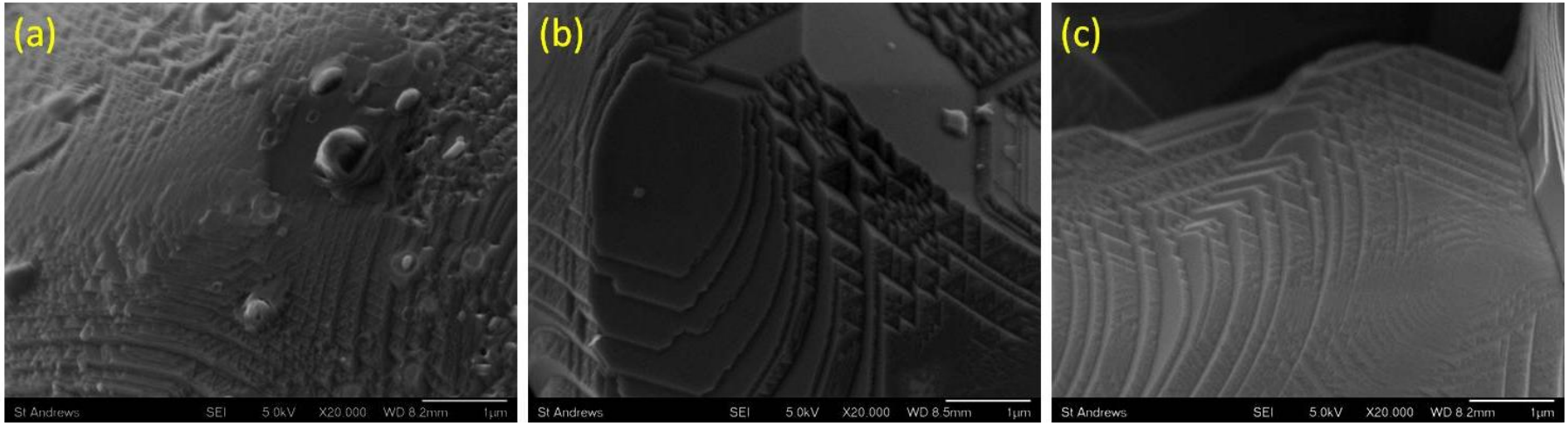

Figure 5-10 SEM images of 950 °C reduced LSGT10 coated with ruthenium in air at different temperatures for 6 h after 2nd reduction for 30 h, a. coated with ruthenium at 1100 °C, b. coated with ruthenium at 1200 °C, c. coated with ruthenium at 1300 °C

5.4.3 Investigation of coating LSGT10 with ruthenium catalyst in 5% H_2

The boiling point of ruthenium metal is 4150 °C, which is much higher than that of RuO_2 [226]. Therefore, the ruthenium nitrate impregnated samples were fired in 5% H_2 at high temperatures (1000 °C and 1300 °C) to explore the possibility of doping ruthenium into the perovskite from its surface in reducing atmosphere, although Ru metal would be less likely to react with the oxides. This experiment also serves as a point of comparison for when the perovskite was coated with ruthenium in air. In addition, the possibility of the volatilization of RuO_2 when the sample was coated in an oxidizing environment can be minimised as well. The morphologies of the samples after they were fired in 5% H_2 were first studied by SEM since the technique could provide a very straightforward view of whether or not ruthenium had entered the perovskite lattice (see Figure 5-11). According to Figure 5-11, the ruthenium particles remained on the surface of the perovskite after firing. Likewise, when the sample was heated at 1300 °C, it seemed that the ruthenium was still present on the surface, also at the grain boundaries, suggesting a surface migration during thermal treatment. The samples were also examined by backscattering in the SEM. According to the results, the reducing atmosphere turned the RuO_2 into well dispersed metallic particles which stayed mainly on the grain boundaries instead of the surface of the perovskite grains (see Figure 5-12).

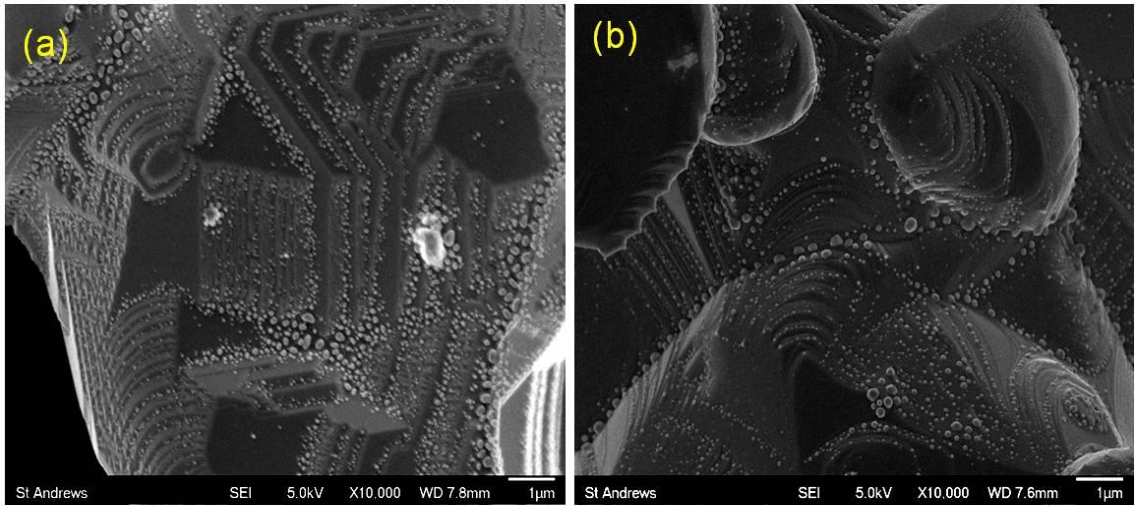

Figure 5-11 SEM images of 950 °C reduced LSGT10 coated with ruthenium in 5% H_2 at different temperatures for 12 h, a. coated with ruthenium at 1000 °C, b. coated with ruthenium at 1300 °C

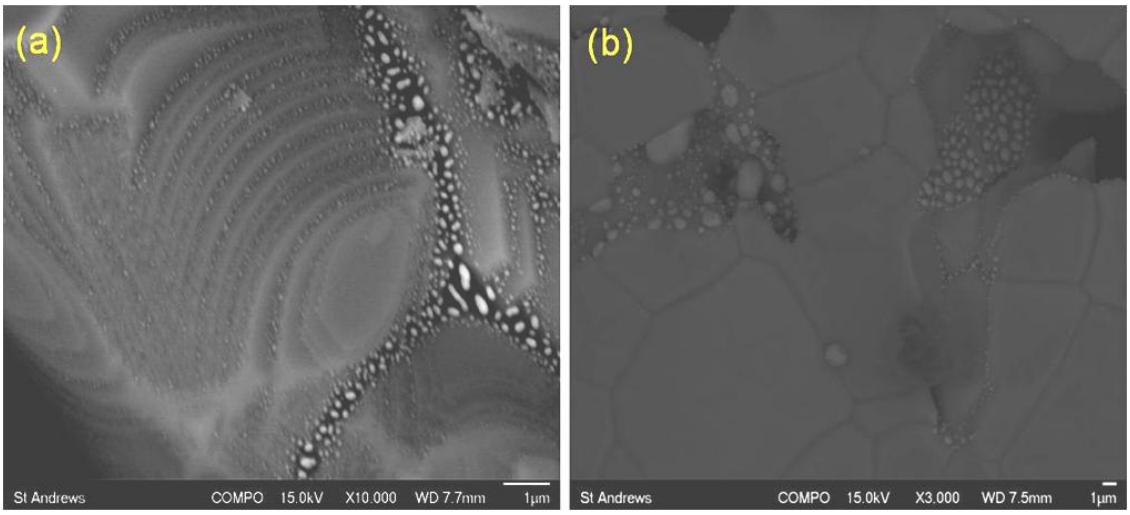

Figure 5-12 Backscattering images of 950 °C reduced LSGT10 coated with ruthenium in 5% H_2 at different temperatures for 12 h, a. coated with ruthenium at 1000 °C, b. coated with ruthenium at 1300 °C.

5.4.4 Ru exsolution from LSGT investigation

Since there was no exsolution observed from any of the ruthenium coated samples, it was suspected that the ruthenium may have evaporated during heating at high temperatures since the boiling point of ruthenium oxide is 1200 °C and it will decompose above that temperature if it is not stabilized in the perovskite. It was not yet known whether the B-site vacancies created by the Ga loss would provide a great enough driving force for the ruthenium to enter the perovskite lattice before it decomposed. In order to confirm that ruthenium had been doped in the surface of the perovskite, the ruthenium coated samples were studied by EDS after they were reduced in 5% H_2 for 30 h (see Figure 5-13). According to Figure 5-13, ruthenium was detected in samples which were coated at all temperatures. Therefore, it can be confirmed that at least some of the ruthenium was doped into the surface of the perovskite. The next challenge was to exsolve the ruthenium from the perovskite.

In order to promote the ruthenium exsolution from the perovskite, higher reduction temperatures were applied to LSGRT and 950 °C reduced LSGT10 which was coated with ruthenium at 1200 °C. The reason that the latter material was chosen, instead of samples which had been coated at different coating temperatures, was because at this temperature it seemed that the ruthenium had only just started entering the lattice of LSGT10. This may make it easier for ruthenium to exsolve from the perovskite since it may still be in the surface layer of the perovskite. According to the XRD and SEM

results, not all of the ruthenium had diffused into the perovskite when the sample was coated at 1100 °C, since the peak of ruthenium oxide can still be observed from the XRD pattern of the sample and the ruthenium oxide particles were still present on the surface of the perovskite. When the LSGT10 was coated at 1300 °C, it was possible that ruthenium had diffused to the bulk of the perovskite, which placed it in a similar situation to the ruthenium in LSGRT.

The morphologies of the samples reduced at different temperatures were studied by SEM (see Figure 5-14). According to Figure 5-14a and Figure 5-14b, reducing at 1000 °C did not provide a great enough driving force for ruthenium to exsolve from the perovskite. However, when the sample LSGRT was reduced at 1300 °C, two types of particles were observed on the surface of the perovskite: nanoparticles, and particles which had a similar morphology to the perovskite. The presence of the new particles on the surface of the perovskite after reduction at high temperatures may be due to the fact that, at 1300 °C, the perovskite structure was re-organized due to the high temperature. Therefore, it seemed that ruthenium was very stable in the LSGT10 perovskite lattice even if it was coated into the perovskite from its surface. One of the few possible ways to exsolve it from the LSGT10 perovskite lattice was to reduce the ruthenium containing sample at very high temperature. In this way, the perovskite would have enough energy to re-structure itself since the other perovskite-like particle also exsolved from the perovskite.

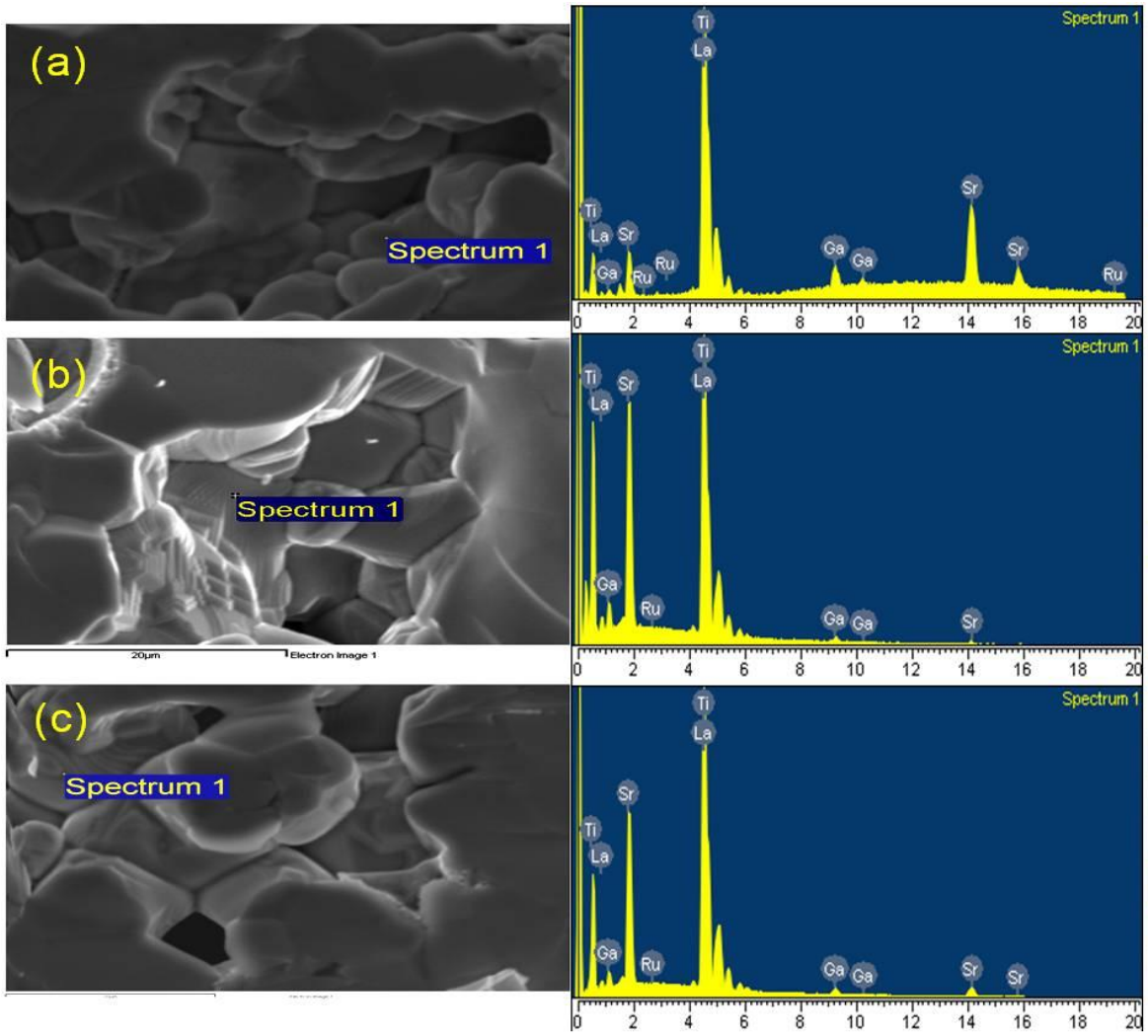

Element	Weight%	Atomic%
Ti K	38.27	59.02
Ga K	8.01	8.42
Sr L	12.07	10.33
Ru L	0.08	0.06
La L	41.57	22.17
Totals	100	

Element	Weight%	Atomic%
Ti K	29.98	49.13
Ga K	2.82	3.17
Sr L	29.30	26.25
Ru L	0.12	0.09
La L	37.78	21.35
Totals	100	

Element	Weight%	Atomic%
Ti K	31.78	51.47
Ga K	3.15	3.50
Sr L	26.35	23.38
Ru L	0.09	0.07
La L	38.64	21.58
Totals	100	

Figure 5-13 EDS of 950 °C reduced LSGT10 coated with ruthenium in air at different temperatures for 6 h after 2nd reduction for 30 h, a. coated with ruthenium at 1100 °C, b. coated with ruthenium at 1200 °C, c. coated with ruthenium at 1300 °C

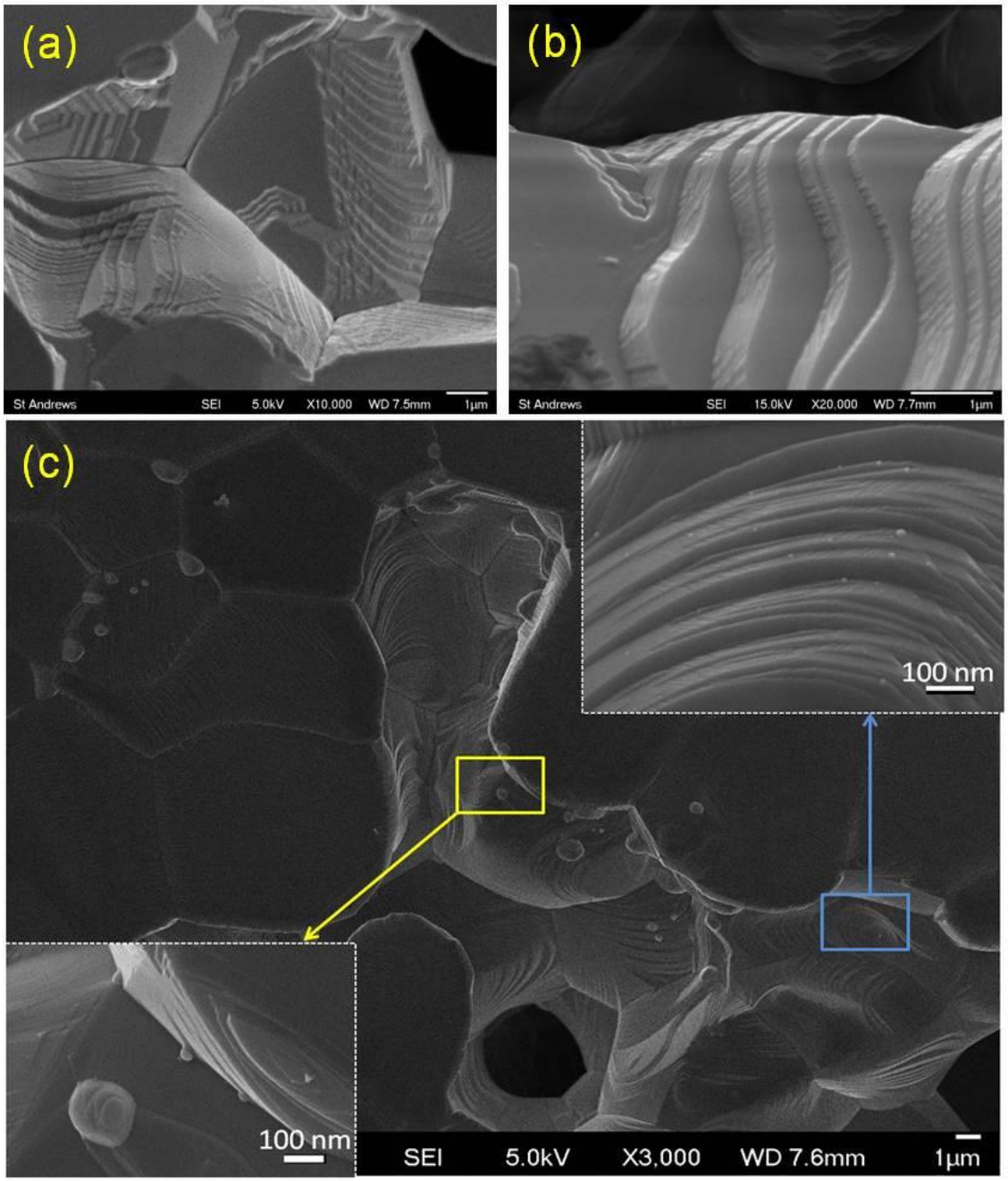

Figure 5-14 SEM images of ruthenium containing perovskite which were reduced at higher temperatures for 20 h: a. LSGRT reduced at 1000 °C, b. 950 °C reduced LSGT10 coated with ruthenium at 1200 °C for 6 h which was reduced at 1000 °C, c. LSGRT reduced at 1300 °C

5.5 Conclusions

In this chapter, single phase ruthenium doped strontium titanate LSGRT was synthesized by solid state methods which confirmed the possibility of doping ruthenium into the A-site deficient titanate. Due to sample preparation method, it was difficult to identify if ruthenium was doped into the 950 °C reduced LSGT10 perovskite from its

surface via VT-XRD. However, when the samples were studied in the form of pellets, it was found that ruthenium had been doped into the 950 °C reduced LSGT10 at both 1200 °C and 1300 °C in air. This was confirmed by XRD and EDS. The 950 °C reduced LSGT10 was also coated with ruthenium in reducing atmosphere. However, the ruthenium oxide on the surface of the perovskite grains was reduced into metal particles and did not enter the perovskite lattice.

Despite the fact that the ruthenium was doped into the perovskite in LSGRT, it was difficult to exsolve it from the perovskite during reduction at 930 °C. Neither could the ruthenium which was coated into the LSGT10 perovskite exsolve from the perovskite under the same reducing conditions. This could be due to the fact that the ionic radius of Ru^{4+} (CN = 6) is very close to those of the atoms on the B-site of the perovskite (Ga^{3+}, CN = 6 and Ti^{4+}, CN = 6). Therefore, ruthenium is more stable in the perovskite lattice compared to nickel and palladium, which were reported in the previous chapters. This was confirmed by reducing the ruthenium coated sample at 1000 °C, where ruthenium exsolution still could not be observed. The fact that nanoparticles were only present when the sample was reduced at 1300 °C also supports this argument, since the reducing temperature was finally high enough that the perovskite was able to reorganise its whole structure.

Chapter 6

Coating $La_{0.75}Sr_{0.25}Cr_{0.5}Mn_{0.5}O_3$ (LSCM) with ruthenium catalyst

6.1 Introduction

The possibility of coating a different perovskite by a different method from the previous chapters is going to be investigated in this chapter. The perovskite material to be coated with catalyst was $La_{0.75}Sr_{0.25}Cr_{0.5}Mn_{0.5}O_3$ (LSCM), which was first reported by Tao and Irvine [111]. This perovskite material has been demonstrated to show high electrical conductivity in air and very good stability in both fuel and air conditions in high temperature fuel cells environments. It is a very promising replacement material of the traditional Ni-YSZ electrode material which has problems with carbon deposition and poor redox tolerance in SOFC. However, one of the drawbacks of the material is that it shows poor electronic conductivity and ionic conductivity in reducing atmosphere [111, 227, 228]. In addition, another major limitation of the material is its insufficient catalytic activity when acting as an electrode material, as has been reported by McIntosh *et al* [229]. Strategies to enhance the catalytic activity of the LSCM material involve impregnating the catalyst onto the surface of the material or doping the catalyst into the material [88, 230, 231].

According to Barison *et al*, the catalytic activity and selectivity of the LSCM perovskite was notably improved by dispersing Ru catalyst on the surface of the perovskite with a microwave assisted method. The Ru catalyst existed in the form of the metal nanoparticles on the surface of LSCM perovskite after the coating procedure. However, partial agglomeration of the Ru metal nanoparticles was observed after the catalytic test of the sample [231]. A report from Monteiro *et al* suggests that the electronic transport and catalytic properties of the perovskite can be improved by replacing the B-site cations of the perovskite with Ru. Ru nano particle exsolution was also observed after the sample was heated in a reducing atmosphere [88]. It is almost beyond doubt that the addition of catalyst to the perovskite will help to improve the performance of the perovskite and ruthenium has been one of the most common catalysts used for this purpose [112, 231-234]. The challenge of the current situation is how to use smaller amounts of catalyst while achieving higher performance of the perovskite and maintaining the stability of the catalyst on its surface.

One of the possible solutions to the problem above is to dope the catalyst into the

perovskite from its surface, thus forming a core-shell structure with a catalyst doped shell. Boulfard *et al* have observed Ni nanoparticles on the surface of LSCM after mixing nickel nitrate solution with the LSCM and CGO in a ball mill followed by heat treatment in oxidising atmosphere and reduction in H_2. It seemed that the Ni formed a solid solution with the A-site deficient LSCM during firing in air and then exsolved on the surface of the perovskite after the sample was treated in the reducing atmosphere [96]. If that is the case, it should be possible for other catalysts with similar cation sizes to be doped into the LSCM perovskite from its surface in the same way. When nickel reacted with the perovskite, the procedure can be illustrated as the equation shown below:

$$ABO_{3-\delta} + \alpha B'O \xrightarrow{\text{Oxidation}} ABB'_{\alpha}O_{3-\delta'} \qquad \text{Eq. } 6-1$$

The nickel oxide reacted with the perovskite in an oxidising atmosphere at high temperature and formed a new solid solution containing the catalyst in the perovskite structure. One of the possible reasons for the realization of the above equation is that the perovskite is known for its abundance of different cations on its A-site and B-site. One of the other possible driving forces for the formation of the perovskite based on the above equation is Schottky defects in the perovskite, since these naturally exist in the perovskite and stabilize its crystal structure. In addition, another possible contributor to the formation of the nickel containing LSCM solid solution in the paper may be the ball milling process adopted in the experiment. Ball milling can enhance the homogeneity of the mixture and break the agglomerates of the perovskite thus increasing the contact surface between different components in the reagent. Another advantage of the ball milling process is that it will create more defects in the perovskite, thus making it easier for the catalyst to react with the perovskite [235, 236].

When the nickel catalyst exsolves from the LSCM perovskite, the process can be illustrated by Eq 6-2,

$$ABB'_{\alpha}O_{3-\delta'} \xrightarrow{\text{Exsolution}} ABO_{3-\delta} + \alpha B' \qquad \text{Eq. } 6-2$$

This means that the reaction of nickel catalyst with LSCM perovskite is reversible. In

LSCM, the Mn on the B site is known to reinforce the oxide ion mobility in the perovskite since Mn can adopt lower coordination environments [237]. Therefore, compared to the strontium titanate based perovskite in which titanium has a stronger preference for 6-fold coordination environment, it is more likely for ruthenium to be coated into the LSCM perovskite and exsolve after reduction.

The idea of the experiment is shown below in Figure 6-1. LSCM with a known perovskite grain size was first coated with ruthenium catalyst. Upon heating, the ruthenium started to enter the LSCM grains to form a surface core-shell structure with LSCM as the core and Ru doped LSCM as the thin shell. The assumed molecular formula of the shell was $La_{0.75}Sr_{0.25}Cr_{0.5}Mn_{0.5}Ru_{0.05}\ O_{3-\delta'}$ (LSCMRu0.05). After normalizing the B-sites, the perovskite in the shell would become A-site deficient. In the perovskite grain, 20% of the grain size in diameter was assumed to be LSCMRu0.05. The amount of Ru used in the experiment was then 1.08 wt% with respect to LSCM. After reduction, the ruthenium particles are expected to separate from the perovskite and form nanoparticles on the surface of the perovskite. The nanoparticles would re-dissolve into the perovskite lattice, forming the core-shell structure again upon re-oxidation. The nano particle exsolution process would be reversible so that the ruthenium catalyst can go back into the perovskite upon heating in air and exsolve upon reduction.

It is a widely held view that a larger active surface area will give rise to higher performance in both fuel cell and catalysis applications. In order to ensure the high surface area of the sample, the perovskite was prepared by an adaptation of a previously reported combustion method instead of the solid state method [166]. The average particle size of LSCM was then estimated by SEM so as to decide the amount of ruthenium to be coated onto LSCM. After the LSCM was mixed with ruthenium catalyst, VT-XRD was used to detect the structural change of LSCM when it was coated with ruthenium catalyst at different temperatures, thus probing the temperature at which the ruthenium would dissolve in or exsolve from the perovskite. The possibility of re-oxidising ruthenium back into the perovskite and re-exsolving it afterwards was also explored by in-situ VT-XRD. SEM, TEM, EDS and TGA were used to study the structural and morphological change of the sample. Uncoated LSCM was also studied by VT-XRD and TGA for the purpose of comparison.

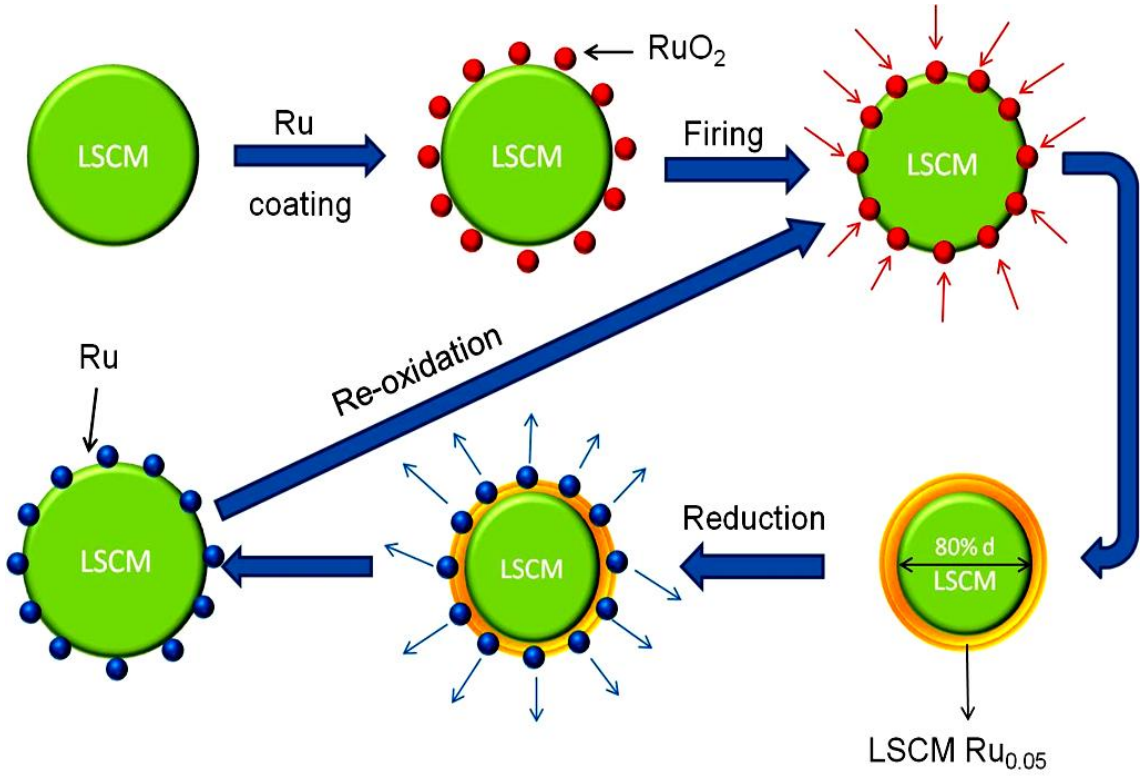

Figure 6-1 Illustration of reversible process of ruthenium catalyst doping LSCM perovskite from the surface and exsolve afterwards as nanoparticles

6.2 Experimental section (VT-XRD procedure)

The method of preparing the sample was the same as for the ruthenium coated LSGT perovskite in the previous chapter. The only difference was that the sample was naturally a very fine powder and did not need to be crushed. All of the samples in the experiment were heated at a ramp rate of 10 °C/min in the VT-XRD instrument. The heating program for the *in situ* VT-XRD investigation of the structural change of the samples is shown below. First of all, the sample was heated in air to observe the structure and phase change of the sample from room temperature to 1100 °C, in order to determine the temperature at which Ru would diffuse into the perovskite. After cooling down to room temperature, the sample was heated to the selected high temperature in 5% H_2 to observe the structure and phase change of the sample at different temperatures and find temperature at which the Ru catalyst would exsolve from the perovskite. After collecting the XRD data of the sample at high temperatures in a reducing atmosphere, the gas in the VT-XRD instrument was switched to air. A quick re-oxidation was carried out at the same temperature with a 2 theta range of 9-25 degrees to explore the reversibility of ruthenium entering the perovskite. The sample was heated for 4 h and

the data were collected every one hour before the atmosphere was changed back to 5% H_2. After measuring the XRD of the sample for four hours in the reducing atmosphere, the sample was cooled down to room temperature in 5% H_2. During the process of the sample cooling down, the sample was also studied by VT-XRD in case there was any structural change.

After finding out the temperature at which the ruthenium would diffuse into the perovskite in air and exsolve in 5% H_2, the LSCM perovskite pre-coated with ruthenium was heated at the selected temperature in air for 11 h to allow enough time for all of the ruthenium to diffuse into the perovskite. This also permitted an evaluation of the time required for the ruthenium to diffuse into the perovskite in air. The sample was then heated at the selected temperature for 20 h in 5% H_2 to evaluate how long it would take the ruthenium to exsolve from the perovskite. The sample was then re-oxidised for 11 h and re-reduced for 20 h at the selected temperature to assess the possibility of the exsolved ruthenium re-dissolving into the perovskite in air and exsolving again in a reducing atmosphere. For comparison, *in situ* VT-XRD of as prepared LSCM was also carried out using the same heating program as the LSCM pre-coated with ruthenium.

6.3 Methodology for comparing the structure of LSCM

It should be noted that the structure of LSCM will change from rhombohedral to cubic when it is heated above 500 °C or reduced at high temperatures, as has been reported by Tao and Irvine [238]. In order to compare the unit cells with different symmetries, a pseudo cubic cell parameter (a_p) is defined here. In this assumption, the perovskite is assumed to have only one single ABO_3 unit in a unit cell instead of multiple units in the perovskite. The method of calculating the pseudo cubic cell parameter is listed below,

$$a_p = \sqrt[3]{\frac{V_{uc}}{n_{uc}}} \qquad \text{Eq. } 6-3$$

where V_{uc} is the volume of the real unit cell of the perovskite and n_{uc} is the number of ABO_3 units contained within a real unit cell. As for LSCM, a real unit of the perovskite at room temperature contains 6 ABO_3 units. Therefore, n_{uc} for the LSCM before its

structural change should be 6.

6.4 Particle size analysis of LSCM

According to the experimental plan, the amount of ruthenium catalyst to be coated into the LSCM perovskite depends primarily on the size of the perovskite particles. For that reason, it is important to first evaluate the size of the LSCM perovskite particles before coating it with ruthenium catalyst. Since the perovskite particle sizes are varied, the average particle size is used as the criterion to decide the amount of the ruthenium catalyst to be coated into the LSCM perovskite. In addition, all of the LSCM perovskite grains are assumed to be spherical so that the diameter of the grains can represent the size of the perovskite particles. Based on the above assumption, the particle size of the perovskite was measured using the SEM images of LSCM. Figure 6-2 shows the particle size distribution of the as prepared LSCM powder. The main particle size range of the LSCM perovskite is between 200 and 300 nm. According to Figure 6-2, the average particle size of the as prepared LSCM is 284 nm. Since the aim of the experiment was to dope Ru into the surface of the LSCM perovskite forming LSCMRu0.05 on the outside layer, the calculation of the weight percentage of ruthenium catalyst to be doped into the perovskite is shown below.

There are multiple ways to calculate the weight percentage of ruthenium catalyst to be doped into the perovskite and the method chosen for this work is shown below. It assumes that the ruthenium catalyst has entered the surface of the perovskite forming a core-shell structure with the shell consisting of LSCMRu0.05 while the core remained as LSCM (see Figure 6-3). Since the mass increase of the shell caused by the addition of ruthenium is very small, the molar mass and the density of the shell are hypothesized to be the same as the LSCM so as to simplify the calculation process. The mass of the ruthenium in the shell and the mass of the shell are m_{Ru} and m_s respectively. First, the weight percent of Ru catalyst in LSCMRu0.05 w_1 is calculated as shown in Eq. 6-4,

$$w_1 = \frac{m_{Ru}}{m_s} \times 100\% = \frac{0.05M_{Ru}}{M_{LSCMRu}} \times 100\% \qquad \text{Eq. } 6-4$$

The mass of the core and the whole grain is m_c and m_g respectively. Then the weight

percentage of the shell in regards to the whole grain w_2 is calculated as shown in Ed. 6-5,

$$w_2 = \frac{m_s}{m_g} \times 100\% = (1 - \frac{m_c}{m_g}) \times 100\% \qquad \text{Eq. } 6-5$$

Since the density of the shell is assumed to be the same as that of *the core*, Eq.6-5 then becomes

$$w_2 = \left(1 - \frac{V_c}{V_g}\right) \times 100\% = \left(1 - (\frac{d_c}{d_g})^3\right) \times 100\% \qquad \text{Eq. } 6-6$$

where V_c is the volume of the core with d_c being its diameter, and V_g is the volume of the whole perovskite grain with d_g being its diameter. Combining Eq.6-4 and Eq.6-6, the weight percent of the ruthenium catalyst with respect to the whole perovskite grain w_3 is

$$w_3 = w_1 \times w_2 = 0.05 \times \frac{M_{Ru}}{M_{LSCM}}\left(1 - (\frac{d_c}{d_g})^3\right) \times 100\% \qquad \text{Eq. } 6-7$$

In the experiment plan, the depth of ruthenium diffused into the perovskite was assumed to be 20% of the whole perovskite grains, therefore $\frac{d_c}{d_g} = 0.8$. After substituting the molar mass of Ru and LSCM into Eq 6-7, the weight percentage of the ruthenium with regards to the whole perovskite grains is 1.08 wt%. The above method to calculate the weight percentage of the ruthenium catalyst can also be used to calculate the amount of other catalyst to be coated into the perovskite by replacing the molar mass of Ru with the molar mass of the corresponding catalyst to be coated. In addition, the amount of catalyst to be coated into the perovskite can be altered by changing the depth of ruthenium diffusion under this experiment condition.

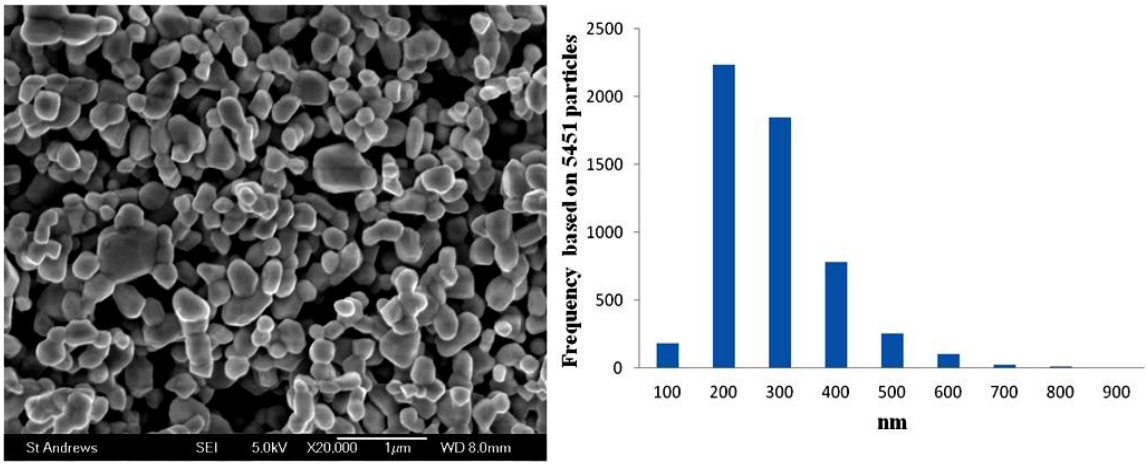

Figure 6-2 SEM image of as prepared LSCM powder and the corresponding particle size distribution by image analysis

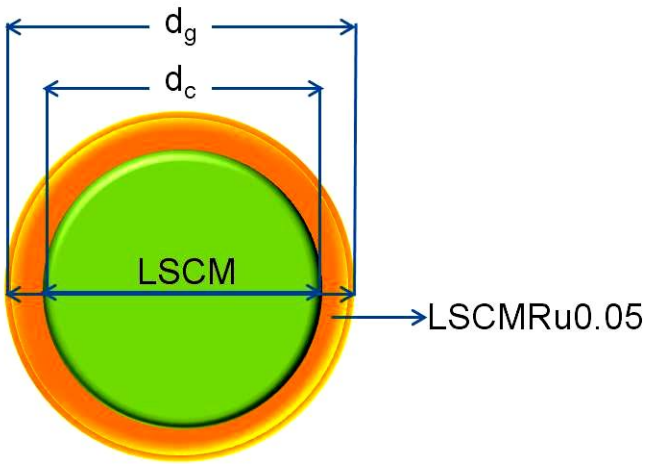

Figure 6-3 A schematic diagram of the core-shell structure of LSCM perovskite with ruthenium doped LSCM in the shell

6.5 In-situ VT-XRD investigation of LSCM coated with Ru catalyst at different temperatures

Figure 6-4 shows the *in situ* VT-XRD patterns of LSCM pre-coated with ruthenium during the heating from room temperature to 1100 °C. According to Figure 6-4, the structure of the perovskite started to change from rhombohedral to cubic as the temperature rose. At 1000 °C, the majority of the structure of the perovskite changed to cubic. This agrees with the point that LSCM would change to a cubic structure above 500 °C, as has been reported earlier [238]. Apart from the structural change of the perovskite with temperature, the intensities of XRD peaks of RuO_2 also dropped as the heating temperature went up. At 900 °C, no RuO_2 peaks were observed any more.

Above 900 °C, there were not any obvious structural changes according to the VT-XRD patterns. This may indicate that as the temperature increased, the ruthenium started to enter the perovskite grains. The temperature of 900 °C may provide sufficient driving force for ruthenium to diffuse into the perovskite. After the VT-XRD cooled down to room temperature, there were no RuO_2 peaks observed in the VT-XRD patterns, suggesting that ruthenium had diffused into the perovskite.

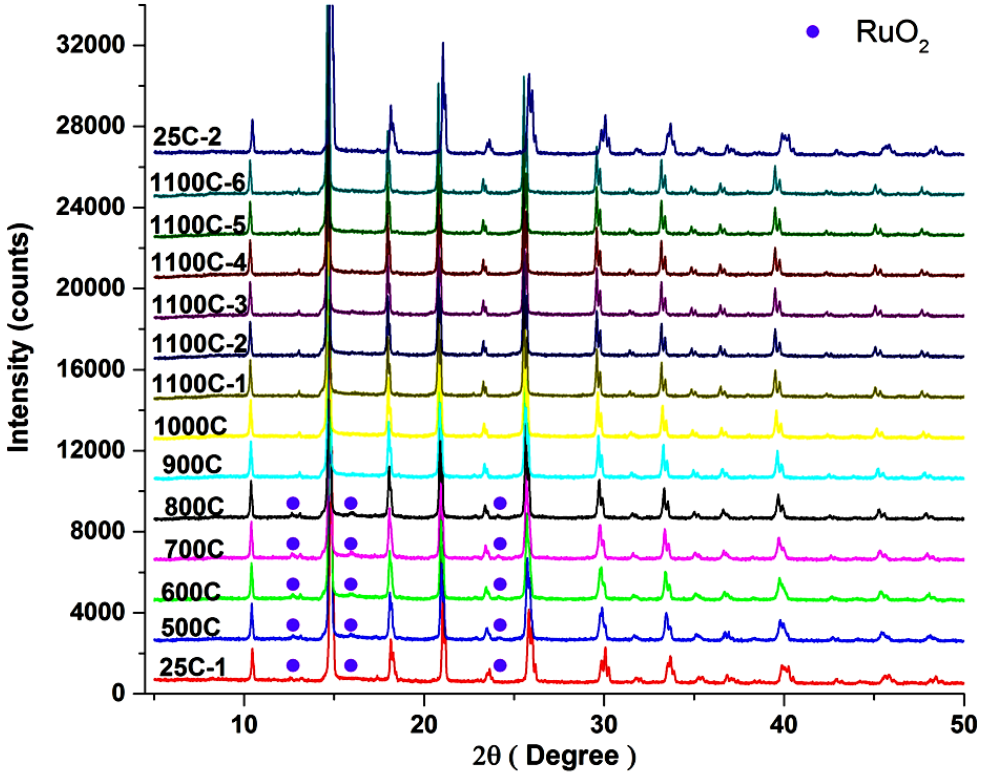

Figure 6-4 In situ VT-XRD patterns of LSCM pre-coated with ruthenium oxide during heating stage from room temperature to 1100 °C

The VT-XRD pattern of the sample which was reduced at different temperatures in 5% H_2 is shown in Figure 6-5. According to Figure 6-5, at 600 °C, the XRD peaks of the perovskite with Ruddlesden–Popper structure (K_2NiF_4) started to show up as a second phase suggesting a structural change of the LSCM perovskite during the reduction. This was not surprising since LSCM phases tend to break down when the oxygen content drops below 2.75 [227]. There were many potential cation combinations for the 2nd phase with K_2NiF_4 structure observed in the experiment, such as Sr_2MnO_4, Sr_2CrO_4, Sr_2RuO_4, etc. The K_2NiF_4 will reflect main cations but will also yield MO where Mn is likely but could be others that are easier to reduce [238]. As the temperature went up, the intensities of the 2nd phase peaks became higher, suggesting that more 2nd phase was

formed and the 2nd phase became more crystallized. Other than that, there were no obvious changes observed from the VT-XRD patterns when the sample was reduced at different temperatures.

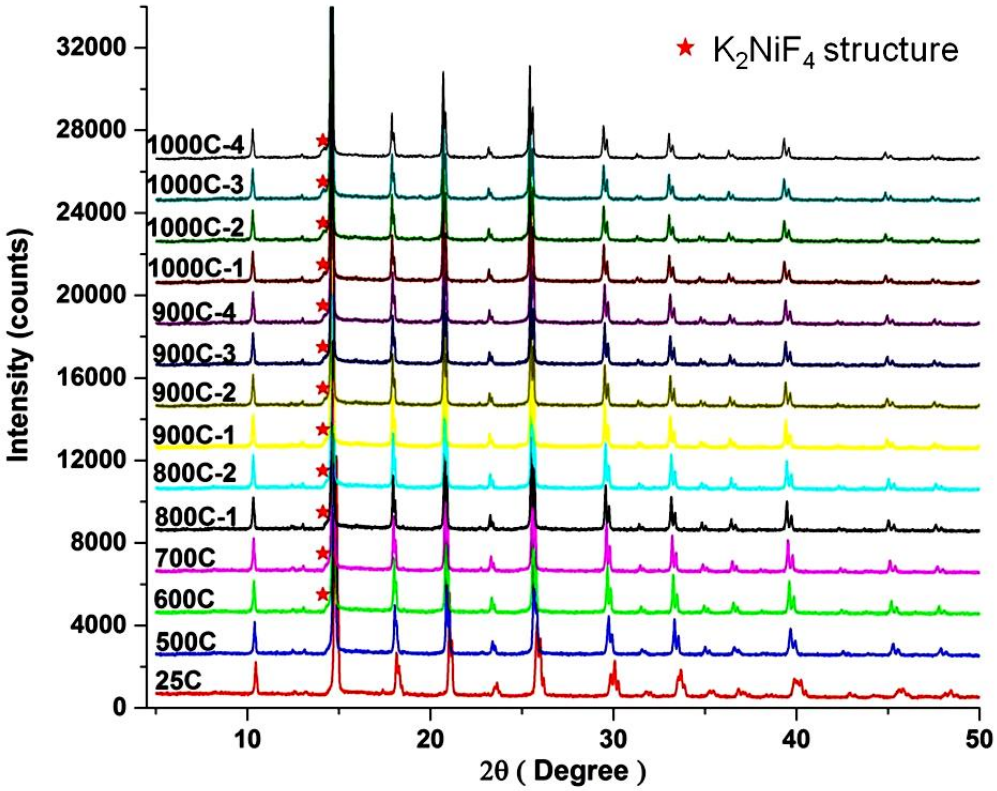

Figure 6-5 In situ VT-XRD patterns of LSCM coated with ruthenium oxide during heating stage from room temperature to 1000 °C in 5% H_2

A quick re-oxidation of the sample was carried out at 1000 °C with the 2 theta range of 9-25 degrees (see Figure 6-6). The reason to collect the data at the above 2 theta range was because it seemed to be the main 2 theta range where the obvious phase change of the perovskite can be observed. Compared to Figure 6-5, the peaks of the 2nd phase with K_2NiF_4 structure almost disappeared even if the sample was heated for only one hour. As the sample was heated for longer, there was no obvious change according to the VT-XRD. However, once the atmosphere inside the instrument was changed to 5% H_2, the same 2nd phase started showing up again within the 1st hour of heating in 5% H_2, indicating that this is a reversible process (see Figure 6-7). As the sample was reduced for longer, the peak of the 2nd phase was getting sharper, implying that more 2nd phase was formed and the 2nd phase was becoming more crystalline. When the sample was cooling down, the XRD peaks of the sample kept shifting to the higher 2 theta angle, suggesting that the unit cell of the perovskite was shrinking as the temperature getting

lower. When the sample cooled down to room temperature, the 2nd phase was still present in the perovskite XRD pattern.

There are a few possible explanations to the appearance of the 2nd phase. One possible explanation is that the temperature at which the sample was reduced was too high (above 900 °C), thus causing the decomposition of the perovskite. However, this could not explain why the 2nd phase started showing up even when the sample was reduced at lower temperatures (below 900 °C). In addition, the appearance of the 2nd phase seemed reversible since it mostly disappeared during the re-oxidation process and emerged again during re-reduction. Another possible reason for cause of the 2nd phase could be that the ruthenium was doped into the perovskite from the surface and changed its reducibility. Raj *et al* has reported that replacing La with Pr made it easier for LSCM to decompose possibly due to the oxidation state drop of Mn caused by Pr^{4+} in as prepared $Pr_{0.75}Sr_{0.25}Cr_{0.5}Mn_{0.5}O_{3-\delta}$ [239]. Similarly, Ru^{4+} replacing Cr/Mn would have similar effect which changed the extent of transition between Cr^{3+}/Mn^{3+} and Cr^{3+}/Mn^{4+}, and made the perovskite sample easier to be reduced. Further work is needed to confirm which assumption is more plausible.

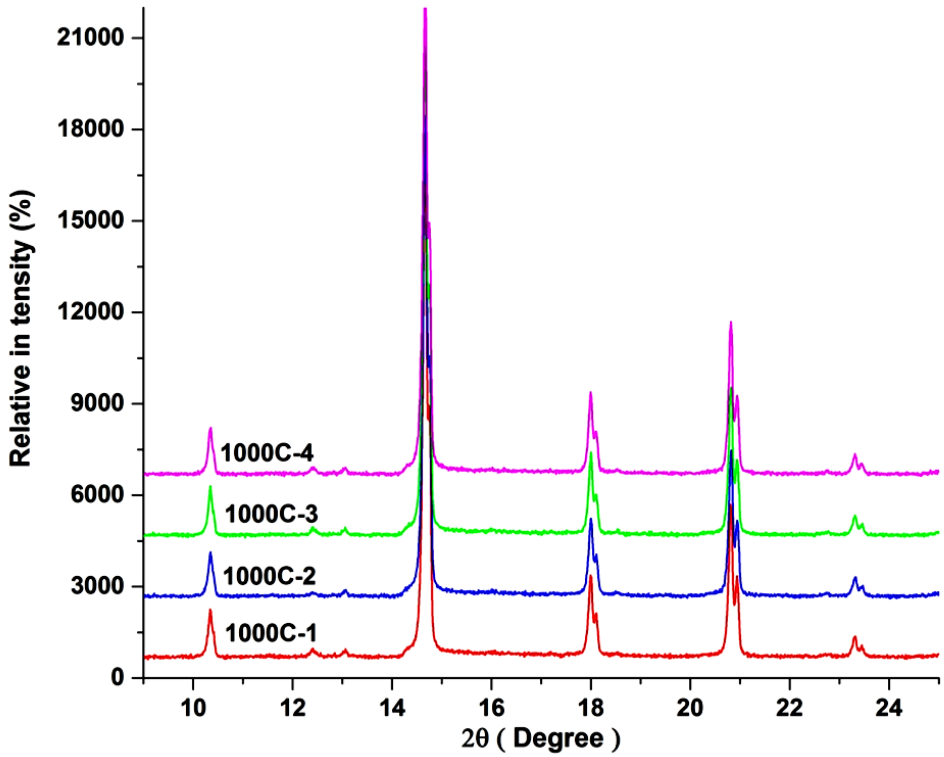

Figure 6-6 In situ VT-XRD patterns of LSCM coated with ruthenium during re-oxidation at 1000 °C in air

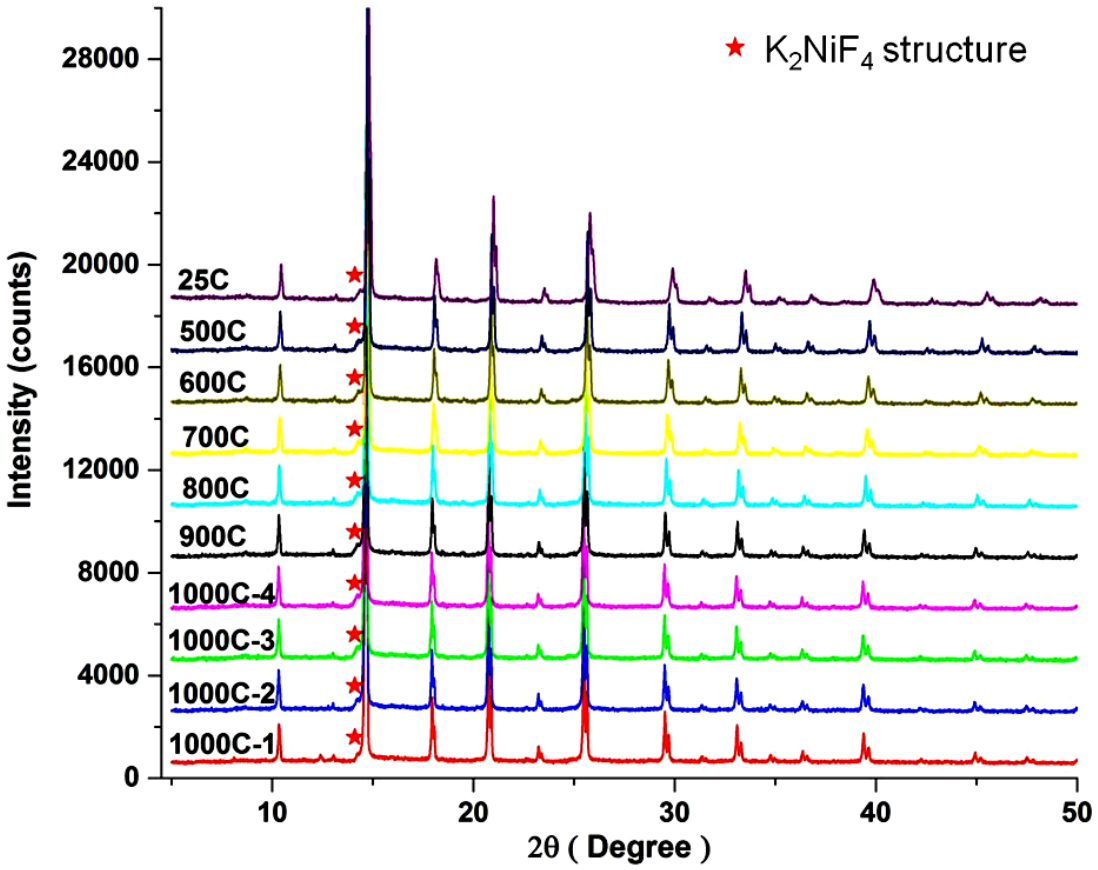

Figure 6-7 In situ VT-XRD patterns of LSCM coated with ruthenium during re-reduction at 1000 °C and cooling down process in 5% H_2

According to the VT-XRD patterns of LSCM perovskite coated with ruthenium at different temperatures and different atmospheres, it seemed that there would be a phase segregation of the perovskite producing another perovskite with the K_2NiF_4 structure during the reduction process. The phase segregation seemed reversible since it disappeared in the re-oxidation process and re-appeared during the re-reduction process. However, has ruthenium been doped into the perovskite during the heating? Was the phase segregation caused by ruthenium coating or not? The answer to the first question will be given in the later discussion. The answer to the 2nd question will be provided in the next section.

In order to better understand the structural change of the LSCM perovskite during the coating, the VT-XRD data was refined and the change of the unit cell parameter of the sample throughout the experiment was shown in Figure 6-8. According to Figure 6-8 section a, the unit cell volume of the perovskite increased as the temperature rose. At 1100 °C, the unit cell parameter stayed relatively the same even if the sample was

heated for a longer time. When the sample was heated in 5% H_2, compared to when being heated in air, the unit cell parameter of the sample was generally larger when it was reduced in 5% H_2 at different temperatures, suggesting that the perovskite started reducing even at 500 °C. Similar to when it was heated in air, the unit cell of the perovskite was expanding as the sample was reduced at higher temperatures (see Figure 6-8 section b). At 800 °C, no obvious change was observed when the sample was heated for a longer period of time. At 900 °C, there was a gradual rise in the unit cell parameters as the perovskite was heated for an extended duration. The same trend was also observed when the sample was reduced at 1000 °C. The expansion of the unit cell in the reducing atmosphere should be due to the large number of oxygen vacancies ($V_O^{\cdot\cdot}$) and reduced cations on the B-site (Mn^{2+}) generated during the reduction process [240]. In section c of Figure 6-8, there was a sharp drop in the size of the unit cell parameter when the sample was re-oxidised. When the sample was reduced again, the unit cell of the perovskite increased to the larger size once more (see Figure 6-8 section d). As the sample was reduced for longer at 1000 °C, similar to when it was reduced for the 1st time, the unit cell of the LSCM perovskite gradually grew larger due to the large number of defects in the perovskite caused by reduction. During the cooling process, the unit cell parameter of the sample decreased as the temperature dropped; this was due to the reverse thermal expansion of the sample. In section e of Figure 6-8, when comparing the unit cell parameter of the sample at room temperature, it revealed a slight increase in the unit cell parameter of the perovskite after the LSCM perovskite was coated with ruthenium at temperature indicating that ruthenium might be doped into the perovskite from the surface.

According to the XRD result, it seemed that ruthenium started diffusing into the perovskite when the temperature was above 900 °C. However, it was difficult to confirm from the results that ruthenium had exsolved from the perovskite after reduction. To identify if ruthenium had exsolved from the perovskite during reduction, the reduced sample was examined by TEM and EDS to see if there were any exsolved particles on the surface (See Figure 6-9). According to Figure 6-9, it can be confirmed that the nanoparticles observed on the surface of the LSCM grains are ruthenium particles. Combined with the VT-XRD results, it is almost certain that the ruthenium did enter the LSCM grains when the ruthenium coated perovskite was heated in air. The coated ruthenium was also able to exsolve from the perovskite during reduction.

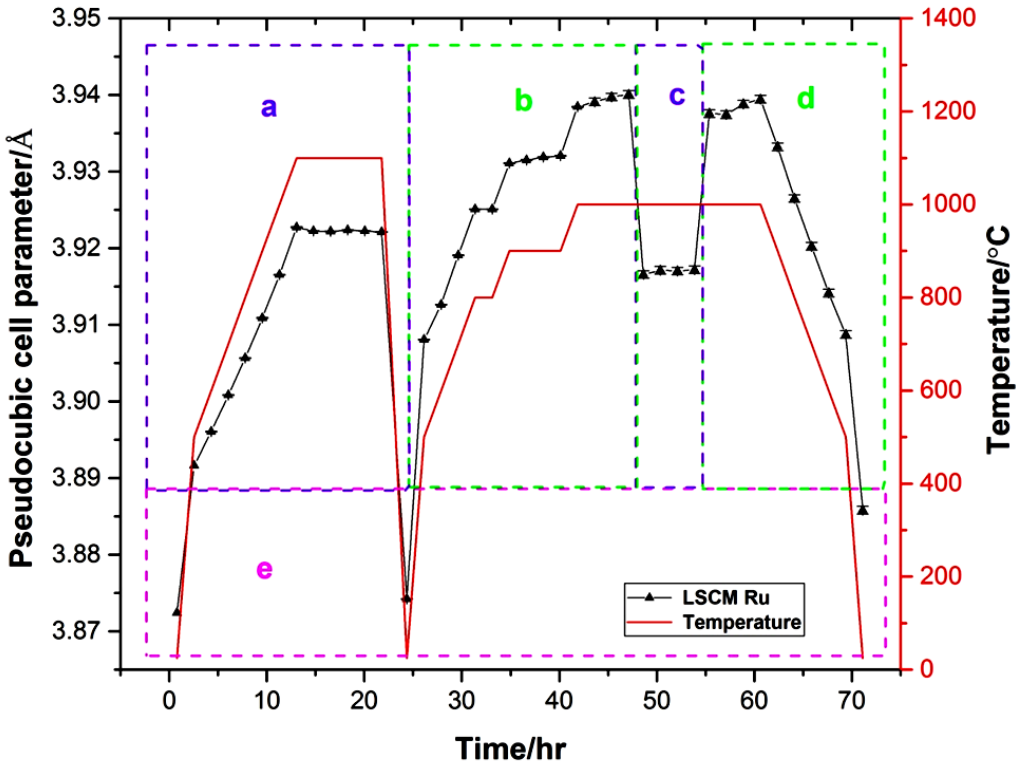

Figure 6-8 The change of the unit cell parameters of the LSCM perovskite when it was coated with ruthenium throughout the experiment in VT-XRD: a. the LSCM perovskite was heated in air at different temperatures after it was pre-coated with ruthenium; b. the sample was reduced in 5% H_2 at various temperatures; c. the sample was re-oxidised in air at 1000 °C; the sample was re-reduced in 5% H_2 at 1000 °C and cooled down in the same atmosphere; e. the unit cell parameter change of the sample at room temperature

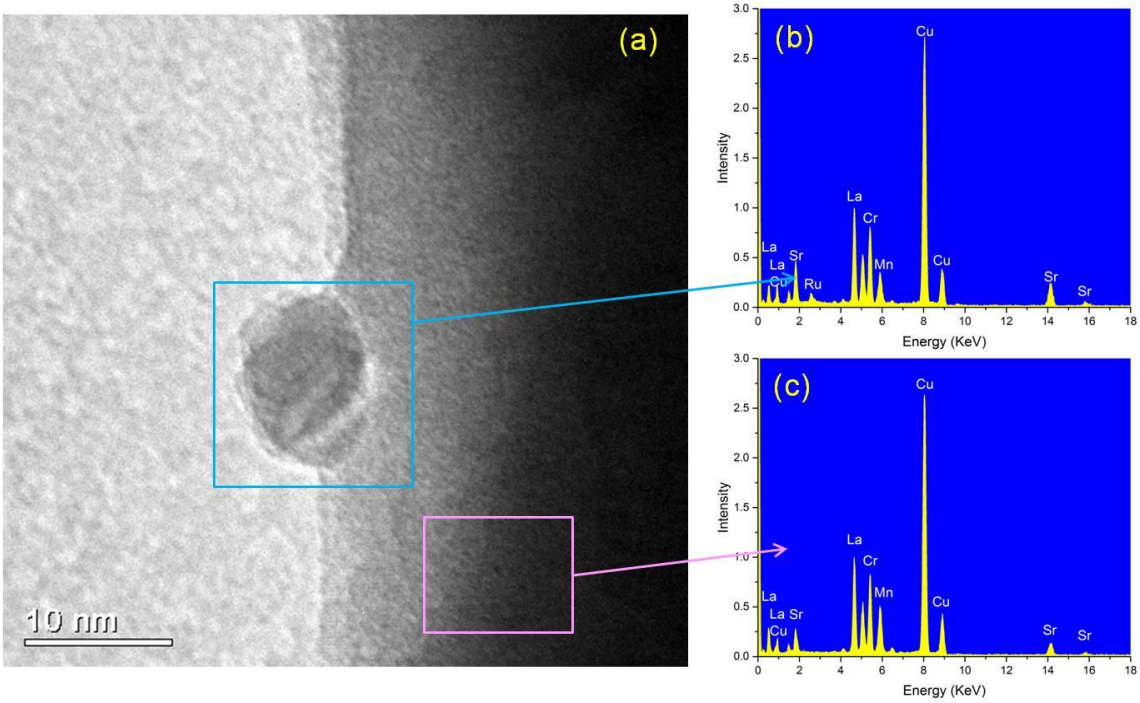

Figure 6-9 TEM and EDX images of ruthenium coated LSCM after reduction in 5% H_2 in VT-XRD

6.6 Investigation of ruthenium coating LSCM perovskite at fixed temperature via VT-XRD

Although the possibility of Ru entering the LSCM perovskite at high temperature had been confirmed, it was still unknown how long it would take for ruthenium to fully diffuse into the perovskite and fully exsolve from the perovskite grains during reduction. According to the unit cell change of the LSCM coated with ruthenium catalyst when the perovskite was being reduced, it seemed that 4 h was not long enough for the sample to be fully reduced since the unit cell was still expanding at the end of the reduction at high temperatures (see Figure 6-8). In addition, it was still uncertain whether the exsolved Ru would be able to go back to the perovskite again upon heating in air and exsolve from the perovskite again upon reduction. In order to find the answer, another *in situ* VT-XRD of ruthenium coating LSCM experiment was carried out at 1000 °C in different atmospheres for a sufficient length of time.

The reason to choose 1000 °C instead of 900 °C as the temperature to investigate the mechanism of ruthenium entering the perovskite was to ensure that the ruthenium had a sufficient thermodynamic driving force to enter the perovskite grains in air and exsolve from the perovskite in reducing atmosphere. The *in situ* VT-XRD patterns of ruthenium coating LSCM at 1000 °C are shown in Figure 6-10a. According to Figure 6-10a, XRD peaks of RuO_2 were present at room temperature and during the 1st hour of heating at 1000 °C in XRD patterns of the sample. There was no sign of RuO_2 after the sample was heated for longer than 2 hours, suggesting that the ruthenium may have diffused into the LSCM perovskite within the 1st hour of heating at 1000 °C. When the sample was reduced in 5% H_2 as shown in Figure 6-10b, a very small peak of the 2nd phase perovskite with K_2NiF_4 structure showed up in the XRD pattern even during the first hour of heating. Similar to the previous experiment, the intensity of the peak of the 2nd phase slowly increased as the sample was reduced for the first 4 hours. However, when the sample was reduced for more than 4 hours, very little change in the intensity of the 2nd phase peak was observed. After the sample was cooled down to room temperature, the 2nd phase was still present in the XRD pattern. When the ruthenium coated LSCM perovskite was re-oxidised in air, the 2nd phase perovskite which had K_2NiF_4 structure disappeared immediately once the sample reached a temperature of 1000 °C (see Figure

6-10c). No other phases were apparent in the VT-XRD patterns of the sample throughout the whole re-oxidation process. When the sample was re-reduced in 5% H_2, the 2nd phase with K_2NiF_4 structure again showed up almost immediately and showed similar behaviour as when the sample had been reduced in 5% H_2 for the first time.

When the as prepared LSCM was heated in air, the VT-XRD patterns of it are similar to that of ruthenium coating LSCM with the exception of RuO_2 presence (see Figure 6-11a). When the sample was reduced in 5% H_2, the 2nd phase perovskite with K_2NiF_4 structure was also observed in the XRD patterns, suggesting that its presence was not purely caused by coating with Ru (see Figure 6-11b&d). However, the intensity of the peak of the 2nd phase was smaller compared to the ones in the case of ruthenium coated LSCM, thus indicating that the ruthenium coating process may promote the formation of the 2nd phase in the perovskite even if it is not the direct cause of it. The 2nd phase also disappeared within the first hour of heating of as prepared LSCM at 1000 °C during re-oxidation. This further confirms that the 2nd phase perovskite with K_2NiF_4 structure was the result of intergrowth of the LSCM perovskite itself when it was exposed to the reducing atmosphere, rather than being influenced by ruthenium coating (see Figure 6-11c).

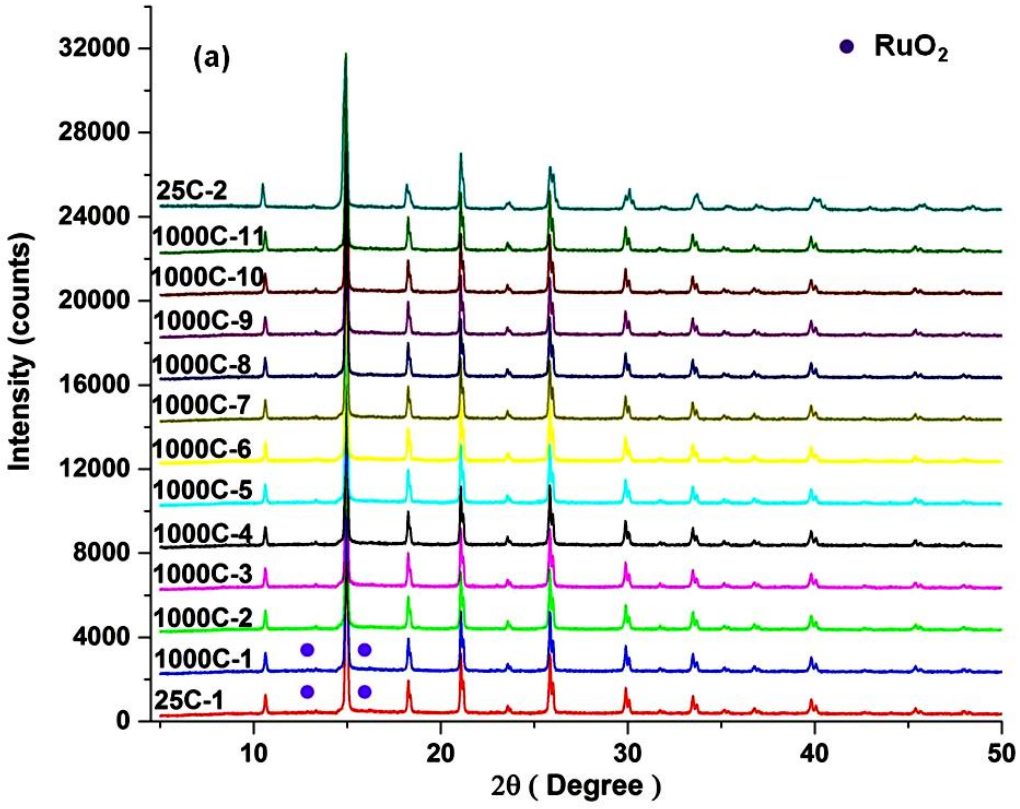
(a)
RuO2
25C-2
1000C-11
1000C-10
1000C-9
1000C-8
1000C-7
1000C-6
1000C-5
1000C-4
1000C-3
1000C-2
1000C-1
25C-1
Intensity (counts)
2θ (Degree)

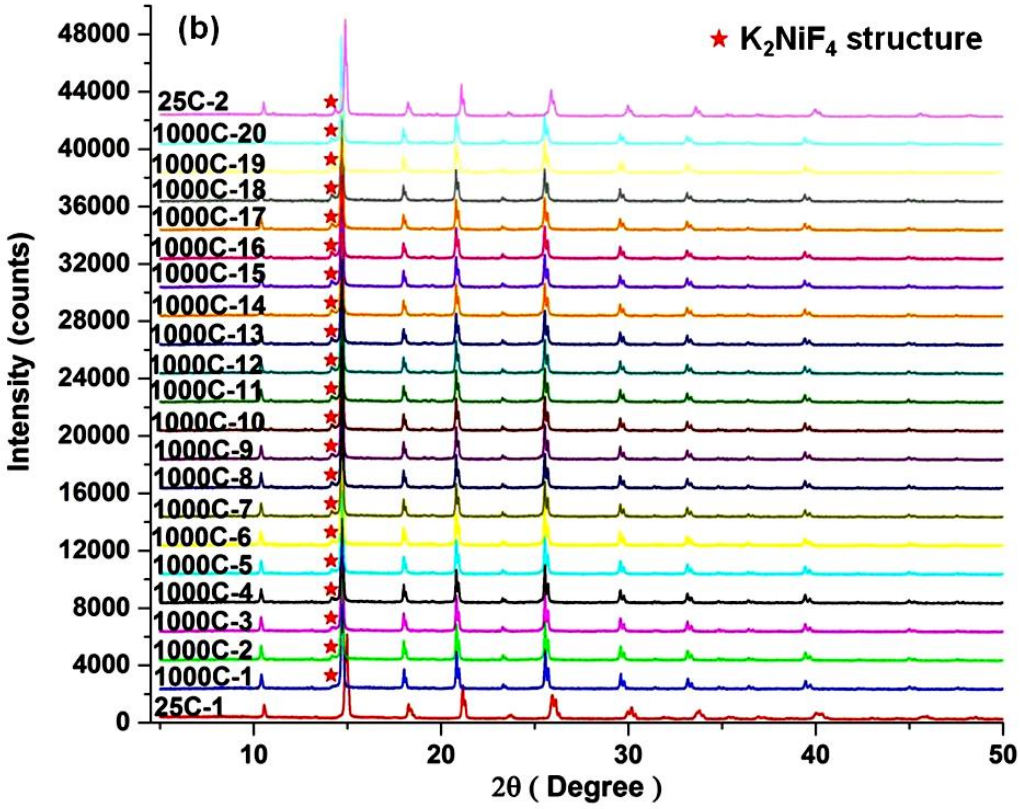
(b)
K2NiF4 structure
25C-2
1000C-20
1000C-19
1000C-18
1000C-17
1000C-16
1000C-15
1000C-14
1000C-13
1000C-12
1000C-11
1000C-10
1000C-9
1000C-8
1000C-7
1000C-6
1000C-5
1000C-4
1000C-3
1000C-2
1000C-1
25C-1
Intensity (counts)
2θ (Degree)

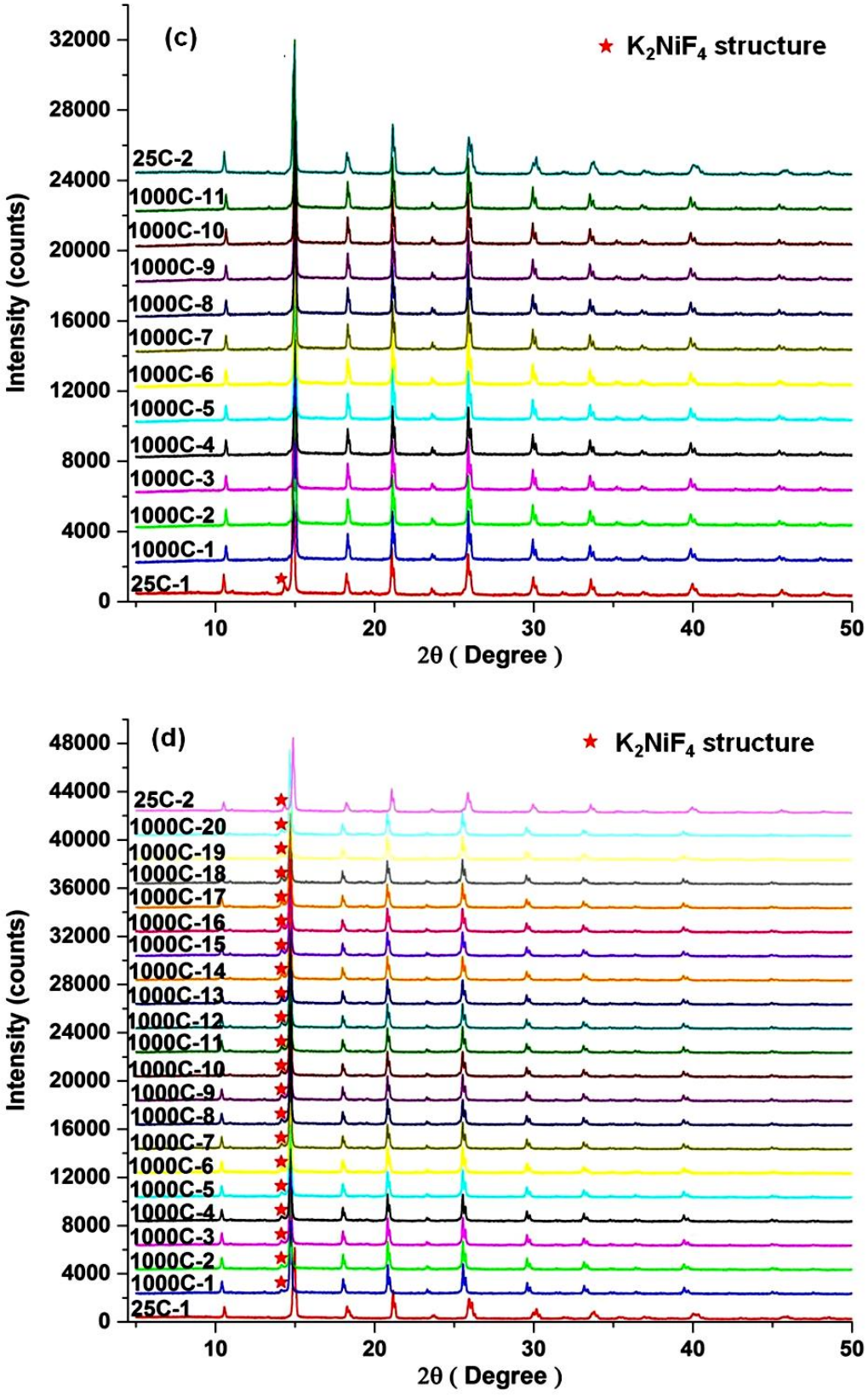

Figure 6-10 In situ VT-XRD of Ru coating LSCM at 1000 °C under different atmospheres: a. ruthenium coating LSCM in air, b. reduction of ruthenium coated LSCM, c. re-oxidation of ruthenium coated LSCM, d. Re-reduction of ruthenium coated LSCM

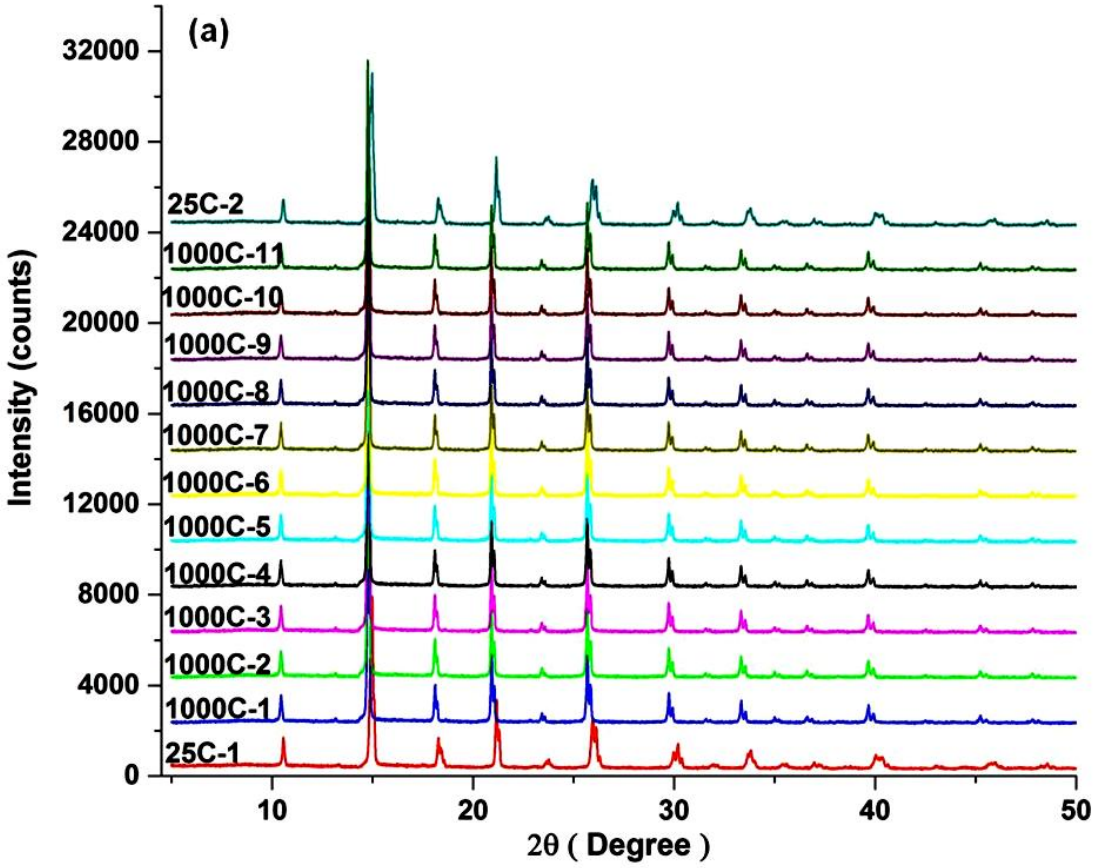
(a)
Intensity (counts)
2θ (Degree)
25C-2
1000C-11
1000C-10
1000C-9
1000C-8
1000C-7
1000C-6
1000C-5
1000C-4
1000C-3
1000C-2
1000C-1
25C-1

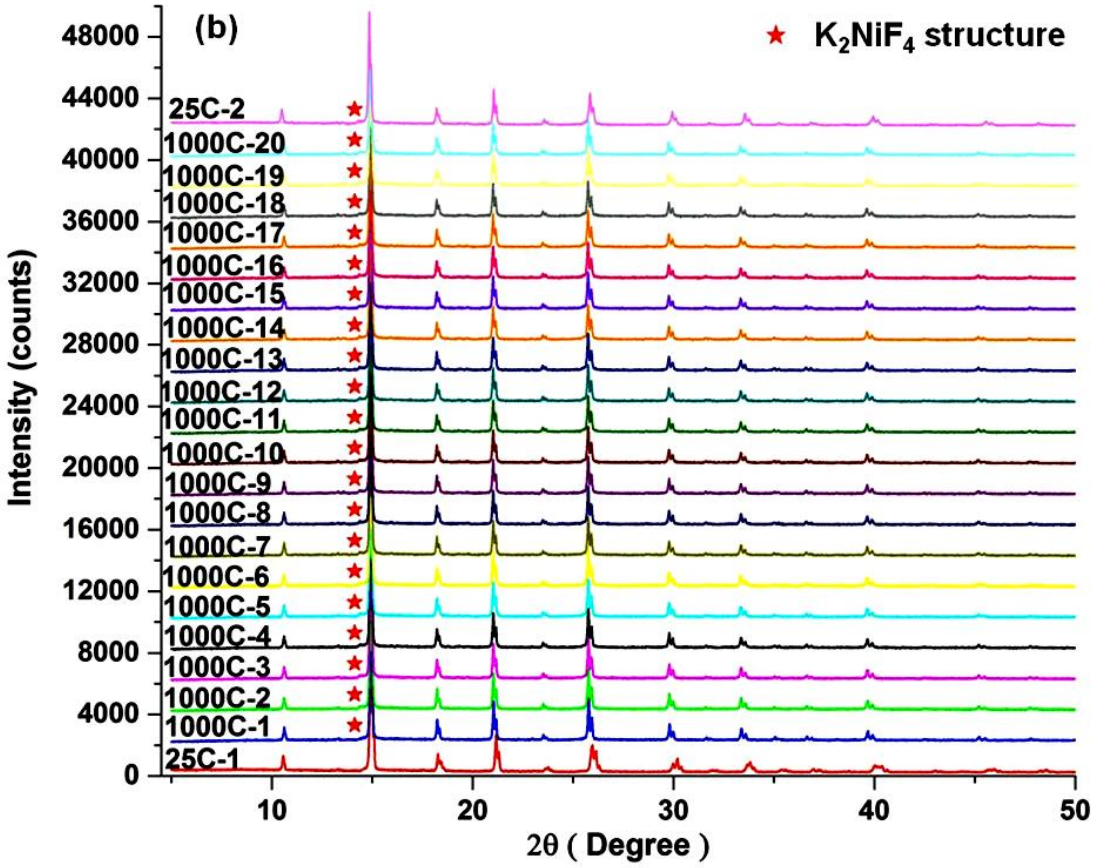
(b)
★ K2NiF4 structure
Intensity (counts)
2θ (Degree)
25C-2
1000C-20
1000C-19
1000C-18
1000C-17
1000C-16
1000C-15
1000C-14
1000C-13
1000C-12
1000C-11
1000C-10
1000C-9
1000C-8
1000C-7
1000C-6
1000C-5
1000C-4
1000C-3
1000C-2
1000C-1
25C-1

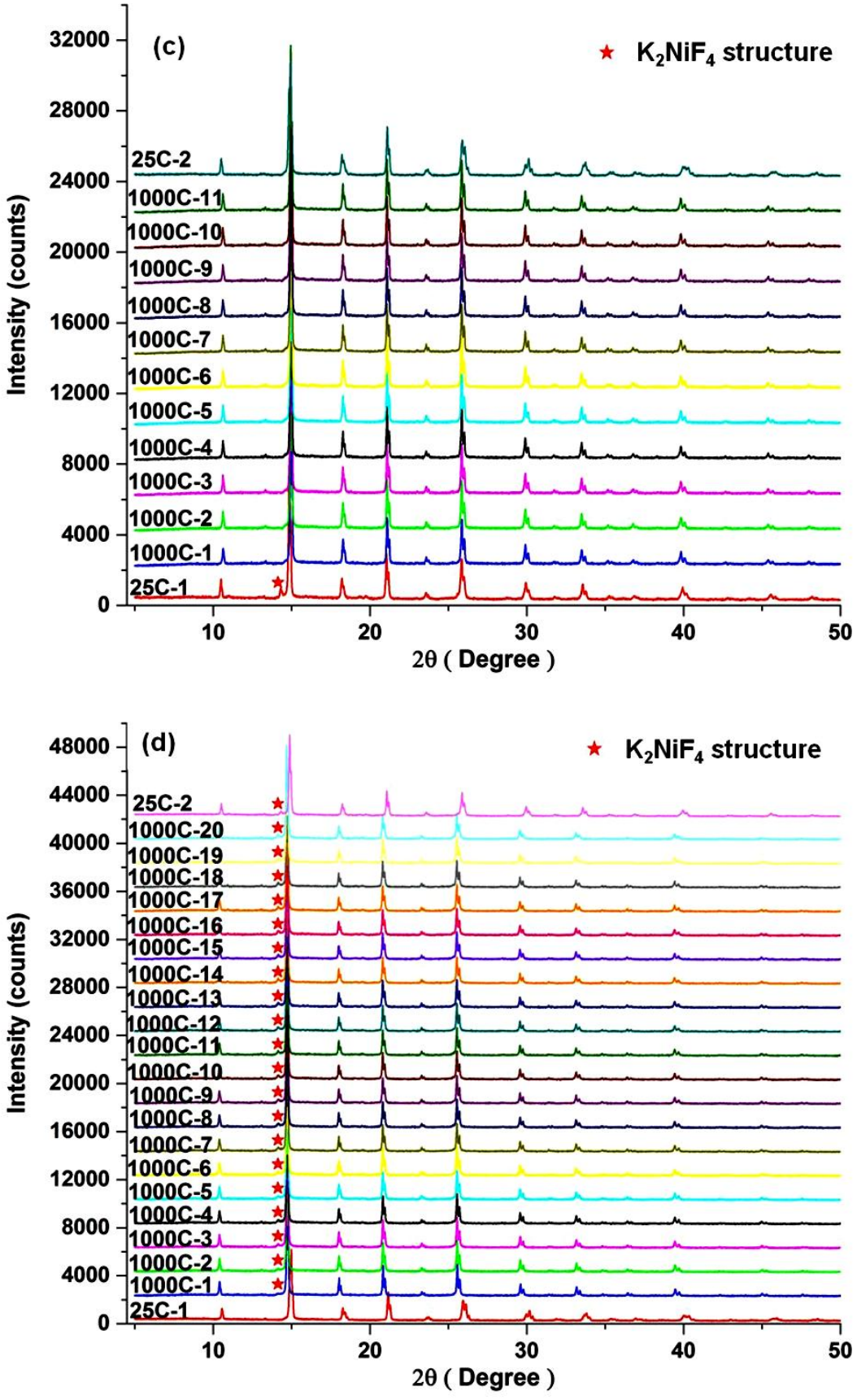

Figure 6-11 In situ VT-XRD of as prepared LSCM at 1000 °C under different atmospheres: a. heating LSCM in air, b. reduction of LSCM, c. re-oxidation of LSCM, d. re-reduction of LSCM

After refining the XRD patterns, the change of the unit cell parameters of ruthenium coated LSCM and as prepared LSCM throughout the experiment is shown in Figure 6-12. According to Figure 6-12 section a, the unit cells of ruthenium coated LSCM and as prepared LSCM both expanded quickly during the first 4 hours of heating, especially the as prepared LSCM. After that, the unit cell parameters of both samples increased at a much slower speed. The unit cell parameters of ruthenium coated LSCM are generally larger when compared to those of as prepared LSCM. It seems that ruthenium entered the perovskite very quickly at the beginning of the heating, therefore causing the unit cell of ruthenium coated LSCM to be larger than that of uncoated LSCM (Ru^{4+} = 0.62 Å (CN = 6) > Cr^{3+} = 0.615 Å (CN = 6) > Mn^{3+} = 0.58 Å (CN = 5) > Mn^{4+} = 0.53 Å (CN = 6)) [240, 241]. Since ruthenium entered the LSCM perovskite and took up space in the unit cell of LSCM at the beginning of the experiment, there was less free space for the ruthenium coated LSCM to expand in comparison to the uncoated LSCM. This explains why the unit cell of as prepared LSCM grew faster at the beginning of the experiment than that of ruthenium coated LSCM. According to section b of Figure 6-12, the differences between the unit cell parameters of the ruthenium coated LSCM and uncoated LSCM became much smaller when the samples were being reduced. This indicated that the Ru had exsolved from the LSCM perovskite and so the unit cells of both samples were closer in size. Interestingly, when the samples were re-oxidised, the unit cell parameter of the ruthenium coated LSCM became smaller than that of the uncoated LSCM (see Figure 6-12 section c). This may indicate that the ruthenium did not go back into the perovskite during re-oxidation [242]. Hence, the unit cell of ruthenium coated LSCM expanded by the Ru catalyst started shrinking when the sample was re-oxidised. Even if the sample gained oxygen while heating in air, the oxygen gained by the perovskite was not enough to make up for the volume loss caused by the absence of ruthenium. As a result, the unit cell of ruthenium coated LSCM became smaller than that of uncoated LSCM. Upon re-reduction, the unit cell parameter of ruthenium coated LSCM again became larger than that of uncoated LSCM (see Figure 6-12 section d). In addition, the differences in the unit cell parameters of the two samples became larger as the samples were reduced for longer, suggesting that the ruthenium coated LSCM had better reducibility.

Throughout the course of the experiment the changes in the unit cell parameters were monitored for both samples at room temperature (see Figure 6-12 section e). It can be

noted that, after heating in air for the first time, the unit cell parameters of ruthenium coated LSCM became larger than those of uncoated LSCM. This agrees with the trend of unit cell parameters changes of both samples at high temperature, confirming that the ruthenium did enter the LSCM perovskite. After reduction, the unit cell parameters of ruthenium coated LSCM became smaller than those of the uncoated LSCM, indicating that the ruthenium did exsolve from the perovskite. After re-oxidation, the unit cell parameters of both samples became the same, suggesting that the exsolved Ru did not go back into the perovskite. After re-reduction, the changes in the unit cell parameters are the same as those of the samples after the first reduction, with the unit cell parameters of the ruthenium coated LSCM becoming smaller than those of the uncoated LSCM. It is worth pointing out that, after both reductions, the above trends at room temperature were different from the trends observed at high temperature in reducing atmosphere. The reason for this phenomenon might be due to the fact that the ruthenium separated from the ruthenium coated LSCM during the reduction. The vacancies left by ruthenium in the perovskite allowed more free space for the perovskite to expand at high temperatures. When the temperature of the sample dropped, the unit cell of the ruthenium coated LSCM also shrank more because of the vacancies. Therefore the unit cell parameter of the ruthenium coated LSCM was smaller than that of the uncoated LSCM at room temperature.

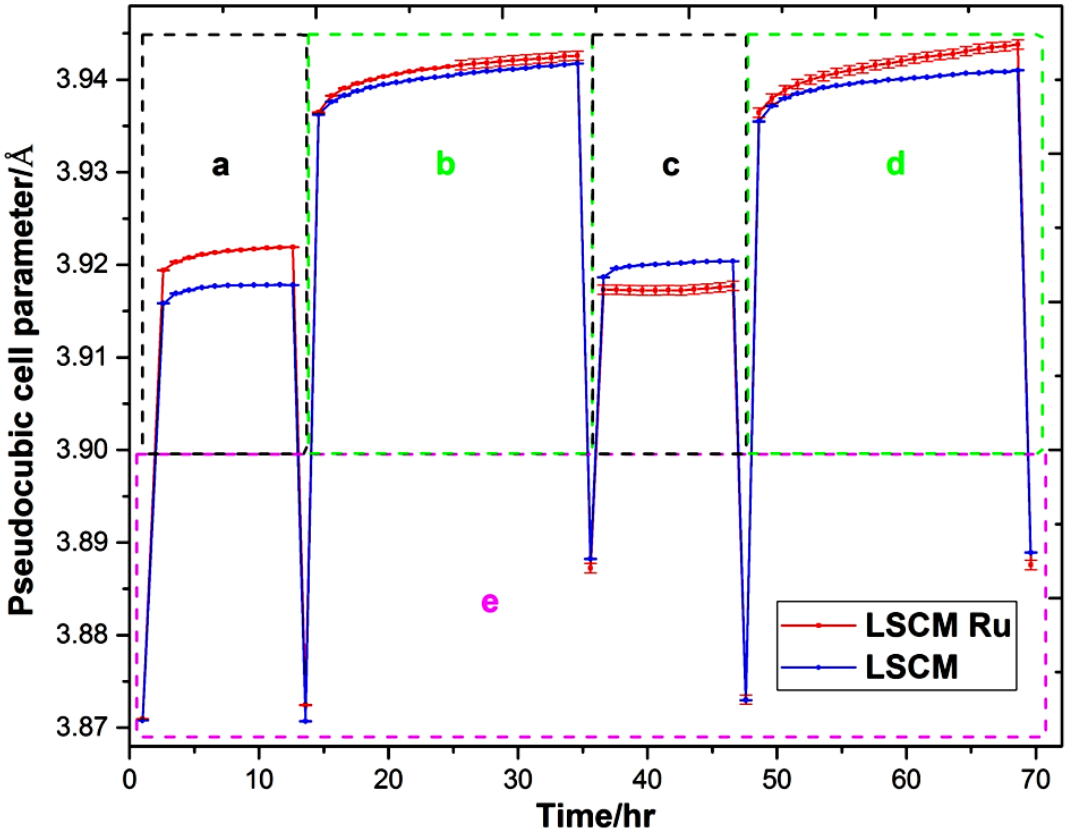

Figure 6-12 The change of the pseudo cubic unit cell parameters of the ruthenium coated LSCM perovskite and as prepared LSCM perovskite throughout the experiment in VT-XRD: a. the samples were heated in air at 1000 °C for 11h; b. the samples were reduced in 5% H_2 at 1000 °C for 20 h; c. the samples were re-oxidised in air at 1000 °C for 11h; d. the samples were re-reduced in 5% H_2 at 1000 °C for 20 h; e. the unit cell parameter change of the samples at room temperature

According to the VT-XRD results, it seemed that it took 4 hours for ruthenium to completely enter the LSCM perovskite grains at 1000 °C. Once the ruthenium exsolved from the perovskite in reducing atmosphere, it seemed unable to re-dissolve into the perovskite lattice when it was again exposed in air at the same temperature. In order to confirm this result, the morphology of the ruthenium coated sample was first checked by SEM (see Figure 6-13). According to Figure 6-13a, the surface of the LSCM perovskite was clean after it was coated with ruthenium catalyst at high temperatures. After reduction, it seemed that there were some nanoparticles on the surface of the perovskite (see Figure 6-13b). However, it was difficult to see them clearly. After re-oxidation, the surface of the perovskite became clear again, suggesting that either ruthenium had diffused back into the perovskite or it had become ruthenium oxide on the surface of the perovskite (see Figure 6-13c). Since the particle sizes of the LSCM perovskite and exsolved ruthenium catalyst were very small, it was difficult to tell from

the SEM result. There seemed to be small amount of particles on the surface of the perovskite after re-reduction (see Figure 6-13d). Unfortunately, due to the small size of the LSCM perovskite particles, it was difficult to confirm the presence of ruthenium nano particle exsolution.

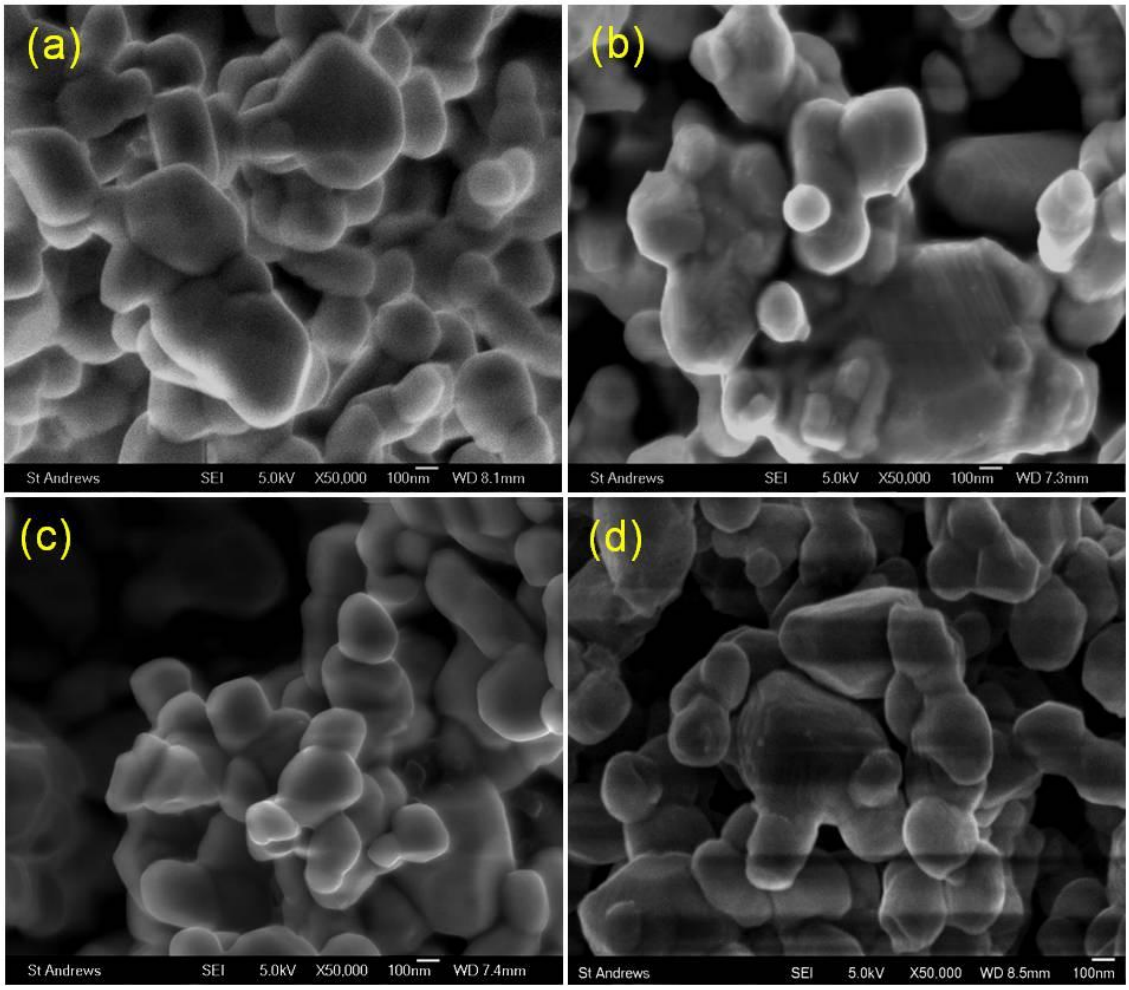

Figure 6-13 SEM images of ruthenium coated LSCM under different experimental treatment: a. fired in air, b. after reduction, c. after re-oxidation, d. after re-reduction

In order to confirm the composition of the particles on the surface of the perovskite after reduction, the sample was studied by TEM (see Figure 6-14). The surface of the sample was clear after heating in air according to Figure 6-14a. After reduction, nanoparticles of ruthenium can be observed on the surface of the LSCM perovskite (see Figure 6-14b). This agrees well with the results of the VT-XRD and SEM analyses. After re-oxidation, no particles were observed on the surface while, according to the VT-XRD result, it seemed that ruthenium nanoparticles did not go back into the perovskite after re-oxidation (see Figure 6-14c). More experiments are needed to determine whether or not

exsolved ruthenium nanoparticles are able to re-dissolve into the perovskite upon re-oxidation. After re-reduction, the Ru nanoparticles showed up again on the surface of the LSCM perovskite (see Figure 6-14d). The sizes of the ruthenium particles did not increase upon further reduction, which is in agreement with the fact that exsolved particles generally possess better long term stability in reducing atmospheres [81, 243].

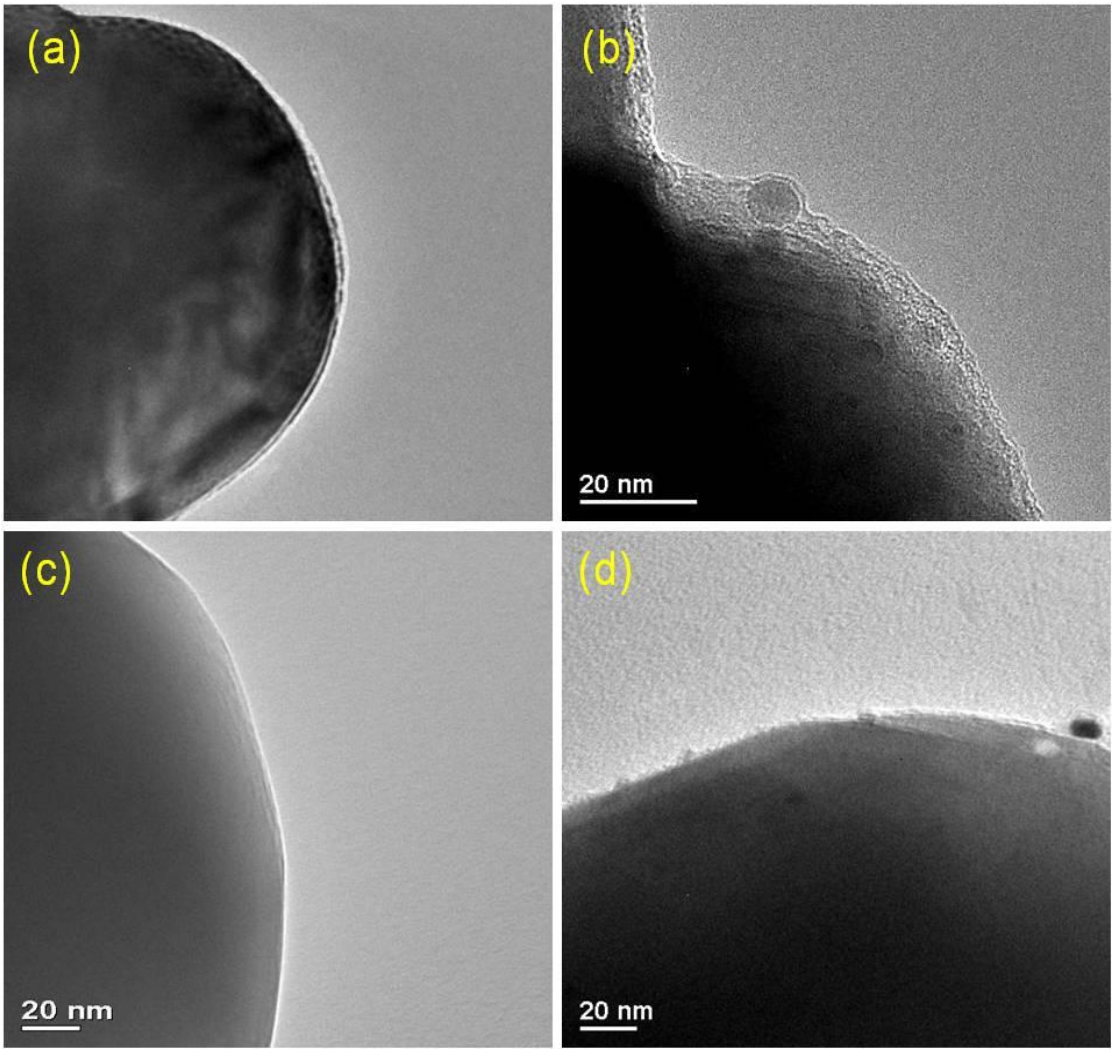

Figure 6-14 TEM images of the ruthenium coated LSCM under different experimental treatment: a. fired in air, b. after reduction, c. after re-oxidation, d. after re-reduction

In order to better understand the process of ruthenium coating LSCM, the ruthenium coated LSCM and uncoated LSCM were also studied by TGA with the same heating program as the *in situ* VT-XRD experiment (see Figure 6-15). When the samples were heated in air, the weight of ruthenium coated LSCM increased before the temperature reached 1000 °C, while there was a slight weight loss for the as prepared LSCM. However, when the temperature reached 1000 °C, the weight of the ruthenium coated

LSCM decreased, while there was no obvious change in the weight of the uncoated LSCM perovskite throughout the heating at high temperature. This might be caused by the partial evaporation of ruthenium oxide at high temperature due to its volatile nature. After the samples were cooled down to room temperature, a weight loss of 0.38 wt% for ruthenium coated LSCM was observed and the weight of uncoated LSCM stayed almost the same. Despite the fact that both samples lost weight when they were heated up in 5% H_2, the rate of the weight loss of the ruthenium coated LSCM was much faster than that of uncoated LSCM. When the temperature reached 1000 °C, the rate of the weight loss for both samples became much slower, suggesting that the reduction of both samples were very fast processes during the first few hours. A weight loss of 2.75 wt% for ruthenium coated LSCM and 1.39 wt% for as prepared LSCM was observed after the reduction. Obviously, the ruthenium coated LSCM lost more oxygen during the reduction, indicating that the ruthenium coated LSCM had better reducibility than uncoated LSCM.

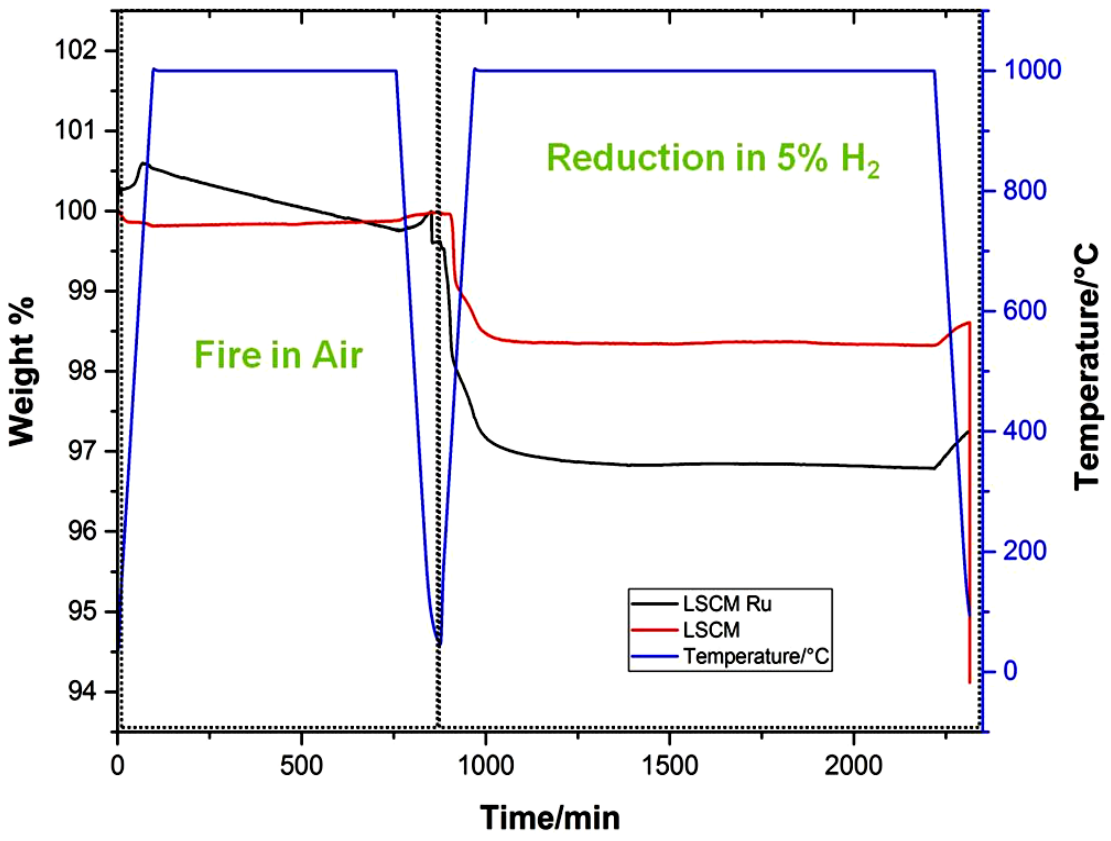

Figure 6-15 TGA of ruthenium coated LSCM and as prepared LSCM during heating in air and heating in 5% H_2

6.7 Discussions and Conclusions

In this chapter, the possibility of coating ruthenium into the LSCM perovskite with the aid of a ball milling method has been explored via VT-XRD. It has been found that the ruthenium started to enter the grains of LSCM perovskite at around 900 °C. There was no obvious structural change in the ruthenium coated LSCM perovskite when heating in air at different temperatures. When the ruthenium coated sample was reduced at different temperatures, a 2nd phase which has the K_2NiF_4 structure was observable in the perovskite from 600 °C and up. Combined with the result of TEM and EDX, it can be confirmed that the ruthenium catalyst was able to diffuse into the LSCM perovskite upon heating in air and exsolve as nanoparticles after reduction. The reason that ruthenium was able to exsolve from LSCM rather than LSGT as shown in the previous chapter might be due to the difference between the host lattices of the two perovskites. Since Mn on the B-site of LSCM is able to adopt lower coordination environment, the oxide ion mobility is higher than that in LSGT, where 6-fold coordination environment is strongly preferred. As a result, there are more hopping sites for ruthenium cations in LSCM, thus making it easier for ruthenium to exsolve from the perovskite lattice.

When the ruthenium coated LSCM was heated at 1000 °C to investigate the mechanism of ruthenium doping the LSCM perovskite from the surface, it seemed that the process of ruthenium entering the perovskite lattice was very fast. The unit cells of both coated and uncoated LSCM became larger within the first four hours when they were heated in air at 1000 °C, and they remained almost unchanged even when they were heated for longer. During reduction, it has been confirmed that the presence of the 2nd phase which had the K_2NiF_4 type structure was not caused by ruthenium doping, as the same 2nd phase was also found in the uncoated LSCM. It seemed that the exsolved ruthenium particles did not re-dissolve into the perovskite upon re-oxidation according to the VT-XRD result, while the TEM result showed that there were no ruthenium particles on the surface of the LSCM perovskite after re-oxidation. Further experiments need to be performed in order to confirm whether ruthenium had re-dissolved into the LSCM perovskite or not. The ruthenium nanoparticles observed after re-reduction still remained the same size as the ones after the initial reduction and did not grow bigger as had been observed when the catalyst was impregnated onto the perovskite. In addition,

it has been found that the ruthenium coated LSCM showed better reducibility than the uncoated LSCM.

Chapter 7

Coating $La_{0.75}Sr_{0.25}Cr_{0.5}Mn_{0.5}O_3$ (LSCM) with palladium catalysts

7.1 Introduction

In the previous chapter, the possibility of coating a ruthenium catalyst into LSCM perovskite was demonstrated. It seemed that the perovskite defects and the ball milling process promoted the catalyst to diffuse into the perovskite. This chapter will study the possibility of coating a palladium catalyst into LSCM perovskite using the same coating method that was described in Chapter 6. In addition, oxygen was also applied when coating the LSCM perovskite with palladium at high temperatures, since a more oxidising atmosphere would help maintain palladium in the form of oxide, thus helping the palladium to diffuse into the LSCM perovskite. The possibilities of synthesizing palladium containing LSCM perovskite $La_{0.75}Sr_{0.25}Cr_{0.5}Mn_{0.49}Pd_{0.01}O_{3-\delta}$ (LSCMP) and exsolving Pd from the perovskite have also been investigated. The structures of the samples were studied using a STOE X-ray diffractometer with a Cu-Kα X-ray source at room temperature, while the morphologies of the samples were studied by either SEM or TEM. EDX was used for some samples to identify their chemical compositions.

7.2 Experimental section

7.2.1 Coating procedure

The coating procedure was the same as was described in section 2.5 of chapter 2, apart from the use of a tube furnace instead of a VT-XRD instrument to heat the samples after pre-treatment. When each sample was heated in air, it was heated at 1000 °C for 11 h employing the same heating program as for the ruthenium coated LSCM. When the samples were heated in oxygen, they were heated at 700 °C - 1300 °C for 12 h (heating rate 5 °C/min). The palladium catalyst used to coat the LSCM perovskite was in the form of palladium nitrate solution and the weight percentage of Pd used for coating was 1.14 wt% with regards to the LSCM.

7.2.2 Synthesis of LSCMP

LSCMP was prepared using the same combustion method as mentioned for LSCM in section 2.2 of chapter 2. The precursor powder was calcined at 1000 °C and 1100 °C for

8 h to form the desired structure (heating rate 5 °C/min) respectively. The purity of the sample was examined using a STOE X-ray diffractometer with a Cu-Kα X-ray source.

7.2.3 Reduction

The reductions of all of the samples in this chapter were carried out at 1000 °C for 24 h in 5% H_2 in a tube furnace (heating rate 5 °C/min).

7.3 Coating LSCM with palladium in air investigation

Using the same coating procedure as for the ruthenium coated LSCM, the palladium coated LSCM was studied by XRD after it was heated in air for 11 h. The XRD pattern of the sample is shown in Figure 7-1. Compared to as prepared LSCM, a PdO peak was observed in the XRD pattern of the palladium coated LSCM after it was fired in air. After refining the data, there was a slight increase in the pseudo unit cell parameter of the palladium coated sample which indicated that there might be some palladium diffused into the perovskite grains (a_p (LSCMPd) = 3.8722, a_p (LSCM) = 3.8720). In order to confirm whether or not any palladium had diffused into the LSCM perovskite while heating in air, the morphology of the sample was studied by SEM as shown in Figure 7-2. According to the picture, there were fewer palladium oxide particles on the surface of the perovskite than expected, considering the obvious peak of PdO that was observed in the XRD pattern. This might be due to the fact that LSCM perovskite was in the form of a very fine powder. Therefore, it did not have as large perovskite grains as LSGT10 perovskites in chapter 4, which had enough surface area for PdO particles to be seen more easily in SEM.

After the sample was reduced in 5% H_2, it was studied by TEM to see if any palladium nano particle exsolution had taken place (see Figure 7-3). According to the TEM result, no palladium nano particle exsolution was found on the surface of the perovskite. The palladium particles observed in the experiment were almost 200 nm in size. They seemed more like particles deposited on the surface of the LSCM which had agglomerated after heating over an extended period of time instead of having exsolved from the lattice of the perovskite [122, 244]. Therefore, it seemed that the palladium catalyst had not dissolved into the perovskite while heating in air. The reason for this

might be that the palladium existed in the form of palladium oxide after the LSCM coated with palladium nitrate was heated at low temperature. However, palladium oxide will start to decompose to palladium metal at above 750 °C in air and the process is reversible once the temperature decreases [245]. The palladium oxide may not have started dissolving into the LSCM perovskite lattice before it decomposed to metal. Once the palladium oxide became palladium metal at high temperatures, it became even more difficult for it to enter the LSCM perovskite grains, as has been observed in the case of ruthenium metal in the previous chapter. Therefore, the palladium catalyst stayed in the form of metal on the surface of the sample throughout the heating at high temperatures in air. After the sample was cooled down, palladium metal became an oxide again, which explains why the PdO was observed in the XRD pattern.

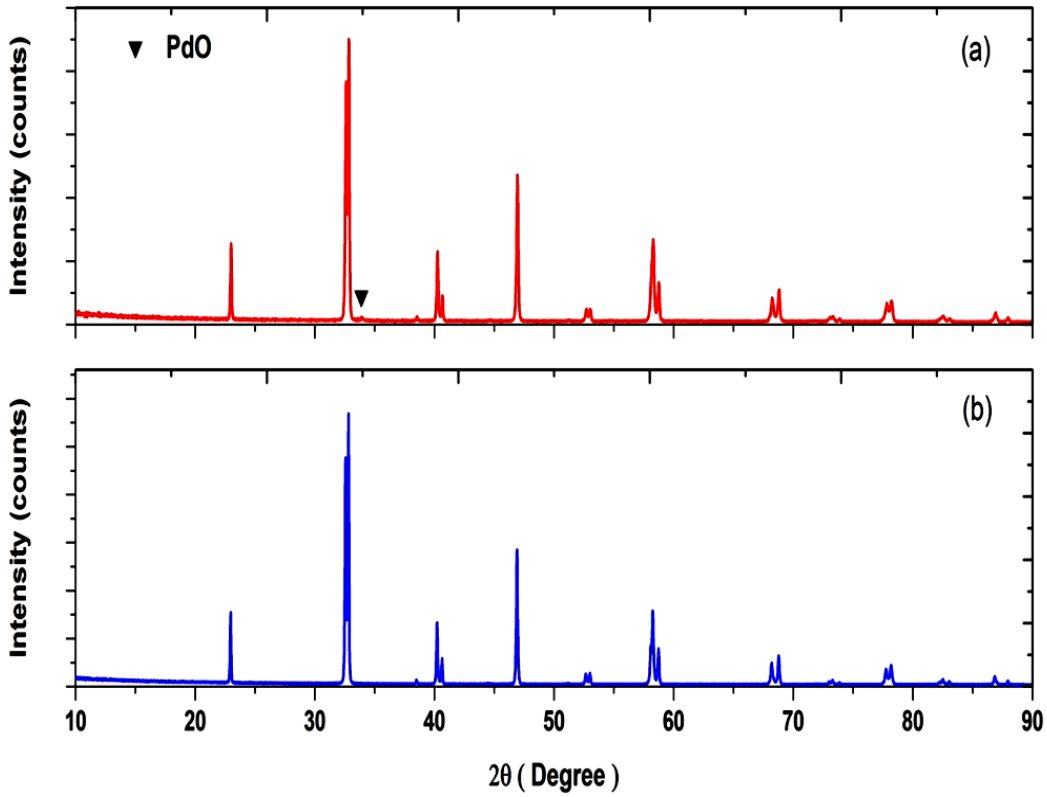

Figure 7-1 XRD patterns of LSCM perovskite: (a) coated with palladium catalyst at 1100 °C in air, (b) as prepared LSCM

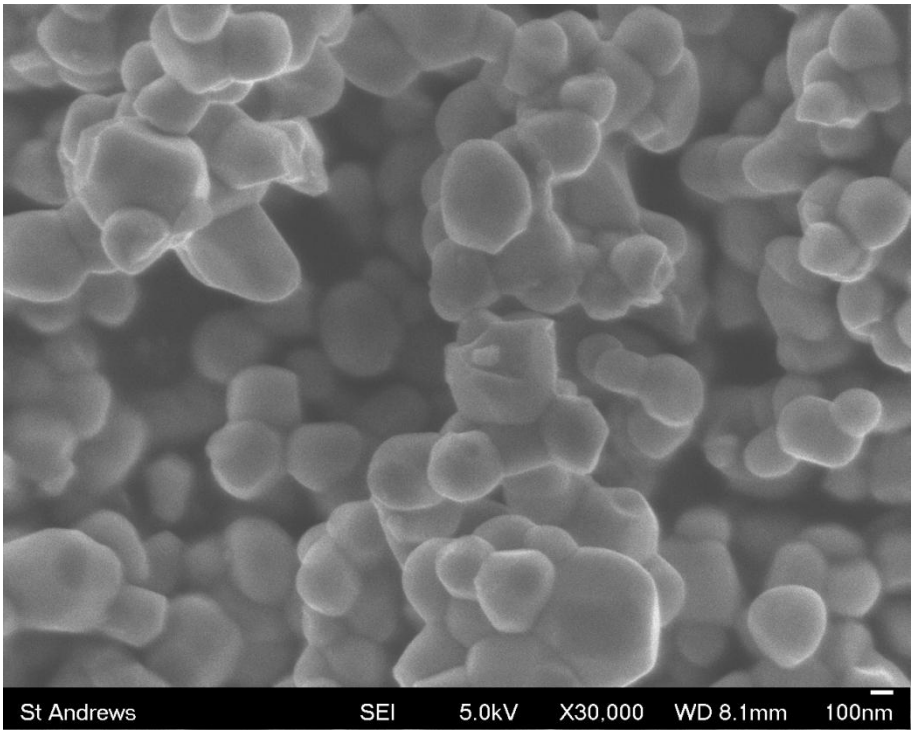

Figure 7-2 SEM image of LSCM coated with palladium at 1100 °C for 8h in air

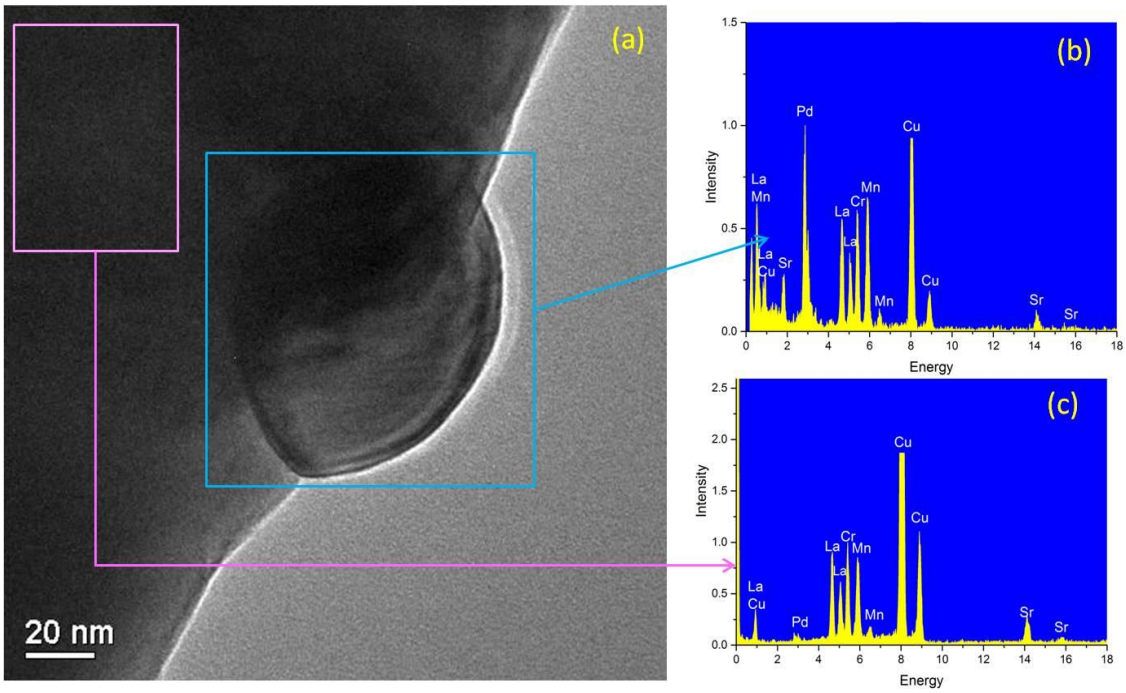

Figure 7-3 TEM and EDX image of LSCM coated with palladium at 1100 °C in air after reduction

7.4 Investigation of coating LSCM with palladium in oxygen atmosphere

The fact that palladium oxide decomposed to palladium metal when it was being heated

at high temperatures seemed to make it more difficult for palladium to dissolve into the LSCM perovskite. A similar phenomenon was also noticed when LSGT perovskite was coated with palladium oxide in Chapter 4. For that reason, the coating atmosphere was changed to oxygen since a higher oxygen partial pressure would help maintain the stability of PdO at high temperatures. Moreover, lower coating temperatures (700 °C and 900 °C) and higher coating temperatures (1300 °C) were also investigated, since it is more likely for palladium to stay in the form of oxide at lower temperatures, and higher temperatures will increase the reactivity of the sample which may promote the diffusion of the palladium into the perovskite.

The XRD patterns of the LSCM coated with palladium in oxygen at different temperatures are shown in Figure 7-4. According to the XRD patterns, the perovskite maintained its structure throughout the process of heating in oxygen and PdO was observed in the XRD patterns of every sample. When the sample was coated at 700 °C, the intensities of the peaks of the PdO were smaller compared to the ones for the samples which were coated at 900 °C and 1100 °C. This may be due to the fact that the palladium oxide was not crystallized enough at this temperature. When the sample was coated at 1300 °C, the intensities of the PdO peaks became small again. This may be due to the fact that more palladium had diffused into the perovskite lattice at this temperature.

Figure 7-5 shows the XRD patterns of the samples after they were reduced. According to the XRD results, the structure of the perovskite changed from rhombohedral to primitive cubic structure after reduction, which was in agreement with the literature [238]. In addition, 2^{nd} phases of MnO and $La_{0.6}Sr_{1.4}MnO_4$ (Ruddlesden–Popper structure, K_2NiF_4) were observed in the XRD patterns of all of the samples, regardless of their coating temperatures. The appearance of the 2^{nd} phases in the reduced sample is expected, and MnO should be the result of a phase segregation from the K_2NiF_4 spinel phase [238]. Moreover, the positions of the $La_{0.6}Sr_{1.4}MnO_4$ peaks shifted as the coating temperature changed.

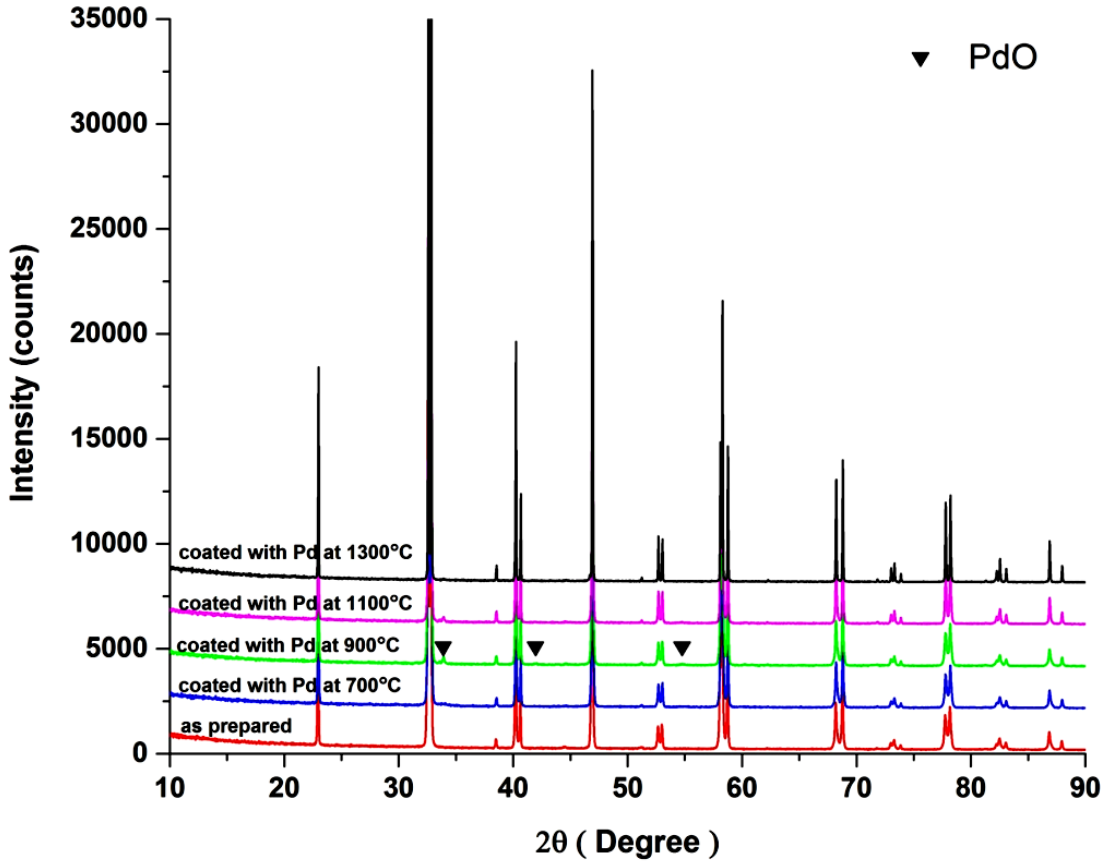

Figure 7-4 XRD patterns of LSCM perovskite coated with palladium catalyst in O_2 for 12 h at different temperatures

It seemed that it was the more oxidising environment, rather than the high temperature, caused the phase separation from the LSCM perovskite, since the intensities of the peaks were higher when the sample was coated at low temperatures. The presence of MnO in the XRD pattern supports the above point. In addition, Yokokawa *et al* compared the thermodynamic stability of perovskites and their related compounds, and reported the possibility of the co-existence of the AMO_3, A_2MO_4, and A_2O_3 (or MO) in the A^{III}-M-O system. This is under the condition that the enthalpy of formation of perovskites (δ_p) is larger than that of A_2MO_4 (δ_K), in conjunction with the condition that δ_p, $\delta_K < 0$ [246]. Therefore, the presence of the perovskite sample together with MnO and $La_{0.6}Sr_{1.4}MnO_4$ (K_2NiF_4 structure) might be due to the fact that the stabilization energy of LSCM perovskite is larger than $La_{0.6}Sr_{1.4}MnO_4$. Correspondingly, it was thermodynamically favourable for them to co-exist under the experimental condition.

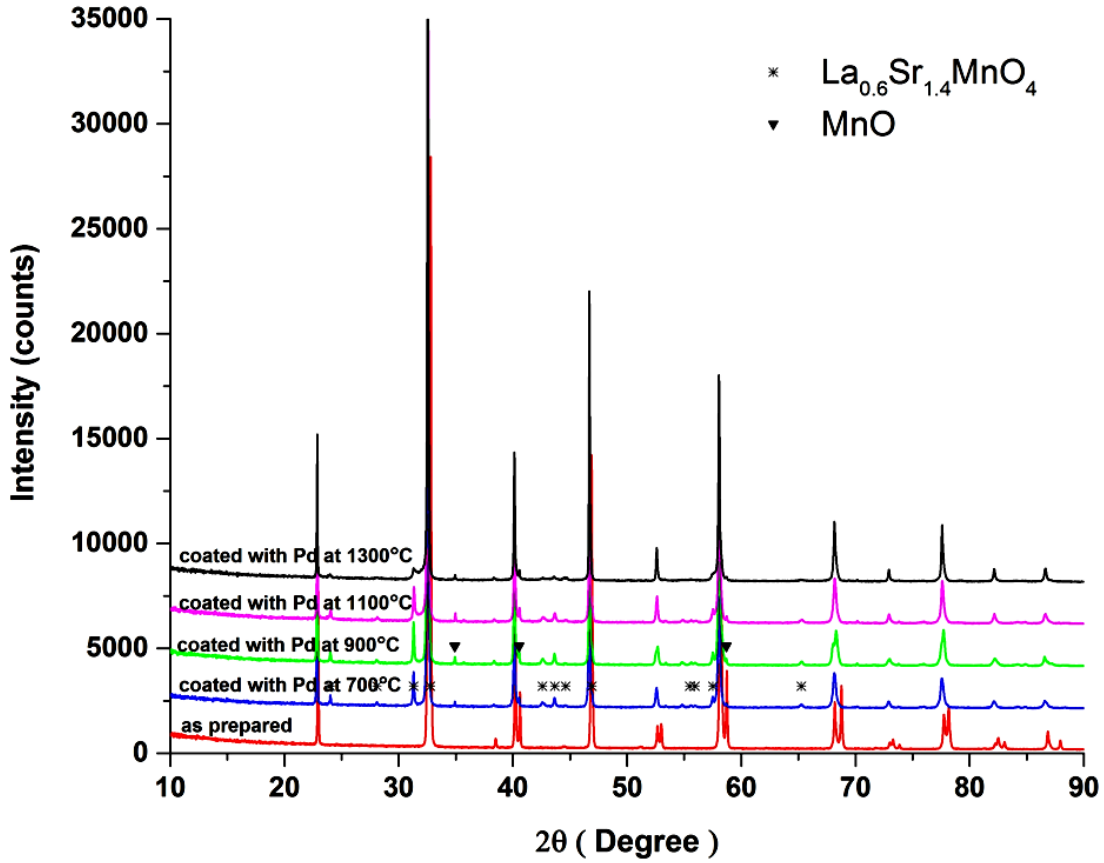

Figure 7-5 XRD patterns of LSCM perovskite coated with palladium catalyst in O_2 for 12 h at different temperatures after reduction

After refining the XRD data, the changes in the unit cells of the samples corresponding to the different environments were compared in the form of pseudo cubic unit cell parameters a_p (see Figure 7-6). According to the graph, there was very little change in the unit cell parameters of the samples after they were coated with palladium in oxygen at different temperatures. After reduction, the differences between the unit cell parameters of the samples coated at different temperatures was also very small. The volume of the sample increased by 1.2-1.3% after reduction, which was smaller than the reported volume change of as prepared LSCM [238]. This might be due to the decomposition of the perovskite caused by the reduction treatment.

Since the XRD peak position of the Pd metal overlapped with the LSCM, it is difficult to tell if there was any palladium exsolution by looking at the XRD patterns. According to the unit cell parameter data, there was also very little change observed, which could not provide enough information to confirm whether or not the palladium had exsolved from the perovskite. A better way to investigate any possible palladium exsolution was

to study the morphology of the sample. The surface of the LSCM coated with palladium after reduction was studied by SEM as shown in Figure 7-7. According to the SEM images, the palladium catalyst particles observed on the surface of the perovskite were generally very large and there was no nano particle exsolution observed. It seemed that the palladium was still not able to dissolve into the lattice of LSCM perovskite, even in an oxidising environment. This may be due to the same reason as when LSCM was coated with palladium in air: the palladium oxide decomposed to palladium metal before it started entering the perovskite grains. Since palladium metal is non-reactive with LSCM perovskite, the palladium metal ended up adhering to the surface of the LSCM perovskite and became an oxide again after the sample cooled down [247, 248]. As a result, the palladium did not enter the LSCM perovskite by the coating method, which also explains why there was very little change in the unit cell parameters of the perovskite even if the sample was coated with palladium at different temperatures.

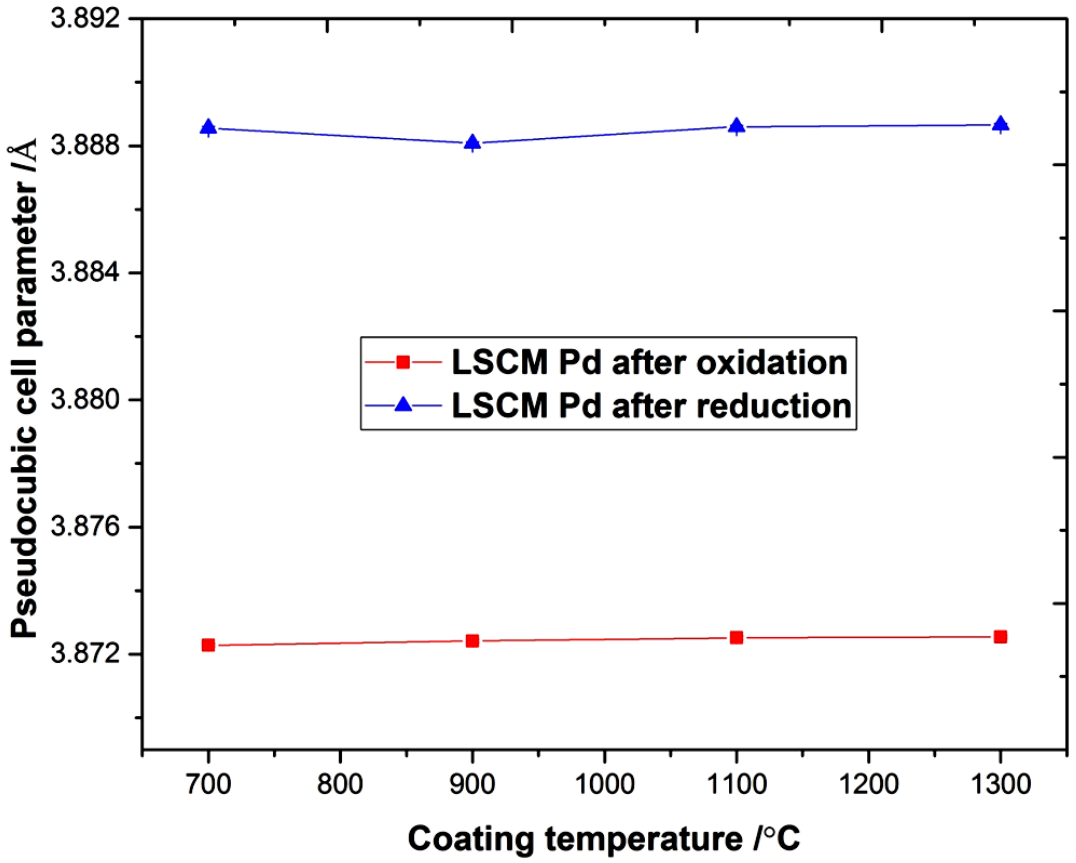

Figure 7-6 The change of the pseudo cubic unit cell parameters of LSCM perovskite coated with palladium at different temperatures in oxygen and after reduction

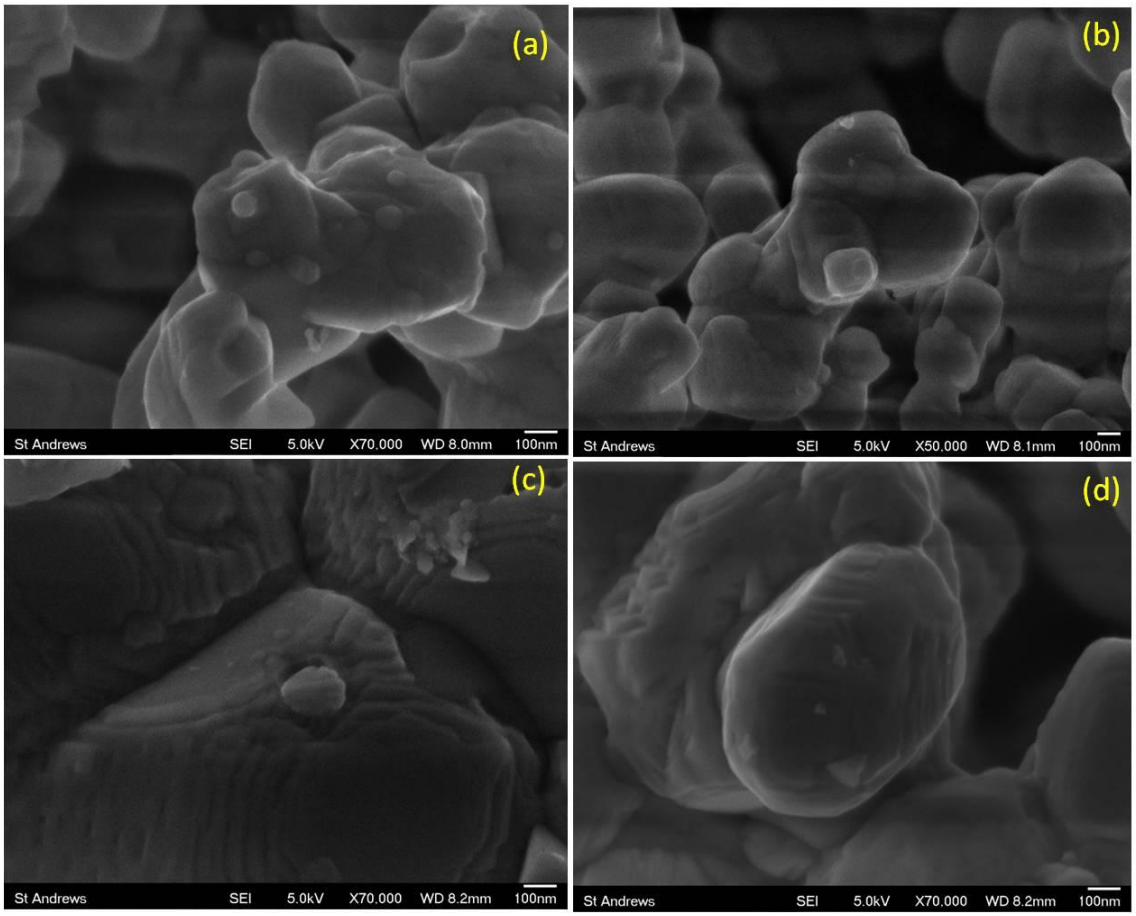

Figure 7-7 SEM images of LSCM perovskite coated with palladium in O_2 at different temperatures after reduction: a. 700 °C , b. 900 °C , c.1100 °C , d. 1300 °C

7.5 Synthesis of $La_{0.75}Sr_{0.25}Cr_{0.5}Mn_{0.49}Pd_{0.01}O_{3-\sigma}$ and investigation of Pd exsolution

Although palladium did not enter the LSCM perovskite grains by the coating method, it is still worth investigating whether or not it is possible for palladium to be doped on the B-site of the LSCM perovskite. In order to answer the question, perovskite with the nominal stoichiometry of $La_{0.75}Sr_{0.25}Cr_{0.5}Mn_{0.49}Pd_{0.01}O_{3-\sigma}$ (LSCMP) was synthesised by the combustion method. The XRD patterns of the LSCMP precursor which was fired at 500 °C and when it was calcined at 1000 °C and 1100 °C are shown in Figure 7-8. According to the XRD patterns, the perovskite had already started to crystallize at 500 °C since the sample showed peaks of the perovskite, even if they are quite wide. When the LSCMP was fired at 1000 °C, it had formed the rhombohedral structure with $La_2Pd_2O_5$ present as a 2^{nd} phase. When the sample was heated at higher temperature, there was no obvious structural change observed in its XRD pattern compared to the

one synthesised at 1000 °C.

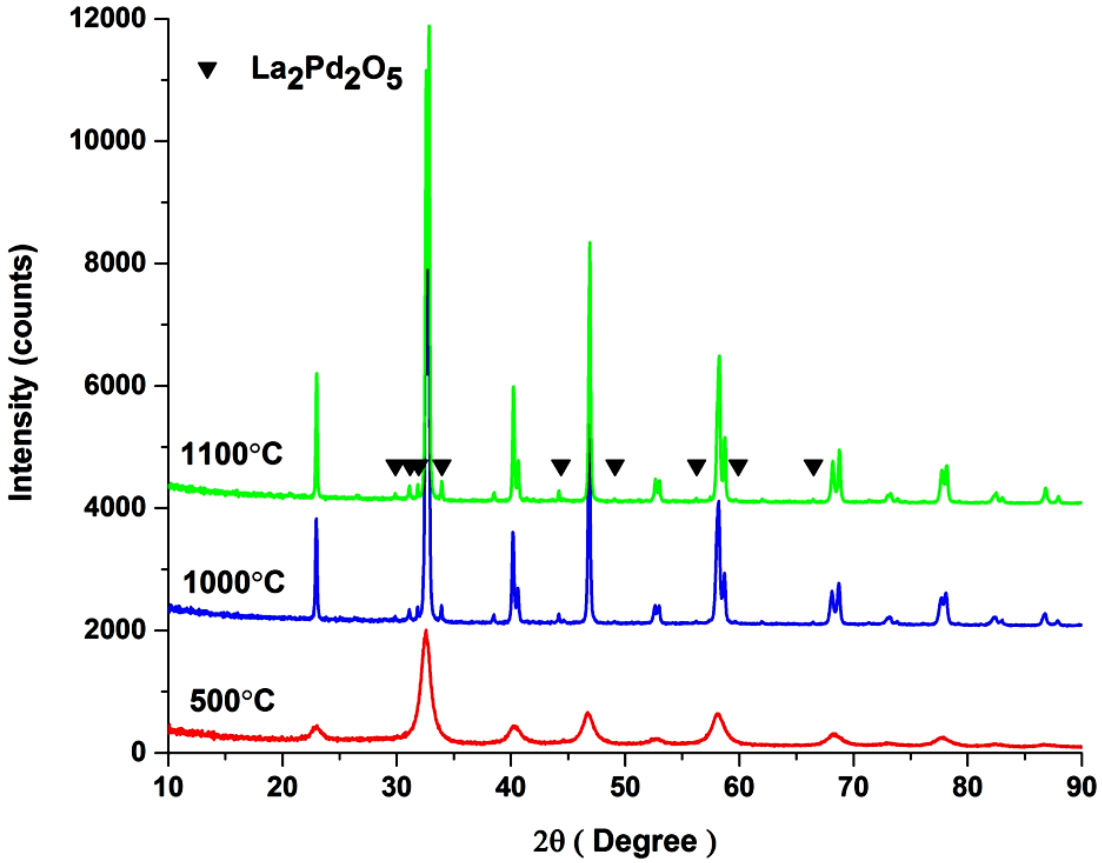

Figure 7-8 Room temperature XRD patterns of the precursor of LSCMP, LSCMP synthesised at 1000 °C and LSCMP synthesised at 1100 °C in air

Table 7-1 lists the unit cell parameters of LSCMP heated at different temperatures after refinement of the XRD data. Both of the synthesised samples had rhombohedral structures. It was discovered that, when the LSCMP was calcined at 1000 °C, there was 0.042 mol $La_2Pd_2O_5$ formed per mole of LSCMP. It seemed that the majority of the palladium formed $La_2Pd_2O_5$ with La, indicating that the formation of $La_2Pd_2O_5$ was more favourable for palladium when forming a solid solution with different cations. This was confirmed by comparing the unit cell parameters of LSCMP synthesised at different temperatures and the quantity of $La_2Pd_2O_5$ 2nd phase generated at different temperatures. As the firing temperature increased, the unit cell of the sample became smaller. The reason for this phenomenon may be due to the fact that there was more $La_2Pd_2O_5$ (0.045 mol) formed when the sample was calcined at 1100 °C, thus leaving the rest of LSCMP with less La and potentially less Pd in the structure if the palladium was able to be doped into the lattice of the LSCMP perovskite. As a result, the unit cell

of LSCMP prepared at higher temperature showed smaller unit cell parameters.

Firing temperature / °C	Space group	Unit cell parameters (Å)	Unit cell volume (Å^3)	2nd phase
1000	R-3c	a= 5.50527(11) c = 13.33488(31)	350.008(13)	$La_2Pd_2O_5$
1100	R-3c	a = 5.50044(8) c = 13.32698(24)	349.186(10)	$La_2Pd_2O_5$

Table 7-1 Unit cell parameters of LSCMP calcined at different temperatures in air

The morphologies of the samples were also studied by SEM as shown in Figure 7-9. The synthesised perovskite samples showed similar morphologies to LSCM (see Figure 6-2), but with much smaller particle sizes, even when synthesised at the same temperature (see Figure 7-9a). When the sample was synthesised at a higher temperature (1100 °C), the particle size of the perovskite increased and the sample became more crystallized (see Figure 7-9b). There were no other different phases observed on the surface of the samples.

Even if it seemed that the majority of palladium formed $La_2Pd_2O_5$, it was still worth checking whether the rest of the palladium had formed a solid solution of LSCMP and was able to exsolve from the perovskite after reduction. In order to find the answer, the LSCMP which was synthesised at 1000 °C was reduced in 5% H_2 and then studied by TEM and EDS (see Figure 7-10). The particles observed on the surface of the sample were quite large in size and did not look like exsolved nanoparticles. Therefore, it seemed that the palladium was unable to occupy the B-site of LSCM perovskite system.

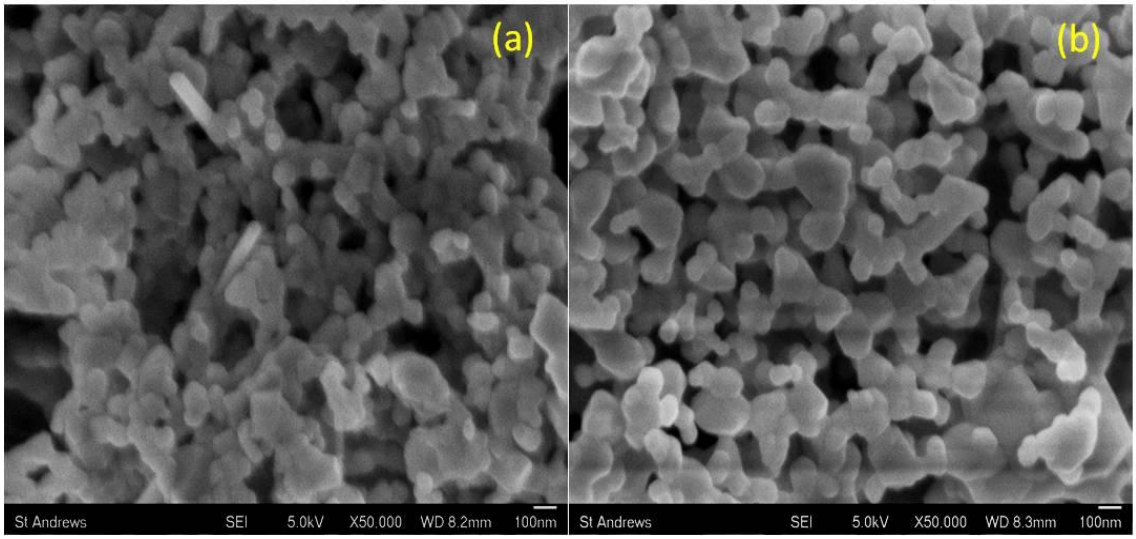

Figure 7-9 SEM images of LSCMP synthesised at different temperatures in air: a. 1000 °C, b. 1100 °C

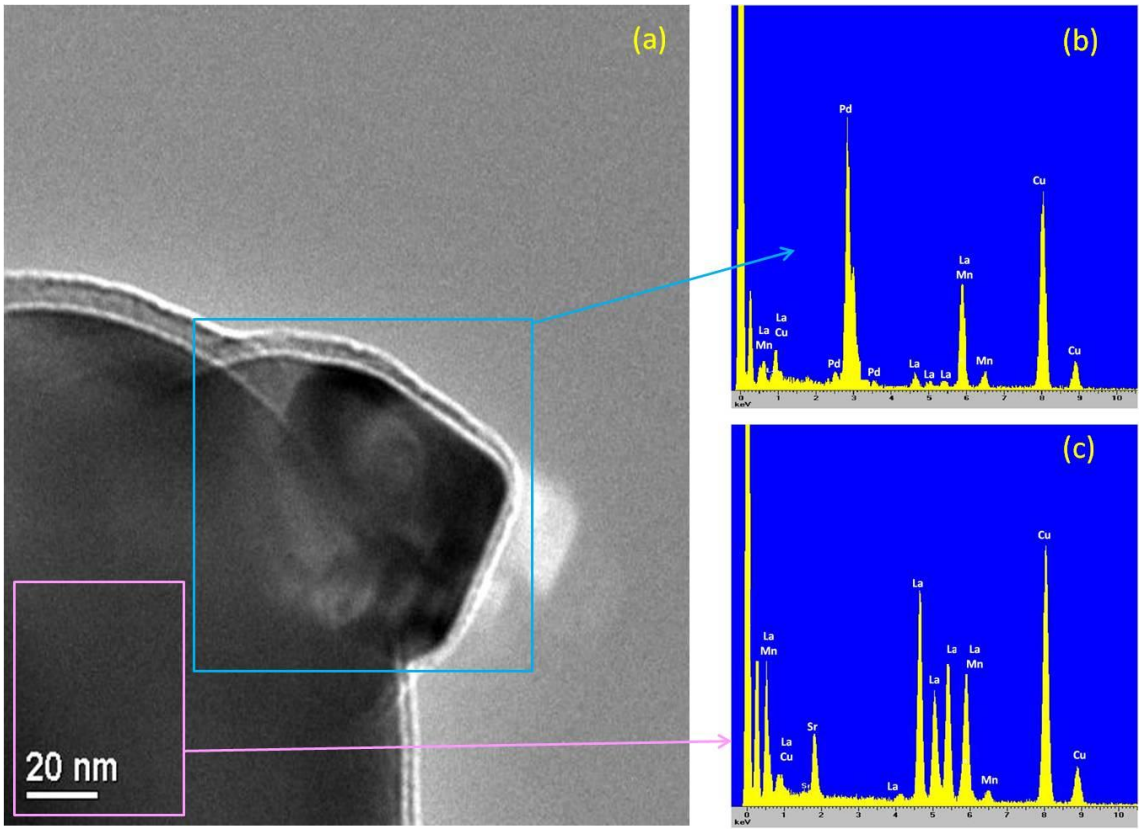

Figure 7-10 TEM and EDS of LSCMP synthesised at 1000 °C after reduction in 5% H_2

7.6 Discussion

According to the experimental results, it seemed that palladium was unable to be incorporated into the B-site of the LSCM perovskite. This was the case regardless of whether the LSCM was coated with Pd or the catalyst was one of the starting

components during the process of perovskite synthesis. However, in Chapter 4, it was demonstrated that palladium was able to enter the grains of the LSGT perovskite, and also form a solid solution with the A-site deficient titanate system. Palladium nano particle exsolution was also observed in the aforementioned chapter. So the question is why palladium was unable to fit into the B-site of LSCM based perovskite system.

One of the possible reasons to the above question is that the formation of the 2nd phase $La_2Pd_2O_5$ observed during the synthesis of LSCMP is more thermodynamically favourable, since the majority of the palladium added in the system formed the above 2nd phase. Another possible reason may be due to the fact that, in the LSCM system, Mn exists in the form of Mn^{3+}/Mn^{4+} on the B-site of the LSCM perovskite which increases the oxygen ion mobility in the perovskite. However, at the same time, Mn can adopt more than one type of coordination environment, meaning that the structure of the LSCM perovskite is not as rigid as an A-site deficient titanate system in which Ti strongly prefers 6-fold coordination. In order to fit palladium into the B-site of the perovskite, it requires square planar 4-fold coordination, which will eliminate more oxygen from the perovskite according to the result in Chapter 4. This requires the structure of the perovskite to be strong enough to withstand the oxygen loss from the system. Meanwhile, the LSCM system could not satisfy this requirement due to the flexibility of the Mn cation. As a result, it is difficult for palladium to be doped into the LSCM containing perovskite.

7.7 Conclusion

In this chapter, the possibility of coating palladium into the LSCM perovskite with the aid of the ball milling method has been investigated. Both air and oxygen atmospheres were explored when coating palladium into the LSCM perovskite at different temperatures. However, it seemed that palladium was unable to be incorporated into the LSCM perovskite *via* either of these methods.

In addition, the probability of doping palladium into the B-site of the perovskite with the composition of LSCMP has been explored. Instead of occupying the B-site of the perovskite, the majority of palladium formed 2nd phase with La during the process of combustion synthesis. The higher the synthesis temperature was, the more 2nd phase was

formed in the final perovskite. There was no palladium exsolution observed after reduction either, which confirmed indirectly that the palladium was unable to be incorporated into the B-site of the perovskite. This might be due to the fact that it required a more rigid perovskite structure for palladium to be doped into the perovskite, since it may involve changing the coordination environment of the cations of the perovskite.

Chapter 8

Catalysis test of LSGT10 perovskite coated with nickel catalyst

8.1 Introduction

In order to investigate the influence of the catalyst coating on the performance of the perovskite, RWGS catalysis tests were carried out using the samples as catalysts. Perovskites have been considered as potential catalysts for catalytic application due to their capability of alternating the catalytic and electrocatalytic properties by accommodating various cations on the A and B site. Kim *et al* has tested $BaZr_{0.8}Y_{0.16}Zn_{0.04}O_3$ as catalyst for RWGS reactions at 600 °C for 5h and reported a conversion rate of 37.5% for CO_2 and a 97% selectivity of CO [249]. Daza *et al* reported a CO_2 conversion rate of 25% when using $La_{1-X}Sr_XCoO_{3-\delta}$ ($0 \leq X \leq 1$ in steps of 0.25) as catalyst for chemical looping RWGS (RWGS-CL) reaction. According to the report, the best experimental condition for maximum CO generation was isothermal reduction at 500 °C and CO_2 conversion at 850 °C [161]. In their later report which incorporated Fe into the perovskite, $La_{0.75}Sr_{0.25}Co_{(1-Y)}Fe_YO_3$ (Y = 0, 0.5, 0.75 and 1), the conversion temperature was reduced by 300 °C with the conversion rate of 15% [161].

In this chapter, we mainly focus on the discussion of the experimental results to exemplify the effect of catalyst coating on the catalytic activity of LSGT10 perovskite for RWGS reaction. Due to the limitation of time, only a few samples tested as a preliminary investigation. More tests will be carried out in the future to further study the influence of the catalyst coating. Samples which were tested for LSGT10 series include as prepared LSGT10 (LSGT10 AP), LSGT10 coated with nickel catalyst at 1300 °C (LSGT10Ni) and after it was reduced at 930 °C in 5% H_2 for 20h (LSGT10Ni red). The reason to choose LSGT10 coated with nickel catalyst and after it was reduced was to find out in which form the catalyst coating worked better for improving the performance of the perovskite. For comparison purpose, as prepared LSGT10 was also tested under the same condition. For the same purposes, samples which were selected for LSCM series include as prepared LSCM (LSCM AP), LSCM coated with ruthenium catalyst at 1000 °C (LSCMRu) and after it was reduced at 1000 °C in 5% H_2 for 20h (LSCMRu red)

8.2 RWGS catalysis test result and discussion

Catalytic performances of all samples for the RWGS reaction were measured as a function of time. The catalysis test result of LSGT10 based perovskite samples is shown in see Figure 8-1. All samples showed 100% selectivity for CO. The CO_2 conversion rate when using as prepared LSGT10 as catalyst was increasing with time during the first hour of testing and peaked at 70.4%. Afterwards, it started to decrease slowly with time until the end of the test. Both LSGT10Ni and LSGT10Ni red showed much more stable catalytic activities than uncoated LSGT10. Both samples showed a quick rise in the catalytic activity during the first hour of testing. Then the CO_2 conversion rate of LSGT10Ni increased slowly with time, while LSGT10Ni red mostly stabilize at a fixed conversion rate during the rest of the experiment. The slow increase of the catalytic activity of LSGT10Ni might be caused by the fact that the LSGT10Ni was being reduced which might eventually also produce nickel nanoparticles during the experiment since there was excess H_2 in the gas mixture.

The average CO_2 conversion rates for the three samples during the test are 64.1% (LSGT10 AP), 79.7% (LSGT10Ni) and 86.6% (LSGT10Ni red). It suggests that the addition of nickel catalyst into LSGT10 perovskite has successfully increased the catalytic performance of LSGT10. On average, the conversion rate of CO_2 was increased by 15.6% when nickel catalyst existed in the perovskite lattice and 22.5% when nickel catalyst existed in the form of exsolved nanoparticles. Compared to the nickel catalyst which existed in the surface lattice of LSGT10, it seemed that the nickel catalyst worked better at improving the performance of LSGT10 after exsolving from the perovskite as nanoparticles.

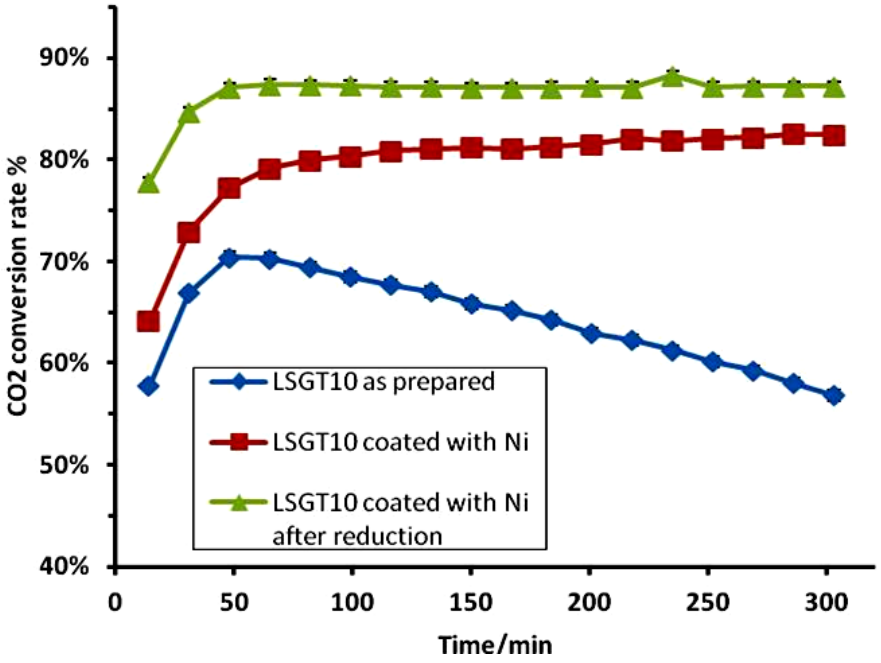

Figure 8-1 Results of catalytic RWGS reactions over as prepared LSGT10, LSGT10 coated with nickel catalyst at 1300 °C and LSGT10 coated with nickel catalyst after reduction. CO_2 conversion rate is plotted as a function of reaction time for 5h at 900 °C.

The catalytic test results of LSCM related perovskite samples are shown in Figure 8-2. All three samples started to stabilize after the first hour of RWGS reactions and maintain the same level of catalytic activity during the rest of the test. It is worth pointing out that compared to as prepared LSGT10, as prepared LSCM showed better stability and mostly maintained a fixed CO_2 conversion rate throughout the experiment once it stabilized. The CO_2 conversion rate of LSCMRu was slightly higher but very close to that of LSCM AP. A more obvious improvement in the catalytic performance in RWGS reactions was seen from the LSCMRu red sample. In addition, traces of CH_4 were detected in the outlet gases of LSCMRu and LSCMRu red. However, due to the negligible quantity of CH_4 compared to the amount of CO, 0.012% (LSCMRu) and 0.013% (LSCMRu red), the CO selectivity of both samples were still very high. The average CO_2 conversion rates for the three samples during the test were 82.0% (LSCM AP), 82.6% (LSCMRu) and 84.6% (LSCMRu red). The addition of ruthenium coating into the LSCM perovskite did improve the performance of the sample although it was not as much as nickel coating LSGT10. Similar to nickel catalyst coating LSGT10 perovskite, it seemed that ruthenium catalyst improved the performance of LSCM perovskite more after it exsolved from the perovskite lattice as nanoparticles.

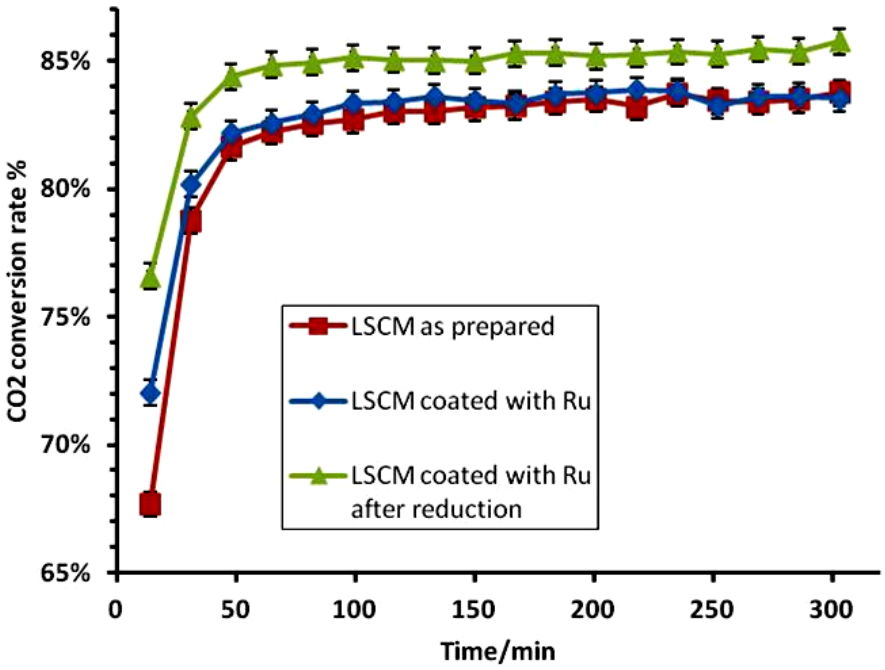

Figure 8-2 Results of catalytic RWGS reactions over as prepared LSCM, LSCM coated with Ru catalyst at 1000 °C and LSCM coated with ruthenium catalyst after reduction. CO_2 conversion rate is plotted as a function of reaction time for 5h at 900 °C.

8.3 Conclusion

A few LSGT10 related samples and LSCM related samples have been tested for the RWGS reaction as a quick method to preliminarily investigate the influence of catalyst coating on the performance of the perovskite. It has been proved that the catalyst coating in the experiment did improve the catalytic activity of the samples to a different degree depending on the catalyst and sample. In addition, it seemed that when the catalysts existed in the form of exsolved nanoparticles, the performance of the perovskite was improved further compared to when the catalysts existed inside the perovskite lattice. For LSGT10, nickel catalyst coating improved its catalytic activity by 15.6% when nickel catalyst existed in the perovskite lattice and 22.5% when nickel catalyst existed in the form of exsolved nanoparticles. For LSCM, ruthenium catalyst coating improved its catalytic activity by 0.6% when ruthenium catalyst existed in the perovskite lattice and 2.6% when ruthenium catalyst existed in the form of exsolved nanoparticles. The CO selectivity of LSGT10 related samples was 100%. The CO selectivity of LSCM AP was 100% and almost 100% after adding ruthenium catalyst since traces of CH_4 were observed. Comparatively, it seemed that the ruthenium catalyst did not improve the catalytic activity of LSCM perovskite as much as nickel catalyst did

at improving LSGT10. This might be due to the fact that ruthenium might not be as active as nickel catalyst in catalyzing the RWGS reactions. More experiments will be carried out later in the future to further study the effect of different catalyst on the performance of the perovskites.

9. Summary

This work aims to improve the performance of A-site deficient titanate based perovskites and $LaCrO_3$ based perovskites with small quantities of catalysts (Ni, Ru and Pd) as potential cost-effective fuel cell materials for PEMFC applications. The technique employed in this experiment involves integrating the impregnation and exsolution methods, in order to form a catalyst doped layer or a layer of catalyst partially anchored on the surface of the perovskite. The optimisation was achieved by using the well-known flexibility of the perovskites for accommodating various cations and defects in the lattice.

The A-site deficient titanate used as the substrate material for catalyst coating was $La_{0.4}Sr_{0.4}Ga_xTi_{1-x}O_{3-x/2}$ (x = 0.06, 0.1) since this material would lose Ga from its surface when it was first reduced in 5% H_2. This project aimed to take advantage of the Ga depleted layer, by preserving it through a fast cooling process, and fill the Ga vacancies with catalysts from the surface of the perovskite. Nickel was firstly used as the catalyst to be coated onto the perovskite from its surface as a pre-investigation for the later experiments. It has been demonstrated that it is possible to dissolve the nickel catalyst into the LSGT perovskite lattice from its surface. The dissolved nickel catalyst was also able to exsolve to the surface of the perovskite as nanoparticles after being reduced in 5% H_2. The same experimental method was later applied to ruthenium and palladium catalyst to be coated onto LSGT perovskite. However, compared to nickel catalyst, each of them reacted very differently to the same coating process due to their different properties. Different coating atmosphere and heating time was used for both catalysts in order to dissolve them into the perovskite from the surface. After the catalyst coated samples were reduced in 5% H_2, only palladium managed to exsolve from the perovskite as nanoparticles. In order to understand the mechanism of palladium incorporating the A-site deficient titanate, different assumptions were proposed and A-site deficient titanate doped with palladium with different stoichiometries were prepared and studied based on the assumptions. The results showed that Pd^{2+} adopts a square planar 4-fold coordination on the B-site of the A-site deficient titanate.

The $LaCrO_3$ based perovskite used as a substrate material to be coated with catalyst was $La_{0.75}Sr_{0.25}Cr_{0.5}Mn_{0.5}O_3$ (LSCM). The perovskite was firstly coated with ruthenium catalyst with the assist of ball milling procedure. The sample was studied by VT-XRD in order to find out the optimal temperature to coat the LSCM perovskite with ruthenium catalyst. Combined with the TEM and EDX results, it can be confirmed that ruthenium catalyst was able to dissolve into the LSCM perovskite lattice upon heating in air and exsolve as nanoparticles after reduction. The reducibility of the LSCM perovskite has also been shown to be improved by the ruthenium catalyst coating. More experiments need to be carried out in order to confirm whether or not the exsolved ruthenium catalyst could re-dissolve into the LSCM perovskite. Palladium catalyst did not successfully dissolve into the LSCM perovskite from its surface even if heating the perovskite in oxygen at high temperatures. An effort was made to dope palladium into LSCM perovskite by combustion method. However, single phase was not obtained and palladium formed 2^{nd} phases with the other cations.

A few samples were selected for the catalytic tests of RWGS reactions as a preliminary study of the effect of catalyst coating on the performance of the perovskite. The experimental results showed that the catalyst coating method did help to improve the performance of the perovskite. It seemed that ruthenium catalyst improved the performance of the LSCM perovskite by a smaller degree compared to nickel catalyst coating LSGT10 perovskite. However, more experiments need to be carried out to confirm the assumption.

The possibility of utilising a combination of impregnation and exsolution methods to modify the surface of the perovskite with small amounts of different catalysts has been demonstrated in this study. This work has revealed that the ability of a catalyst to dissolve from the surface of the perovskite not only depends on the size difference between the catalyst cation and the B-site of the perovskite. Other factors such as the heating atmosphere and heating temperature, heating time, and the stability of the host lattice may also affect whether or not the catalyst is able to dissolve into the perovskite. The core concepts of this study can be very beneficial for reducing the amount of catalyst required, especially in the case of noble metal catalysts. Future work may even apply this technique to other fields such as SOFC, catalysis, electrochemical devices, etc.

References

1. *Survey of energy resources*, 1998, World Energy Council.
2. *2015 World Energy Issues Monitor*, 2015, World Energy Council, 62–64 Cornhill London EC3V 3NH, United Kingdom: United Kingdom.
3. Alessandro Clerici, M.A., Petroleo Brasileiro S.A., *World Energy Resources 2013 survey*, 2013: World Energy Council.
4. Chefurka, P. *World Energy to 2050, Forty Years of Decline*. 2007 [cited 2007; Available from: http://www.paulchefurka.ca/WEAP2/WEAP2.html.
5. Grove, W.R., *XXIV. On voltaic series and the combination of gases by platinum.* Philosophical Magazine Series 3, 1839. **14**(86): p. 127-130.
6. Nernst, W., *Z Electrochem.* 1899. **6**: p. 41-43.
7. Bezian, J., *Report from the Centre d'Energetique de l'Ecole des Mines de Paris*. p. 1-44.
8. *The Fuel Cell Today Industry Review 2011*. Fuel Cell Today, 2011(Johnson Matthey PLC): p. 40.
9. Minh, N.Q. and T. Takahashi, *Chapter 1 - Introduction*, in *Science and Technology of Ceramic Fuel Cells*1995, Elsevier Science Ltd: Oxford. p. 1-14.
10. Boudghene Stambouli, A. and E. Traversa, *Fuel cells, an alternative to standard sources of energy.* Renewable and Sustainable Energy Reviews, 2002. **6**(3): p. 295-304.
11. Solid State Ionics and Electroceramics Research Group, C.I.o.T. *Fuel Cells for Sustainable Energy - Science meets social responsibility*. 2013; Available from: http://addis.caltech.edu/research/FCs%20for%20sustain%20energy.html.
12. James, L. *Renewable fuel cell power from biogas*. 2001 [cited 2001 Nov-Dec]; Available from: http://www.jxj.com/magsandj/rew/2001_06/renewable_fuel_cell.html.
13. Li, Q., et al., *Approaches and Recent Development of Polymer Electrolyte Membranes for Fuel Cells Operating above 100 °C.* Chemistry of Materials, 2003. **15**(26): p. 4896-4915.
14. Shao, Y., et al., *Proton exchange membrane fuel cell from low temperature to high temperature: Material challenges.* Journal of Power Sources, 2007. **167**(2): p. 235-242.
15. Li, Q., et al., *High temperature proton exchange membranes based on polybenzimidazoles for fuel cells.* Progress in Polymer Science (Oxford), 2009. **34**(5): p. 449-477.
16. Liu, Y., et al., *A review of high-temperature polymer electrolyte membrane fuel-cell (HT-PEMFC)-based auxiliary power units for diesel-powered road vehicles.* Journal of Power Sources, 2016. **311**: p. 91-102.
17. *EG&G Services, Fuel Cell Handbook, 5th ed., Parsons Inc.* January 2002]; Available from: http://www.fuelcells.org/fchandbook.pdf.
18. Gottesfeld, S. and T.A. Zawodzinski, *Polymer Electrolyte Fuel Cells*, in *Advances in Electrochemical Science and Engineering*2008, Wiley-VCH Verlag GmbH. p. 195-301.
19. Mougenot, M., et al., *High Performance plasma sputtered PdPt fuel cell electrodes with ultra low loading.* International Journal of Hydrogen Energy, 2011. **36**(14): p. 8429-8434.
20. Cavarroc, M., et al., *Performance of plasma sputtered fuel cell electrodes with ultra-low Pt loadings.* Electrochemistry Communications, 2009. **11**(4): p. 859-861.
21. Ruiz, N., A.R. Pierna, and M. Sanchez, *Low loading Pt catalysts based on* $Ni_{59}Nb_{40}Pt_{0.6}X_{0.4}$ *(X = Pd, Rh, Ru, Co) as anodes and Nafion XL membranes as support in PEMFCs*. International Journal of Hydrogen Energy, 2014. **39**(10): p. 5319-5325.
22. Wilson, M.S., J.A. Valerio, and S. Gottesfeld, *Low platinum loading electrodes for polymer electrolyte fuel cells fabricated using thermoplastic ionomers.* Electrochimica Acta, 1995. **40**(3): p. 355-363.
23. Carmo, M.P., et al., *Alternative supports for the preparation of catalysts for low-temperature fuel cells: the use of carbon nanotubes.* Journal of Power Sources, 2005. **142**(1–2): p. 169-176.
24. Kim, S.K., et al., *Radiolytic Preparation of Electrocatalysts with Pt-Co and Pt-Sn Nanoparticles for a Proton Exchange Membrane Fuel Cell.* Journal of Nanomaterials, 2014. **2014**: p. 8.
25. Yano, H., et al., *New CO tolerant electro-catalysts exceeding Pt-Ru for the anode of fuel cells.* Chemical Communications, 2005(9): p. 1212-1214.
26. Shao-Horn, Y., et al., *Instability of Supported Platinum Nanoparticles in Low-Temperature Fuel Cells.* Topics in Catalysis, 2007. **46**(3): p. 285-305.
27. Kinoshita, K. and S. Electrochemical, *Electrochemical oxygen technology*1992, New York: Wiley.

28. Scibioh, M.A. and B. Viswanathan, *The Status of Catalysts in PEMFC Technology*, in *Catalysis for Alternative Energy Generation*, L. Guczi and A. Erdôhelyi, Editors. 2012, Springer New York: New York, NY. p. 329-368.
29. Tang, Y., et al., *A facile synthesis of Pd/C cathode electrocatalyst for proton exchange membrane fuel cells.* International Journal of Hydrogen Energy, 2011. **36**(1): p. 725-731.
30. Fernández, J.L., et al., *Pd−Ti and Pd−Co−Au Electrocatalysts as a Replacement for Platinum for Oxygen Reduction in Proton Exchange Membrane Fuel Cells.* Journal of the American Chemical Society, 2005. **127**(38): p. 13100-13101.
31. Gadgil, M.M., R. Sasikala, and S.K. Kulshreshtha, *CO oxidation over Pd/SnO_2 catalyst.* Journal of Molecular Catalysis, 1994. **87**(2–3): p. 297-309.
32. Echigo, M., et al., *Development of residential PEFC cogeneration systems: Ru catalyst for CO preferential oxidation in reformed gas.* Catalysis Today, 2003. **84**(3–4): p. 209-215.
33. Kim, Y.H., S.D. Yim, and E.D. Park, *Selective CO oxidation in a hydrogen-rich stream over Ru/SiO_2.* Catalysis Today, 2012. **185**(1): p. 143-150.
34. Kim, Y.H., et al., *Selective CO removal in a H_2-rich stream over supported Ru catalysts for the polymer electrolyte membrane fuel cell (PEMFC).* Applied Catalysis A: General, 2009. **366**(2): p. 363-369.
35. Gao, Y., et al., *Preferential oxidation of CO in a H_2-rich stream over multi-walled carbon nanotubes confined Ru catalysts.* International Journal of Hydrogen Energy, 2013. **38**(36): p. 16665-16676.
36. Zagal, J.H., *Metallophthalocyanines as catalysts in electrochemical reactions.* Coordination Chemistry Reviews, 1992. **119**: p. 89-136.
37. Ham, D.J. and J.S. Lee, *Transition Metal Carbides and Nitrides as Electrode Materials for Low Temperature Fuel Cells.* Energies, 2009. **2**(4): p. 873-899.
38. Zhong, H., et al., *A novel non-noble electrocatalyst for oxygen reduction in proton exchange membrane fuel cells.* Journal of Power Sources, 2007. **164**(2): p. 572-577.
39. Doi, S., et al., *Zirconium Nitride and Oxynitride for New Cathode of Polymer Electrolyte Fuel Cell.* ECS Transactions, 2006. **1**(6): p. 17-25.
40. Kim, J.H., et al., *Oxygen reduction reaction of Ta-C-N prepared by reactive sputtering with heat treatment.* Electrochemistry, 2007. **75**(2): p. 166-168.
41. Lee, K., L. Zhang, and J. Zhang, *A novel methanol-tolerant Ir-Se chalcogenide electrocatalyst for oyxgen reduction.* Journal of Power Sources, 2007. **165**(1): p. 108-113.
42. *Precious Metals Management: prices*. Available from: http://www.platinum.matthey.com/prices/price-charts.
43. Peña, M.A. and J.L.G. Fierro, *Chemical Structures and Performance of Perovskite Oxides.* Chemical Reviews, 2001. **101**(7): p. 1981-2018.
44. Suntivich, J., et al., *Design principles for oxygen-reduction activity on perovskite oxide catalysts for fuel cells and metal–air batteries.* Nat Chem, 2011. **3**(7): p. 546-550.
45. Grimaud, A., et al., *Double perovskites as a family of highly active catalysts for oxygen evolution in alkaline solution.* Nat Commun, 2013. **4**.
46. Chen, Z., et al., *Highly Active and Durable Core–Corona Structured Bifunctional Catalyst for Rechargeable Metal–Air Battery Application.* Nano Letters, 2012. **12**(4): p. 1946-1952.
47. Cheng, F. and J. Chen, *Lithium-air batteries: Something from nothing.* Nat Chem, 2012. **4**(12): p. 962-963.
48. Savinell, R.F., *Oxygen-reduction catalysts: Picking perovskites.* Nat Chem, 2011. **3**(7): p. 501-502.
49. Xu, J.-J., et al., *Synthesis of Perovskite-Based Porous $La_{0.75}Sr_{0.25}MnO_3$ Nanotubes as a Highly Efficient Electrocatalyst for Rechargeable Lithium–Oxygen Batteries.* Angewandte Chemie International Edition, 2013. **52**(14): p. 3887-3890.
50. Villaseca, L., B. Moreno, and E. Chinarro, *Perovskites based on La(Sr)-Mn-O system as electrocatalyst in PEM fuel cell of high temperature.* International Journal of Hydrogen Energy, 2012. **37**(8): p. 7161-7170.
51. Tejuca, L.G. and J.L.G. Fierro, *Properties and Applications of Perovskite-Type Oxides*2000: Taylor & Francis.
52. Ishihara, T., *Structure and Properties of Perovskite Oxides*, in *Perovskite Oxide for Solid Oxide Fuel Cells*, T. Ishihara, Editor 2009, Springer US: Boston, MA. p. 1-16.
53. Tao, S. and J.T.S. Irvine, *Discovery and characterization of novel oxide anodes for solid oxide fuel cells.* The Chemical Record, 2004. **4**(2): p. 83-95.
54. Yokokawa, H., et al., *Thermodynamic stabilities of perovskite oxides for electrodes and other electrochemical materials.* Solid State Ionics, 1992. **52**(1): p. 43-56.

55. Atkinson, A., et al., *Advanced anodes for high-temperature fuel cells.* Nat Mater, 2004. **3**(1): p. 17-27.
56. Hyodo, T., et al., *Catalytic Activities of Rare Earth Manganites for Cathodic Reduction of Oxygen in Alkaline Solution.* Journal of The Electrochemical Society, 1996. **143**(11): p. L266-L267.
57. Borriello, I., G. Cantele, and D. Ninno, *Ab initio investigation of hybrid organic-inorganic perovskites based on tin halides.* Physical Review B, 2008. **77**(23): p. 235214.
58. Wolfram, T. and S. Ellialtioglu., *Electronic and Optical Properties of d-Band Perovskites*2006: Cambridge University Press.
59. Neagu, D. and J.T.S. Irvine, *4.15 - Perovskite Defect Chemistry as Exemplified by Strontium Titanate A2 - Reedijk, Jan*, in *Comprehensive Inorganic Chemistry II (Second Edition)*, K. Poeppelmeier, Editor 2013, Elsevier: Amsterdam. p. 397-415.
60. Shannon, R., *Revised effective ionic radii and systematic studies of interatomic distances in halides and chalcogenides.* Acta Crystallographica Section A, 1976. **32**(5): p. 751-767.
61. Megaw, H.D., *Ferroelectricity in Crystals*, 1957, Methuen & Co Ltd: London.
62. Allan, N.L., et al., *Atomistic lattice simulations of the ternary fluorides AMF_3(A = Li, Na, K, Rb, Cs; M = Mg, Ca, Sr, Ba).* Journal of Materials Chemistry, 1991. **1**(6): p. 1035-1039.
63. Goodenough, J.B., *General Considerations*, in *Localized to Itinerant Electronic Transition in Perovskite Oxides*, J.B. Goodenough, Editor 2001, Springer Berlin Heidelberg: Berlin, Heidelberg. p. 1-16.
64. Howard, C.J. and H.T. Stokes, *Octahedral tilting in cation-ordered perovskites - a group-theoretical analysis.* Acta Crystallographica Section B, 2004. **60**(6): p. 674-684.
65. Howard, C.J. and H.T. Stokes, *Structures and phase transitions in perovskites - a group-theoretical approachThis article is dedicated to Helen D. Megaw (1907-2002), in appreciation of her many contributions to the crystallography of inorganic and mineral compounds, including her seminal studies of perovskites. Some of the material was presented by CJH in the Megaw memorial session at the 21st European Crystallography Meeting, Durban, South Africa, August 2003.* Acta Crystallographica Section A, 2005. **61**(1): p. 93-111.
66. Glazer, A., *Simple ways of determining perovskite structures.* Acta Crystallographica Section A, 1975. **31**(6): p. 756-762.
67. Woodward, P., *Octahedral Tilting in Perovskites. II. Structure Stabilizing Forces.* Acta Crystallographica Section B, 1997. **53**(1): p. 44-66.
68. Howard, C.J. and H.T. Stokes, *Group-Theoretical Analysis of Octahedral Tilting in Perovskites.* Acta Crystallographica Section B, 1998. **54**(6): p. 782-789.
69. Glazer, A., *The classification of tilted octahedra in perovskites.* Acta Crystallographica Section B, 1972. **28**(11): p. 3384-3392.
70. Howard, C.J., et al., *Crystal structures and phase transition in the system $SrTiO_3$–$La_{2/3}TiO_3$.* Journal of Solid State Chemistry, 2004. **177**(8): p. 2726-2732.
71. Howard, C.J.K., Brendan J., *The orthorhombic and rhombohedral phases of $LaGaO_3$ - a neutron powder diffraction study.* Journal of Physics: Condensed Matter, 1999. **11**(16): p. 3229-3236.
72. Kennedy, B.J., et al., *Structural Characterization of the Perovskite Series $La_{1-x}Sr_xCr_{1-x}Ti_xO_3$.* Journal of Solid State Chemistry, 2000. **155**(2): p. 455-457.
73. Lufaso, M.W. and P.M. Woodward, *Prediction of the crystal structures of perovskites using the software program SPuDS.* Acta Crystallographica Section B, 2001. **57**(6): p. 725-738.
74. Garcia-Fernandez, P., et al., *Key Role of Covalent Bonding in Octahedral Tilting in Perovskites.* The Journal of Physical Chemistry Letters, 2010. **1**(3): p. 647-651.
75. Howard, C.J., B.J. Kennedy, and P.M. Woodward, *Ordered double perovskites - a group-theoretical analysis.* Acta Crystallographica Section B, 2003. **59**(4): p. 463-471.
76. Neagu, D., et al., *In situ growth of nanoparticles through control of non-stoichiometry.* Nature chemistry, 2013. **5**(11): p. 916-23.
77. Ruddlesden, S.N. and P. Popper, *New compounds of the K_2NiF_4 type.* Acta Crystallographica, 1957. **10**(8): p. 538-539.
78. Williams, T., et al., *On the crystal structures of $La_2Ti_2O_7$ and $La_5Ti_5O_{17}$: High-resolution electron microscopy.* Journal of Solid State Chemistry, 1991. **93**(2): p. 534-548.
79. Anderson, M.T., J.T. Vaughey, and K.R. Poeppelmeier, *Structural similarities among oxygen-deficient perovskites.* Chemistry of Materials, 1993. **5**(2): p. 151-165.
80. Ruddlesden, S.N. and P. Popper, *The compound $Sr_3Ti_2O_7$ and its structure.* Acta Crystallographica, 1958. **11**(1): p. 54-55.
81. Neagu, D., et al., *Nano-socketed nickel particles with enhanced coking resistance grown in situ by redox exsolution.* Nat Commun, 2015. **6**: p. 8120.

82. Kobsiriphat, W., et al., *Nickel- and Ruthenium-Doped Lanthanum Chromite Anodes: Effects of Nanoscale Metal Precipitation on Solid Oxide Fuel Cell Performance.* Journal of The Electrochemical Society, 2010. **157**(2): p. B279-B279.
83. Nishihata, Y., et al., *Self-regeneration of a Pd-perovskite catalyst for automotive emissions control.* Nature, 2002. **418**(6894): p. 164-167.
84. Katz, M.B., et al., *Reversible precipitation/dissolution of precious-metal clusters in perovskite-based catalyst materials: Bulk versus surface re-dispersion.* Journal of Catalysis, 2012. **293**: p. 145-148.
85. Tsekouras, G., D. Neagu, and J.T.S. Irvine, *Step-change in high temperature steam electrolysis performance of perovskite oxide cathodes with exsolution of B-site dopants.* Energy & Environmental Science, 2013. **6**(1): p. 256-266.
86. Horvath, G., et al., *Segregation driving forces in perovskite titanates.* Sensors and Actuators B: Chemical, 1996. **32**(2): p. 93-99.
87. Chen, D., et al., *Nonstoichiometric Oxides as Low-Cost and Highly-Efficient Oxygen Reduction/Evolution Catalysts for Low-Temperature Electrochemical Devices.* Chemical Reviews, 2015. **115**(18): p. 9869-9921.
88. Monteiro, N.K., et al., *A direct ethanol anode for solid oxide fuel cell based on a chromite-manganite with catalytic ruthenium nanoparticles.* International Journal of Hydrogen Energy, 2012. **37**(12): p. 9816-9829.
89. Arrivé, C., et al., *Exsolution of nickel nanoparticles at the surface of a conducting titanate as potential hydrogen electrode material for solid oxide electrochemical cells.* Journal of Power Sources, 2013. **223**: p. 341-348.
90. Sun, Y., et al., *A-site deficient perovskite: the parent for in situ exsolution of highly active, regenerable nano-particles as SOFC anodes.* Journal of Materials Chemistry A, 2015. **3**(20): p. 11048-11056.
91. Tanaka, H., et al., *Design of the intelligent catalyst for Japan ULEV standard.* 6th Congress on Catalysis and Automotive Pollution Control, 2004. **30-31**: p. 389-396.
92. Tanaka, H., et al., *The intelligent catalyst having the self-regenerative function of Pd, Rh and Pt for automotive emissions control.* Catalysis Today, 2006. **117**(1-3): p. 321-328.
93. Taniguchi, M., et al., *The self-regenerative Pd-, Rh-, and Pt-perovskite catalysts.* Topics in Catalysis, 2007. **42-43**(1-4): p. 367-371.
94. Matsumura, D., et al., *Dynamic structural change in Pd-perovskite automotive catalyst studied by time-resolved dispersive x-ray absorption fine structure.* Journal of Applied Physics, 2010. **107**(12): p. 124319-124319.
95. Tanaka, H., et al., *Regeneration of palladium subsequent to solid solution and segregation in a perovskite catalyst: An intelligent catalyst.* Topics in Catalysis, 2001. **16-17**(1-4): p. 63-70.
96. Boulfrad, S., et al., *Pre-coating of LSCM perovskite with metal catalyst for scalable high performance anodes.* International Journal of Hydrogen Energy, 2013. **38**(22): p. 9519-9524.
97. Zhou, X., et al., *Progress in La-doped $SrTiO_3$ (LST)-based anode materials for solid oxide fuel cells.* RSC Advances, 2014. **4**(1): p. 118-131.
98. Verbraeken, M.C., et al., *Modified strontium titanates: from defect chemistry to SOFC anodes.* RSC Advances, 2015. **5**(2): p. 1168-1180.
99. R. Slater, P., D. P. Fagg, and J. T. S. Irvine, *Synthesis and electrical characterisation of doped perovskite titanates as potential anode materials for solid oxide fuel cells.* Journal of Materials Chemistry, 1997. **7**(12): p. 2495-2498.
100. Neagu, D. and J.T.S. Irvine, *Enhancing Electronic Conductivity in Strontium Titanates through Correlated A and B-Site Doping.* Chemistry of Materials, 2011. **23**(6): p. 1607-1617.
101. Neagu, D. and J.T.S. Irvine, *Structure and Properties of $La_{0.4}Sr_{0.4}TiO_3$ Ceramics for Use as Anode Materials in Solid Oxide Fuel Cells.* Chemistry of Materials, 2010. **22**(17): p. 5042-5053.
102. Savaniu, C.D. and J.T.S. Irvine, *La-doped $SrTiO_3$ as anode material for IT-SOFC.* Solid State Ionics, 2011. **192**(1): p. 491-493.
103. Verbraeken, M.C., et al., *Short Stack and Full System Test Using a Ceramic A-Site Deficient Strontium Titanate Anode.* Fuel Cells, 2015. **15**(5): p. 682-688.
104. Tsekouras, G. and J.T.S. Irvine, *The role of defect chemistry in strontium titanates utilised for high temperature steam electrolysis.* Journal of Materials Chemistry, 2011. **21**(25): p. 9367-9367.
105. Tesfai, A.T., C. Savaniu, and J.T. Irvine, *Fabrication and Development of Perovskite Anode Supported Planar SOFCs.* ECS Transactions, 2011. **35**(1): p. 557-563.
106. Burnat, D., et al., *Synthesis and performance of A-site deficient lanthanum-doped strontium titanate by nanoparticle based spray pyrolysis.* Journal of Power Sources, 2012. **201**: p. 26-36.

107. Li, X., et al., *Electrical conductivity and structural stability of La-doped $SrTiO_3$ with A-site deficiency as anode materials for solid oxide fuel cells.* International Journal of Hydrogen Energy, 2010. **35**(15): p. 7913-7918.
108. Yaqub, A., et al., *Synthesis and characterization of B-site doped $La_{0.20}Sr_{0.25}Ca_{0.45}TiO_3$ as SOFC anode materials.* International Journal of Hydrogen Energy, 2015. **40**(1): p. 760-766.
109. Li, Y., et al., *Efficient Carbon Dioxide Electrolysis Based on Perovskite Cathode Enhanced with Nickel Nanocatalyst.* Electrochimica Acta, 2015. **153**: p. 325-333.
110. Fergus, J.W., *Lanthanum chromite-based materials for solid oxide fuel cell interconnects.* Solid State Ionics, 2004. **171**(1–2): p. 1-15.
111. Tao, S. and J.T.S. Irvine, *A redox-stable efficient anode for solid-oxide fuel cells.* Nat Mater, 2003. **2**(5): p. 320-323.
112. Kobsiriphat, W., et al., *$La_{0.8}Sr_{0.2}Cr_{1-x}Ru_xO_{3-\delta}$–$Gd_{0.1}Ce_{0.9}O_{1.95}$ solid oxide fuel cell anodes: Ru precipitation and electrochemical performance.* Solid State Ionics, 2009. **180**(2–3): p. 257-264.
113. Madsen, B.D., et al., *Nucleation of nanometer-scale electrocatalyst particles in solid oxide fuel cell anodes.* Journal of Power Sources, 2007. **166**(1): p. 64-67.
114. Bierschenk, D.M., et al., *Pd-substituted $(La,Sr)CrO_{3-\delta}$–$Ce_{0.9}Gd_{0.1}O_{2-\delta}$ solid oxide fuel cell anodes exhibiting regenerative behavior.* Journal of Power Sources, 2011. **196**(6): p. 3089-3094.
115. Jardiel, T., et al., *New SOFC electrode materials: The Ni-substituted LSCM-based compounds $(La_{0.75}Sr_{0.25})(Cr_{0.5}Mn_{0.5-x}Ni_x)O_{3-\delta}$ and $(La_{0.75}Sr_{0.25})(Cr_{0.5-x}Ni_xMn_{0.5})O_{3-\delta}$.* Solid State Ionics, 2010. **181**(19-20): p. 894-901.
116. Delahaye, T., et al., *Electrochemical properties of novel SOFC dual electrode $La_{0.75}Sr_{0.25}Cr_{0.5}Mn_{0.3}Ni_{0.2}O_{3-\delta}$.* Solid State Ionics, 2011. **184**(1): p. 39-41.
117. Papargyriou, D. and J.T.S. Irvine, *Nickel nanocatalyst exsolution from (La,Sr) (Cr,M,Ni)O_3 (M = Mn,Fe) perovskites for the fuel oxidation layer of Oxygen Transport Membranes.* Solid State Ionics.
118. Li, H., et al., *Chromate cathode decorated with in-situ growth of copper nanocatalyst for high temperature carbon dioxide electrolysis.* International Journal of Hydrogen Energy, 2014. **39**(36): p. 20888-20897.
119. Ruan, C. and K. Xie, *A redox-stable chromate cathode decorated with in situ grown nickel nanocatalyst for efficient carbon dioxide electrolysis.* Catalysis Science & Technology, 2015. **5**(3): p. 1929-1940.
120. Komiyama, M., *Design and Preparation of Impregnated Catalysts.* Catalysis Reviews, 1985. **27**(2): p. 341-372.
121. Lee, S.-Y. and R. Aris, *The Distribution of Active ingredients in Supported Catalysts Prepared by Impregnation.* Catalysis Reviews, 1985. **27**(2): p. 207-340.
122. Jiang, S.P., et al., *Fabrication and Performance of Impregnated Ni Anodes of Solid Oxide Fuel Cells.* Journal of the American Ceramic Society, 2005. **88**(7): p. 1779-1785.
123. Li, J., et al., *$BaCe_{1-x}Pd_xO_{3-\delta}$ $(0 \le x \le 0.1)$: Redox Controlled Ingress and Egress of Palladium in a Perovskite.* Chemistry of Materials, 2007. **19**(6): p. 1418-1426.
124. Jiang, S.P., et al., *Nanostructured palladium–$La_{0.75}Sr_{0.25}Cr_{0.5}Mn_{0.5}O_3$/$Y_2O_3$–$ZrO_2$ composite anodes for direct methane and ethanol solid oxide fuel cells.* Journal of Power Sources, 2008. **185**(1): p. 179-182.
125. Irvine, J.T.S., *Microstructural Engineering of SOFC and SOEC Electrode Interfaces.* 2013. **57**(1): p. 1297-1305.
126. Liu, Z., et al., *Fabrication and modification of solid oxide fuel cell anodes via wet impregnation/infiltration technique.* Journal of Power Sources, 2013. **237**: p. 243-259.
127. Gorte, R.J. and J.M. Vohs, *Nanostructured anodes for solid oxide fuel cells.* Current Opinion in Colloid & Interface Science, 2009. **14**(4): p. 236-244.
128. Vohs, J.M. and R.J. Gorte, *High-Performance SOFC Cathodes Prepared by Infiltration.* Advanced Materials, 2009. **21**(9): p. 943-956.
129. Ding, D., et al., *Enhancing SOFC cathode performance by surface modification through infiltration.* Energy & Environmental Science, 2014. **7**(2): p. 552-575.
130. Jiang, S.P., *Nanoscale and nano-structured electrodes of solid oxide fuel cells by infiltration: Advances and challenges.* International Journal of Hydrogen Energy, 2012. **37**(1): p. 449-470.
131. Kim, T., et al., *A study of carbon formation and prevention in hydrocarbon-fueled SOFC.* Journal of Power Sources, 2006. **155**(2): p. 231-238.
132. Jiang, S.P., *A review of wet impregnation—An alternative method for the fabrication of high performance and nano-structured electrodes of solid oxide fuel cells.* Materials Science and Engineering: A, 2006. **418**(1–2): p. 199-210.

133. Gross, M.D., J.M. Vohs, and R.J. Gorte, *Recent progress in SOFC anodes for direct utilization of hydrocarbons.* Journal of Materials Chemistry, 2007. **17**(30): p. 3071-3077.
134. Gorte, R.J., J.M. Vohs, and S. McIntosh, *Recent developments on anodes for direct fuel utilization in SOFC.* Solid State Ionics, 2004. **175**(1–4): p. 1-6.
135. Irvine, J.T.S., et al., *Evolution of the electrochemical interface in high-temperature fuel cells and electrolysers.* Nature Energy, 2016. **1**: p. 15014.
136. Lou, X., et al., *Controlling the morphology and uniformity of a catalyst-infiltrated cathode for solid oxide fuel cells by tuning wetting property.* Journal of Power Sources, 2010. **195**(2): p. 419-424.
137. Choi, Y., et al., *Highly Efficient Layer-by-Layer-Assisted Infiltration for High-Performance and Cost-Effective Fabrication of Nanoelectrodes.* ACS Applied Materials & Interfaces, 2014. **6**(20): p. 17352-17357.
138. Sholklapper, T.Z., et al., *Synthesis of Dispersed and Contiguous Nanoparticles in Solid Oxide Fuel Cell Electrodes.* Fuel Cells, 2008. **8**(5): p. 303-312.
139. Muradov, N.Z. and T.N. Veziroğlu, *"Green" path from fossil-based to hydrogen economy: An overview of carbon-neutral technologies.* International Journal of Hydrogen Energy, 2008. **33**(23): p. 6804-6839.
140. Centi, G. and S. Perathoner, *Opportunities and prospects in the chemical recycling of carbon dioxide to fuels.* Catalysis Today, 2009. **148**(3–4): p. 191-205.
141. Wang, W., et al., *Recent advances in catalytic hydrogenation of carbon dioxide.* Chemical Society Reviews, 2011. **40**(7): p. 3703-3727.
142. Carl Bosch, W.W., *Producing hydrogen*, U. pat, Editor 1914.
143. Daza, Y.A. and J.N. Kuhn, *CO_2 conversion by reverse water gas shift catalysis: comparison of catalysts, mechanisms and their consequences for CO_2 conversion to liquid fuels.* RSC Advances, 2016. **6**(55): p. 49675-49691.
144. Ginés, M.J.L., A.J. Marchi, and C.R. Apesteguía, *Kinetic study of the reverse water-gas shift reaction over CuO/ZnO/Al_2O_3 catalysts.* Applied Catalysis A: General, 1997. **154**(1–2): p. 155-171.
145. Chen, C.-S., W.-H. Cheng, and S.-S. Lin, *Enhanced activity and stability of a Cu/SiO_2 catalyst for the reverse water gas shift reaction by an iron promoter.* Chemical Communications, 2001(18): p. 1770-1771.
146. Oshima, K., et al., *Low temperature catalytic reverse water gas shift reaction assisted by an electric field.* Catalysis Today, 2014. **232**: p. 27-32.
147. Chen, C.S., J.H. Wu, and T.W. Lai, *Carbon Dioxide Hydrogenation on Cu Nanoparticles.* The Journal of Physical Chemistry C, 2010. **114**(35): p. 15021-15028.
148. Chen, C.-S., W.-H. Cheng, and S.-S. Lin, *Study of reverse water gas shift reaction by TPD, TPR and CO_2 hydrogenation over potassium-promoted Cu/SiO_2 catalyst.* Applied Catalysis A: General, 2003. **238**(1): p. 55-67.
149. Rodriguez, J.A., et al., *CO_2 hydrogenation on Au/TiC, Cu/TiC, and Ni/TiC catalysts: Production of CO, methanol, and methane.* Journal of Catalysis, 2013. **307**: p. 162-169.
150. Chen, C.-S. and W.-H. Cheng, *Study on the Mechanism of CO Formation in Reverse Water Gas Shift Reaction Over Cu/SiO_2 Catalyst by Pulse Reaction, TPD and TPR.* Catalysis Letters, 2002. **83**(3): p. 121-126.
151. Goguet, A., et al., *Spectrokinetic Investigation of Reverse Water-Gas-Shift Reaction Intermediates over a Pt/CeO_2 Catalyst.* The Journal of Physical Chemistry B, 2004. **108**(52): p. 20240-20246.
152. Jacobs, G. and B.H. Davis, *Reverse water-gas shift reaction: steady state isotope switching study of the reverse water-gas shift reaction using in situ DRIFTS and a Pt/ceria catalyst.* Applied Catalysis A: General, 2005. **284**(1–2): p. 31-38.
153. Jin, T., et al., *Infrared and x-ray photoelectron spectroscopy study of carbon monoxide and carbon dioxide on platinum/ceria.* The Journal of Physical Chemistry, 1987. **91**(23): p. 5931-5937.
154. Kusama, H., et al., *CO_2 hydrogenation reactivity and structure of Rh/SiO_2 catalysts prepared from acetate, chloride and nitrate precursors.* Applied Catalysis A: General, 2001. **205**(1–2): p. 285-294.
155. Liu, C., T.R. Cundari, and A.K. Wilson, *CO_2 Reduction on Transition Metal (Fe, Co, Ni, and Cu) Surfaces: In Comparison with Homogeneous Catalysis.* The Journal of Physical Chemistry C, 2012. **116**(9): p. 5681-5688.
156. Liu, Y. and D. Liu, *Study of bimetallic Cu–Ni_y-Al_2O_3 catalysts for carbon dioxide hydrogenation.* International Journal of Hydrogen Energy, 1999. **24**(4): p. 351-354.

157. Matsubu, J.C., V.N. Yang, and P. Christopher, *Isolated Metal Active Site Concentration and Stability Control Catalytic CO2 Reduction Selectivity*. Journal of the American Chemical Society, 2015. **137**(8): p. 3076-3084.
158. Wang, W., et al., *Reverse water gas shift over In_2O_3–CeO_2 catalysts.* Catalysis Today, 2016. **259, Part 2**: p. 402-408.
159. Zhao, B., Y.-x. Pan, and C.-j. Liu, *The promotion effect of CeO2 on CO2 adsorption and hydrogenation over Ga2O3.* Catalysis Today, 2012. **194**(1): p. 60-64.
160. Daza, Y.A., et al., *Carbon Dioxide Conversion by Reverse Water–Gas Shift Chemical Looping on Perovskite-Type Oxides.* Industrial & Engineering Chemistry Research, 2014. **53**(14): p. 5828-5837.
161. Daza, Y.A., et al., *Isothermal reverse water gas shift chemical looping on $La_{0.75}Sr_{0.25}Co_{(1-Y)}Fe_YO_3$ perovskite-type oxides.* Catalysis Today, 2015. **258, Part 2**: p. 691-698.
162. Kim, D.H., et al., *Dopant Effect of Barium Zirconate-Based Perovskite-Type Catalysts for the Intermediate-Temperature Reverse Water Gas Shift Reaction.* ACS Catalysis, 2014. **4**(9): p. 3117-3122.
163. Jia, L., et al., *Influence of copper content on structural features and performance of pre-reduced $LaMn_{1-x}Cu_xO_3$ ($0 \leq x < 1$) catalysts for methanol synthesis from CO_2/H_2.* Journal of Rare Earths, 2010. **28**(5): p. 747-751.
164. Zhan, H., et al., *Methanol synthesis from CO_2 hydrogenation over La–M–Cu–Zn–O (M = Y, Ce, Mg, Zr) catalysts derived from perovskite-type precursors.* Journal of Power Sources, 2014. **251**: p. 113-121.
165. Jia, L., et al., *Carbon dioxide hydrogenation to methanol over the pre-reduced $LaCr_{0.5}Cu_{0.5}O_3$ catalyst.* Catalysis Communications, 2009. **10**(15): p. 2000-2003.
166. Chanquía, C.M., et al., *Synthesis and characterization of pure-phase $La_{0.75}Sr_{0.25}Cr_{0.5}Mn_{0.5}O_{3-\delta}$ nanocrystallites for solid oxide fuel cell applications.* Journal of Nanoparticle Research, 2012. **14**(9): p. 1104-1104.
167. Purdue and University. *Scanning Electron Microscope*. 2014; Available from: https://www.purdue.edu/ehps/rem/rs/sem.htm.
168. Savile Bradbury, D.C.J., Brian J. Ford. *Transmission electron microscope (TEM)*. 2016 [cited 2016 February 27]; Available from: http://www.britannica.com/technology/transmission-electron-microscope.
169. Neagu, D., *Materials and microstructures for high temperature electrochemical devices through control of perovskite defect chemistry*, 2013, University of St Andrews.
170. Bowker, M., A. Nuhu, and J. Soares, *High activity supported gold catalysts by incipient wetness impregnation.* Catalysis Today, 2007. **122**(3–4): p. 245-247.
171. Eyssler, A., et al., *The Effect of the State of Pd on Methane Combustion in Pd-Doped $LaFeO_3$.* The Journal of Physical Chemistry C, 2010. **114**(10): p. 4584-4594.
172. Park, B.H. and G.M. Choi, *Ex-solution of Ni nanoparticles in a $La_{0.2}Sr_{0.8}Ti_{1-x}Ni_xO_{3-\delta}$ alternative anode for solid oxide fuel cell.* Solid State Ionics, 2014. **262**(0): p. 345-348.
173. Ishihara, T., et al., *Fe doped $LaGaO_3$ perovskite oxide as an oxygen separating membrane for CH_4 partial oxidation.* Solid State Ionics, 2002. **152–153**: p. 709-714.
174. Sartipi, S., A.A. Khodadadi, and Y. Mortazavi, *Pd-doped $LaCoO_3$ regenerative catalyst for automotive emissions control.* Applied Catalysis B: Environmental, 2008. **83**(3–4): p. 214-220.
175. Konta, R., et al., *Photocatalytic Activities of Noble Metal Ion Doped $SrTiO_3$ under Visible Light Irradiation.* 2004: p. 8992-8995.
176. Yoon, H., et al., *Ru-doped lanthanum strontium titanates for the anode of solid oxide fuel cells.* International Journal of Hydrogen Energy, 2015. **40**(34): p. 10985-10993.
177. Shin, T.H., et al., *Self-recovery of Pd nanoparticles that were dispersed over La(Sr)Fe(Mn)O_3 for intelligent oxide anodes of solid-oxide fuel cells.* Chemistry (Weinheim an der Bergstrasse, Germany), 2012. **18**(37): p. 11695-702.
178. Yamaji, K., et al., *Compatibility of $La_{0.9}Sr_{0.1}Ga_{0.8}Mg_{0.2}O_{2.85}$ as the electrolyte for SOFCs.* Solid State Ionics, 1998. **108**(1–4): p. 415-421.
179. Yamaji, K., et al., *Chemical stability of the $La_{0.9}Sr_{0.1}Ga_{0.8}Mg_{0.2}O_{2.85}$ electrolyte in a reducing atmosphere.* Solid State Ionics, 1999. **121**(1–4): p. 217-224.
180. Yamaji, K., et al., *Vaporization process of Ga from doped LaGaO3 electrolytes in reducing atmospheres.* Solid State Ionics, 2000. **135**(1–4): p. 389-396.
181. Agnieszka, J. and G. Barbara, *Chromium, nickel and vanadium mobility in soils derived from fluvioglacial sands.* J Hazard Mater, 2012. **238**: p. 315-22.
182. Dias, F.J., et al., *Properties of Ni / YSZ porous cermets for SOFC anode substrates prepared by tape casting and coat-mix 1 process.* 1999. **93**: p. 107-111.

183. Nabae, Y., et al., *Direct Oxidation of Methane by Pd–Ni Bimetallic Catalyst over Lanthanum Chromite Based Anode for SOFC.* Chemistry Letters, 2005. **34**(6): p. 774-775.
184. Datye, A.K., et al., *Particle size distributions in heterogeneous catalysts: What do they tell us about the sintering mechanism?* Catalysis Today, 2006. **111**(1–2): p. 59-67.
185. Jiang, S.P. and W. Wang, *Novel structured mixed ionic and electronic conducting cathodes of solid oxide fuel cells.* Solid State Ionics, 2005. **176**(15–16): p. 1351-1357.
186. Nie, L., et al., *Effects of pore formers on microstructure and performance of cathode membranes for solid oxide fuel cells.* Journal of Power Sources, 2011. **196**(23): p. 9975-9979.
187. Prestat, M., et al., *Effect of graphite pore former on oxygen electrodes prepared with $La_{0.6}Sr_{0.4}CoO_{3-\delta}$ nanoparticles.* Electrochemistry Communications, 2010. **12**(2): p. 292-295.
188. Sanson, A., P. Pinasco, and E. Roncari, *Influence of pore formers on slurry composition and microstructure of tape cast supporting anodes for SOFCs.* Journal of the European Ceramic Society, 2008. **28**(6): p. 1221-1226.
189. Haslam, J.J., et al., *Effects of the use of pore formers on performance of an anode supported solid oxide fuel cell.* Journal of the American Ceramic Society, 2005. **88**(3): p. 513-518.
190. Kumar, G.S., M. Raja, and S. Parthasarathy, *High performance electrodes with very low platinum loading for polymer electrolyte fuel cells.* Electrochimica Acta, 1995. **40**(3): p. 285-290.
191. Antolini, E., *Palladium in fuel cell catalysis.* Energy & Environmental Science, 2009. **2**(9): p. 915-931.
192. Bianchini, C. and P.K. Shen, *Palladium-Based Electrocatalysts for Alcohol Oxidation in Half Cells and in Direct Alcohol Fuel Cells.* Chemical Reviews, 2009. **109**(9): p. 4183-4206.
193. Grigoriev, S.A., et al., *On the possibility of replacement of Pt by Pd in a hydrogen electrode of PEM fuel cells.* International Journal of Hydrogen Energy, 2007. **32**(17): p. 4438-4442.
194. Say, Z., et al., *Palladium doped perovskite-based NO oxidation catalysts: The role of Pd and B-sites for NO_x adsorption behavior via in-situ spectroscopy.* Applied Catalysis B: Environmental, 2014. **154-155**: p. 51-61.
195. Li, X., et al., *Pd-Doped Perovskite: An Effective Catalyst for Removal of NO_x from Lean-Burn Exhausts with High Sulfur Resistance.* ACS Catalysis, 2013. **3**(6): p. 1071-1075.
196. Ai, N., et al., *Performance and stability of nano-structured Pd and $Pd_{0.95}M_{0.05}$ (M = Mn, Co, Ce, and Gd) infiltrated Y_2O_3–ZrO_2 oxygen electrodes of solid oxide electrolysis cells.* International Journal of Hydrogen Energy, 2013. **38**(36): p. 16569-16578.
197. Zhang, H., et al., *Shape-Controlled Synthesis of Pd Nanocrystals and Their Catalytic Applications.* Accounts of Chemical Research, 2013. **46**(8): p. 1783-1794.
198. Aricò, A.S., et al., *Synthesis of Pd_3Co_1@Pt/C core-shell catalysts for methanol-tolerant cathodes of direct methanol fuel cells.* Chemistry - A European Journal, 2014. **20**(34): p. 10679-10684.
199. Chen, A. and C. Ostrom, *Palladium-Based Nanomaterials: Synthesis and Electrochemical Applications.* Chemical Reviews, 2015. **115**(21): p. 11999-12044.
200. Composition, A.B., et al., *On the State of Pd in Perovskite-Type Oxidation Catalysts of.* Chemistry of Materials, 2012. **24**(10): p. 1864-1875.
201. Lee, W., et al., *Cation size mismatch and charge interactions drive dopant segregation at the surfaces of manganite perovskites.* J Am Chem Soc, 2013. **135**(21): p. 7909-25.
202. Tellez, H., et al., *Relating surface chemistry and oxygen surface exchange in $LnBaCo_2O_5$ air electrodes.* Faraday Discussions, 2015. **182**(0): p. 145-157.
203. Chen, Y., et al., *Impact of Sr segregation on the electronic structure and oxygen reduction activity of $SrTi_{1-x}Fe_xO_3$ surfaces.* Energy & Environmental Science, 2012. **5**(7): p. 7979.
204. Han, J., D.Y. Zemlyanov, and F.H. Ribeiro, *Catalytic combustion of methane on palladium single crystals.* Catalysis Today, 2006. **117**(4): p. 506-513.
205. Xiong, Y. and Y. Xia, *Shape-Controlled Synthesis of Metal Nanostructures: The Case of Palladium.* Advanced Materials, 2007. **19**(20): p. 3385-3391.
206. Fabien, S., et al., *Growth shapes of supported Pd nanocrystals on $SrTiO_3$.* Physical Review B, 2005. **72**(16).
207. Deak, D.S., *Strontium titanate surfaces.* Materials Science and Technology, 2007. **23**(2): p. 127-136.
208. Szot, K. and W. Speier, *Surfaces of reduced and oxidized $SrTiO_3$ from atomic force microscopy.* Physical Review B, 1999. **60**(8): p. 5909-5926.
209. Battle, P.D., et al., *A-Site Cation-Vacancy Ordering in $Sr_{1-3x/2}La_xTiO_3$: A Study by HRTEM.* Journal of Solid State Chemistry, 2000. **149**(2): p. 360-369.
210. Liu, D.-J. and M. Krumpelt, *Activity and Structure of Perovskites as Diesel-Reforming Catalysts for Solid Oxide Fuel Cell.* International Journal of Applied Ceramic Technology, 2005. **2**(4): p. 301-307.

211. Trasatti, S., *Electrocatalysis in the anodic evolution of oxygen and chlorine.* Electrochimica Acta, 1984. **29**(11): p. 1503-1512.
212. Ding, J., et al., *Platinum and platinum–ruthenium nanoparticles supported on ordered mesoporous carbon and their electrocatalytic performance for fuel cell reactions.* Electrochimica Acta, 2005. **50**(15): p. 3131-3141.
213. Dagle, R.A., Y. Wang, and G. Xia, *Selective CO methanation catalysis*, 2007.
214. Ma, H., et al., *Study of ruthenium oxide catalyst for electrocatalytic performance in oxygen evolution.* Journal of Molecular Catalysis A: Chemical, 2006. **247**(1–2): p. 7-13.
215. Pavlova, S., et al., *Syngas production by CO_2 reforming of methane using LnFeNi(Ru)O_3 perovskites as precursors of robust catalysts.* Catalysis Science & Technology, 2012. **2**(10): p. 2099.
216. Morimoto, Y. and E.B. Yeager, *Comparison of methanol oxidations on Pt, Pt|Ru and Pt|Sn electrodes.* Journal of Electroanalytical Chemistry, 1998. **444**(1): p. 95-100.
217. Watanabe, M. and S. Motoo, *Electrocatalysis by ad-atoms: Part III. Enhancement of the oxidation of carbon monoxide on platinum by ruthenium ad-atoms.* Journal of Electroanalytical Chemistry and Interfacial Electrochemistry, 1975. **60**(3): p. 275-283.
218. Si, Y., et al., *CO Tolerance of Carbon-Supported Platinum-Ruthenium Catalyst at Elevated Temperature and Atmospheric Pressure in a PEM Fuel Cell.* Journal of The Electrochemical Society, 2004. **151**(11): p. A1820-A1824.
219. R.G.Johnston. *Oxides Containing Ruthenium in Nuclear Waste Disposal*. 1980.
220. Panić, V.V., et al., *The properties of electroactive ruthenium oxide coatings supported by titanium-based ternary carbides.* Surface and Coatings Technology, 2007. **202**(2): p. 319-324.
221. Mota, N., et al., *Insights on the role of Ru substitution in the properties of $LaCoO_3$-based oxides as catalysts precursors for the oxidative reforming of diesel fuel.* Applied Catalysis B: Environmental, 2012. **113–114**: p. 271-280.
222. Mota, N., et al., *Ruthenium Effect on Formation Mechanism and Structural Characteristics of $LaCo_{1-x}Ru_xO_3$ Perovskites and Its Influence on Catalytic Performance for Hydrocarbon Oxidative Reforming.* The Journal of Physical Chemistry C, 2015. **119**(29): p. 16708-16723.
223. Over, H., *Surface Chemistry of Ruthenium Dioxide in Heterogeneous Catalysis and Electrocatalysis: From Fundamental to Applied Research.* Chemical Reviews, 2012. **112**(6): p. 3356-3426.
224. Cockcroft, J.K. and A.N. Fitch, *Chapter 2 Experimental Setups*, in *Powder Diffraction: Theory and Practice*2008, The Royal Society of Chemistry. p. 20-57.
225. Hubbell, J.H. and S.M. Seltzer. *X-Ray Mass Attenuation Coefficients*. 1996; Available from: https://www.nist.gov/pml/x-ray-mass-attenuation-coefficients.
226. Lide, D.R., *CRC Handbook of Chemistry and Physics, 84th Edition,*2003, Boca Ration, FL: CRC Press.
227. Tao, S. and J.T.S. Irvine, *Synthesis and Characterization of $La_{0.75}Sr_{0.25}Cr_{0.5}Mn_{0.5}O_{3-\delta}$, a Redox-Stable, Efficient Perovskite Anode for SOFCs.* Journal of The Electrochemical Society, 2004. **151**(2): p. A252-A252.
228. Plint, S.M., et al., *Electronic transport in the novel SOFC anode material $La_{1-x}Sr_xCr_{0.5}Mn_{0.5}O_{3\pm\delta}$.* Solid State Ionics, 2006. **177**(19–25): p. 2005-2008.
229. Bruce, M.K., M. van den Bossche, and S. McIntosh, *The Influence of Current Density on the Electrocatalytic Activity of Oxide-Based Direct Hydrocarbon SOFC Anodes.* Journal of The Electrochemical Society, 2008. **155**(11): p. B1202.
230. Nabae, Y., et al., *Direct Oxidation of Methane by Pd-Ni Bimetallic Catalyst over Lanthanum Chromite Based Anode for SOFC.* Chemistry Letters, 2005. **34**(6): p. 774-775.
231. Barison, S., et al., *Novel Ru/$La_{0.75}Sr_{0.25}Cr_{0.5}Mn_{0.5}O_{3-\delta}$ catalysts for propane reforming in IT-SOFCs.* Solid State Ionics, 2010. **181**(5-7): p. 285-291.
232. Sauvet, A.L. and J. Fouletier, *Catalytic properties of new anode materials for solid oxide fuel cells operated under methane at intermediary temperature.* Journal of Power Sources, 2001. **101**(2): p. 259-266.
233. Paturzo, L., et al., *An Ru-based catalytic membrane reactor for dry reforming of methane—its catalytic performance compared with tubular packed bed reactors.* Catalysis Today, 2003. **82**(1–4): p. 57-65.
234. Lo Faro, M., et al., *Propane conversion over a Ru/CGO catalyst and its application in intermediate temperature solid oxide fuel cells.* Journal of Applied Electrochemistry, 2007. **37**(2): p. 203-208.
235. Fernández-Bertran, J.F., *Mechanochemistry: an overview*, in *Pure and Applied Chemistry*1999. p. 581.

236. Bruckmann, A., A. Krebs, and C. Bolm, *Organocatalytic reactions: effects of ball milling, microwave and ultrasound irradiation.* Green Chemistry, 2008. **10**(11): p. 1131-1141.
237. Zwick, A., et al., *Lattice modes in the linear chain compound $ZrTe_5$.* Solid State Communications, 1982. **44**(2): p. 89-94.
238. Tao, S. and J.T.S. Irvine, *Phase Transition in Perovskite Oxide $La_{0.75}Sr_{0.25}Cr_{0.5}Mn_{0.5}O_3$ observed by in Situ High-Temperature Neutron Powder Diffraction.* 2006(9): p. 5453-5460.
239. Raj, E.S. and J.T.S. Irvine, *Synthesis and characterization of $(Pr_{0.75}Sr_{0.25})_{1-x}Cr_{0.5}Mn_{0.5}O_{3-\delta}$ as anode for SOFCs.* Solid State Ionics, 2010. **180**(40): p. 1683-1689.
240. Wan, J.-H., J.H. Zhu, and J.B. Goodenough, *Solid Oxide Fuel Cell with a $La_{0.75}Sr_{0.25}Cr_{0.5}Mn_{0.5}O_3$ Anode and an LSGM Electrolyte.* Meeting Abstracts, 2006. **MA2005-01**(30): p. 1216.
241. Shannon, R.D., Acta. Crystallogr., Sect. A, 1976. **32**: p. 751.
242. Périllat-Merceroz, C., et al., *Synthesis and Study of a Ce-Doped La/Sr Titanate for Solid Oxide Fuel Cell Anode Operating Directly on Methane.* Chemistry of Materials, 2011. **23**(6): p. 1539-1550.
243. Shiozaki, R., et al., *Partial oxidation of methane over a Ni/BaTiO3 catalyst prepared by solid phase crystallization.* Journal of the Chemical Society, Faraday Transactions, 1997. **93**(17): p. 3235-3242.
244. Jiang, S.P., Y.Y. Duan, and J.G. Love, *Fabrication of High-Performance Ni / Y_2O_3 ZrO_2 Cermet Anodes of Solid Oxide Fuel Cells by Ion Impregnation.* Journal of The Electrochemical Society, 2002. **149**(9): p. A1175-A1183.
245. Earnshaw, A.N.G., *27 - Nickel, Palladium and Platinum A2 - GREENWOOD, N.N*, in *Chemistry of the Elements (Second Edition)*, A. Earnshaw, Editor 1997, Butterworth-Heinemann: Oxford. p. 1144-1172.
246. Yokokawa, H., et al., *Thermodynamic stability of perovskites and related compounds in some alkaline earth-transition metal-oxygen systems.* Journal of Solid State Chemistry, 1991. **94**(1): p. 106-120.
247. Boulfrad, S., C. Mark, and J.T.S. Irvine, *Adhesion and Percolation Parameters in Two Dimensional Pd–LSCM Composites for SOFC Anode Current Collection.* Advanced Functional Materials, 2010. **20**(5): p. 861-866.
248. Muñoz, M.C., et al., *Adhesion at metal–ZrO_2 interfaces.* Surface Science Reports, 2006. **61**(7): p. 303-344.
249. Perathoner, S. and G. Centi, *CO_2 Recycling: A Key Strategy to Introduce Green Energy in the Chemical Production Chain.* ChemSusChem, 2014. **7**(5): p. 1274-1282.